How often do unknown fathers tangle family trees? p. 1030

Peroxisomes and Long Covid pp. 1039 & 1054

Nanosheets strengthen solar cells pp. 1040 & 1069

Science

$15
7 MARCH 2025
science.org

AAAS

FATE OF THE FORESTS

Tropical forest responses to climate change pp. 1057 & 1058

Congratulations

2025 HILL PRIZES RECIPIENTS

Congratulations to these six recipients and their winning proposals for pivotal research and scientific innovation.

HILL PRIZES

Kenneth M. Hargreaves, D.D.S., Ph.D.
UT Health San Antonio

David J. Mangelsdorf, Ph.D. (NAM, NAS)
UT Southwestern Medical Center

Peter J. Hotez, M.D., Ph.D. (NAM)
Baylor College of Medicine

Robert De Lorenzo, M.D.
EmergenceMed LLC

James Chelikowsky, Ph.D.
The University of Texas at Austin

Joan Frances Brennecke, Ph.D. (NAE)
The University of Texas at Austin

$3 Million Awarded by Lyda Hill Philanthropies to Texas Researchers to Accelerate High-Risk, High-Impact Ideas

The Hill Prizes are selected by a committee of Texas Academy of Medicine, Engineering, Science and Technology (TAMEST) members who identify and recognize exceptional innovators by providing seed funding to advance groundbreaking science highlighting Texas as a premier destination for world-class research.

Each 2025 Hill Prizes recipient received $500K for their winning proposal.

LYDA HILL PHILANTHROPIES

TAMEST
Texas Academy of Medicine, Engineering, Science and Technology

Applications for the 2026 Hill Prizes will open on May 1, 2025.

LEARN MORE ▸ TAMEST.org/Hill-Prizes

CONTENTS

7 MARCH 2025
VOLUME 387 • ISSUE 6738

1030

NEWS

IN BRIEF

IN DEPTH

FEATURES

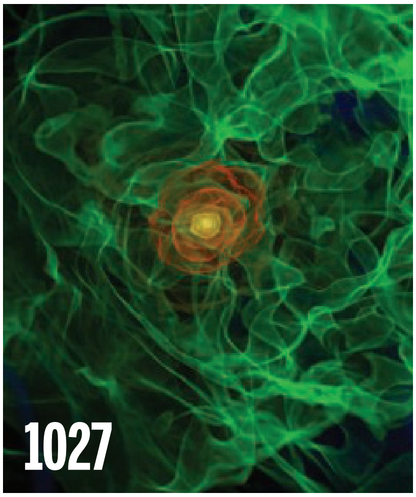

1027

CREDITS: (TOP TO BOTTOM) KU LEUVEN: RALF KAEHLER AND TOM ABEL/KIPAC/STANFORD/SLAC

INSIGHTS

PERSPECTIVES

POLICY FORUM

NEW ENGLAND
Biolabs®

Celebrating 50 years of Passion for Science.

We all share a passion for science. Curiosity inspires us. The research community's quest to find answers to pressing global issues, such as improving human health, addressing food shortages, and combating climate change, is what drives us.

NEB was created by scientists for scientists, and we prioritize the advancement of science, stewardship of the environment, and giving back to the world around us. Since our establishment in 1974, we have remained committed to developing high quality, innovative products that not only empower your research but also our own. Our profits have always funded an extensive research program, which we believe is critical for staying connected to our customers and helping to drive scientific breakthroughs.

As we reflect on the last 50 years and look toward the future, we are excited to support your research and help you address these complex challenges.

We hope that by working together, we can shape the science of tomorrow.

Thank you for your continued trust and support. Find out how you can help us celebrate 50 years by visiting
www.neb.com/NEBturns50

Products and content are covered by one or more patents, trademarks and/or copyrights owned or controlled by New England Biolabs, Inc (NEB). The use of trademark symbols does not necessarily indicate that the name is trademarked in the country where it is being read; it indicates where the content was originally developed. See www.neb.com/trademarks. The use of these products may require you to obtain additional third-party intellectual property rights for certain applications. For more information, please email busdev@neb.com.

© Copyright 2024, New England Biolabs, Inc.; all rights reserved.

BOOKS *ET AL.*

LETTERS

RESEARCH

IN BRIEF

RESEARCH ARTICLES

DEPARTMENTS

ON THE COVER

In Mesoamerican cloud forests, such as this one in the El Triunfo Biosphere Reserve in Mexico, climate change and deforestation are leading to plant species moving upslope. However, an analysis of forest plant traits from across the tropical Americas suggests that forests are not changing fast enough to keep up with climate change. See pages 1057 and 1058. *Photo: Luis F. Rivera Lezama*

PHOTO: DAVID W. INOUYE

SCIENCE (ISSN 0036-8075) is published weekly on Friday, except last week in December, by the American Association for the Advancement of Science, 1200 New York Avenue, NW, Washington, DC 20005. Periodicals mail postage (publication No. 484460) paid at Washington, DC, and additional mailing offices. Copyright © 2025 by the American Association for the Advancement of Science. The title SCIENCE is a registered trademark of the AAAS. Domestic individual membership, including subscription (12 months): $165 ($74 allocated to subscription). Domestic institutional subscription (51 issues): $2865; Foreign postage extra: Air assist delivery: $135. First class, airmail, student, and emeritus rates on request. Canadian rates with GST available upon request, GST #125488122. Publications Mail Agreement Number 1069624. **Printed in the U.S.A.**
Change of address: Allow 4 weeks, giving old and new addresses and 8-digit account number. **Postmaster:** Send change of address to AAAS, P.O. Box 96178, Washington, DC 20090–6178. **Single-copy sales:** $15 each plus shipping and handling available from backissues.science.org; bulk rate on request. **Authorization to reproduce** material for internal or personal use under circumstances not falling within the fair use provisions of the Copyright Act can be obtained through the Copyright Clearance Center (CCC), www.copyright.com. The identification code for *Science* is 0036-8075. *Science* is indexed in the *Reader's Guide to Periodical Literature* and in several specialized indexes.

Science AAAS

Editor-in-Chief Holden Thorp, hthorp@aaas.org

Executive Editor Valda Vinson

Editor, Research Jake S. Yeston **Editor, Insights** Lisa D. Chong **Deputy Executive Editor** Lauren Kmec

DEPUTY EDITORS Stella M. Hurtley (UK), Phillip D. Szuromi, Sacha Vignieri **SR. EDITORS** Caroline Ash (UK), Michael A. Funk, Angela Hessler, Di Jiang, Priscilla N. Kelly, Marc S. Lavine (Canada), Sarah Lempriere (UK), Mattia Maroso, Yevgeniya Nusinovich, Ian S. Osborne (UK), L. Bryan Ray, H. Jesse Smith, Keith T. Smith (UK), Jelena Stajic, Peter Stern (UK), Yury V. Suleymanov, Valerie B. Thompson, Brad Wible **ASSOCIATE EDITORS** Jack Huang, Sumin Jin, Bianca Lopez, Sarah Ross (UK), Madeleine Seale (UK), Corinne Simonti, Ekeoma Uzogara **SENIOR LETTERS EDITOR** Jennifer Sills **NEWSLETTER EDITOR** Christie Wilcox **RESEARCH & DATA ANALYST** Jessica L. Slater **LEAD CONTENT PRODUCTION EDITORS** Chris Filiatreau, Harry Jach **SR. CONTENT PRODUCTION EDITOR** Amelia Beyna **CONTENT PRODUCTION EDITORS** Anne Abraham, Robert French, Julia Haber-Katris, Nida Masiulis, Abigail Shashikanth, Suzanne M. White **SR. EDITORIAL MANAGERS** Carolyn Kyle, Beverly Shields **SR. PROGRAM ASSOCIATE** Maryrose Madrid **EDITORIAL ASSOCIATES** Aneera Dobbins, Joi S. Granger, Lisa Johnson, Anita Wynn **SR. EDITORIAL COORDINATORS** Jeffrey Hearn, Alexander Kief, Ronmel Navas, Jerry Richardson, Isabel Schnaidt, Alice Whaley (UK), Brian White **EDITORIAL COORDINATORS** Clair Goodhead (UK), Kat Kirkman, Samantha Price **ADMINISTRATIVE COORDINATOR** Karalee P. Rogers **ASI DIRECTOR, OPERATIONS** Janet Clements (UK) **ASI OFFICE MANAGER** Victoria Smith **ASI SR. OFFICE ADMINISTRATORS** Dawn Titheridge (UK), Jessica Waldock (UK) **COMMUNICATIONS DIRECTOR** Meagan Phelan **DEPUTY DIRECTOR** Matthew Wright **SENIOR WRITERS** Walter Beckwith, Joseph Cariz **WRITERS** Abigail Eisenstadt, Mahathi Ramaswamy **SENIOR COMMUNICATIONS ASSOCIATES** Zachary Graber, Sarah Woods **COMMUNICATIONS ASSOCIATES** Kiara Brooks, Haley Riley, Mackenzie Williams

News Editor Tim Appenzeller

NEWS MANAGING EDITOR John Travis **INTERNATIONAL EDITOR** David Malakoff **DEPUTY NEWS EDITORS** Rachel Bernstein, Shraddha Chakradhar, Elizabeth Culotta, Martin Enserink, David Grimm, Eric Hand, Kelly Servick, Matt Warren (Europe) **SR. CORRESPONDENTS** Daniel Clery (UK), Jon Cohen, Jeffrey Mervis, Elizabeth Pennisi **ASSOCIATE EDITORS** Jeffrey Brainard, Michael Price **NEWS REPORTERS** Adrian Cho, Jennifer Couzin-Frankel, Phie Jacobs, Jocelyn Kaiser, Rodrigo Pérez Ortega (Mexico City), Robert F. Service, Erik Stokstad, Paul Voosen, Meredith Wadman **CONTRIBUTING CORRESPONDENTS** Vaishnavi Chandrashekhar, Dan Charles, Warren Cornwall, Andrew Curry (Berlin), Ann Gibbons, Sam Kean, Eli Kintisch, Kai Kupferschmidt (Berlin), Andrew Lawler, Mitch Leslie, Virginia Morell, Dennis Normile (Tokyo), Cathleen O'Grady, Elisabeth Pain (Careers), Charles Piller, Richard Stone (Senior Asia Correspondent), Gretchen Vogel (Berlin), Lizzie Wade (Mexico City) **CAREERS** Katie Langin (Associate Editor) **INTERNS** Hannah Richter **COPY EDITORS** Julia Cole (Senior Copy Editor), Hannah Knighton, Cyra Master (Copy Chief) **ADMINISTRATIVE SUPPORT** Meagan Weiland

Creative Director Beth Rakouskas

DESIGN MANAGING EDITOR Chrystal Smith **GRAPHICS MANAGING EDITOR** Chris Bickel **PHOTOGRAPHY MANAGING EDITOR** Emily Petersen **MULTIMEDIA MANAGING PRODUCER** Kevin McLean **DIGITAL DIRECTOR** Kara Estelle-Powers **DESIGN EDITOR** Marcy Atarod **DESIGNER** Noelle Jessup **SENIOR SCIENTIFIC ILLUSTRATOR** Noelle Burgess **SCIENTIFIC ILLUSTRATORS** Austin Fisher, Kellie Holoski, Ashley Mastin **SENIOR GRAPHICS EDITOR** Monica Hersher **GRAPHICS EDITOR** Veronica Penney **SENIOR GRAPHICS SPECIALISTS** Holly Bishop, Nathalie Cary **SENIOR PHOTO EDITOR** Charles Borst **PHOTO EDITOR** Elizabeth Billman **SENIOR PODCAST PRODUCER** Sarah Crespi **SENIOR VIDEO PRODUCER** Meagan Cantwell **SOCIAL MEDIA STRATEGIST** Jessica Hubbard **SOCIAL MEDIA PRODUCER** Sabrina Jenkins **WEB DESIGNER** Jennie Pajerowski

Chief Executive Officer and Executive Publisher Sudip Parikh

Publisher, Science Family of Journals Bill Moran

DIRECTOR, BUSINESS SYSTEMS AND FINANCIAL ANALYSIS Randy Yi **DIRECTOR, BUSINESS OPERATIONS & ANALYSIS** Eric Knott **MANAGER, BUSINESS OPERATIONS** Jessica Tierney **MANAGER, BUSINESS ANALYSIS** Cory Lipman **BUSINESS ANALYSTS** Kurt Ennis, Maggie Clark, Isacco Fusi **BUSINESS OPERATIONS ADMINISTRATOR** Taylor Fisher **DIGITAL SPECIALIST** Marissa Zuckerman **SENIOR PRODUCTION MANAGER** Jason Hillman **SENIOR MANAGER, PUBLISHING AND CONTENT SYSTEMS** Marcus Spiegler **CONTENT OPERATIONS MANAGER** Rebecca Doshi **SENIOR CONTENT & PUBLISHING SYSTEMS SPECIALIST** Jacob Hedrick **SENIOR PRODUCTION SPECIALIST** Kristin Wowk **PRODUCTION SPECIALISTS** Kelsey Cartelli, Audrey Diggs **DIGITAL PRODUCTION MANAGER** Lisa Stanford **ADVERTISING PRODUCTION OPERATIONS MANAGER** Deborah Tompkins **DESIGNER, CUSTOM PUBLISHING** Jeremy Huntsinger **SR. TRAFFIC ASSOCIATE** Christine Hall **SPECIAL PROJECTS ASSOCIATE** Shantel Agnew

MARKETING DIRECTOR Sharice Collins **ASSOCIATE DIRECTOR, BUSINESS DEVELOPMENT** Justin Sawyers **GLOBAL MARKETING MANAGER** Allison Pritchard **ASSOCIATE DIRECTOR, MARKETING SYSTEMS & STRATEGY** Aimee Aponte **JOURNALS MARKETING MANAGER** Shawana Arnold **MARKETING ASSOCIATES** Ashley Hylton, Lorena Chirinos Rodriguez, Jenna Voris **SENIOR DESIGNER** Kim Huynh

DIRECTOR AND SENIOR EDITOR, CUSTOM PUBLISHING Erika Gebel Berg

DIRECTOR, PRODUCT & PUBLISHING DEVELOPMENT Chris Reid **DIRECTOR, PRODUCT MANAGEMENT** Kris Bishop **PRODUCT DEVELOPMENT MANAGER** Scott Chernoff **PUBLISHING PLATFORM MANAGER** Jessica Loayza **SR. PRODUCT ASSOCIATE** Robert Koepke **PRODUCT ASSOCIATES** Caroline Breul, Anne Mason

ASSOCIATE DIRECTOR, INSTITUTIONAL LICENSING MARKETING Kess Knight **BUSINESS DEVELOPMENT MANAGER** Rasmus Andersen **ASSOCIATE DIRECTOR, INSTITUTIONAL LICENSING SALES** Ryan Rexroth **INSTITUTIONAL LICENSING MANAGER** Nazim Mohammedi, Claudia Paulsen-Young **SENIOR MANAGER, INSTITUTIONAL LICENSING OPERATIONS** Judy Lillibridge **MANAGER, RENEWAL & RETENTION** Lana Guz **SYSTEMS & OPERATIONS ANALYST** Ben Teincuff **FULFILLMENT ANALYST** Aminta Reyes

ASSOCIATE DIRECTOR, US ADVERTISING Stephanie O'Connor **US MID WEST, MID ATLANTIC AND SOUTH EAST SALES** Chris Hoag **US WEST COAST SALES** Lynne Stickrod **ASSOCIATE DIRECTOR, INTERNATIONAL** Roger Goncalves **SALES REP, ROW** Sarah Lelarge **SALES ADMIN ASSISTANT, ROW** Victoria Glasbey **DIRECTOR OF GLOBAL COLLABORATION AND ACADEMIC PUBLISHING RELATIONS, ASIA** Xiaoying Chu **ASSOCIATE DIRECTOR, INTERNATIONAL COLLABORATION** Grace Yao **SALES MANAGER** Danny Zhao **MARKETING MANAGER** Kilo Lan **ASCA CORPORATION, JAPAN** Rie Rambelli (Tokyo), Miyuki Tani (Osaka)

DIRECTOR, COPYRIGHT, LICENSING AND SPECIAL PROJECTS Emilie David **RIGHTS AND PERMISSIONS ASSOCIATE** Elizabeth Sandler **LICENSING ASSOCIATE** Virginia Warren **RIGHTS AND LICENSING COORDINATOR** Dana James **CONTRACT SUPPORT SPECIALIST** Michael Wheeler

---

EDITORIAL
science_editors@aaas.org

NEWS
science_news@aaas.org

INFORMATION FOR AUTHORS
science.org/authors/science-information-authors

REPRINTS AND PERMISSIONS
science.org/help/reprints-and-permissions

MULTIMEDIA CONTACTS
SciencePodcast@aaas.org
ScienceVideo@aaas.org

MEDIA CONTACTS
scipak@aaas.org

PRODUCT ADVERTISING & CUSTOM PUBLISHING
advertising.science.org/products-services
science_advertising@aaas.org

CLASSIFIED ADVERTISING
advertising.science.org/science-careers
advertise@sciencecareers.org

JOB POSTING CUSTOMER SERVICE
employers.sciencecareers.org
support@sciencecareers.org

MEMBERSHIP AND INDIVIDUAL SUBSCRIPTIONS
science.org/subscriptions

MEMBER BENEFITS
aaas.org/membership/benefits

INSTITUTIONAL SALES AND SITE LICENSES
science.org/librarian

EDITORIAL

Is the air we breathe safe?

Kimberly Prather is a distinguished professor at Scripps Institution of Oceanography with a joint appointment in the Department of Chemistry and Biochemistry at the University of California San Diego, La Jolla, CA, USA. kprather@ucsd.edu

Kelley Barsanti is a scientist in the Atmospheric Chemistry Observations and Modeling Laboratory at the NSF National Center for Atmospheric Research, Boulder, CO, USA. barsanti@ucar.edu

Is the air we breathe safe? This seemingly straightforward question is often unanswerable because regulations, monitoring approaches, and reporting structures cannot keep up with the rapid human-induced shifts to the planet and atmosphere. The air is becoming more burdened by pollutants from new sources such as intense fires at the wildland-urban interface, an ever-expanding area where human development meets natural habitats. Air pollution is the second leading cause of human death worldwide, a statistic that excludes numerous indoor and acute outdoor exposures. To protect public health everywhere, air quality standards must be modernized, advanced instrumentation mobilized, and collaborative networks established to move air quality assessment into the 21st century.

A major challenge is updating the Air Quality Index (AQI). The AQI was developed by the United States Environmental Protection Agency and is a key global metric for communicating air quality. However, it only accounts for a handful of pollutants targeted in the 1970s, leaving out thousands of more recently identified volatile organic compounds and other airborne toxins that originate from contemporary building materials, industrial processes and accidents, and urban fires. This includes the burning of homes, cars, plastics, batteries, and other matter at burgeoning urban-wildland boundaries. Consider the 2025 fires in Los Angeles, California, where AQI readings reported “good” air quality once visible smoke blew offshore. This misleadingly suggested that the air was safe even though invisible toxins were still being released. In its current form, the AQI cannot accurately convey the risks of toxins released from such urban fires.

> “Air pollution is the second leading cause of human death worldwide...”

Airborne bioparticles, such as bacteria, fungi, and viruses, also affect human health, yet remain understudied. Although respiratory viruses such as influenza and severe acute respiratory syndrome coronavirus 2 have drawn attention, other microbes—particularly those released outdoors by fires—are often overlooked. Inconsistent sampling and analysis protocols make it difficult to compare their prevalence over time and space and to assess overall health impacts. A coordinated global mapping system that draws on contributions from government, academic, private, and community scientists could merge bioparticle and chemical pollutant data from a given location with a time-linked event map. This would provide a comprehensive view of atmospheric composition and air quality and substantially improve predictive models.

Existing air quality metrics, monitoring networks, and pollutant databases are insufficient to quantify the extent to which urban fires increase harmful air pollutants. Furthermore, standards for human exposures based on the effects of a growing multitude of air pollutants on health are needed. The gap between research and regulations is reminiscent of the aftermath of 9/11, when first responders were wrongly assured of safe air, only to face serious health issues later. Sadly, responses to episodic and evolving air pollution threats remain inadequate.

Although indoor air pollutants pose health risks—particularly in urban settings where people spend about 90% of their time indoors—the problem is more manageable with specialized filters for fine particles and activated carbon filters for harmful gases. Such interventions are inexpensive and can reduce daily exposure, but are unfortunately limited to major pollution events such as wildfires. Increasing accessibility to these filtration methods for indoor air management would substantially improve global public health.

Meanwhile, although technology exists to characterize air pollutants, epidemiological studies are hindered by fragmented data collection methods, inconsistent analysis protocols, and siloed data storage. Transformative progress requires coordinated measurement efforts, standardized protocols, and open-access global frameworks that link pollutant levels with location-specific variables. By integrating meteorological data, health data, computational systems biology, and artificial intelligence into a global mapping system, baselines can be established, anomalies identified, and the pollutant mixtures posing great risks to health identified.

People everywhere face air quality challenges that demand equitable solutions. In the United States, concern over air pollutants is surging at a moment when federal support for environmental protections is under threat. Yet, with adequate funding from diverse sources, scientists can tackle this solvable problem. By harnessing existing technologies, developing a global mapping system, forming strong inclusive partnerships, and establishing health-based metrics for emerging airborne pollutants, the ubiquitous and challenging question of whether the air is safe to breathe could well be answered.

–Kimberly Prather and Kelley Barsanti

10.1126/science.adx1128

NEWS

IN BRIEF

Edited by **Jeffrey Brainard**

A tugboat pushes a container ship at a port in Qingdao, China. The country is a large manufacturer of research equipment.

PHOTO: YU FANGPING/FEATURE CHINA/FUTURE PUBLISHING VIA GETTY IMAGES

TRUMP TRACKER

Tariffs imposed, scientists reinstated, peer review partly revived

LAB EQUIPMENT INFLATION
Costs for lab and medical equipment are expected to rise in the United States after President Donald Trump this week expanded tariffs to include all imports from the U.S.'s three largest trading partners. Goods from Mexico and Canada face tariffs of 25%, and those from China have a 20% tariff, up from 10% in February. The three countries are deeply involved in the manufacture of scientific instruments used in the U.S., and the tariffs are expected to disrupt supply chains for these products globally. China has already introduced its own retaliatory measures, including a ban on imports of genetic sequencers from the U.S. company Illumina. According to Reuters, China makes up about 7% of Illumina's sales.

NSF EMPLOYEES RETURN The U.S. National Science Foundation (NSF) this week reinstated all but two of 86 full-time employees who had probationary status because they had been recently hired or promoted. The agency had fired them on 18 February as part of a purge of workers across dozens of federal agencies, ordered by the Trump administration. Not affected by NSF's action, however, are some 84 part-time scientists dismissed at the same time. NSF's announcement came after a federal judge on 27 February ordered the White House Office of Personnel Management to rescind the directive to fire probationary employees.

SOME NIH PEER REVIEW RESTARTS The U.S. National Institutes of Health (NIH) has resumed scheduling at least some meetings essential to approving new grants. Fifty "study section" panels are expected to start meeting later this month and into April, on topics such as kidney disease and cancer drugs. The administration continued this week to block the *Federal Register* notices required for meetings of the NIH institute councils that provide a second, mandatory level of peer review. The delays have delayed reviews of at least 16,000 grant proposals, NPR reported.

COLLINS DEPARTS NIH Former NIH Director Francis Collins announced his retirement, effective 28 February, in a statement that defended NIH and its staff. Collins, 74, who joined the agency in 1993 to lead the public effort to sequence the human genome, stepped down as director in 2021 but still ran a 12-person lab on the agency's campus in Bethesda, Maryland. In his statement, he writes that NIH was long "seen as a high priority and a nonpolitical bipartisan effort." In an indirect reference to job cuts there by the Trump administration—some on the false pretense that the employees were underperforming—he calls his NIH colleagues "individuals of extraordinary intellect and integrity, selfless and hard-working. … They deserve the utmost respect and support of all Americans." (see story, p. 1028).

DEFENSE SOCIAL SCIENCE CUT
The U.S. Department of Defense (DOD) has canceled dozens of grants in a landmark project designed to fund social science research with important implications for national security. The Minerva Research Initiative also withdrew a solicitation for new grants. Many researchers worry the administration will dismantle the entire program, which has supported studies of violent extremism, military deterrence, and threats from climate change, for example. In 2020, during Trump's first term, some DOD officials proposed diverting its funding to other priorities—despite a review the year before by the National Academies of Sciences,

Engineering, and Medicine that lauded research funded by the initiative.

CREDIT CARD FREEZE The White House issued a 30-day freeze on use of government-issued credit cards, which has blocked federal health scientists from traveling to conferences and purchasing lab supplies. The executive order, issued on 26 February, will also require a written, publicly posted justification for federally funded conference travel. Among the blocked cards are so-called government purchase cards, which some senior government scientists had used for costs below $10,000, such as for critical lab reagents for detecting pathogens. One told *Science* this avoids the expense of a multimonth contract solicitation.

INTERNSHIPS CURTAILED NSF and NIH are shrinking their support for long-running programs that offer summer research opportunities to thousands of college students, many from groups historically underrepresented in science. In recent weeks, NSF decided not to renew grants from its $80-million-a-year Research Experiences for Undergraduates program to several universities, prompting them to end their internships. The reasons appear to include NSF's concern that the program may clash with Trump's ban on funding aimed at promoting diversity. NIH, for its part, paused its Summer Internship Program, which supports college students through medical school graduates. An NIH official describes the step as "a challenging decision" and says NIH hopes to resume the program in 2026.

GROUPS STAND UP More than 40 scientific societies and other organizations—representing nearly 100,000 scientists across many fields—have signed a letter urging members of Congress to preserve federally funded research and protect federal scientists. The letter, organized by the Union of Concerned Scientists, remains open for more signers.

Asilomar redux ponders new risks

GOVERNANCE | At a meeting last week in California to mark the 50th anniversary of a landmark conference on scientific self-regulation, researchers explored risks and benefits posed by current-day biotechnologies—but the event, unlike its predecessor, ended with no consensus public statement. At the original Asilomar Conference on Recombinant DNA, molecular biologists famously grappled with the pros and cons of their new molecular tools. Last week's sessions at the successor gathering—the Spirit of Asilomar and the Future of Biotechnology, held at the same location as the one in 1975—featured a far more diverse group of scientists and also included ethicists, lawyers, conservationists, national security experts, and former government officials. The topics discussed, also wide ranging, included the promises and perils of using artificial intelligence in biology, creating synthetic cells, studying dangerous pathogens in the lab, and genetically modifying crops. Working groups are expected to issue statements that outline ways to reduce the risks of these novel technologies without stifling innovation.

Asteroid's impact risk falls

SPACE DEFENSE | After crunching additional data, astronomers last week downgraded the risk that the asteroid 2024 YR4 will strike Earth in 2032, pegging it at just 0.004%. That estimate, from NASA's Center for Near-Earth Object Studies, is well below the 3.1% probability given for the 40- to 90-meter-wide object just the week before, the greatest risk ever calculated for an object of this size or larger. NASA says there is still a 1.7% chance the space rock could hit the Moon in December 2032.

Commercial probe sticks landing

PLANETARY SCIENCE | In its first attempt, Firefly Aerospace on 2 March became the first private company or organization to land a probe on the Moon without a hitch. Its Blue Ghost M1 lander, funded by a $101 million contract from NASA's Commercial Lunar Payload Services (CLPS) program, touched down on an ancient volcanic plain on the Moon's near side. Unlike two private landers that tipped over during touchdown last year, limiting their capability, the Blue Ghost remained upright and has begun its scheduled 2 weeks of science operations. Its instruments include a vacuumlike sampler to capture lunar soil, a small heat probe, and a sounder that will record variations in the Moon's electric and magnetic field to study its interior. The Blue Ghost could soon have company: Another CLPS contractor, Intuitive Machines, was scheduled to put down a lander on the Moon's south pole this week after *Science* went to press, and a lander from a company in Japan was en route.

#MeToo, not fraud, hits citations

PUBLISHING | Scholars accused of sexual misconduct see a drop in their citations after public allegations, whereas those accused of scientific misconduct do not, a study has found. A research team examined the citation trajectories of researchers publicly accused of sexual misconduct, such as astronomer Geoff Marcy of the University of California, Berkeley, and scientific misconduct, such as nutrition researcher Brian Wansink, formerly of Cornell University. The team focused only on scholars whose accusations had received media attention to ensure that other researchers would likely have heard the allegations. They plotted the researchers' growing citations for 10 years before the allegations, and 3 years after. Compared with controls matched on their discipline, prominence, and other characteristics, researchers accused of sexual misconduct suffered a "citation penalty," but those accused of scientific misconduct were unaffected, on average, the study's authors report this week in *PLOS ONE*. They also surveyed other researchers, who said they would be more likely to cite someone accused of sexual misconduct than scientific misconduct—the opposite of what the citation analysis showed.


With Earth in the distance, the Blue Ghost lander cast a shadow after alighting on the Moon.

PHOTO: FIREFLY AEROSPACE

GLOBAL HEALTH

Health aid cuts spur African calls for self-reliance

Researchers say crisis is an opportunity to reduce dependence on foreign donors

By **Abdullahi Tsanni**, *in Lagos, Nigeria*

For many African researchers and health officials, the past 6 weeks have been nothing short of shocking. The freeze on U.S. foreign aid, followed by the 25 February announcement that President Donald Trump's administration had terminated 90% of all awards from the U.S. Agency for International Development (USAID), have caused outrage and despair around the continent. Billions in funding for disease control vanished overnight, clinical trials were abruptly halted, and hundreds of local collaborators were sent home. Models predict that hundreds of thousands of lives are at risk if the funding is not replaced.

But as the scope of the devastation sinks in, the cuts are also rekindling discussions about Africa's dependence on foreign aid to support its people's health. The sudden U.S. withdrawal is a "wake-up call that we cannot rely on other countries to fund the things that we need to do," says Salim Abdool Karim, who runs the Centre for the AIDS Programme of Research in South Africa. "We have to become self-reliant."

Indeed, some African scientists see the U.S. move as an opportunity. "Let Trump teach us a lesson, it's a good thing, so that African governments can start taking responsibility," says molecular biologist Christian Happi, who heads the Institute of Genomics and Global Health at Redeemer's University in Ede, Nigeria. "This whole attitude of begging, crying, and throwing hands up needs to stop." Countries now "have a golden opportunity to do, under duress, what they should have done during relatively calm periods," Olusoji Adeyi, president of a Washington, D.C.–based consultancy named Resilient Health Systems and former World Bank official, wrote in a 25 February commentary in *Development Today*. In the future, health assistance programs—which can run for decades—should have a "sunset" date after which country governments take over, argued Adeyi, who is from Nigeria.

USAID spent some $12 billion in sub-Saharan Africa in 2024, largely in humanitarian and health aid. Most of that now appears to be gone—although at press time the administration was reversing course on some terminated awards. Among the programs that were axed are the President's Malaria Initiative (PMI), which fights malaria in dozens of African nations, and projects for delivering vaccines against polio, rotavirus, and COVID-19. But the biggest hit is to the President's Emergency Plan for AIDS Relief (PEPFAR), which supports HIV treatment and prevention programs in more than 20 countries on the continent. PEPFAR's largest beneficiary, South Africa—which has more people living with HIV than any other country—will lose $439.5 million this fiscal year. The program's sudden termination "was deliberately brutal, deliberately disruptive, and chaotic," Karim says. "They want the world to know they call the shots."

Africa is highly dependent on other types of foreign health aid as well. The Global Fund to Fight AIDS, Tuberculosis, and Malaria spends about 70% of its $5 billion annual budget to provide African countries with drugs, mosquito nets, diagnostics, and training. Gavi, the Vaccine Alliance spent some $1.2 billion in 2023 to provide Africa with vaccines for 20 infectious diseases. (Both receive funding from the U.S. government that has not been affected so far.)

Africa's dependence on such aid has deep roots. Many countries inherited health systems that primarily served their former colonizers, says Francisca Mutapi, a Zimbabwean infectious diseases researcher who co-directs the Global Health Academy at the University of Edinburgh. Even today, the priorities of global health funders do not always align with African needs. Many countries are eager to strengthen health systems across the board, for example, but donors often prefer to focus on high-profile diseases for which progress is easier to monitor. And donors often don't coordinate their work, leaving unaddressed needs. "When you don't have self-determination, you're always following and dancing to someone else's tune," Mutapi says. Many donor countries also

PHOTO: FOTO24/GALLO IMAGES VIA GETTY IMAGES

A boy gets tested for HIV at a U.S.-funded clinic in Johannesburg.

PHOTO: FANNY CATTANI

expect political favors in return for their largesse, says Catherine Kyobutungi, executive director of the Nairobi-based African Population and Health Research Center: “They dangle foreign aid as a carrot and the political class in Africa found itself hooked.”

Despite a 2001 pledge by African Union member states to allocate at least 15% of their annual budget to health, the average in 2021 was only 5.7%. And too often, money has been lost to waste and corruption, says Nigerian virologist Oyewale Tomori, former president of the Nigerian Academy of Science.

The current crisis has led some countries to take action. On 14 February, the Nigerian legislature approved an additional $200 million to offset the shortfall from the U.S. health aid cuts, and the ministries of health of Botswana, Cameroon, and Kenya have pledged to mobilize domestic resources to finance HIV care for their citizens. South Africa already funds 83% of its HIV/AIDS program; Karim says it should take full responsibility.

But no country in the region can replace the funding immediately. In Uganda, for example, where 1.4 million people are living with HIV/AIDS, U.S. aid funds 60% of control programs. “The change has been so drastic and immediate without sufficient time for most countries to be able to build mitigation plans,” says Ntobeko Ntusi, president and CEO of the South African Medical Research Council.

In a 24 February essay in *The Conversation*, Mutapi suggested several steps African countries could take to reduce their dependence. New funding mechanisms, such as a tobacco tax, are one possibility. (Her home country, Zimbabwe, has had a 3% “AIDS levy” on income and business profits since 1999.) Public-private partnerships, such as a 2015 agreement between the Kenyan government and GE Healthcare to provide radiology services, could allow African countries to take more responsibility for health, Mutapi wrote. Countries could also join hands to boost the production of drugs and vaccines in Africa, for example by harmonizing regulation. (African philanthropists could fill gaps, too.) “The solutions for Africa’s health problems are not going to come from the West,” Mutapi says.

Happi hopes the loss of U.S. aid will lead to more such ideas. “African governments have gotten to the point whereby they feel that the crisis in their own countries should be solved by others,” he says. “The center of gravity for Africa’s health development should be in Africa.” ■

Abdullahi Tsanni is a science journalist based in Dakar, Senegal.

EARTH SCIENCE

Gas trapped in rocks gives snapshots of ancient atmosphere

Early results show oxygen rising hundreds of millions of years earlier than expected

By **Paul Voosen**

Earth’s atmosphere, the veneer of gases that makes most life possible, has changed dramatically over time. Bubbles of ancient air trapped in polar ice cores provide reliable archives of the past 6 million years—but that’s less than 0.002% of Earth’s history. For the eons before that, which saw the origin and proliferation of life, researchers have had to infer the atmosphere’s composition from evidence of its chemical effects on metals and minerals preserved in ancient rocks.

But now a small group of researchers is taking a more direct approach: analyzing minute pockets of ancient liquid and gas trapped inside salts, veins of quartz, and crystallized magma. From samples that stretch back more than 3 billion years, they’re extracting direct records of noble gases, oxygen, nitrogen, and carbon dioxide. It’s a big leap forward in the study of Earth’s history, says Morgan Schaller, a geochemist at Rensselaer Polytechnic Institute (RPI) who is leading one effort: “I don’t think anybody expected to get pristine samples of air from these reservoirs.”

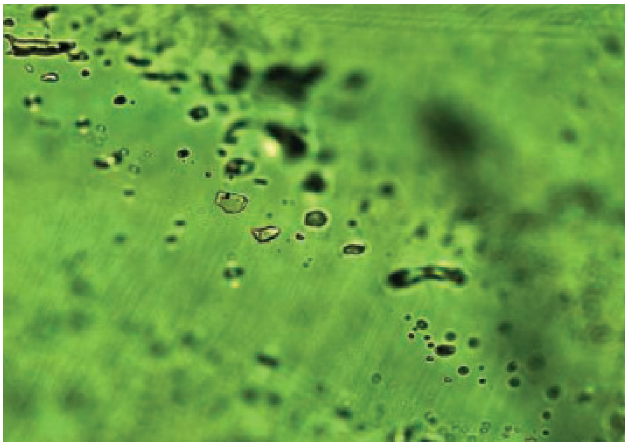

Tiny inclusions of gas and fluid in agate minerals capture ancient atmosphere.

Much of what researchers are learning from these samples is still preliminary. But the work, some of which was presented late last year at the annual meeting of the American Geophysical Union (AGU), is already verifying some assumptions about atmospheric history—and upending others. Schaller’s group has recently found direct evidence, for example, that oxygen levels were high enough to support animal respiration long before the first animals appeared less than 800 million years ago.

The atmosphere has always been a reflection of the planet below it—and in the beginning, 4.5 billion years ago, Earth’s surface was an ocean of magma. It gained an atmosphere as gases seeped out of that magma and were released by later volcanic eruptions and the impacts of asteroids and comets. Over time, nitrogen grew to dominate the air, because it’s extremely stable and too heavy, unlike hydrogen or helium, to escape to space. Oxygen was largely absent until about 3 billion to 3.5 billion years ago, when the first photosynthesizing microbes began to release it.

Just how the atmosphere evolved after that has been a mystery—which is why direct evidence would come in so handy. Geologists have long known that rocks can capture bits of the atmosphere. As magma cools, for example, imperfections in the growing crystals can trap the surrounding liquids and gases in fluid inclusions. But tapping into those time capsules has not been easy. “You’d think it’d be straightforward, find a gas and analyze it,” says Raymond Burgess, a geochemist at the University of Manchester. “But things are never simple looking that far back in geological time.”

To get at the gases, researchers crush rocks. In a vacuum-sealed press, they ramp up the pressure step by step. Different parts of the sample fail at different pressures, releasing discrete pulses of the trapped gases, which are whisked into a mass spectrometer for analysis. Repeat that on enough rocks, and you may capture enough gas to see the ancient signal. “The key is crushing kind of an insane quantity,” says Rita Parai, a geochemist at Washington University in St. Louis (WUSTL). By "insane," she means, say, 10 grams of rock.

Even then, getting enough gas to analyze takes luck. One of the first to succeed was Bernard Marty, a geochemist at the University of Lorraine. In the early 2010s, he began targeting inclusions trapped in quartz veins and barite crystal deposits in Western Australia that formed during the Archaean, more than 3 billion years ago. Radiometric dating using noble gas isotopes in the inclusions indicated they were equally old, and Marty's group eventually convinced its skeptical peers. "It is Archaean air. It's very ancient air," says Guillaume Avice, a geochemist at the Paris Institute of Planetary Physics who trained with Marty.

Noble gases can reveal more than age. Because the gases—argon, neon, xenon—don't react chemically with other elements, they're good tracers of the physical processes, such as volcanic outgassing, that influenced the atmosphere.

Avice's group has lately been working at the 11-kilometer-wide Dhala impact structure in central India, where a large meteorite struck some 2 billion years ago. After the impact, hot water filled cracks in the landscape, and dissolved minerals eventually precipitated out as hydrothermal agate. Noble gases extracted from inclusions in the agate, Avice and his colleagues reported at the AGU meeting, are the first atmospheric sample from the Proterozoic, the eon after the Archean. The amount of argon-40 was barely higher than Archean levels, Avice says, suggesting volcanic activity may have slowed for several hundred million years, causing a lull in outgassing.

> **"I don't think anybody expected to get pristine samples of air from these reservoirs."**
>
> **Morgan Schaller**
> Rensselaer Polytechnic Institute

Those gases ultimately come from Earth's mantle, and Parai's team has seen them at their source, in rocks from what is now Greenland. They analyzed a 3-billion-year-old anorthosite, a type of crystallized magma that formed when one tectonic plate was subducted under another at an oceanic trench. "This is a snapshot of a 3-billion-year-old subduction zone," Parai says. From it, WUSTL graduate student Samuel Patzkowsky recovered noble gases that, he and Parai think, come from both the ancient mantle and seawater that was equilibrated with the air.

Schaller, meanwhile, has traced ancient nitrogen, oxygen, and more—the atmospheric components most relevant to life. To do so, his group studies halites: salts deposited in very shallow lakes, as seen today in Death Valley. During the day, as the water heats, the salt crystallizes out and forms rafts at the surface, which can then trap parcels of air and water, gently preserving the gases. As the rafts become rocks, the fluid inclusions "manage to survive a long time," Schaller says.

The tricky thing about them, though, is that they confine both air and water in a closed space, and some of the air will dissolve into the water, skewing the measurements of atmospheric composition. But over the past decade, as Schaller has built up his halite protocol, he has developed a method to account for that process.

Another group, led by Nigel Blamey, a geochemist at Western University, has also studied halite inclusions—with astonishing results. In a 2016 paper in *Geology*, the researchers reported that the air 815 million years ago was 11% oxygen. A study Blamey plans to publish soon finds oxygen levels of 16%—close to the present concentration—in 2-billion-year-old rocks from Russia. Both results are far higher than expected; the conventional view has been that oxygen remained very low, except for a few short spikes, until some 800 million years ago, and that its rise then helped trigger the evolution of animals. As a result Blamey's work has faced skepticism, says Timothy Lyons, a biogeochemist at the University of California, Riverside.

Schaller doubts Blamey's results largely because they do not correct for the dissolved gas, as he does. In a study published in December 2024 in *Gondwana Research*, he and RPI graduate student Justin Park ran that correction on Blamey's original data. They found that the atmosphere 815 million years ago was not 11%, but 6.6% oxygen—still higher than indirect estimates, but not by much.

In work presented at the AGU meeting, Schaller and Park extended their own halite record back to 1.4 billion years ago. That's smack in the middle of the "boring billion," a time when tectonics and climate were thought to be stable and evolution slow. Using samples from deposits off the northwest shore of Lake Superior, they found an oxygen level of 1%. That doesn't sound like much, but it's higher than expected, and would have been enough to support the development of early animals—though there's no fossil record of them that far back.

"The boring billion is becoming much more interesting," Schaller says. As is all of Earth's history, now that there's a new way to see it. ■

BIOMEDICINE

Psychedelic trials face downsides of the 'trip'

New studies aim to separate participant expectations from drug effects

By **Jennifer Couzin-Frankel**

Sign up for a clinical trial of a psychedelic drug and you're agreeing to a potentially bizarre experience. "All of a sudden, your dead grandma or Satan is in front of you," says psychiatrist Charles Raison of the University of Wisconsin–Madison. Some think this consciousness-altering "trip" underlies the potential benefits of drugs such as psilocybin and LSD, which are under study to treat depression, trauma, chronic pain, and more. But the trip can also be a roadblock to assessing the drugs' effects on health, making it near-impossible to conceal who is getting an active substance and who's been assigned to placebo—a trial strategy called blinding that aims to keep participants' expectations from skewing their response to a drug.

This "functional unblinding" is not unique to psychedelics, but it's especially pronounced in this drug class. The U.S. Food and Drug Administration (FDA) has expressed concern about the issue in psychedelic trials. And it was among the critiques FDA advisers leveled at Lykos Therapeutics, whose application for MDMA to treat post-traumatic stress disorder (PTSD) FDA rejected last summer.

Now, scientists and companies are experimenting with trial designs meant to shield participants from recognizing what they're getting, or to separate expectations from the drug's impact on health. These include incorporating a range of doses; giving the drug, with permission, to people who are asleep; and misleading participants about how a trial is set up.

Companies running large-scale psychedelic trials mostly view unblinding as inevitable. Participants "are going to feel [the drug], that's just how it is," says Rob Barrow, CEO of MindMed, which has late-stage trials underway to test LSD's ability to ease anxiety. But he believes there are ways to parse a drug's efficacy even if people know they're getting it. In one recent trial, MindMed recruited 198 people with anxiety, giving some a placebo and the others LSD at one of four doses. Virtually all who received active drug correctly guessed that they'd gotten it. But those on the two higher doses saw clinically meaningful reductions in anxiety, whereas those on the lower doses didn't. That split means the benefit "has to be due to something other than thinking you're getting drug," Barrow says. MindMed is using a lower, nontherapeutic dose as well as a higher dose in an ongoing phase 3 trial, and hopes to report results next year.

The standard practice of blinding participants is complicated in psychedelic trials.

ILLUSTRATION: DANE_MARK VIA STOCK PHOTO. ADAPTED BY N. JESSUP/*SCIENCE*

Compass Pathways, a biotech testing psilocybin in treatment-resistant depression, tried a different twist: giving everyone the drug, at different doses, so that all might expect benefits. This study, too, showed a greater reduction of depression at higher doses.

Academic researchers, meanwhile, are running smaller trials with more unorthodox strategies that might blunt the risk of unblinding and shed light on how the "trip" plays into drug effectiveness. Raison has been experimenting with having people sleep through their trips, as a way to understand how much a conscious psychedelic experience matters. Two volunteers received psilocybin while in a deep sleep with a sedative, and 1 week later both "swore they got placebo," Raison says. He is now developing a larger study in which people who report reduced emotional well-being will be randomized to get psilocybin or placebo while either awake or asleep, to tease out how the trip influences longer term effects on emotional state.

Raison is also studying psilocybin alongside midazolam, which makes participants drowsy throughout their trip and disrupts their memory of it afterward. He's preparing to launch a study of 68 people with reduced emotional well-being who will get either an ultralow or higher dose of psilocybin, with or without midazolam. Raison hopes to learn whether a trip that's experienced but then forgotten can still confer benefits.

Another approach is to administer psychedelics to patients under general anesthesia for preplanned surgery, when they can't possibly know whether they got a drug or a placebo. Boris Heifets, an anesthesiologist at Stanford University, tried this a few years ago with ketamine, an anesthetic that can have hallucinogenic effects. (A form of the compound was approved to treat depression in 2019.) He found that the placebo group reported more improvement in depression than is common in psychedelic drug studies, which he suspects was because of participants' beliefs they may have gotten ketamine and benefited from it.

But studies in anesthetized patients have their own challenges. Some types of anesthesia and sedation can themselves have antidepressant effects or otherwise affect the brain, notes Katherine Nautiyal, a behavioral neuroscientist at Dartmouth College. She is trying to sort out those effects by studying psychedelics administered alongside various anesthetics in mice.

Other researchers are using innovative strategies in awake participants. One involves giving the control group an "active placebo" that mimics some immediate effects of a psychedelic without its potential psychiatric benefits. Heifets helped design a study, led by Stanford psychiatrist Carolyn Rodriguez, that will compare MDMA with another psychoactive substance, methamphetamine, in people with obsessive-compulsive disorder. Another study, in active-duty service members with PTSD, compares MDMA with amphetamine.

Still other studies aim to confuse participants about how the experiment is set up. Harriet De Wit, an experimental psychologist at the University of Chicago (UChicago), has run such studies of psychoactive drugs, including psychedelics, in healthy people to parse the drugs' biological effects. She tells participants they might get any one of a number of different pills—a stimulant, a tranquilizer, or a placebo, for example—when in fact only one drug and a placebo are part of the study. This strategy makes it harder for volunteers to discern what they're given. For example, someone handed placebo who slept poorly the night before may interpret their sleepiness after taking the unidentified pill as an indication that they've received a sedative. De Wit can then better isolate drug biology, without the confounding effects of expectations.

Typically, "We cannot deceive" participants in trials, for example by not disclosing a drug they might get, says Christopher Daugherty, a medical oncologist at UChicago and chair of the institutional review board that has reviewed many of De Wit's studies. But telling participants they could receive one of four drugs and alerting them to possible side effects—even if two of those drugs aren't on offer—"are all true statements," Daugherty explains.

Heifets and psychiatrist Josh Woolley at the University of California, San Francisco make a similar case for their psilocybin study, which is recruiting 30 people with chronic lower back pain. Participants are told they'll get psilocybin within a range of dosages, perhaps with a stimulant or a sleeping pill, or with placebo. But the trial may not include all those combinations; its true design hasn't been publicly released. As with De Wit's studies, the researchers hope participants' uncertainty about what they got will reduce the impact of their expectations and yield more reliable results.

In January, Woolley and colleagues published a paper in *JAMA Psychiatry* analyzing studies that embrace this strategy. They acknowledged "significant ethical risks," but also the potential to "improve interpretability and impact" of psychedelic trials. Informed consent is the foundation for ethical research, but good research also demands studies designed to give clear answers, Woolley says. It's "unethical to do uninformative studies," he says, "studies where you don't actually learn anything." ■

Dozens of ecologists analyzed the same data on blue tit chick growth—and came up with different results.

PHOTO: DAVID TIPLING/NPL/MINDEN

REPLICATION CRISIS

Given the same data, ecologists arrive at different conclusions

First "many analysts" study in ecology highlights powerful role that subjective choices can play in research

By **Cathleen O'Grady**

Give a group of scientists the same data and the same research question, and they should come up with similar answers—in theory. But they don't, according to a paper published last month in *BMC Biology*, which finds that 246 ecologists analyzing the same data sets reached widely varying conclusions, with some finding effects in totally opposite directions.

The paper is the latest in a line of "many analyst" projects that examine how results can vary because of scientists' decisions during data analysis—and the first to study the effects in ecology. "I was really excited to see this study," says University of Bern metascientist Ian Hussey, who was not involved with the research. Past work has mostly focused on psychology and other behavioral sciences, he says. "I have noticed an unfortunate hubris in other domains that say, well, we have our house in better order."

Elliot Gould, a Ph.D. student at the University of Melbourne, was skeptical that ecology has its house in better order. Ecologists deal with complex systems that contain a huge amount of natural variability, they say, and have to make many decisions about what kind of statistical analyses to run. To find out how much those decisions affect the results, Gould and their colleagues recruited 246 ecologists, working in 174 teams, to answer two different research questions, each based on a single data set.

The first question asked how the growth of blue tit chicks is influenced by competition with siblings in the nest. The analysis teams, who were all given the same data from 452 blue tit broods in an Oxfordshire woodland, came up with a wide range of answers. Five found no relationship between brood size and chick size, five found mixed results, and 64 found that chicks grew more slowly if they had more siblings, but with different levels of certainty and effect sizes.

The spread of results for the second research question was even more dramatic. Gould and their colleagues gave the analysis teams data from 18 sites in Australia that were taking part in a project to restore various species of *Eucalyptus* on agricultural land, and asked them to determine whether the amount of grass cover affected the success and survival of the seedlings. The teams who analyzed this data set did not agree at all: Eighteen concluded that more grass cover hampered *Eucalyptus* survival, six said it improved survival, and 31 found the grass had no effect.

The findings match up with the results of previous many-analyst studies, and show "the powerful role of subjective researcher choices in scientific projects," says Eric Uhlmann, an organizational psychologist at the European Institute of Business Administration, who co-authored the first such project in psychology in 2018.

In some cases, there is established best practice to guide analysts—but other choices are more arbitrary, Gould says: Researchers have to decide which variables to control for, for example, and how to deal with missing data. "And those different choices that we make can kind of multiply."

It's impossible to know whether the problem affects an entire field from just one or two examples, says Eötvös Loránd University metascientist Balazs Aczel. To find out, he is running a project to have multiple analysts each tackle a question from 100 randomly chosen social science papers. But similar findings have popped up in a range of fields—including neuroscience and economics—and suggest "we are facing a very serious issue," he says.

Not all researchers think the findings are so alarming. Joe Bak-Coleman, an ecologist by training and now a computational social scientist at the University of Konstanz, says studies like these ask scientists to analyze data outside their specific area of expertise. Yet expertise plays an important role in winnowing down the choice of analyses, he says. Scientists already familiar with blue tits, for instance, would have a better idea about what analyses to run. Still, many-analyst studies suggest researchers across fields could benefit from better training in analysis, he adds.

Anne Scheel, a metascientist at Utrecht University, says the many-analyst findings don't mean fields like ecology and psychology can't pinpoint reliable results. Such fields tend to ask broad questions that leave a lot of choices up to researchers. But that's a problem that can be fixed by being more precise, she says. "The harder sciences seem to have more success coming to consensus on difficult questions," she says. "I think that has something to do with how precisely things are defined." ■

ASTRONOMY

Finally, stars made from only primordial gas?

Shortcut method pinpoints a galaxy apparently formed from just hydrogen and helium

By **Daniel Clery**

Staring deep into space and far back in time, astronomers may have spotted a galaxy full of stars made from only the primordial gas created in the Big Bang. Such "population III stars" would have formed from hydrogen and helium and nothing else, and researchers have searched for them for decades, racking up many disputed sightings. If confirmed, the discovery, made with NASA's JWST space observatory, opens a window on the starting point of the chemical enrichment of the universe, in which the heavier elements needed to make planets and life began to be forged in stellar explosions.

"It's very exciting," says astronomer Elka Rusta of the University of Florence. "We hypothesize that [population III stars] exist from theory, but they have never been directly observed."

The nature of population III stars remains uncertain. Most theorists think they were huge, with masses up to 1000 times that of the Sun, 10 times larger than any star around today. That's because a cloud of gas collapsing to form a star needs to cool. As atoms in the gas collide, they become ionized, which enables them to lose energy by emitting photons. But tightly bound hydrogen and helium atoms are hard to ionize, unlike the heavier elements found in later generations of stars. So a cloud of primordial gas would just keep growing as it pulled in more gas under its own gravity, reaching an enormous size before finally becoming dense enough to ignite nuclear fusion in its core.

The gigantic stars that resulted would also burn hot and fast, ending in a supernova explosion after just a few million years. That brief first flash of population III stars is hard to spot in galaxies that went on to shine steadily for billions of years with smaller, longer lived stars. But the spectrum of the light from the giant stars might give them away. Different elements absorb and emit characteristic wavelengths of light. Population III stars would produce very strong emission lines for hydrogen and helium and would lack any spectral lines produced by heavier elements.

Astronomers have struggled to find stars that bear all the hallmarks of population III, however. Even with JWST's sharp vision, gathering enough light to measure a galaxy's spectrum takes time. And, to perform such spectroscopy, the telescope must focus on only small patches of sky, making the odds of finding a rare population III galaxy very slim. However, Rohan Naidu, an astronomer at the Massachusetts Institute of Technology, and his colleagues found a way to speed up the search, as they described in a January preprint posted to the arXiv server.

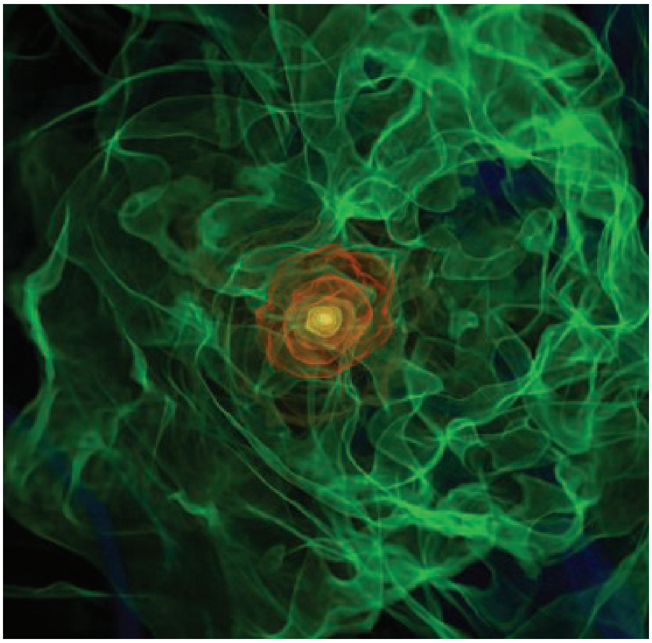

The very first round of starmaking, as shown in this computer simulation, only had hydrogen and helium as ingredients.

IMAGE: RALF KAEHLER AND TOM ABEL (KIPAC/STANFORD/SLAC)

Since JWST launched in 2021, its near-infrared camera has surveyed millions of objects. These surveys don't record a detailed spectrum for each object, but use a series of filters to measure a source's brightness in as many as a dozen broad wavelength bands. Naidu and colleagues realized they could do a quick and dirty search for population III galaxies by looking for a few key signatures, such as objects that were bright in a band containing a prominent hydrogen line and dim in another containing a line from a heavier element, such as oxygen. "This is an approach that really yields results if you're looking for very rare objects," says astronomer David Sobral of Lisbon University.

Scanning data on hundreds of thousands of galaxies, the team came up with two candidates, and one known as GLIMPSE-16043 was a particularly good match. "If you had to manufacture a population III galaxy in a factory, you couldn't come up with a better specimen," Naidu says. Viewed as it was when the universe was about 850 million years old, GLIMPSE-16043 has a mass of roughly 100,000 solar masses, the team estimates. That low mass makes it a dwarf galaxy, and its stars had been burning for less than 5 million years, the researchers think. "It has these signatures of extremely hot stars and barely any oxygen," Naidu says, "and it's very, very faint, which is what you expect for these types of sources."

The team still refers to it as a candidate because without a detailed spectrum it's impossible to rule out other, less exciting possibilities. For example, GLIMPSE-16043 could be a cloud of lingering primordial gas that is being energized by light from a black hole gorging on matter. Or it could simply be a smaller cluster of stars much closer to Earth that is mimicking a population III spectrum. To settle the issue, "ultimately, you will need spectroscopy," Sobral says. Naidu says JWST officials have awarded the project some high-priority observing time in June to get a spectrum.

If population III stars prove to be big and bright, the ultraviolet light they emit could have played a key role in the youthful universe: ionizing the neutral hydrogen gas between galaxies. And small primordial galaxies like GLIMPSE-16043 could be the predecessors of ultrafaint dwarf galaxies close to our own Milky Way that appear to contain very ancient stars only slightly enriched by heavier elements, notes Tim Beers of the University of Notre Dame. Some astrophysicists think those current stars are the children of population III stars, Beers says, and by studying them astrophysicists could learn about their ancient forebears. "I find it exciting that you can draw a straight line from what we see around the Milky Way to this proposed birthplace." ■

TRUMP ADMINISTRATION

Ban on renewing senior scientists shakes NIH

Agency appeals policy that could dramatically shrink its in-house research program

By **Jocelyn Kaiser**

Researchers this week stepped up pleas to Congress and President Donald Trump's administration to save the jobs of a select group of senior scientists at the National Institutes of Health (NIH) who are set to be let go soon because of a White House–imposed hiring freeze.

The scientists—who number at least 30 and possibly more than 100—were hired under rules that allow NIH to offer salaries higher than the federal pay scale in order to attract top talent. They hold 1- to 4-year terms that have long been routinely renewed. But the Department of Health and Human Services (HHS), NIH's parent agency, has said it will not renew positions that are now expiring.

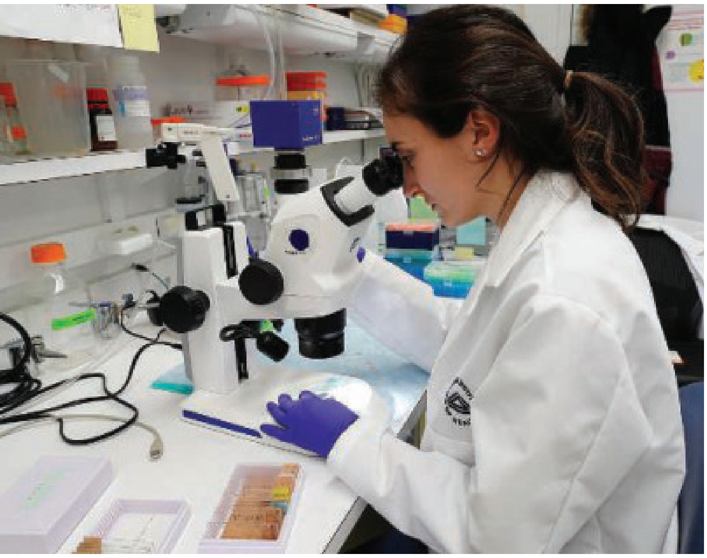

Many labs at the National Institutes of Health could soon lose their leaders.

PHOTO: NATIONAL INSTITUTES OF HEALTH

The move marks the Trump administration's latest blow to NIH's $5.2 billion intramural program, its in-house research in Bethesda, Maryland. Less well known than the agency's $39 billion extramural program, which gives grants to researchers at outside institutions, it includes basic research labs and a research hospital that treats patients with rare diseases—and helps showcase NIH's work and build support from Congress, those familiar with it say.

Most of some 4000 NIH scientists have been hired under the special pay rules, established by a statute known as Title 42. Roughly one-fifth hold tenured positions that do not require renewal. Most of the remainder, however, hold term-limited jobs, and a ban on renewals could eventually affect the vast majority of the intramural program's staff scientists, research fellows, and tenure-track investigators.

"Stopping renewals of Title 42 employees would be devastating to the intramural research program and to NIH as a whole," says Joshua Gordon, former director of the National Institute of Mental Health. At one larger NIH institute, "There are entire branches that would be gutted within 6 months" because so many principal investigators are coming up for renewal, a scientist there says.

A group of scientists who have just passed their renewal date have been given a reprieve—albeit without pay—until 8 March while NIH acting Director Matthew Memoli appeals the policy to HHS.

One of those staff scientists, who asked to remain anonymous because of the vulnerability of his job, had given up a tenured university position and a well-funded lab in order to move to NIH about 3 years ago. He made the move, he says, because NIH offered cutting-edge resources and a chance to do "blue-sky research with high stakes but potentially high reward." A board of outside researchers had even recommended him for NIH's tenure track, which could lead to a permanent position.

But in late February, his supervisor delivered the bad news: The scientist would soon be put on leave without pay because his term was reaching its renewal date. If the appeal fails, "the rug would basically be pulled out from under me," he says.

Memoli is also hoping to restore the positions of 15 tenure-track researchers who recently lost their jobs as part of the governmentwide firings of probationary workers. But many NIH researchers are not optimistic.

"They are firing some of our best people, not our worst," says the NIH scientist from the large institute. HHS had no comment; the White House has said term-limited positions should not be renewed to help downsize the federal workforce.

Also in limbo are the intramural program's trainee programs. One, a "postbac" program that employs some 1600 recent college graduates, is key to staffing many labs and launching young scientists' careers, one NIH senior scientist says. "It is incredibly well organized and it's the backbone of the intramural program. The best and the brightest apply."

"Think of Elon Musk whippersnappers," another scientist says. "It's the same idea here; you do science and figure out if you're going to medical school or graduate school or industry."

NIH has also canceled its summer internship programs for college students through medical school graduates. The program's director, Sharon Milgram, emailed researchers last week to "share the sad news" and said NIH hopes to resume the program next year.

"The medical piece [of NIH], the training piece, and the basic discovery piece are all going to take a huge hit if the intramural program continues to sustain the attacks that it is currently sustaining," says Carol Greider, a Nobel laureate and a molecular biologist at the University of California Santa Cruz.

The program "is a vital component of our efforts to improve cancer treatment and diagnosis," adds University of Colorado immunologist Leslie Berg, who chairs a panel that reviews the National Cancer Institute's intramural senior scientists. Those researchers have access to technologies, partnerships with drug companies, and patients "that are not possible in the extramural research community," Berg says.

Foreign scientists hired under Title 42 have even more reason to worry because when their jobs end, their visas require they leave the country within 60 days unless they obtain a new position. Many have put down roots, bought houses, and have children in school.

The staff scientist awaiting word on his appeal says the decision could seal his professional fate. If a renewal doesn't come through, "it's the end of my career," he told *Science*, because it would take years to rebuild his lab at another institution. ■

With reporting by Meredith Wadman.

Colossal Biosciences genetically altered a mouse (left) to express traits reminiscent of the long-extinct woolly mammoth, including a long, coarse coat.

PHOTO: COLOSSAL BIOSCIENCES

GENOMICS

Mouse with a mammoth's pelt makes superfuzzy debut

Birth of rodent with coat genetically modified to resemble the extinct species raises ethical and conservation concerns

By **Phie Jacobs**

Before you ask, no, it doesn't have little tusks. But like the woolly mammoth that inspired it, the new genetically engineered mouse from Colossal Biosciences—a biotech company striving to bring extinct species like the mammoth, dodo, and Tasmanian tiger back from the dead—does have thick, wavy hair with a coarse texture. To create the animal's fluffy golden coat, scientists combed through dozens of ancient genomes, then modified multiple mouse genes in one fell swoop.

The engineered mouse allows the team to confirm that changes to specific genes produce mammothlike traits—"a super-exciting proof of principle," says Tom Gilbert, an evolutionary geneticist at the University of Copenhagen who is an adviser to Colossal but didn't participate in the work. But many other researchers say the achievement, described in a preprint posted this week on bioRxiv, is technically impressive but not groundbreaking.

"The researchers have succeeded in nudging the mouse genome in the direction of a mammoth genome, which is a first," Louise Johnson, an evolutionary biologist at the University of Reading, said in a comment to the U.K. Science Media Centre. "But of the 10 different mutations engineered into the mice, only a few actually make the mouse gene closer to a known mammoth gene." Others note that many research labs have already succeeded in editing multiple DNA sequences at once in an effort to treat genetic diseases or engineer desirable traits into crops. As Henry Greely, a bioethicist at Stanford University, puts it, the Colossal woolly mouse has the "aww factor" but is missing the "awe."

Colossal's strategy for bringing back long-extinct animals is to sequence the vanished creatures' genomes from ancient DNA and edit the DNA of a closely related species to match. Asian elephants are mammoths' closest living relatives, but as Colossal CEO and co-founder Benjamin Lamm notes, these enormous animals would be tough to breed and study in the lab. Mice, a lab staple, are small and breed fast, and they are no strangers to having their genome manipulated.

The team began by exploring a data set of 121 mammoth and elephant genomes, looking for places where the mammoth had diverged from its cousins. They zeroed in on a handful of genes impacting hair length, thickness, and color, as well as lipid metabolism—genes that also show up in mice. Then, using a combination of three gene-editing technologies, they made eight simultaneous tweaks to the mouse genome, resulting in changes to seven genes. By breaking a gene called *FGF5*, for example, the team created mice with extra-long hair, whereas similar edits to *FAM83G*, *FZD6*, and *TGM3* produced curly whiskers and a woolly, wavy coat. Colossal's woolly mice also have a modified version of a melanin production gene, making their fur golden instead of black.

Evolutionary biologist Beth Shapiro, who serves as Colossal's chief science officer, says the woolly mouse demonstrates that scientists "can drive phenotypic changes using these technologies and ancient DNA as the guide for selecting them" while also ensuring that the animals remain healthy. The "adorability" was an unintended consequence, Lamm says.

For some, the cute creature raises darker concerns about the wisdom and ethics of de-extinction. Although Colossal argues that the return of extinct species could help make modern-day habitats more resilient to climate change, Gilbert dismisses this idea as "complete crap," arguing it would be extraordinarily difficult to re-embed an animal in an ecosystem that has changed dramatically since it went extinct. Practical concerns aside, many scientists view de-extinction as an expensive stunt that could actually harm conservation efforts. "If there's not a purpose," says ecologist Douglas McCauley of the University of California, Santa Barbara, "then we're just making monsters in the lab."

But the Colossal team is still on track to have a mammothlike calf born to an elephant in 2028, Lamm says, and the woolly mouse is a steppingstone. The team plans to test whether its genetic changes make the animals more cold tolerant, much like woolly mammoth. The little creature, he adds, is offering "some really new and cool insight into the edits that we're going to need to make for the mammoth project." ■

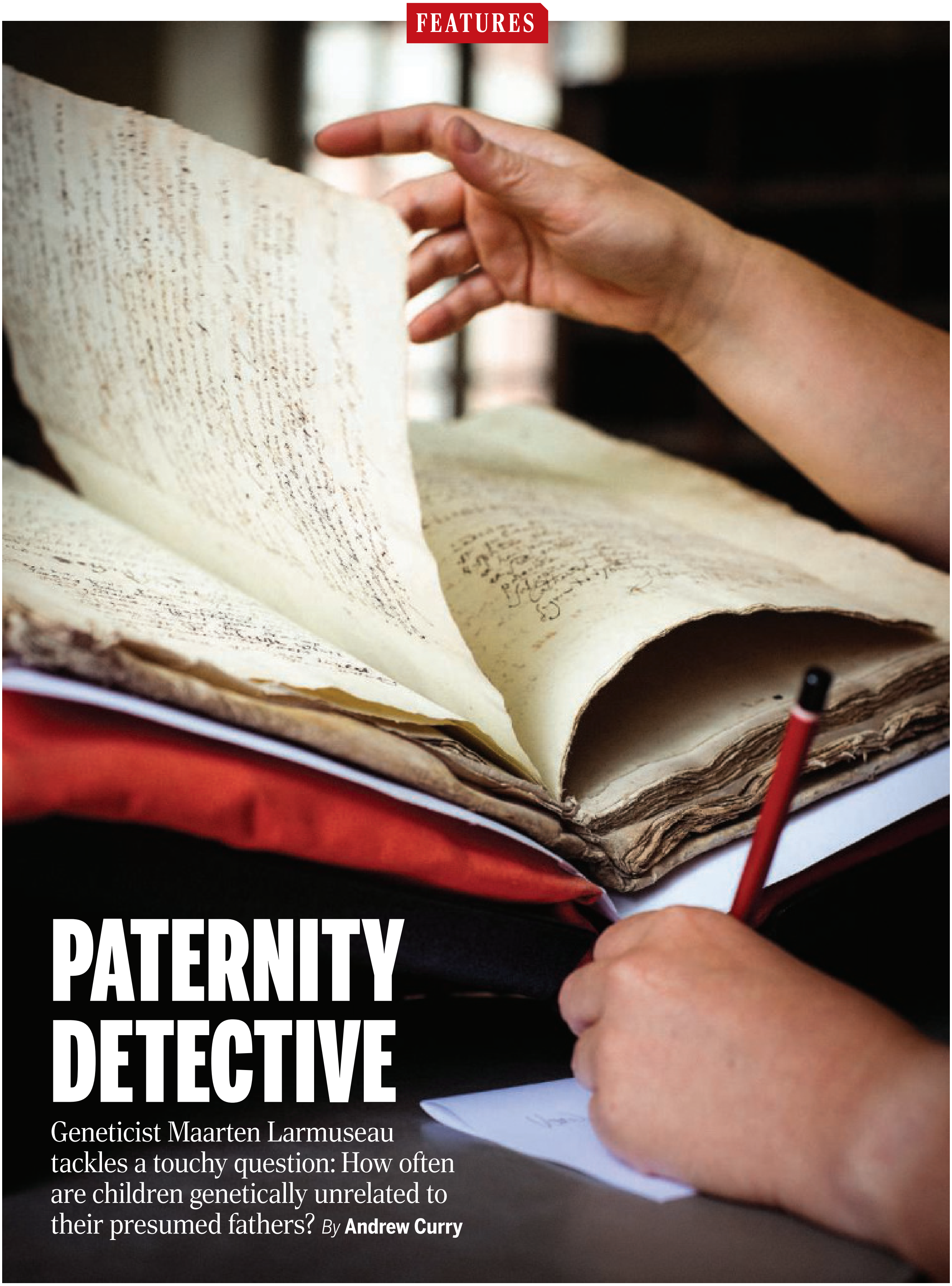

PATERNITY DETECTIVE

Geneticist Maarten Larmuseau tackles a touchy question: How often are children genetically unrelated to their presumed fathers? *By* **Andrew Curry**

Centuries-old documents help researchers reconstruct family trees, which can be compared with DNA to find discrepancies.

PHOTO: KU LEUVEN

On the wall of his living room in Lier, Belgium, Werner van Beethoven keeps a family tree. Thirteen generations unfurl along its branches, including one that shows his best known relative, born in 1770: Ludwig van Beethoven, who forever redefined Western music with compositions such as the *Fifth Symphony*, *Für Elise*, and others. Yet that sprig held a hereditary, and potentially scandalous, secret.

That Beethoven, Werner learned to his dismay in 2023, is biologically unrelated to Werner and his contemporary kin. This uncomfortable fact was brought to light by Maarten Larmuseau, a geneticist at KU Leuven who specializes in answering a question relatively few others have explored: How often do women have children with men they're not partnered with?

In most societies, kinship is at least partly socially constructed, and for example can include adoption and stepfamilies. Yet questions about biological paternity have roiled families and fueled cultural anxieties for eons. Male authors have written about hidden paternity for millennia, including in Greek dramas and *The Canterbury Tales*; William Shakespeare and Molière wrote plays about it. Knowing a child's biological father is also important for forensically identifying cadavers, recording accurate medical histories, and charting the manifold ways in which people structure families around the world.

Although intentional deception about a child's paternity can cause legal records and biological paternity to diverge, sexual violence can also be involved, and some legal fathers are fully aware they are not a child's biological father, but choose to keep that fact secret. Researchers sidestep fraught terminology by dubbing all such cases paternal discrepancy, false paternity, or—Larmuseau's preferred term—extra-pair paternity (EPP). (The term does not include instances of adoptions and out-of-wedlock births where the biological father's identity is known.) To find out how often it takes place, he's developed a method that combines genealogical records with DNA tests of living people. His technique can turn up evidence of unexpected or misattributed paternity dating back centuries.

Such investigations have made Larmuseau a pioneer in the growing field of genetic genealogy. "He's contributing very carefully collected, curated data and well-executed research to an area where we didn't have any good data," says Mark Jobling, a geneticist at the University of Leicester. Larmuseau's findings suggest that for all the shock and scandal that surround a case such as Beethoven's, EPP in humans is quite rare. Though an oft-repeated zombie statistic posits that as many as 10% of children are fathered outside of marriage, he has found that over the past 500 years, the rate in Europe is much closer to 1%.

It has shot up at times of social change, his findings show, and researchers studying some other cultures have documented higher rates. But in most societies, the rate of EPP appears far lower than anxieties about it would suggest. "One message is everybody stop panicking," Larmuseau says, "because it's not the problem you think it is."


Maarten Larmuseau wondered how many of his grandparents (pictured) he was biologically related to.

PHOTO: KU LEUVEN

IN HIS OFFICE on the edge of Leuven's medieval city center, Larmuseau keeps a reproduction of a 17th century Dutch painting showing a man at the bedside of his wife, who has just given birth. Various visual cues poke fun at the man for being a cuckold, unwittingly acting as the father of another man's baby: a limp sausage, someone holding "cuckold horns" over the hapless husband's head, and a snickering crowd. "It shows everybody is laughing at him because he's not the father," Larmuseau says. "He's been betrayed, and maybe he's the only one who doesn't know." It's a reminder that paternity has long been a cultural obsession in Europe.

That's a function of how human fatherhood works, some evolutionary biologists have argued. Human fathers make unusually large investments in raising their offspring. As a result, the argument goes, men have evolved to be especially wary of raising children fathered by others.

As a doctoral student, Larmuseau worked on a species that is sometimes used as a case study of EPP in the animal kingdom: sand gobies, tiny fish native to the Baltic and Mediterranean seas. Goby males invest in their offspring, building nests and caring for fertilized eggs, whereas females lay eggs and leave. Sometimes, a male goby will sneak into the nests of other males, fertilize the eggs, and then flit away, leaving the duped dad to raise another fish's kids.

Later, working in a forensic genetics lab as a postdoc, Larmuseau wondered how often similar behavior in people might complicate efforts to solve crimes or identify cadavers from their DNA. But he found that asking about the phenomenon tended to yield more giggles than grants. "It's really a taboo," he says. "There's so much literature on extra-pair paternity in pair-bonded bird and fish species, but in humans we didn't know anything."

In the absence of reliable numbers, scientists speculated. In his 1991 book *The Third Chimpanzee: The Evolution and Future of the Human Animal*, biologist Jared Diamond claimed the adultery rate among humans

Celebrating the Birth, by 17th century Dutch artist Jan Steen, depicts a cuckolded husband surrounded by a snickering crowd.

IMAGE: WALLACE COLLECTION/BRIDGEMAN IMAGES

was between 5% and 30%. In a widely cited 1997 paper, University of Reading evolutionary biologist Mark Pagel argued EPP was so common in humans that babies evolved to be indistinguishable at birth, concealing their true paternity as a protective mechanism.

Eventually, a consensus emerged, based mostly on back-of-the-envelope calculations from early genetic paternity testing. In an article in *The Lancet* published the same year as Diamond's book, researchers reported the idea that 10% of children were the product of a clandestine affair, but complained there were no solid data to either confirm or disprove the figure. Nonetheless, it continued to be repeated by journalists and researchers. Eventually it took on a life of its own.

If the 10% figure is accurate, many family histories are not what they seem, and genealogy might be a pointless exercise. Larmuseau's own great-uncle was passionate about exploring the family's history. But after reading that 10% of children weren't related to their legal fathers, "he totally lost his appetite for genealogy," Larmuseau says. "For him, it was really problematic."

Undeterred, Larmuseau took up the hobby, exploring his family's history and eventually compiling a spreadsheet containing thousands of ancestors, dating back to his namesake—his great-great-great-great-great-great-great-grandfather Maarten Larmuseau, an innkeeper born in 1625—and beyond. He couldn't help but wonder: Were Diamond and the others right? "It's fascinating, as a biologist," Larmuseau says. "How many of these legal and social ancestors are also biological ancestors?"

Existing evidence was questionable. Estimates based on paternity tests are biased, as people paying for a test often already suspect EPP. Studies based on bone marrow donor samples and other sources suggested that in modern populations the rate is low, but that may be because of modern birth control rather than an evolved mating strategy. And asking people on the street about their sexual behavior seemed fraught with ethical and bias issues. "It's really hard to study the present," Larmuseau says, "so I looked to the past."

He decided to start local. Beginning in 2009 as a newly minted Ph.D., he collected family trees going back to the 1400s with the help of Belgian and Dutch genealogy and heritage enthusiasts. Then he independently verified the trees. When hobbyists didn't have the information he needed, he scoured census archives and drove to small Flemish and Dutch village churches to look through parish records of marriages and baptisms.

Working from the old documents, Larmuseau identified thousands of men living today who, according to genealogical records, should all be distantly related on their father's side. The next step was to swab their DNA and put their official ancestry to the test.

Often local history societies helped him contact candidates. Other times he opened the phonebook and cold-called them, or simply knocked on doors with mouth swabs and consent forms in hand. "Sometimes I just went to everyone with a certain surname in a village and asked them to take a DNA test," Larmuseau recalls. "One year I did 300 households." The men were informed that he was looking for EPP in their ancestry, and any hesitation was enough to exclude them from the study.

The mouth swabs yielded Y chromosomes, which are passed from father to son over many generations. When a family tree is accurate, the Y chromosomes will match: Two great-great-grandsons of the same man might not know each other, but they will share identical Y chromosomes.

But every once in a while, Larmuseau encountered men whose genealogies suggested they should have matching Y chromosomes, but didn't. Each mismatch provided Larmuseau with genetic evidence of at least one case of EPP. He used a statistical model to estimate when the EPP event took place based on the length of the reconstructed pedigrees.

After an initial estimate published in 2013, Larmuseau kept collecting data. In a 2019 *Current Biology* article based on testing the Y chromosomes of 513 pairs of distantly related men, Larmuseau calculated that over the past 500 years, the EPP rate in Belgium and the Netherlands was about 1.5%. "To have some evidence for what the rate really was, and how that played out in those societies, is super interesting," Jobling says.

Subsequent studies elsewhere in Europe by Larmuseau and others came up with essentially the same results: In European societies since at least the Middle Ages, the likelihood a child's recorded father wasn't the genetic father was vanishingly small—typically 1%, or less.

In Beethoven Larmuseau found a high-profile counterexample. Investigating the composer's paternity wasn't the original goal of the study; instead, he and Walter Sluydts, an amateur genealogist, hoped to use Y chromosomes from living van Beethovens to authenticate locks of hair kept as souvenirs of the renowned composer. In 2019, the researchers contacted Werner van Beethoven and a handful of his distant relatives to ask whether they would contribute DNA.

Four years later, Larmuseau gathered Werner and five other living van Beethovens in a conference room at KU Leuven to deliver the results. The famous composer's Y chromosome was inherited not from the common ancestor of all the van Beethovens living today, but from an unknown father—perhaps the result of an extramarital affair in the generations before he was born. For Werner, it was crushing news. "I'm pretty proud of my family name," he says. "That's why I was disappointed the composer wasn't a real van Beethoven biologically."

Yet that twist in the composer's ancestry didn't necessarily involve premeditated infidelity or deception. Historical and literary sources document infertile men knowingly encouraging their wives to take lovers to ensure offspring, for example. Sexual violence or coercion undoubtedly accounted for some of these pairings as well. "In the last 500 years, it's not common that males are betrayed by their mates on purpose to produce children who are not biologically his," Larmuseau says. (In Beethoven's case, there's historical evidence his paternal grandparents had a rocky marriage, but no way to be sure that was the generation when his ancestry diverged.)

Data from non-European societies suggest the obsession with biological paternity crosses cultural boundaries. In 2012, University of Michigan evolutionary anthropologist Beverly Strassmann published an analysis of the impact of religion on EPP in Mali's Dogon society.

Among people practicing traditional Dogon religion, contraception is uncommon and women are pregnant or breastfeeding much of the time. During rare intervals when women are menstruating, they sleep in designated huts. "Going to a menstrual hut flags that a woman will be able to become pregnant within the next few months," she says. "That makes it hard to obscure who the father is, keeping EPP rates low."

Strassmann says men's efforts to monitor and control women's sexuality—embedded in major world religions and social norms in many parts of the world—are a strategy to avoid investing in other men's genetic offspring instead of their own.

Based on Y chromosome and other genetic data, Strassmann found an overall rate of cuckoldry of 2% among the Dogon, comparable to what Larmuseau went on to find in Western Europe. (The rate among Dogon Christians, who don't use menstrual huts, was twice as high as those practicing traditional religion.)

How a tree gets tangled

Because Y chromosomes are passed unchanged from father to son, descendants of a common male ancestor all share Y chromosomes even 10 or more generations later. When two men whose family trees say they are distantly related through their paternal line don't share a Y chromosome, it's proof another man's DNA is part of the mix—what geneticist Maarten Larmuseau calls an "extra-pair paternity event."

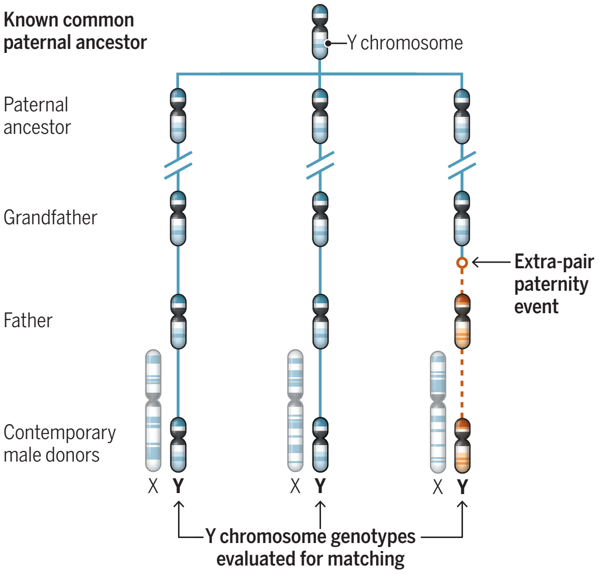

GRAPHIC: N. BURGESS/*SCIENCE*

THE OBSESSION with genetic paternity isn't universal. South American tribes such as the Yanomami believe multiple men can contribute to a child's paternity by having sex with the same woman. Among the Nyimba of Nepal, women traditionally have multiple husbands—all of whom are expected to act as fathers to all of their spouse's children. "There are lots of examples that counter this stereotype of wily women versus bamboozled men," says Brooke Scelza, an evolutionary biologist at the University of California, Los Angeles.

One of the best documented is found among the Himba people of Namibia. When Scelza first visited Himba villages 15 years ago, she was surprised by how openly women discussed children fathered with partners outside of marriage. "It ran against so much of what we as evolutionary biologists think," she says. "This looked really different from what Maarten Larmuseau and other people were finding in Europe."

Intrigued, Scelza worked with the community to conduct anonymized paternity testing. The results showed the EPP rate among the Himba was 48%. Fathers were usually aware of which children were theirs biologically, while simultaneously considering themselves the social and legal fathers of all their wives' children. "It's not that they're being duped—these men still really consider themselves the social fathers, even if they're not the biological fathers," Scelza says. "It really shows the importance of getting this kind of data from other regions."

Even in Europe, people regularly make decisions that belie the view that paternity and parenting is primarily a biological investment, including caring for stepchildren, adoption, and fostering. "There's no genetic kinship there, and people are investing resources in children who are not related to them at all," Jobling says. "I'm a bit skeptical of applying these sociobiological ideas to human behavior. I think it's a bit more complicated than that."

Larmuseau acknowledges such cases. "Biology is not necessary to have a good family and be a good parent," he says. "But it still matters to many people." Precisely how common EPP is, he says, appears to be a function of trade-offs: In patriarchal societies where women risk social stigma or violence for having a baby with another man, EPP is likely to stay low; in settings where it's accepted or tolerated, such as the Himba, it's unsurprising that the rates are higher.

Even in Western societies, EPP rates seem to have varied depending on social conditions, Larmuseau notes. Working with historians, he charted how rates in Belgium and the Netherlands correlated with socioeconomic variables including income, religion, social class, and urbanization over the past 500 years. One of the biggest rises in EPP came in the 19th century, when cities across Europe boomed and people shifted from the countryside to factory jobs.

Using a data set that included information on where people lived as well as their occupations and their churches, Larmuseau added detail to the picture, using pedigrees of varying lengths to help guess when EPP events took place. He showed that in the crowded, impoverished, largely anonymous 19th century slums of major Belgian and Dutch cities, the EPP rate increased sixfold, cresting at close to 6%. Women living in rural areas, meanwhile—in small villages where everyone's comings and goings were fuel for gossip—were the least likely to have babies with men other than their husbands.

It's not just that women in cities were freer to choose extramarital partners, says Francesc Calafell, a geneticist at Pompeu Fabra University who collaborated with Larmuseau on the 2019 paper. EPP has to be seen in a larger context of sexual coercion and violence, which may have increased during periods of social change or when women began working in factories. "One can romanticize it as some sort of sexual escapade or flirting or whatnot," Calafell says. "In many cases what we see is that the reality was much darker than that."

EVERY YEAR, people around the world spend more than $5 billion exploring and documenting their genealogy. In Belgium, where Larmuseau has spent most of his life, seven in 10 people say they're interested in their family history. The Belgian government even funds genealogy nonprofits to help amateurs navigate archives and online genealogy resources.

That interest has turned Larmuseau into a minor Belgian celebrity: He gives public lectures once or twice a week, regularly appears on local news shows, and occasionally gets stopped on the street by people with questions about their family trees.

On a gray November Saturday in 2024, 400 people gathered in a university lecture hall in Leuven. They were there to hear the results from Larmuseau's latest project, dubbed MamaMito. After more than a decade chasing Y chromosomes and paternal lineages through dusty archives and cheek swabs, in 2019 he turned to mitochondrial DNA, which is passed exclusively from mothers to daughters.

Larmuseau says he wanted to ensure that suspected cases of EPP based on Y chromosome data were in fact what they seemed: an unacknowledged father, not a case of babies switched between mothers, a secret adoption, or 17th century identity fraud, for example. "If I see problems on the maternal line, then I'd know changes on paternal line weren't necessarily extra-pair paternity," Larmuseau says.

Finding the "foremothers" of Belgian and Dutch people living today is a more complicated endeavor than tracing paternal lines. Maternal genealogies are harder to follow, partly because women tended to change their last names each generation, and partly because women were more likely to move away from their hometowns to marry.

But when Larmuseau put out a call for volunteers in 2020, thousands of people rose to the task. During the pandemic many used digitized parish birth and marriage registries, notary documents, and property deeds to reconstruct their maternal family trees. Mirroring his Y chromosome work, Larmuseau and his team then collected DNA samples from distantly related women who should have common maternal ancestors to see whether the legal genealogies matched the biological lineage.

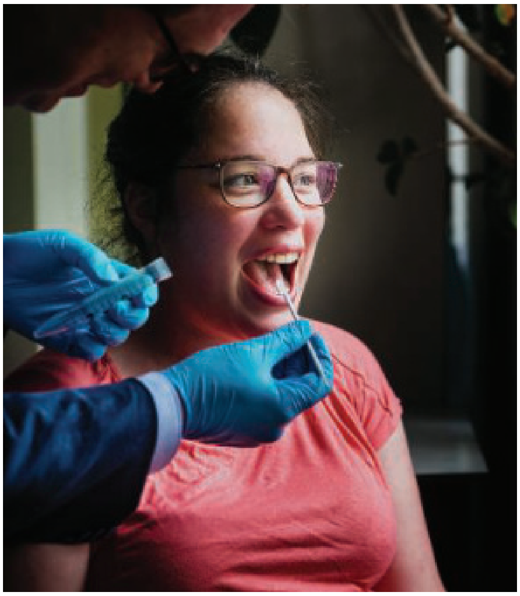
Maarten Larmuseau took cheek swabs from female volunteers to check mitochondrial DNA against their documented family.

After checking and double-checking the maternal family trees of hundreds of people against their mitochondrial DNA, he found no surprises. "That gives me confidence that when there are problems in the paternal line, it's most likely extra-pair paternity," he says, "rather than the far less likely scenarios of baby switches or secret adoptions."

These findings aren't just of historical interest. Forensic identifications of plane crashes or disaster victims sometimes rely on matching DNA with living relatives. Research into rare diseases, genetic counseling, and even standard family medical histories rely on accurate ancestry to map out hereditary conditions, an exercise that would be all but meaningless if the EPP rate were 30%, or even 10%.

That the rate is significantly lower in most cultures is good news for those efforts. Yet Larmuseau points out that even an EPP rate of 1% represents a lot of people. Around the world, an estimated 30 million people have taken direct-to-consumer DNA tests, which means roughly 300,000 may have been surprised by the news their biological father isn't who they expect. These revelations often come with no preparation or counseling, which Larmuseau and others say can be psychologically traumatizing.

That's part of the reason Larmuseau doesn't test siblings, or people with parents, grandparents, or great-grandparents in common, because the consequences of uncovering a painful family secret in the recent past are too high. And he offers counseling to people upset by findings from a century or more ago. "Some people are angry, or disgusted, or mad at Maarten," says Jan Geypen, a genealogist who works for Histories, a Belgian heritage nonprofit that helped connect Larmuseau to study participants. "If something's wrong with the family tree, they think maybe we made a mistake, or the science is wrong, or they ask us to check again. But shit happened in the past, right?"

These reactions highlight the stigma that female infidelity still carries in Western society, as well as the deep connection many feel with distant ancestors. For his part, Werner van Beethoven initially wondered whether working with Larmuseau had been a mistake. "For a while I thought, maybe it would have been better if they didn't do this research," he says. "Then the composer might still be 100% a van Beethoven," as far as anyone would know.

In the years since, he's come to terms with the broken branches on his family tree. "It's incredible that they have the tools to find this out," he says. "And now they have more information about the composer and his family."

In the meantime, he's dug deeper into his family history, uncovering relatives including Josijne van Vlasselaer, who was burned as a witch in 1595. ("She was a strong woman," van Beethoven says, "with special ideas.") He hasn't given up on the best known van Beethoven, either. "After a while, I thought, maybe he's not a real Beethoven biologically, but legally he's got the same name, and I'm proud of it," van Beethoven says. "There are illegitimate kids in every family. There's no shame in it." ■

PHOTO: AN VAN GIJSEGEM

eppendorf & Science
PRIZE FOR
NEURO
BIOLOGY

2024 Winner
Laura Seeholzer, Ph.D.
University of California San Francisco,
School of Medicine, USA

For research on airway neuroendocrine cells responding to external threats

Application Deadline
June 15, 2025

Call for Entries 2025

Eppendorf & Science Prize for Neurobiology
The annual Eppendorf & Science Prize for Neurobiology is an international prize which honors young scientists for outstanding neurobiological research based on methods of molecular, cellular, systems, or organismic biology. If you are 35 years of age or younger and doing great research, now is the time to submit an entry for this prize.
It’s easy to apply! Write a 1,000-word essay and tell the world about your work.

eppendorf.com/prize

As the winner, you could be next to receive
- Prize money of US$25,000
- Publication of your work in *Science*
- Full support to attend the Prize Ceremony held in conjunction with the Annual Meeting of the Society for Neuroscience in the USA
- 10-year AAAS membership and online subscription to *Science*
- Complimentary products worth US$1,000 from Eppendorf
- An invitation to visit Eppendorf in Hamburg, Germany

eppendorf Science AAAS

AAAS® and Science® are registered trademarks of the American Association for the Advancement of Science, USA. Eppendorf® and the Eppendorf Brand Design are registered trademarks of Eppendorf SE, Germany. All rights reserved, including graphics and images. Copyright © 2025 by Eppendorf SE. Photography: Brian Carey, figMedia

INSIGHTS

PERSPECTIVES

There is still very little available data on butterfly abundance for many parts of the United States.

ECOLOGY

Butterfly populations flutter bye

Systematic analysis reveals decades-long decline in US butterfly population abundance

By **Brian D. Inouye**[1,2]

Quantifying insect diversity patterns is challenging given that many species are obscure or still undescribed. However, the bright colors of butterflies are a source of delight that have captivated observers for centuries, enabling the collection of valuable data on butterfly diversity and abundance and making it possible to study long-term changes in butterfly communities. Studies combining historical records and citizen science data have reported large butterfly population declines in western Europe (*1*) and the western US (*2*). On page 1090 of this issue, Edwards *et al.* (*3*) report the assembly of the most comprehensive dataset of systematic, decades-long butterfly monitoring within the contiguous US. The study reveals a worrying decline in total butterfly abundance, the magnitude of which is in line with global estimates of insect declines (*4*).

Edwards *et al.* analyzed butterfly sightings and catches from >76,000 surveys carried out across the past couple of decades at ~2500 distinct sampling locations, representing all regions of the US. These data contain entries for more than 12 million butterflies, collected by professionals and networks of dedicated amateur naturalists, reflecting the continuing broad appeal of butterfly watching. From this comprehensive dataset, the authors observed a 22% decrease in total butterfly abundance across the contiguous US from 2000 to 2020, with declines apparent in all regions and for most species. They also saw butterfly species tending to expand their distributions toward the north, consistent with earlier studies of butterfly range shifts (*5*, *6*).

Despite being one of the most widely monitored insect groups, butterflies are conspicuously absent from samples of the most common types of insect traps, for the simple reason that they tend to be too large-bodied to fit into trap openings. Because of this limitation, the landmark study that reported a large decline in insect abundance across southern Germany over the past 27 years (*7*) as well as subsequent meta-analyses (*4*) and new studies (*8*, *9*) have not relied on butterfly data. However, the declines reported by Edwards *et al.* confirm that the broad geographic and taxonomic extent of insect declines extends to butterflies as well.

Average trends in abundance can obscure important differences among regions and species; it is species and populations that are management targets and may go extinct, not averages. The statistical models used by Edwards *et al.* account for differences in sampling approach and seasonality, which allowed them to make robust comparisons of the expected butterfly diversities that would be observed using a standardized search. They found that butterfly declines differed among US regions, with the steepest declines in the southwest. Variation among species was observed to be much greater than variation among regions, and although a handful of species increased in abundance during the study period, far more species showed steep declines. The data showed that at least 74 butterfly species have declined in abundance by more than 50%, although the authors only had sufficient data for detailed analyses of half of the species found in the US, and rare species may be even more likely to show declines. Species' traits, such as wingspan and host plant associations, did not help to explain which species were declining. Although Edwards *et al.* used a huge quantity of survey data, there are still many parts of the US for which there is very little data. Increased monitoring and spatially replicated monitoring, even for short-term studies, would help resolve uncertainties about the status of rare species and help tease apart potential causes of changes in butterfly abundance (*10*).

Insects comprise roughly half of all multicellular species and have essential roles in terrestrial ecosystems, making declines in insect abundance and diversity concerning for many reasons, not only for butterfly watchers. For example, insect declines have been implicated in population declines for bird species whose primary food source is insects (*11*). Declines in insects that are available as prey are likely to affect many kinds of predators, from generalists such as birds to specialists such as parasitoids. However, because insect populations can increase rapidly when conditions are favorable, previous research has focused on ways to control pests and reduce populations during outbreaks, rather than on investigating ways to monitor or reverse broad insect declines.

Many factors have been implicated as potential causes of insect declines (*12*), including habitat loss associated with agricultural intensification or urbanization, increasing pesticide use, and shifts in weather patterns linked to climate change. Butterfly species that require grassland habitats are particularly at risk (*1*, *8*) because natural grasslands face pressures from agriculture and other land-use conflicts and may be more vulnerable to anthropogenic nitrogen deposition than other habitats. Pesticides, particularly neonicotinoids, have been implicated in butterfly declines in California (*13*), as well as in declines of many other kinds of insects (*14*). Weather anomalies and an increased frequency of drought conditions, both associated with climate change, likely contribute to declines in insect populations in all areas (*12*), including at sites without changes in land use (*9*).

Solutions to the problem of declining insect and butterfly populations will have to be as varied as the causes, addressing different stressors for different regions and species. Some species may benefit from protecting areas that are likely to be refugia from fires or storms, whereas others may benefit from active habitat restoration and management. Strategies such as promoting narrow, naturally vegetated buffer strips along waterways may offer win-win solutions, because buffer strips can promote butterfly abundance and diversity (*15*) while also protecting water quality and reducing flooding risks. Luckily, learning to identify butterflies and contributing sightings to citizen science databases can be an easy and enjoyable way to help monitor the status of these beautiful insects, and to build support for healthy insect populations more generally. ■

---

[1]Department of Biological Science, Florida State University, Tallahassee, FL, USA. [2]Department of Ecology, Environment and Plant Sciences, Stockholm University, Stockholm, Sweden. Email: binouye@bio.fsu.edu

PHOTO: DAVID W. INOUYE

REFERENCES AND NOTES

1. M. S. Warren *et al.*, *Proc. Natl. Acad. Sci. U.S.A.* **118**, e2002551117 (2021).
2. M. L. Forister *et al.*, *Science* **371**, 1042 (2021).
3. C. B. Edwards *et al.*, *Science* **387**, 1090 (2025).
4. R. van Klink *et al.*, *Science* **368**, 417 (2020).
5. C. Parmesan *et al.*, *Nature* **399**, 579 (1999).
6. J. K. Hill *et al.*, *Proc. Biol. Sci.* **269**, 2163 (2002).
7. C. A. Hallmann *et al.*, *PLOS ONE* **12**, e0185809 (2017).
8. S. Seibold *et al.*, *Nature* **574**, 671 (2019).
9. R. M. Dalton, N. C. Underwood, D. W. Inouye, M. E. Soulé, B. D. Inouye, *Ecosphere* **14**, e4620 (2023).
10. N. Blüthgen, M. Staab, R. Achury, W. W. Weisser, *Biol. Lett.* **18**, 20210666 (2022).
11. D. E. Bowler, H. Heldbjerg, A. D. Fox, M. de Jong, K. Böhning-Gaese, *Conserv. Biol.* **33**, 1120 (2019).
12. D. L. Wagner, E. M. Grames, M. L. Forister, M. R. Berenbaum, D. Stopak, *Proc. Natl. Acad. Sci. U.S.A.* **118**, e2023989118 (2021).
13. M. L. Forister *et al.*, *Biol. Lett.* **12**, 20160475 (2016).
14. W. M. Janousek *et al.*, *Proc. Natl. Acad. Sci. U.S.A.* **120**, e2211223120 (2023).
15. S. Birnbeck, J. Burmeister, S. Wolfrum, B. Panassiti, R. Walter, *Agric. Ecosyst. Environ.* **378**, 109300 (2025).

10.1126/science.adw1633

MATERIALS SCIENCE

Ply for a large stroke

A simple coiling of two or more twisted fibers makes artificial muscles with a high spring index

By **Jun Zhang**

Humans rely on muscle coordination for essential functions such as movement, regulation of blood flow, and respiration. For a synthetic material to mimic biological muscle properties, it needs to generate sufficient mechanical force and deform across large lengths in response to external stimuli. A promising type of artificial muscle, called "coiled muscle," has a substantial actuation range and power when heated. Constructed by coiling a twisted fiber often made of polymers, its functionality is determined by the spring index, which is the ratio of coil diameter to fiber diameter (*1*). Various synthetic materials with high spring indices have been developed (*2*, *3*), but these often require expensive fabrication methods. On page 1101 of this issue, Zhang *et al.* (*4*) report that simple plying of two or more twisted fibers produces a coiled muscle with a high spring index. This approach could lead to a cost-effective way to create artificial muscles at a large scale.

Artificial muscles have a range of potential applications, from soft robotics, prosthetic limbs, and microfluidics to industrial actuators and energy-harvesting systems. Coiled muscles can be made by using household polymers, such as fishing lines and sewing threads, but also with advanced materials such as carbon nanotube yarns (*5*). Rotating movement forces the highly oriented individual chains that constitute a filament into a helical configuration at the microscopic level. When twisting exceeds a certain degree, the fiber starts to coil into a spiral shape macroscopically. Heat contracts the polymer chains in length, which expands the diameter of the filament and causes the coiled string to untwist. The unwinding motion produces substantial force and amplifies the contraction of the fiber by orders of magnitude (*6*). This actuation mechanism of a coiled muscle can generate power density (amount of energy per unit volume) that is comparable with that of jet engines. However, an unavoidable trade-off between stroke and force generation exists. A coiled muscle with a large spring index can produce a giant stroke but reduced actuation force.

Mandrel-free fabrication of artificial muscles

Two or more individually twisted polymer fibers are tethered and plied together. Subsequent heat treatments imprint and equilibrate a spiral shape into the fibers. This can produce a coiled muscle in a large scale with a gradient of spring index along its length.

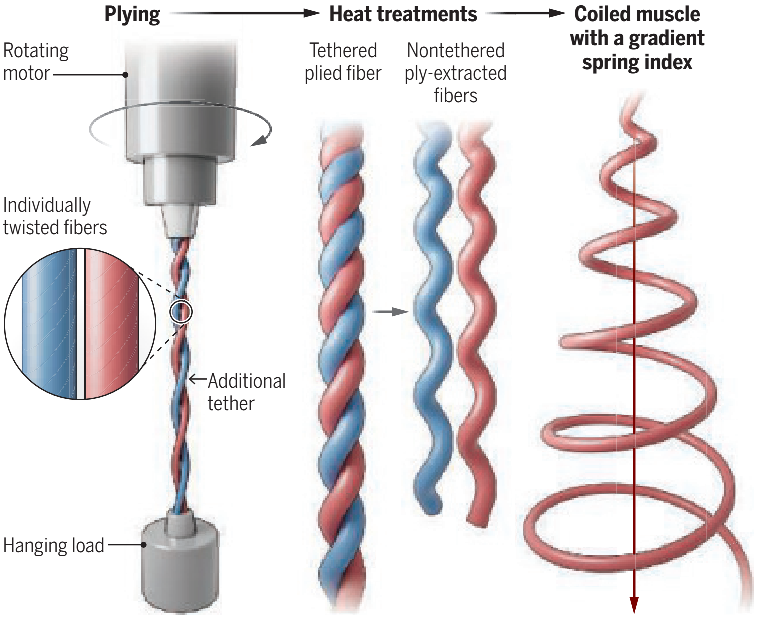

Coiled muscles can be made with self-coiling and mandrel-based coiling methods (*5*). A simple twisting of a tight thread under a high tensile load creates a coiled string without entanglement (*5*). However, a self-coiled muscle often has a small spring index of <1.7, which limits its stroke (contraction) to 10 to 20% of its original length (*7*). Artificial muscles with a large spring index have been fabricated by wrapping a twisted fiber on a mandrel (a cylindrical or tapered support). This method has produced a coiled muscle with a spring index of >2 that can contract by 49% of its original length (*5*). Mandrel-based coiling can also provide an additional control over the helical shape of the fiber. The cylindrical support can be patterned with grooves to form a coiled muscle with a uniform gap between neighboring coils (*8*) or with specific spiral patterns (*9*). However, coiled muscles made by using a mandrel generally have a reduced mechanical force output. Additionally, a mandrel that is often used for a single fabrication is expensive, and the geometry of a coiled muscle is limited by the shape and size of the used mandrel.

Zhang *et al.* made a notable advance by producing high-performance coiled muscles through a mandrel-free process (see the figure). Polyurethane and nylon fishing line fibers were individually twisted just below the level that initiates coiling. Two or more of these twisted strings were then tethered and plied together with a tensile load. Instead of a mandrel, each fiber served as a support for the others. The twisted and coiled polymeric yarns were thermally annealed to imprint the spiral shapes. The fibers were subsequently released and heated for a second time. This step equilibrated the coiled muscle by slightly shrinking the polymer chains and reducing separation between neighboring coils. Zhang *et al.* demonstrated precise control over the spring index by adjusting processing parameters such as number of plies, twist density (number of turns per length of a fiber), and the thermal annealing temperature. Optimizing the plying condition created a coiled muscle with a colossal spring index of 50 and a giant contractile stroke exceeding 97% of its initial length. The mandrel-free method improved both stroke and force output of a coiled muscle compared with those fabricated with mandrels.

One aspect of the mandrel-free coiling method is the ability to produce a coiled muscle with a spring index gradient along the length. Zhang *et al.* separated the twisted fibers into multiple regions by tethering them at various points. This process either introduced additional coils or removed existing coils from an individual region. The resulting coiled muscle exhibited a gradual change in spring index from one end to the other, which is challenging

GRAPHIC: A. MASTIN/*SCIENCE*

Department of Mechanical Engineering, University of Nevada, Reno, NV, USA. Email: jun@unr.edu

to produce with the mandrel-based coiling method. The gradient geometry enables a specific segment to actuate differently from the rest of the coiled muscle. This could be useful for creating artificial muscles with complex strokes.

The mandrel-free coiling method is particularly advantageous for applications that require large strokes but small tensile loads on fibers, such as clothing. Tensile load is essential in the self-coiling process to produce a sufficient gap between neighboring coils to avoid coil-to-coil interference during contraction. Plying inherently gives a large intercoil separation at a small tensile load. Thus, the mandrel-free technique can be applied to flexible textile structures that cannot be self-coiled under a high tensile load. Zhang *et al.* developed a jacket with switching insulation that was constructed by using mandrel-free coiled muscles. Artificial muscles were placed on the exterior of a jacket or in between two fabric layers. The actuation of twisted and coiled fibers opened and closed thermal insulation pores to maintain the body temperature when the ambient temperature changed to –12°C or 43°C. A mandrel-free method could be used to fabricate such smart textiles in a large quantity in an inexpensive way.

Although Zhang *et al.* performed preliminary analyses on the effects of processing conditions such as twist density, load, and annealing temperature on artificial muscle performance, more detailed examination should point to optimal fabrication conditions and geometrical design for certain performance metrics. This would enable modeling of parameters required for desired artificial muscle functions for specific robotic domains. In addition, coiled muscles with a gradient of spring index could potentially bring new actuator designs and robot capabilities, such as stimuli-responsive shape morphing (*10*). Integrating this with other artificial muscle technologies could contribute to realizing soft robots that are capable of performing feats that traditional machines cannot accomplish (*11*). ■

REFERENCES AND NOTES

1. X. Leng *et al.*, *Adv. Intell. Syst.* **3**, 2000185 (2021).
2. S. M. Mirvakili, I. W. Hunter, *Adv. Mater.* **30**, 1704407 (2018).
3. J. Zhang *et al.*, *IEEE Trans. Robot.* **35**, 761 (2019).
4. M. Zhang *et al.*, *Science* **387**, 1101 (2025).
5. C. S. Haines *et al.*, *Science* **343**, 868 (2014).
6. J. D. W. Madden, S. Kianzad, *IEEE Pulse* **6**, 32 (2015).
7. M. C. Yip, G. Niemeyer, *IEEE Trans. Robot.* **33**, 689 (2017).
8. J. Sun, B. Tighe, Y. Liu, J. Zhao, *Soft Robot.* **8**, 213 (2021).
9. C. S. Haines *et al.*, *Proc. Natl. Acad. Sci. U.S.A.* **113**, 11709 (2016).
10. J. Sun, E. Lerner, B. Tighe, C. Middlemist, J. Zhao, *Nat. Commun.* **14**, 6023 (2023).
11. B. Trimmer, *Curr. Biol.* **23**, 639 (2013).

10.1126/science.adw2181

CORONAVIRUS

Lung inflammation drives Long Covid

Peroxisome dysfunction in macrophages impairs lung repair after COVID-19 in mice

By **Alan Sariol**[1] *and* **Stanley Perlman**[2]

Although great strides have been made in understanding and mitigating acute manifestations of COVID-19, post-acute sequelae of severe acute respiratory syndrome coronavirus 2 (SARS-CoV-2) infection (PASC) or “Long Covid”—which includes long-term lung, neurological, and cardiovascular complications—remains a substantial burden to patients and the health care system. The mechanisms that underlie PASC are not clear, but aberrant immune responses have been implicated. On page 1054 of this issue, Wei *et al.* (*1*) report dysfunction in alveolar macrophages—lung-resident immune cells involved in tissue repair—as a contributing factor to persistent lung pathology after SARS-CoV-2 infection. Loss of peroxisomes (organelles involved in oxidative reactions and metabolism) from these macrophages after infection in mice (*Mus musculus*) resulted in impaired regeneration of lung tissue and persistent fibrosis—scar tissue harmful to lung function. These findings elucidate the etiology of postviral lung disease and suggest avenues for therapeutic intervention.

Peroxisomes contain enzymes that facilitate oxidative metabolism of fatty acids as well as enzymes that can neutralize the toxic reactive oxygen species (ROS) that are produced by these metabolic processes. These organelles thus play a critical role in controlling oxidative stress in cells. Wei *et al.* compared postmortem lung tissue samples from individuals with severe, acute COVID-19 with samples from individuals without COVID-19. The authors observed reduced expression of genes encoding peroxisomal proteins and changes to peroxisomal subcellular distribution and morphology (including increased size) in alveolar macrophages from patients with COVID-19. Individuals with pulmonary fibrosis associated with PASC also had fewer peroxisome-containing alveolar macrophages compared with individuals without COVID-19 or PASC. These reductions were recapitulated in mice infected with mouse-adapted strains of SARS-CoV-2 or influenza A virus, which is also associated with postviral lung disease. These observations indicate that peroxisome synthesis and degradation are affected by SARS-CoV-2 infection.

In vitro, Wei *et al.* found that application of type I [interferon-α (IFN-α)] and particularly type 2 (IFN-γ) interferons (cytokines with antiviral and immunomodulatory properties) to alveolar macrophages from mice promoted similar changes to peroxisome number, distribution, and morphology as were observed after infection. Treatment of mice with antibodies that neutralize or block the receptors of these cytokines on alveolar macrophages prevented the peroxisomal changes in these cells, which suggests that the inflammatory response to the virus drives the observed alterations in peroxisomes.

Wei *et al.* took mice in which peroxisomal biogenesis factor 5 (*Pex5*), a gene critical for peroxisome synthesis, is deficient in macrophages, and they infected these mice with SARS-CoV-2. Infection was associated with more severe disease and greater mortality in *Pex5*-deficient mice compared with wild-type mice. This increase in disease severity was associated with the delayed return of cytokines to homeostatic levels after virus clearance along with exacerbated lung infiltration of inflammatory cells. *Pex5*-deficient mice also had increased expression of inflammatory genes and reduced expression of tissue repair genes relative to infected wild-type mice.

Wei *et al.* identified immunohistological signs of abnormal lung repair in *Pex5*-deficient mice. These included reduced numbers of alveolar type 1 (AT1) epithelial cells, which are important for air exchange, and AT2 progenitor cells, which are precursors for AT1 cells. The authors also identified elevated numbers of cells containing high amounts of keratin, type II cytoskeletal 8 ($\text{Krt8}^{\text{high}}$), which is a marker of cells that are in an intermediate state between AT2 and AT1. Persistence of $\text{Krt8}^{\text{high}}$ cells suggests arrested differentiation of AT2 cells, a process that is critical for injury repair. *Pex5*-deficient mice had elevated and sustained production of interleukin-1β (IL-1β), which contributes to the stalling of AT2-to-AT1 differentiation at

---

[1] Department of Medicine, Washington University School of Medicine, St. Louis, MO, USA. [2] Department of Microbiology and Immunology, University of Iowa, Iowa City, IA, USA. Email: stanley-perlman@uiowa.edu

the Krt8^{high} state (*2*, *3*). This IL-1β production was, at least in part, a result of impaired mitochondrial function, which caused an accumulation of cellular ROS (*4*).

Wei *et al.* identified a drug that enhanced lung recovery after SARS-CoV-2 infection in mice. Treatment of wild-type mice with sodium 4-phenylbutyrate (4-PBA)—which induces peroxisome proliferation and is used clinically to treat urea cycle disorders (*5*)—during acute SARS-CoV-2 infection protected against mortality and reduced abnormal lung repair. Furthermore, 4-PBA treatment after clearance of the virus promoted AT2-to-AT1 differentiation and alleviated fibrosis (see the figure). This suggests that peroxisome synthesis might represent an attractive target for therapeutic intervention after acute SARS-CoV-2 infection has subsided.

The study by Wei *et al.* is part of a growing body of literature that suggests that peroxisome dysfunction can occur after viral infections. SARS-CoV-2 infection triggers peroxisomal rearrangement and loss in human cells in vitro (*6*, *7*), and other viruses, such as influenza virus, flaviviruses, and HIV, can disrupt peroxisome function and synthesis in human cells and tissues (*8*–*10*). Although Wei *et al.* focused on SARS-CoV-2–mediated lung disease, similar effects on peroxisome synthesis have been observed in the brains of individuals with COVID-19 and in those of Syrian hamsters (*Mesocricetus auratus*) infected with SARS-CoV-2 (*11*). This suggests that peroxisome dysfunction could also be involved in neurological symptoms of PASC.

This work by Wei *et al.* contributes to a growing understanding of the mechanisms driving PASC. Other recent findings in mouse models of PASC demonstrated a role for pathogenic CD8$^+$ T cells, which are involved in killing virus-infected cells (*3*), and IFN-γ–induced profibrotic monocyte-macrophages, which are blood-derived inflammatory cells that infiltrate the lungs upon infection (*12*). The relative contributions of these different mechanisms to PASC and the effects of therapies on these independent aspects of the disease process remain to be determined. ■

REFERENCES AND NOTES

1. X. Wei *et al.*, *Science* **387**, eadq2509 (2025).
2. J. Choi *et al.*, *Cell Stem Cell* **27**, 366 (2020).
3. H. Narasimhan *et al.*, *Nature* **634**, 961 (2024).
4. C. G. Weindel *et al.*, *Cell* **185**, 3214 (2022).
5. H. Wei *et al.*, *Ann. Neurol.* **47**, 286 (2000).
6. M. Cortese *et al.*, *Cell Host Microbe* **28**, 853 (2020).
7. B. Knoblach *et al.*, *Mol. Biol. Cell* **32**, 1273 (2021).
8. T. Liu *et al.*, *Viruses* **16**, 1309 (2024).
9. J. You *et al.*, *J. Virol.* **89**, 12349 (2015).
10. Z. Xu *et al.*, *PLOS Pathog.* **13**, e1006360 (2017).
11. A. Roczkowsky *et al.*, *Ann. Neurol.* **94**, 531 (2023).
12. C. Li *et al.*, *Sci. Transl. Med.* **16**, eadn0136 (2024).

ACKNOWLEDGMENTS

The authors acknowledge support from the National Institutes of Health (R01 AI129269).

10.1126/science.adw0091

Disruption of lung repair in Long Covid

After mild infection with severe acute respiratory syndrome coronavirus 2 (SARS-CoV-2), alveolar macrophages increase expression of genes related to wound healing, which allows alveolar type 2 (AT2) progenitor cells to differentiate into AT1 cells and contribute to lung repair. In mouse models of severe COVID-19 or in COVID-19 that results in post-acute sequelae of SARS-CoV-2 infection (PASC), type 1 [interferon-α (IFN-α)] and type 2 (IFN-γ) interferons induce peroxisome loss and remodeling in alveolar macrophages. This impairs mitochondrial metabolism, causing accumulation of reactive oxygen species (ROS) and release of interleukin-1β (IL-1β). IL-1β impairs AT2 differentiation, causing arrest at a high keratin, type II cytoskeletal 8 (Krt8^{high}) transitional cell state and pulmonary fibrosis. Treatment with 4-phenylbutyrate (4-PBA) restored peroxisome function and healthy lung repair.

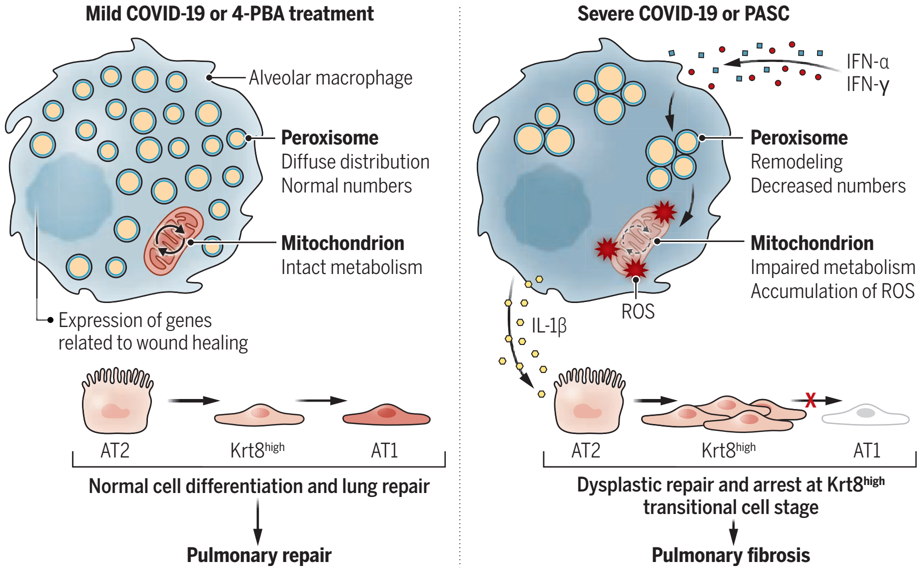

Mild COVID-19 or 4-PBA treatment

Severe COVID-19 or PASC

GRAPHIC: K. HOLOSKI/*SCIENCE*

PHOTOVOLTAICS

Sandwiched between flat barriers

Two-dimensional materials stabilize perovskites for charge transfer under heat and light irradiation

By **Michael Saliba**[1,2] *and* **Weiwei Zuo**[1]

A group of mineral compounds with a distinct crystalline structure, called perovskite, is a cost-effective alternative to conventional semiconductors. Solar cells based on perovskites continue to set new performance standards in sunlight-to-electricity conversion, achieving efficiencies that are comparable to those of established materials such as silicon (*1*). Perovskites in tandem with silicon have also shown higher power conversion efficiencies than that of a single material (*2*). However, long-term stability of perovskite solar cells remains a major hurdle because of the compounds' sensitivity to factors such as heat and light-induced stress. On page 1069 of this issue, Li *et al.* (*3*) report that layers of graphene and polymer reinforce a perovskite film to reduce light-induced structural distortion substantially. This, in addition to a recent study of Zai *et al.* (*4*) that reported perovskite stabilization with molybdenum disulfide (MoS_2), shows how two-dimensional (2D) materials could move perovskite-based devices toward practical applications.

Perovskites for photovoltaics generally follow an ABX_3 structure in which A and B are cations (ionized small molecules or alkali metals for A and post-transition metals for B) and X is an anion, such as a halide ion. Because of the different sizes of the constituent ions and the soft nature of the lattice, local structural distortions can occur in these materials. Defects can form both in the bulk and on the surfaces of a perovskite thin film during the formation of the layer. These imperfections change the internal stress and strain of the film,

---

[1] Institute for Photovoltaics, University of Stuttgart, Stuttgart, Germany. [2] Helmholtz Young Investigator Group FRONTRUNNER, IMD3-Photovoltaik, Forschungszentrum Jülich, Jülich, Germany. Email: michael.saliba@ipv.uni-stuttgart.de

which affect its photoelectric properties (*5*). Some bulk defects can be healed by introducing specific additives during fabrication or repeatedly exposing the film to light with fluctuating intensities (light cycling). However, this poses a risk of introducing additional defects. Surface defects are also problematic because degradation triggered from the surrounding environment (light, moisture, and heat) can gradually spread inward.

Structure of a perovskite solar cell

A three-dimensional perovskite is placed between two charge transport layers that extract and deliver charge carriers. The top and bottom interfaces determine the overall performance of a solar cell. Two-dimensional (2D) materials provide sufficient electrical contacts and protect the perovskite from structural distortions, contaminants, and free ions.

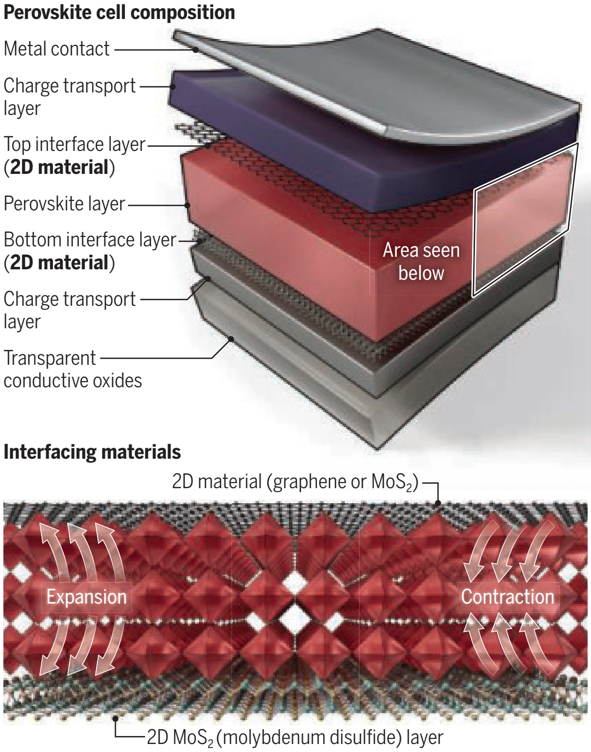

GRAPHIC: A. FISHER/*SCIENCE*

A perovskite solar cell is a multilayer device in which a three-dimensional (3D) perovskite film is sandwiched between two charge extraction layers (see the figure). The top and bottom interfaces (the latter is often described as “buried”) between the two components not only transport charges but also indirectly protect the perovskite absorber from degradation. Thus, it is important to optimize these junctions for the overall performance. A commonly used strategy involves introducing a large molecule with a strong binding interaction on the surface of the perovskite film. This promotes the formation of a 2D layer on top of the 3D perovskite layer (*6*–*8*). Although this method enhances stability to some extent, it does not increase the mechanical strength of the top interface.

Li *et al.* applied a 2D graphene monolayer to the top interface using a polymer poly(methyl methacrylate) as a binder. This polymeric buffer layer contributed to managing the strain at the interface without compromising the inherent properties of graphene. Additionally, the high charge carrier mobility of graphene improved the charge transfer at the interface without strongly affecting the specific energy level alignment between the perovskite and the charge carrier extraction layer, which is related to the open circuit voltage loss. This approach improved the stability of the perovskite films over multiple cycles of light absorption and conversion to electricity. The mechanical strength of graphene also suppressed structural distortions caused by the repeated exposure to light.

Theoretically, both the top and bottom interfaces can effectively suppress lattice deformation caused by light cycling. Although it is relatively easy to modify the top interface after fabricating the perovskite film, engineering the bottom interface is more challenging. The material at the bottom unavoidably influences subsequent formation of the perovskite, constraining the optimization of charge transport. To ensure that the charge is effectively extracted, a self-assembled monolayer—a layer of organized molecules forming a solid surface—is often deposited at the bottom interface. However, this layer is primarily anchored to the substrate with hydrogen bonds that readily break in a polar solvent, which is used in subsequent deposition of the perovskite (*9*). In addition, molecules of a self-assembled monolayer tend to aggregate and make weak physical contact with the perovskite, thereby affecting the performance and stability of the device (*10*). Integrating 2D perovskites between the self-assembled monolayers and the 3D perovskite film (*11*) can overcome these drawbacks by promoting the growth of highly stable, and defect-free, perovskites (*12*). However, in contrast to the top interface, it can be challenging to deposit a thin layer of 2D perovskite at the bottom interface (*13*).

Zai *et al.* transferred a wafer-scale monolayer of MoS_2 at both the top and bottom interfaces. The 2D network structure of MoS_2 can physically block the migration of perovskite ions that are triggered by light irradiation to the carrier transport layer. The MoS_2 chemically stabilizes the perovskite through strong coordination interaction that forms lead sulfide bonds between the two layers. The chemical passivation effectively provides protection against minority carriers that are harmful to device operations by using type I band alignment (a complete overlap of energy bandgap between perovskite and MoS_2). Zai *et al.* provide a practical framework for the application of 2D materials in perovskite-based optoelectronic devices, and the fact that a single-layer tungsten disulfide film also exhibits a similar ideal buffering effect at the perovskite interface proves the generality of this strategy. Zai *et al.* reported that an MoS_2/perovskite/MoS_2 configuration exhibits improved stability with a power conversion efficiency comparable to that of silicon solar cells.

Li *et al.* and Zai *et al.* demonstrate that applying 2D materials at the top and bottom interfaces of a perovskite solar cell could be a universal strategy to address the stability problem. Intrinsically strong and flexible 2D materials with high electrical conductivity are ideal for transferring charge carriers efficiently while providing a physical barrier to protect perovskites from the surrounding environment. The main challenge in using 2D materials is transferring high-quality monolayers in wafer scale. Li *et al.* used a polymer film as an innocuous binder for graphene, whereas Zai *et al.* exploited a bond between lead atoms in the perovskite and sulfur atoms in the MoS_2 layer. The dry transfer method provided simple and reliable top and bottom interface structures. Further development in integrating mechanically robust, defect-free 2D materials into perovskite-based solar cells provides a framework for the long-term stability of the device under complex environmental conditions. ■

REFERENCES AND NOTES

1. US National Renewable Energy Laboratory (NREL) chart, 20 February 2025.
2. J. Liu *et al.*, *Nature* **635**, 596 (2024).
3. Q. Li *et al.*, *Science* **387**, 1069 (2025).
4. H. Zai *et al.*, *Science* **387**, 186 (2025).
5. Y. Shen *et al.*, *Nature* **635**, 882 (2024).
6. Y. Wang *et al.*, *Nature* **635**, 867 (2024).
7. H. Wang *et al.*, *Nature* **634**, 1091 (2024).
8. C. Liu *et al.*, *Nature* **633**, 359 (2024).
9. H. Tang *et al.*, *Science* **383**, 1236 (2024).
10. S. Liu *et al.*, *Nature* **632**, 536 (2024).
11. R. Azmi *et al.*, *Nature* **628**, 93 (2024).
12. S. Sidhik *et al.*, *Science* **384**, 1227 (2024).
13. H. S. Choi *et al.*, *Science* **384**, 60 (2024).

10.1126/science.adw1552

POLICY FORUM

INFECTIOUS DISEASE

Global withdrawal of Sabin oral poliovirus type 2 vaccine in 2016

Evaluation guides strategy for the polio eradication endgame

By **Natalia A. Molodecky**[1], **Roland W. Sutter**[2], **the Switch Evaluation Sounding Board (SESB)**

Live Sabin oral poliovirus vaccine (OPV), a live-attenuated vaccine, is genetically unstable and can revert back to neurovirulence and transmissibility, causing vaccine-associated paralytic poliomyelitis (VAPP) and circulating vaccine-derived poliovirus (cVDPV). Following a resolution of the World Health Assembly (WHA) in 2015, the Global Polio Eradication Initiative (GPEI) set the target for global withdrawal of the type 2 component of OPV (OPV2) for April 2016 (i.e., the switch). Within 12 to 18 months after the switch, it became apparent that the GPEI struggled to close out (stop and confirm absence of transmission) cVDPV2 outbreaks from undetected transmission and new emergences from OPV2 use in outbreak control. In 2023, the GPEI began discussing the global cessation of all Sabin polioviruses, necessitating the discontinuation of bivalent (type 1 and 3) OPV (i.e., bOPV). We attempt to identify and highlight the causes for the post-switch epidemiologic situation and offer some suggestions on how to avert such a development in the future.

In 1988, the WHA, the oversight body of the World Health Organization (WHO), resolved to eradicate poliomyelitis by the year 2000 (*1*). The goal was partly achieved with the eradication of wild poliovirus type 2 (WPV2) globally in 1999, with the last detection in Northern India, and eventual certification of eradication in 2015. In addition, wild poliovirus type 3 was last detected in Nigeria (2012) and Pakistan (2012) and certified as eradicated in 2019. However, as of late 2024, wild poliovirus type 1 (WPV1) continues to circulate in Afghanistan and Pakistan (*2*).

Concomitantly to the efforts to eradicate polio, the GPEI established a road map toward the eventual withdrawal of all OPV, including the three serotypes used in the trivalent OPV (tOPV), starting with OPV2. Although OPV has played a key role in polio eradication and reduced the global polio case burden by >99.9%, its continued use is not compatible with eradication. The continued VAPP burden [around 200 to 400 cases each year (*3*)] was becoming more unacceptable following WPV2 eradication, and cVDPVs (typically emerging and spreading in populations of low immunity, with cVDPV2 most common) posed a threat to reestablishing poliovirus transmission.

The major elements of OPV2 withdrawal were outlined in the 2013–2018 Strategic Plan of Action (*4*). The plan called for certification of WPV2 eradication by the Global Commission for the Certification of Polio Eradication (achieved in late 2015) and specified several prerequisites (readiness criteria) that needed to be met before OPV2 withdrawal could be implemented. Routine immunization (RI) would switch from tOPV to bOPV, and subsequent campaigns would only use bOPV. Inactivated poliovirus vaccine (IPV) would be introduced into RI to mitigate against risk of paralysis from cVDPV2 infection.

Following substantial progress of GPEI toward meeting the readiness criteria, the initial logistical phase of the OPV2 withdrawal was evaluated and deemed successful (*5*). But there followed subsequent struggles to close out outbreaks particularly in countries with suboptimal infrastructures for delivering vaccines, especially the eastern part of the Democratic Republic of the Congo (DRC) and Northern Nigeria (*6*). In the context of the 2023 GPEI discussions toward global cessation of types 1 and 3 vaccines, a review and evaluation of the 2016 switch from tOPV to bOPV was conducted (*7*) to compile the lessons learned and provide input into the bOPV cessation plan.

EVALUATION APPROACH

The Strategy Committee (SC) of GPEI, the managing body for polio eradication, issued a mandate to conduct an external evaluation of the basis and outcome of the switch from tOPV to bOPV in 2016. The evaluation commenced in August 2023 after constitution of the evaluation team by the authors of this report (N.A.M., R.W.S.) and process of the peer panel review for the observations and recommendations.

The evaluation was necessary because the GPEI had started to discuss the withdrawal of Sabin types 1 and 3 contained in bOPV. Even though WPV1 remained in endemic transmission, the initial planning for bOPV withdrawal was underway. The focus of the evaluation was to identify and compile the lessons learned from the 2016 switch. A three-pronged approach was pursued: (i) qualitative evaluation (following the guidelines of the American Evaluation Society) using the 2013–2018 Strategic Plan (*3*) as the template for the evaluation; (ii) quantitative evaluation (conducting additional analyses) using data from the polio information system (POLIS) maintained by the WHO; and (iii) interviews with stakeholders and an extensive peer-review process (including calls for and review of public comments).

The qualitative evaluation followed a process that started with specification of elements for evaluation, determined the standard for each element, evaluated the standard versus achievement, assessed the implication of a "failing" standard, weighed the relevance for the planned bOPV cessation, drew lessons learned, and finally highlighted policy implications. To assist the evaluation team, a seven-member "sounding board" was established, which reviewed progress reports and helped to create standards for elements that were not specified in the 2013–2018 Strategic Plan (*4*) or recommendations of the Strategic Advisory Group of Experts on Immunization (SAGE) (*8*).

The quantitative evaluation focused on specific elements that were identified in the qualitative evaluation and conducting specific analyses to derive or underline the conclusions. A major focus was the in-depth review of outbreak control efforts, focusing on quality, scope, and timeliness (*7*). In addition, the 10 key factors that emerged during our review as contributing to or exacerbating the switch failure were assessed in detail (*7*). The final evaluation element was the extensive peer-review process, starting and ending with a public comment opportunity, using the "sounding board" to guide the evaluation and critically review it, and giving all stakeholders a chance to provide comments and suggestions.

---

[1] The Task Force for Global Health, Atlanta, GA, USA. [2] Tamayo Federal Solutions LLC, Virginia Beach, VA, USA. SESB members and their affiliations are listed at the end of this article. Email: rolandsutter@gmail.com; nmolodecky@gmail.com

Evolving epidemiology post switch

Global withdrawal of the type 2 component of oral poliovirus vaccine (OPV2) occurred in April 2016 (i.e., the switch). Both graphics show the change in circulating vaccine-derived poliovirus type 2 (cVDPV2) cases. The map reflects changes from pre-switch (1 January 2010 to 30 April 2016) to post-switch (1 May 2016 to 30 April 2024) time periods. Data are aggregated at the first subnational administrative division within the country (i.e., state or province, but which can also be called governorates or prefectures). The chart reflects the post-switch period. See (7) and supplementary materials for details on data and methods.

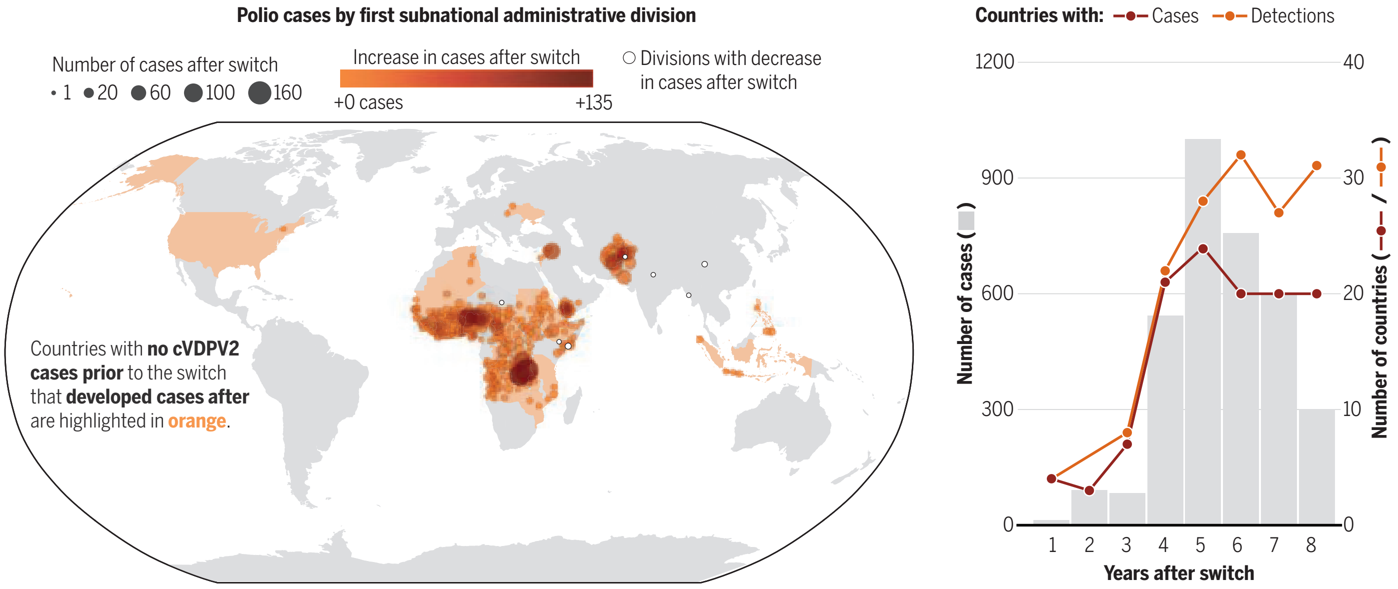

Countries with **no cVDPV2 cases prior** to the switch that **developed cases after** are highlighted in **orange**.

GRAPHIC: V. PENNEY/*SCIENCE*; DATA: WORLD HEALTH ORGANIZATION, POLIO INFORMATION SYSTEM ACCESSED 15 MAY 2024.

POST-SWITCH INCREASE

In the 8 years after the switch (from 1 May 2016 to 30 April 2024), a total of 53 countries were infected with cVDPV2, >3300 children were paralyzed by cVDPV2 (across 43 countries), and >$1.8 billion was spent on outbreak control. The scale of the withdrawal effort was staggering: stopping the use of tOPV in 155 countries; replacing it with bOPV, all in a narrow 2-week window in April 2016; and ensuring introduction of at least one dose of IPV into RI in advance of the switch. See (*7*) for the findings of the qualitative evaluation, including which prerequisites were achieved or not met.

The goal of the switch was to stop the use of Sabin poliovirus type 2 vaccine in order to prevent cVDPV2 (and VAPP). However, since the switch, there has been an approximate 10-fold increase in cVDPV2 case burden. As seen from the pre- and post-switch cVDPV2 cases (see the figure), in the approximately 6½ years pre-switch, 319 cVDPV2 cases were reported across 15 countries. By contrast, over a similar period of time post-switch (by end of 2022), 2967 cVDPV2 cases had already been reported across 38 countries, with widespread transmission continuing to result in high case burden. By 15 May 2024 (end of the evaluation period), a total of 3393 cases had been reported. Data prior to January 2010 are not available. As shown by the number of cVDPV2 cases by year since the switch (see the figure), the initial success was followed by rapid expansion of cVDPV2 outbreaks starting in year 3 (May 2018 to April 2019) after the switch. Figure S1 shows the number of new cVDPV2 emergences by year and demonstrates the continued seeding of cVDPV2 (moment of evolution from OPV2 to cVDPV2) since the switch, including from novel OPV2 (nOPV2) use (highlighting that despite best efforts to create a more genetically stable vaccine, strong preventive and outbreak control measures will still be required for any future OPV withdrawal efforts).

The overriding reason for this failure was the inability of GPEI to close out outbreaks shortly after the switch and in the ensuing 8 years. The contributing factors were suboptimal quality of the outbreak control efforts, inadequate geographic scope, and long delays in timing (*7*), resulting in massively expanding outbreaks in year 4 after the switch and slow progress toward control in subsequent years (see the figure). The failure was aggravated by the inability of GPEI leadership to recognize the seriousness of the evolving problem and take effective corrective action (*7*).

In addition, 10 factors that exacerbated the negative outcomes included (i) IPV supply constraints affecting introduction in RI and use in outbreak control, contributing to the high case burden; (ii) gaps in pre-switch poliovirus type 2 immunity in critical geographies (Nigeria, DRC, and Pakistan), resulting in early seeding events; (iii) continued and undetected cVDPV2 transmission at the time of the switch (Somalia, Syria, and the Philippines); (iv) limited progress in RI and lack of alternative strategies to increase coverage, leaving a weak foundation of type 2 immunity and contributing to the high case burden; (v) limited stockpile of monovalent type 2 OPV (mOPV2), resulting in highly focused and insufficient outbreak response scope; (vi) revisions of outbreak response Standard Operating Protocols (SOPs), reducing the number of rounds and target population, and eliminating IPV from outbreak response; (vii) delays in nOPV2 development and introduction and perceived and communicated risk of mOPV2, resulting in substantial delays in outbreak response; (viii) leftover tOPV vials in storage sites, likely seeding at least one cVDPV2 outbreak; (ix) inadequate or late detection of cVDPV2 (both new emergences and ongoing transmission) delaying implementation of outbreak control measures; and (x) delays in processing and notifying cVDPV2 acute flaccid paralysis cases and environmental surveillance samples, exacerbating delayed responses. Additional details are provided in (*7*).

LESSONS LEARNED

The 2016 Sabin poliovirus type 2 cessation (i.e., switch) was a failure, causing >3300 paralytic poliomyelitis cases, primarily on the African continent, the vast majority of which were entirely preventable. The switch also offers an opportunity to learn and prevent such a failure from ever happening again, especially with the anticipated bOPV withdrawal.

The GPEI was aware of the risks, starting with warnings in 1997 (*9*) and discussion of “a dangerous endgame” (*10*). The end game or exit strategy (*4*) required the removal of the vaccine—the OPV—that had allowed the program to get to the brink of eradication with the certification of eradication of two of the three wild poliovirus serotypes (type 2 and 3) (*11*).

The issue of “fighting fire with fire” (*12*), controlling cVDPV outbreaks with mOPV2 (the same virus that caused the outbreak in the first place), was discussed extensively in the lead-up to the OPV2 cessation in 2016. It was thought at that time that high vaccination coverage would negate this potential problem. However, the series of preventive supplementary immunization activities with tOPV did not achieve sufficiently high coverage to stop or prevent the emergence of cVDPV2 in selected critical geographies (Nigeria, DRC, Pakistan, Syria, Somalia, and the Philippines). Furthermore, high coverage was unlikely in many areas with suboptimal health systems in sub-Saharan Africa. It was essential to rapidly control and interrupt all cVDPV2 chains of transmission before population immunity had decreased sufficiently to allow widespread transmission by years 3 to 4 after the switch. This was further exacerbated by underestimating the reversion potential of OPV2 (emerging into cVDPV2) and the delays in waiting for a nOPV2 vaccine that was expected to be more genetically stable.

Polio eradication requires the removal of all polioviruses from populations (*13*). Without accomplishing this feat, eradication is not possible and only leads to a high level of control that is fragile at best. However, even if polio eradication is not achieved and the program discontinued, we must recognize that more than 20 million children can walk today because of the eradication efforts.

The lessons learned from this evaluation should be considered by policy-makers, program managers, and oversight committees to strengthen the planning and execution of the anticipated withdrawal of bOPV. They are contained in the complete switch evaluation report (*7*) and include proposed triggers and possible prerequisites (to initiate the process and lay the foundation) for a successful bOPV withdrawal.

While focusing on the failure, we must also acknowledge the many countries and WHO regions that successfully implemented the switch and have prevented a substantial number of Sabin type 2–related VAPP cases, the major adverse effect of OPV use. Many of these countries and WHO regions have a stronger health infrastructure and better immunization delivery systems. Eight years after the switch, the vast majority of cVDPV2 outbreaks are ongoing on the African continent and southwestern part of the Arabian Peninsula, and implementing the necessary control measures remains difficult, especially in areas of conflict.

However, given that bOPV vaccine will be used until its withdrawal, GPEI must assume and plan for undetected transmission of poliovirus types 1 and 3. GPEI must operate under the assumption that there will be cVDPV outbreaks in the immediate aftermath of the bOPV withdrawal. To eliminate the risk of continued emergence and transmission of cVDPVs, it is critical to take steps to prevent such emergences, and terminate chains of transmission, if any arise, and avoid the problems that occurred with the tOPV-to-bOPV switch. However, the requirements this time around for bOPV cessation must be more stringent than in 2016. See (*7*) for our suggestions, both in terms of triggers and prerequisites.

Therefore, whether the anticipated bOPV withdrawal, even under greatly enhanced and more stringent requirements, is feasible remains uncertain. A newly developed OPV (i.e., nOPV2), was designed to be genetically more stable and decrease the emergence of cVDPV2. However, since its introduction in March 2021, a total of 18 cVDPV2 outbreaks can be attributable to nOPV2 (an incidence that appears to be lower than one observed after mOPV2 use yet continues to pose a substantial risk) (*14*).

The only poliovirus vaccine that does not seed new emergences of cVDPV is IPV. Expanded use of this vaccine in new strategies (such as fractional IPV using house-to-house modality), especially associated with greatly increased RI coverage, and the introduction of the combination hexavalent vaccine (that includes IPV) could be game changers for RI and polio eradication. But as with every vaccine, to harvest the full potential of hexavalent vaccine, high vaccination coverage will be critical, including in the most difficult parts of the world.

Moreover, the evaluation of the switch has stimulated discussions on current GPEI strategy, including action for strengthening outbreak response [e.g., improving the flow of technical and financial resources to outbreak countries, broadening scope of outbreak responses, and enhancing support to countries for planning and implementing campaigns (*15*)] and work to improve IPV coverage in RI through closer coordination between RI and polio programs.

Polio eradication is a very difficult ambition to achieve, even with the >99.9% decrease in poliomyelitis cases. The next decade will seal the fate of polio eradication—either succeed or fail. Failure will lead to a massive resurgence and will paralyze tens of thousands of children, mostly residing in the poorest countries of the world. ■

REFERENCES AND NOTES

1. World Health Assembly, *Global eradication of poliomyelitis by the year 2000: Resolution 41.28* (World Health Organization, 1988).
2. K. Geiger *et al.*, *MMWR Morb. Mortal. Wkly. Rep.* **73**, 441 (2024).
3. L. R. Platt, C. F. Estívariz, R. W. Sutter, *J. Infect. Dis.* **210** (suppl. 1), S380 (2014).
4. Global Polio Eradication Initiative, Polio Eradication & Endgame Strategic Plan 2013-2018 World Health Organization (2013).
5. M. Patel, S. Cochi, *J. Infect. Dis.* **216** (suppl. 1), S1 (2017).
6. J. P. Bigouette *et al.*, *MMWR Morb. Mortal. Wkly. Rep.* **72**, 366 (2023).
7. N. Molodecky, R. Sutter, “Evaluation of Switch from tOPV to bOPV. Lessons learned and implications for an anticipated bOPV cessation” (2024); https://polioeradication.org/wp-content/uploads/2024/11/Switch-Report-20240930.pdf.
8. World Health Organization, Meeting of the Strategic Advisory Group of Experts on Immunization, October 2014 – conclusions and recommendations [*Wkly. Epidemiol. Rec.* **89**, 561–576 (2014)].
9. A. W. Dove, V. R. Racaniello, *Science* **277**, 779 (1997).
10. N. Nathanson, P. Fine, *Science* **296**, 269 (2002).
11. R. W. Sutter, O. M. Kew, S. L. Cochi, R. B. Aylward, “Poliovirus Vaccine-Live” in *Plotkin’s Vaccines*, S. A. Plotkin *et al.*, Eds. (Elsevier, 2018), chap. 49, pp. 866–917.
12. P. E. Fine, R. W. Sutter, W. A. Orenstein, *Dev. Biol.* **105**, 129, discussion 149-50 (2001).
13. W. R. Dowdle, S. L. Cochi, *Vaccine* **29** (suppl. 4), D70 (2011).
14. C. M. Peak *et al.*, *Vaccines* **12**, 1308 (2024).
15. GPEI Statement on Independent Switch Evaluation Report, https://polioeradication.org/polio-today/preparing-for-a-polio-free-world/opv-cessation/.

ACKNOWLEDGMENTS

The authors acknowledge the contributions of many interested parties that freely answered questions and helped to focus this report, and appreciate suggestions of the public in responding to calls for comments. The authors thank S. Wassilak, Centers for Disease Control and Prevention (CDC), for helping to focus and to guide along the evaluation path. The Switch review (*7*) was promoted and funded by the CDC, Atlanta, GA, USA. The Switch Evaluation Sounding Board was composed of senior polio eradication experts covering epidemiology, virology, clinical medicine, policy, and program implementation: Walter Orenstein[3], Rana Muhammad Safdar[4], Hiroyuki Shimizu[5], J Peter Figueroa[6], Rose Gana Fomban Leke[7], and Sunil Kumar Bahl[8]. John Sever, formerly of Children’s National Medical Center, Washington, DC, USA, was also a member of the SESB but sadly passed away in March 2024 before the Switch Report was finalized. W.O. is a consultant for Sanofi Vaccines and for the Bill & Melinda Gates Foundation. [3]Emory Vaccine Center, Emory University, Atlanta, GA USA. [4]Ministry of National Health Services, Regulation and Coordination, Islamabad, Pakistan. [5]Department of Virology II, National Institute of Infectious Diseases, Tokyo, Japan. [6]Department of Community Health and Psychiatry, University of the West Indies, Kingston, Jamaica. [7]Department of Microbiology, Hematology and Immunology, University of Yaounde I, Yaounde, Cameroon. [8]WHO South-East Asia Regional Office, New Delhi, India.

SUPPLEMENTARY MATERIALS

science.org/doi/10.1126/science.adu6580

10.1126/science.adu6580

An artist's rendering evokes the rich plant life that populated a Permian temperate forest.

IMAGE: RICHARD JONES/SCIENCE SOURCE

PALEOECOLOGY

Plants from the planetary past

Earth's ancient flora comes to life in a vivid romp through 15 fossil sites

By **Ellen D. Currano**

In *When the Earth Was Green*, Riley Black masterfully transforms 15 fossil sites into vibrant, living landscapes that span the history of plants and demonstrate their profound influence on Earth. Some sites are chosen to illustrate key innovations or transitions, such as the colonization of land by liverworts or the appearance of the giant Carboniferous club mosses that, like trees, transformed Earth's surface and climate. Others capture mundane, everyday moments in ancient ecosystems: an apatosaurus grazing Utah's Jurassic salad bar, a Cretaceous mosquito navigating high winds in Myanmar, an autumn day in a 3-million-year-old German forest, or a pair of giant sabercats frolicking in a field of catnip. [The fossil record cannot tell us whether this last event actually occurred, but molecular clocks estimate that catnip originated >10 million years ago (*1*), temporally overlapping with sabercats.]

Black readily admits to making assumptions and embellishments to help the reader "envision what all these long-lost friends of ours were like in life." That this vignette brought joy to a dog person and new knowledge to a professional paleontologist provides justification for her decision. Although the relevant science is, at times, oversimplified to present critical concepts to a nonspecialist audience, the appendices ground the narrative in evidence and lay out where speculation begins.

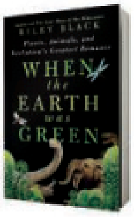

When the Earth Was Green: Plants, Animals, and Evolution's Greatest Romance
Riley Black
St. Martin's Press, 2025.
304 pp.

Important themes and lessons recur throughout the book's chapters. First, Black explicitly addresses common misconceptions about evolution. Evolution, she reminds readers, is inherently nondirectional—species do not "choose" to evolve features, and random chance has played a substantial role in the trajectory of life through time. Today's organisms are not more advanced than those that existed millions of years ago, and a trait that is advantageous at one time may become detrimental when the environment changes.

Black also emphasizes that many complex feedback systems exist between plants and Earth's atmosphere, climate, and sediments and that plants—whose ubiquity often renders them the backdrop for animal lives and experiences—are extraordinary beings in their own right. She chooses to portray plant-animal interactions as a partnership and, at times, even a romance, rather than the more traditional framing as organisms in competition or engaged in an arms race.

Black invites readers not just to see and hear the ancient landscapes she highlights, as one would in a film, but to engage with all their senses. In chapter 14, for example, she writes, a mastodon "squishes and sometimes squelches along a multicolored carpet of wet leaves as she moves, a vast area rug laid down in sodden earth tones. It's getting cold enough at night now that some of the leaves are given a glittering edge of frost as the sun rises, and as the held-over moisture melts, it slips between the millions of discarded botanical sheafs…It's a miniature world that only exists for a few months out of the year, when leaves that sprouted to catch summer breezes come back to the soil and invertebrates huddle beneath their accumulated shelter." I reveled in the sights, sounds, smells, tastes, and touch of these weird and wonderful ecosystems, many of which are so different from anything present on Earth today.

While reading *When the Earth Was Green*, I thought quite a lot about another book I read recently, digital media scholar Maryanne Wolf's *Reader, Come Home: The Reading Brain in a Digital World*. Wolf's thesis in that book is that reading is essential to the development of critical thinking, empathy, and reflection. In my opinion, the real magic that sets Black's book apart from similar works is that the reader is encouraged to engage deeply with the ancient ecosystems in question, to imagine what it would be like to be a mosquito flying through a Cretaceous forest in search of food, or a tiny primate on a raft of uprooted trees bobbing across the Atlantic ~40 million years ago, or a hackberry being eaten by a rhino-like brontothere in the latest Eocene.

In the book's final chapter, Black describes a pilgrimage she made to Utah to sit with Pando, a giant ~14,000-year-old aspen clone. Here, she reflects on how this remarkable being has persisted through millennia of uncertainties and "expand[s] our understanding of what a life can look like, the connections both hidden and obvious where distinct entities create community." *When the Earth Was Green* is an exercise in empathy that left me hopeful about humanity's ability to consider other perspectives, whether those of ancient, exotic organisms or members of our own species. ■

REFERENCES AND NOTES

1. B. T. Drew, K. J. Sytsma, *Am. J. Bot.* **99**, 933 (2012).

10.1126/science.adu5512

The reviewer is at the Department of Botany and the Department of Geology and Geophysics, University of Wyoming, Laramie, WY, USA. Email: ecurrano@uwyo.edu

SCIENCE AND SOCIETY

Artificial intelligence speaks up

An AI safety specialist confronts fears about the future of large language models

These Strange New Minds: How AI Learned to Talk and What It Means
Christopher Summerfield
Viking, 2025. 384 pp.

By **Michael Spezio**

In *These Strange New Minds*, cognitive neuroscientist and artificial intelligence (AI) safety specialist Christopher Summerfield presents a wide-ranging overview of AI for nonspecialists, focusing on what the technology really is, what it might do, and whether it should be feared. We no longer live in "a world where *humans alone generate knowledge*," writes Summerfield. Machines possessing this potential will soon occupy custodial positions in society, he maintains (*1*). His book takes on six broad questions: How did we get here? What is a language model? Do language models think? What should a language model say? What could a language model do? And, are we all doomed?

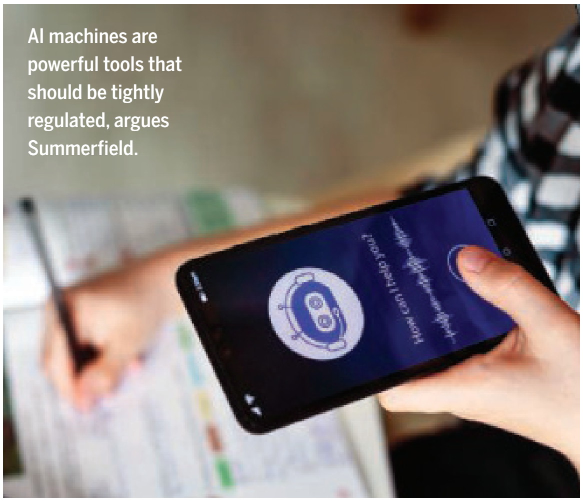

AI machines are powerful tools that should be tightly regulated, argues Summerfield.

Summerfield is a philosophical empiricist who argues that "the meaning of language depends on its evidentiary basis." He is also a functionalist who believes that "it is perfectly possible for the same computational principle to be implemented in radically different physical substrates" and a materialist who sees the mind's activity as identical to "neural computation." But does he believe that AI machines think like humans do, or just that they appear to?

Current AI machines "definitely do not think like people" and "probably never will," Summerfield writes. Yet he dismisses "public intellectuals who have turbocharged their careers by voicing tireless scepticism about AI," who deny that AI machines think at all. To those who say that AI makes too many strange mistakes, he references the work of Noam Chomsky (*2*), writing that AI machine "performance often falls short of its competence."

To those who fear that AI makes human beings no better than "mere automata," Summerfield advises leaving aside dubious moral arguments. To those who view AI machines as simple "stochastic parrots" (*3*), he invokes the "Duck Test": "If something swims like a duck and quacks like a duck, then we should assume that it probably is a duck, rather than inventing abstruse arguments to otherwise explain its behaviour." He does not directly address objections that characterize human thinking in terms of self-conscious, emotionally grounded reasoning (*4*).

Summerfield is more tentative when comparing AI's predictive training to human learning. But AI machines "have learned how to learn, just like a human can," he concedes. He hypothesizes that AI shares metalearning processes with humans, seemingly affirming OpenAI cofounder Sam Altman's 2022 tweet "I am a stochastic parrot and so r u."

To those claiming proof that current AI machines cannot access meaning in language (*5*), Summerfield writes that "words do not become meaningful exclusively because they refer to things that can be seen, heard, touched, tasted or smelled." Meaning for AI machines, he maintains, comes via "the high road of linguistic data," whereas humans usually require "the low road of perceptual data."

Parts 4 and 5 of *These Strange New Minds* briefly engage with some problems and possible scenarios in AI ethics and AI futures, including how personalized AI could lead to even more effective filter bubbles (*6*), further shifting access and power "away from those currently more marginalized in society and towards companies and governments who build the technology and trade in the data that it inevitably yields." While many of the problems in this section seem unsolvable, Summerfield discusses a number of strategies for AI safety engineering. These include an ethical training framework known as "Constitutional AI" and rule-based reward modeling. He acknowledges, however, that fine-tuning AI machines "just lightly grooms the model's replies" and "does not penetrate into the heart of the model and expunge its obnoxious attitudes or abhorrent beliefs."

In the book's final section, Summerfield turns to whether the technology will doom or deliver humankind. Here, he begins by discussing computer scientist Rich Sutton's assertion that humankind should already be planning for the inevitable and great "succession" as AI machines "take over." Neither AI successionists nor its antagonists have much to offer compared with those "whose core members are rooted in the AI safety community, [who] believe that there is an urgent need for AI to be tightly regulated precisely *because* it is so potent a tool," argues Summerfield.

Existential risk groups have alternatively called for AI to be widely and publicly paused or for large government and private investments to design AI monitoring and countermeasures. So far, little headway has been made in either direction, but Summerfield's book offers nonspecialists a good introduction to the issues and some hope that sound efforts in AI safety may see the light of day. ■

The reviewer is at the Psychology, Neuroscience, and Data Science programs at Scripps College, Claremont, CA, USA. Email: mspezio@scrippscollege.edu

REFERENCES AND NOTES

1. See also A. Narayanan, S. Kapoor, *AI Snake Oil: What Artificial Intelligence Can Do, What It Can't, and How to Tell the Difference* (Princeton Univ. Press, 2024).
2. N. Chomsky, *Syntactic Structures* (Mouton, 1957).
3. E. Bender *et al.*, in *Proceedings of the 2021 ACM Conference on Fairness, Accountability, and Transparency*, pp. 610–623.
4. For example, G. Jefferson, *Br. Med. J.* **1**, 1105 (1949); U. Neisser, *Science* **139**, 193 (1963); and U. Neisser *et al.*, *Am. Psychol.* **51**, 77 (1996).
5. Summerfield cites E. M. Bender and A. Koller's influential paper "Climbing towards NLU: On Meaning, Form, and Understanding in the Age of Data" in *Proceedings of the 58th Annual Meeting of the Association for Computational Linguistics*, pp. 5185–5198 (2020). See also recent work on this problem, for example, X. Ohmer *et al.*, *Comput. Linguist.* **50**, 1507 (2024); and N. Asher *et al.*, arXiv:2306.12213 [cs.CL] (2023).
6. See also E. Pariser, *The Filter Bubble: What the Internet Is Hiding from You* (Penguin Press, 2011); and F. Pasquale, *The Black Box Society: The Secret Algorithms That Control Money and Information* (Harvard Univ. Press, 2015).

10.1126/science.adu1567

PHOTO: PORTISHEAD1/ISTOCK PHOTO

LETTERS

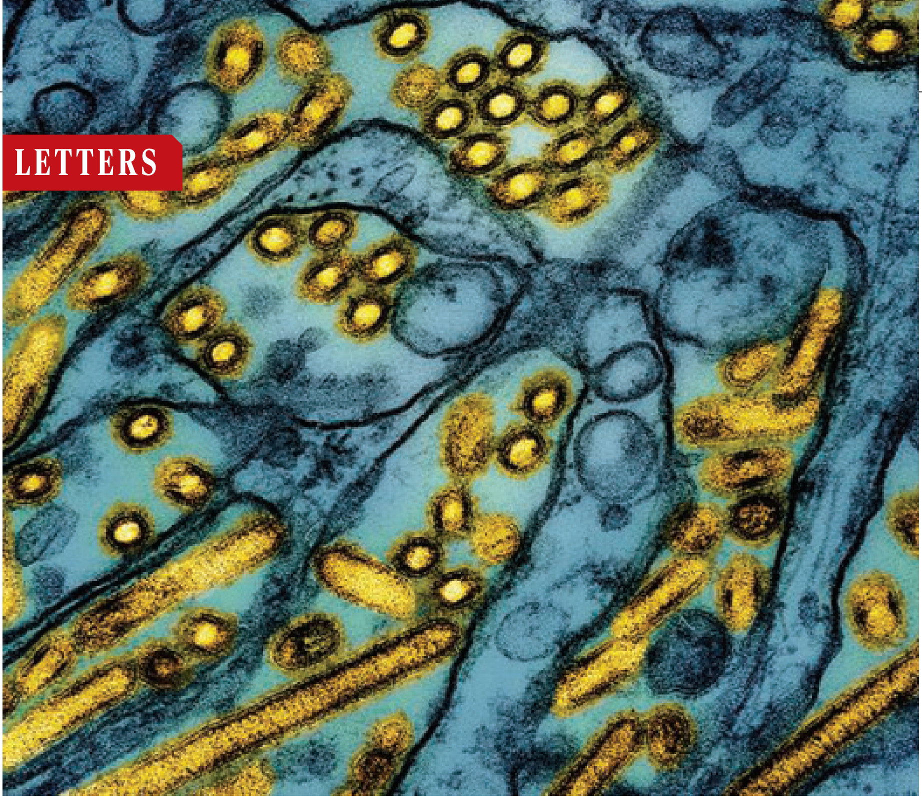

An electron microscope image shows avian influenza A H5N1 virus particles (yellow) in epithelial cells (blue).

PHOTO: CDC/NIAID VIA AP

Edited by **Jennifer Sills**

Prepare now for a potential H5N1 pandemic

The H5N1 virus has crossed species and adapted to mammalian hosts, including dairy cattle, causing widespread exposure and sporadic human illness (*1*). Although most cases have been mild, H5N1 can cause severe disease (*2*). Given H5N1's potential to spread, urgent action is needed to address pandemic preparedness gaps.

Rapid influenza vaccine availability is highly constrained by currently approved technologies, such as protein-based vaccines (*3*, *4*). Vaccine availability is also slowed by the time required to conduct immunogenicity and efficacy assessments and lot release and potency assays (*5*). Furthermore, many regulatory agencies lack the resources and capacity needed to quickly but robustly evaluate pandemic vaccines (*5*). To streamline vaccine development, assessment, production, and access, industry, governments, and regulators should enhance collaboration on new technologies, such as mRNA-based vaccines and vaccines using novel antigens; align regulatory pathways and requirements; and modernize immunogenicity assessment and lot release tools. To ensure equitable access, a global access framework should be established, including an entity that can provide financing and advanced vaccine purchases for low- and middle-income countries.

Immunization programs are complex and demand advance planning. Success requires defined roles, responsibilities, and financing as well as effective information and supply chain management. Strategies should build on experiences from seasonal influenza, COVID-19, and other outbreaks; use existing infrastructure; and engage those who will implement the programs. Immunization and communications planning must be integrated and engage affected communities, and planning must transcend political divisions. Global, federal, state, and local authorities need to clearly understand their responsibilities and the circumstances under which plans activate. Consideration of societal and economic risks from both a pandemic and potential mitigations should be integrated into decision-making. Proactive analysis is also required to prepare for impacts on supply chains for vaccines and source materials as well as effects on health care and other sectors.

To effectively address these gaps, pandemic preparedness initiatives should be urgently resourced and implemented (*6*). First, an effort to develop rapidly scalable pandemic influenza vaccines [building on models such as Operation Warp Speed (*7*)] should engage industry, governments, regulators, and the scientific community, with equitable access supported by a funded global framework. Such an initiative would, ideally, also include development of and access to improved therapeutics, diagnostics, personal protective equipment, and other needed medical countermeasures. Second, a comprehensive outreach and communications program, supported by behavioral science, should work to better understand and respond to concerns about vaccines and rebuild trust in public health. Finally, pandemic response plans should undergo transparent in-depth testing, during which countries should share plans and playbooks and form global collaborations that incorporate different disease scenarios and immunization strategies. Similar initiatives should address ongoing agricultural outbreaks (*8*). Enhancing readiness now can save lives and reduce societal and economic disruption if H5N1 or another outbreak becomes a pandemic.

Jesse L. Goodman[1]*, Norman W. Baylor[2], Rebecca Katz[3], Lawrence O. Gostin[4], Rick A. Bright[5], Nicole Lurie[6], Bruce G. Gellin[7]

[1]Center on Medical Product Access, Safety and Stewardship, Georgetown University Medical Center, Washington, DC, USA. [2]Biologics Consulting Group, Alexandria, VA, USA. [3]Center for Global Health Science and Security, Georgetown University Medical Center, Washington, DC, USA. [4]O'Neill Institute for National and Global Health Law, Georgetown University Law Center, Washington, DC, USA. [5]Bright Global Health, Washington, DC, USA. [6]Coalition for Epidemic Preparedness Innovations, Oslo, Norway. [7]Global Health Institute, Georgetown University, Washington, DC, USA.
*Corresponding author.
Email: jesse.goodman@georgetown.edu

Opinions are the authors' and do not necessarily reflect the views of their institutions.

REFERENCES AND NOTES

1. "H5 bird flu: Current situation" (Centers for Disease Control and Prevention, 2025); https://www.cdc.gov/bird-flu/situation-summary/index.html.
2. "LDH reports first U.S. H5N1-related human death" (Louisiana Department of Health, 2025); https://ldh.la.gov/news/H5N1-death.
3. Center for Infectious Disease Research and Policy, "Influenza vaccines R&D roadmap" (Regents of the University of Minnesota, 2023); https://ivr.cidrap.umn.edu/sites/default/files/IVR_Feb_2023.pdf.
4. "CEPI 2.0 and the 100 days mission" (Coalition for Epidemic Preparedness Innovations, 2024); https://cepi.net/cepi-20-and-100-days-mission.
5. N. W. Baylor, J. L. Goodman, *Vaccines* **10**, 2136 (2022).
6. "H5N1 influenza vaccines and the current outbreak" (Georgetown University Global Health Institute, 2025); https://globalhealth.georgetown.edu/publications/h5n1-influenza-vaccines-and-the-current-outbreak.
7. M. Slaoui, M. Hepburn, *N. Engl. J. Med.* **383**, 1701 (2020).
8. National Academies of Sciences, Engineering, and Medicine, *Potential Research Priorities to Inform U.S. Readiness and Response to Avian Influenza A (H5N1): Proceedings of a Workshop—In Brief*, E. P. Carlin, S. Singaravelu, L. Brown, Eds. (National Academies Press, 2024).

COMPETING INTERESTS

J.L.G. serves on the Board and Science Committee of GSK and as a volunteer member of the board of the nonprofit United States Pharmacopeia. R.A.B. receives nonfinancial support from the Coalition for Epidemic Preparedness Innovations (CEPI) for serving on its scientific advisory committee, receives fees from CEPI and Cidara, and has patents for virus-like particle vaccine design issued to Novavax with no financial gain.

10.1126/science.adw3278

Evolving H5N1 receptor specificity

In their Research Article "A single mutation in bovine influenza H5N1 hemagglutinin switches specificity to human receptors" (6 December 2024, p. 1128), T.-H. Lin *et al.* find that a mutation from glutamine to leucine at the 226 residue in the hemagglutinin protein of the H5N1 influenza virus leads to human receptor specificity, consistent with other work showing that the new H5N1 avian and bovine influenza virus variants exhibit altered receptor binding preferences (*1*, *2*). Traditionally associated with avian-specific α-2,3–linked sialic acid receptors, emerging H5N1 strains display a growing ability to bind humanlike α-2,6–linked sialic acid receptors (*3*, *4*), increasing the risk of human infection.

Recent H5N1 viruses isolated from dairy cows have exhibited an expanded binding breadth to α-2,3–linked sialic acid glycans, a feature mediated by the $\text{Thr}^{199}\rightarrow\text{Ile}$ mutation located outside the receptor binding site (*4*). This shift suggests a mechanism of adaptation in which altered loop structures surrounding the receptor binding site may create a more permissive binding pocket capable of interacting with diverse host receptors, raising substantial concern about the virus's potential for increased zoonotic transmission and the emergence of new pandemic strains.

Analyses of circulating H5N1 isolates in live poultry markets and wild birds reveal continued accumulation of mutations (such as $\text{Asn}^{193}\rightarrow\text{Lys}$ and $\text{Asn}^{193}\rightarrow\text{Asp}$) in the hemagglutinin gene that could further increase the binding affinity of α-2,6–linked sialic acid receptors (*3*, *5*). Continued surveillance and molecular characterization of these viruses, particularly in high-risk interface environments, is critical.

A broader investigation of the molecular mechanisms that underlie H5N1 receptor binding evolution is urgently needed to understand the drivers of this adaptation and to develop targeted interventions. Enhanced global surveillance, cross-species monitoring, and development of broadly neutralizing therapeutics are essential to mitigate the risk of future pandemics. The evolving receptor binding specificity of H5N1 viruses constitutes an imminent public health risk that demands immediate international attention and collaborative research.

Feng Wen[1]*, Jinyue Guo[1], Yong Li[2], Hai Yu[3], Keshan Zhang[1], Tao Ren[4], Shujian Huang[1]

[1]College of Animal Science and Technology, Foshan University, Foshan, Guangdong, China. [2]College of Animal Science and Technology, Jiangxi Agricultural University, Nanchang, China. [3]Shanghai Veterinary Research Institute, Chinese Academy of Agricultural Sciences, Shanghai, China. [4]College of Veterinary Medicine, South China Agricultural University, Guangzhou, Guangdong, China.
*Corresponding author. Email: wenf@fosu.edu.cn

REFERENCES AND NOTES

1. S. Garg *et al.*, *N. Engl. J. Med.* 10.1056/NEJMoa2414610 (2024).
2. C. Gu *et al.*, *Nature* **636**, 711 (2024).
3. F. Wen *et al.*, *Lancet Microbe* 10.1016/j.lanmic.2024.101049 (2024).
4. M. R. Good *et al.*, *Nat. Commun.* **15**, 10768 (2024).
5. S.-G. Jang *et al.*, *Emerg. Microbes Infect.* **13**, 2302854 (2024).

10.1126/science.adw1877

Time to count plastics in climate action

In November, representatives of Paris Agreement signatory countries will meet at the Conference of the Parties (COP30) in Brazil. Before the meeting, each country should strengthen its nationally determined contributions (NDCs) to reducing greenhouse gases by incorporating plastic emissions into its plans. Plastic production and waste contribute substantially to greenhouse gas emissions, yet 94% of Paris Agreement signatory countries (183 countries of 194 total) ignore plastics within their NDC plans, creating a major gap in climate mitigation efforts (*1*). Countries should compile their plastic-related emissions data (*2*) and use the information to amend NDC plans.

About 99% of plastics are derived from fossil fuels, and each stage of the plastic life cycle releases greenhouse gases (*3*). The estimated 450 million tonnes of plastic produced per year account for about 12% of global oil extraction and 8.5% of gas extraction (*4*). Under a business-as-usual trajectory, plastic production will likely triple by 2050 (*5*), with each additional tonne produced from fossil fuels generating 1.89 to 2.3 tonnes of carbon dioxide (CO_2) emissions (*3*). The plastic life cycle contributes roughly 3 to 8% of total global greenhouse gas emissions currently (*6*) and will likely consume 15% of the global carbon budget by 2050 (*7*).

Postconsumption emissions from plastics have been largely overlooked in NDC emission reduction strategies. Only 11 countries out of 194 have included measures to address plastic waste (*1*), despite large plastics making up about 21% of global municipal waste (*8*). About 40 NDCs mention landfill and incineration as waste management methods (*1*), which will undermine mitigation efforts because each kilogram of plastic incineration emits 2.3 kg of CO_2 emissions (*6*). About 80 countries have committed to adopting a circular economy through their NDCs (*9*), but such plans are insufficient without specific goals and actionable strategies focused on plastic waste management.

To keep global warming below 1.5°C, countries should redefine their plastic-related emission reduction targets with interim goals and accountability measures. Goals should include cutting plastic production, redesigning product manufacturing to decouple plastic from fossil fuels, decarbonizing petrochemicals, and incentivizing sustainable manufacturing. Given the failure of negotiations to produce an international legally binding agreement on plastic pollution in 2024 (*10*), the Paris Agreement is even more essential to address the complex challenges of plastics and climate change.

Md Abu Noman[1], Lingzhan Miao[2], Peter I. Macreadie[1], Tanveer M. Adyel[1]*

[1]Centre for Nature Positive Solutions, School of Science, RMIT University, Melbourne, VIC, Australia. [2]Key Laboratory of Integrated Regulation and Resources Development on Shallow Lakes, Ministry of Education, College of Environment, Hohai University, Nanjing, China.
*Corresponding author. Email: tanveer.adyel@rmit.edu.au

REFERENCES AND NOTES

1. "Wasted opportunities: A review of international commitments for reducing plastic- and waste-sector GHG emissions" (GAIA, 2021); https://www.no-burn.org/cop26-ndcs/.
2. X. Zhu, C. Rochman, *Environ. Sci. Tech.* **56**, 3309 (2022).
3. "Reducing plastic production to achieve climate goals: Key considerations for the plastics treaty negotiations" (Center for International Environmental Law, 2023); https://www.ciel.org/reports/reducing-plastic-production-to-achieve-climate-goals-key-considerations-for-the-plastics-treaty-negotiations/.
4. N. Karali, N. Khanna, N. Shah, "Climate impact of primary plastic production" (Berkeley Lab, 2024); https://energyanalysis.lbl.gov/publications/climate-impact-primary-plastic.
5. R. Geyer, J. R. Jambeck, K. L. Law, *Sci. Adv.* **3**, e1700782 (2017).
6. J. Zheng, S. Suh, *Nat. Clim. Change* **9**, 374 (2019).
7. L. A. Hamilton, S. Feit, "Plastic & climate: The hidden costs of a plastic planet" (Center for International Environmental Law, 2019); https://www.ciel.org/wp-content/uploads/2019/05/Plastic-and-Climate-FINAL-2019.pdf.
8. J. W. Cottom, E. Cook, C. A. Velis, *Nature* **633**, 101 (2024).
9. "Lack of consistency in circular economy pledges made in NDCs could hugely undermine climate action efforts" (Waste and Resources Action Programme, 2022); https://www.wrap.ngo/media-centre/press-releases/lack-consistency-circular-economy-pledges-made-ndcs-could-hugely.
10. "Fifth session (INC-5): In-session documents" (United Nations Environment Programme, 2024); https://www.unep.org/inc-plastic-pollution/session-5/documents/in-session.

10.1126/science.adu2738

RESEARCH

IN *SCIENCE* JOURNALS

Edited by **Michael Funk**

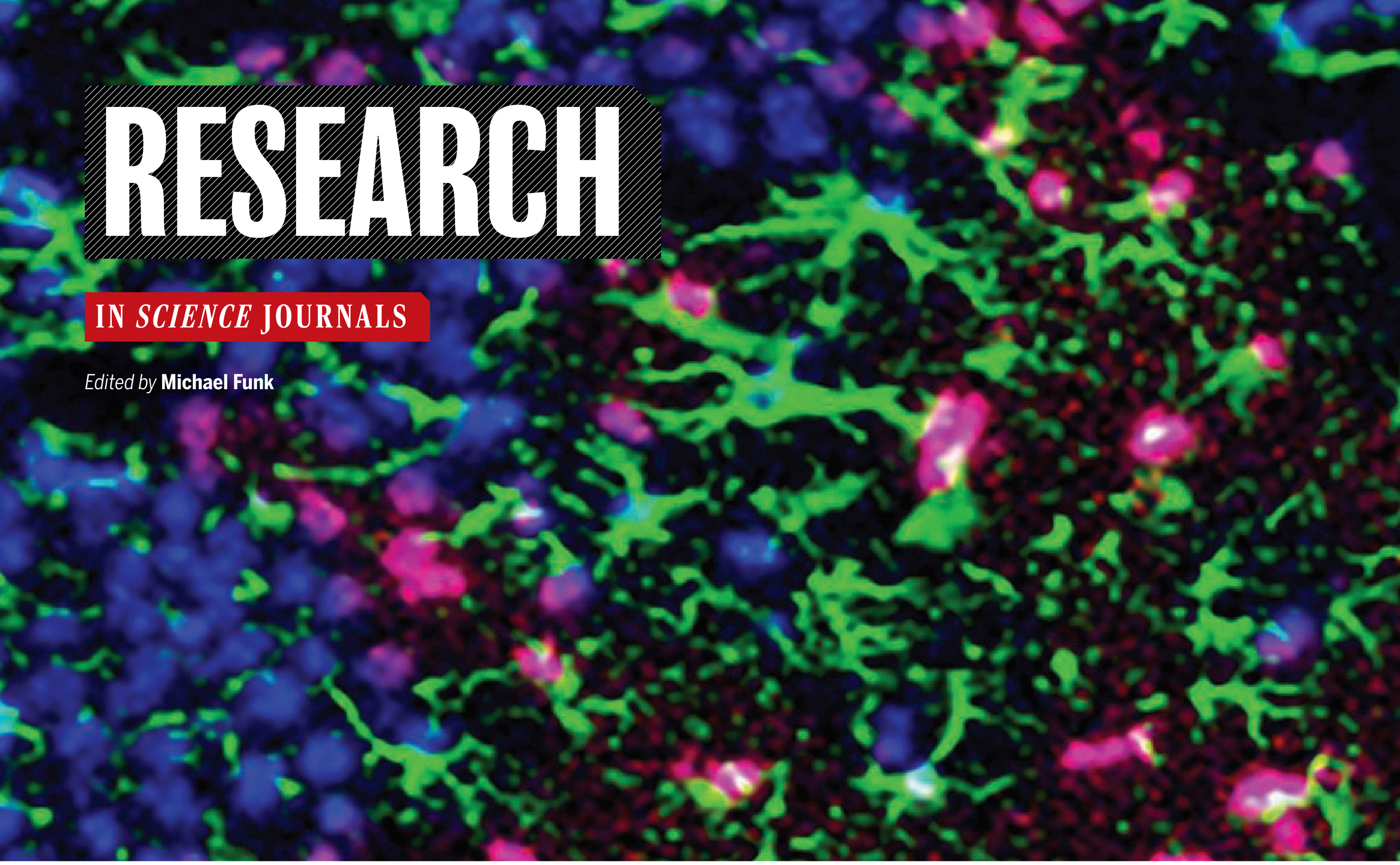

NEUROINFLAMMATION

Acetylation to fuel neuroinflammation

The acetyltransferase GCN5 promotes inflammation in peripheral tissues. Cho *et al*. found that GCN5 mediates inflammation in the brain as well, suggesting that it may be a target for treating neuroinflammatory diseases. In mice, inducing an innate immune response in the periphery that mimics an infection increased the abundance of GCN5 in microglia in the brain. GCN5 acetylated a subunit of the transcription factor NF-κB, thus enabling its activity and the production of inflammatory cytokines and associated proteins. Treating mice with GCN5 inhibitors prevented this response, suggesting that this approach may be used to treat neuroinflammation. —Leslie K. Ferrarelli *Sci. Signal.* (2025) 10.1126/scisignal.adp8973

Fluorescence microscopy image of mouse hippocampus area CA3 reveals localization of GCN5 (red) in microglia, but not astrocytes (green).

ORGANIC CHEMISTRY

Carbon-carbon to carbon-nitrogen

Carbon-nitrogen bonds are cornerstones of modern pharmaceuticals, and chemists continually strive to find more efficient ways to make them. Two studies now report distinct methods of cleaving carbon-carbon double bonds and forming carbon-nitrogen triple bonds in their place. Brägger *et al*. used a hypervalent iodine reagent to produce the nitrile products, whereas Cheng *et al*. used a heterogeneous copper catalyst in conjunction with oxygen. In both cases, the carbon-carbon double bonds served as convenient handles for the transformation of a wide variety of complex molecules. —Jake S. Yeston

Science p. 1083, 10.1126/science.adq8918; p. 1108, 10.1126/science.adq4980

BIODIVERSITY

Butterfly decline

Reports of declining insect populations have received widespread media attention, but evidence for declines has been variable across regions and taxonomic groups. Edwards *et al*. examined trends in the most surveyed taxon: butterflies (see the Perspective by Inouye). Combining data from 35 citizen science programs across the continental US, the authors found declines in overall butterfly abundance over the past 20 years across almost all major regions. Two-thirds of studied species showed declines of more than 10%. Many insects have the potential for rapid population growth and recovery, but habitat restoration, species-specific interventions, and reducing pesticide use are all likely needed to curb population declines. —Bianca Lopez

Science p. 1090, 10.1126/science.adp4671
see also p. 1037, 10.1126/science.adw1633

SPECTROSCOPY

Creating an exciton in a single molecule

Terahertz (THz) scanning tunneling microscopy (STM) is a cutting-edge technique that can manipulate tunneling electrons on subpicosecond timescales using an electric field generated by a THz pulse. THz-STM has been used in recent years to study ultrafast nanometer-scale dynamics induced by charge transfer on solid surfaces. However, there are still many challenges in improving spatiotemporal resolution. Kimura *et al*. successfully demonstrated ultrafast manipulation of exciton formation in a single phthalocyanine molecule on a metal-supported ultrathin insulating film by tailoring the waveform of THz pulses. The presented experimental platform is a

PHOTO: CHO DY, 2024

promising step in studying exciton dynamics with single-molecule precision. —Yury Suleymanov

Science p. 1077, 10.1126/science.ads2776

RANGE SHIFTS

Slow shifts in tropical forests

Species are expected to shift their ranges as the climate changes, but shifts may not occur fast enough, especially for immobile species such as plants. Two papers in this issue assess the degree to which plant species are tracking climate change in the American tropics, where data availability has constrained inference. Ramírez-Barahona *et al*. show that in Mesoamerican cloud forests, climate change and deforestation together have led to a mean upward shift in species ranges since 1979, mainly due to contracting lower range edges. In tropical forests across the Americas, Aguirre-Gutiérrez *et al*. found that tree traits are not shifting fast enough to track climate change based on trait-climate relationships, with smaller shifts in montane forests. —Bianca Lopez

Science p. 1057, 10.1126/science.adl5414, p. 1058, 10.1126/science.adn2559

CELL BIOLOGY

A GPS for protein compartmentalization

Cells contain billions of protein molecules, the amino acid sequences of which encode their functional structures. Deep learning models can now accurately predict such structures from amino acid sequence information. Proteins with shared functions assemble into subcellular compartments to carry out their functions. Kilgore *et al*. have developed a deep learning model called ProtGPS that can predict the compartment localization of proteins based on their sequence. ProtGPS identified disease-associated mutations that change this code and lead to altered subcellular localization of proteins. These results indicate that protein sequences contain both a folding code and a code governing their distribution to subcellular compartments. —Di Jiang

Science p. 1095, 10.1126/science.adq2634

COEVOLUTION

Who's driving evolution?

Proteins are translated from messenger RNA (mRNA), and the levels of these biomolecules are often correlated for a given gene. However, this observation is at odds with the fact that many variants that alter gene expression do not alter protein levels. Cope *et al*. tested several phylogenetic models relating mRNA and protein levels in coupled transcriptomic and proteomic data from skin samples across 10 mammals. They found that evolution primarily acting on protein levels best fit the data, with gene expression driven to accommodate those optimal levels. These mRNA values did not match perfectly and are likely amplified due to post-transcriptional mechanisms such as translational efficiency or protein degradation. —Corinne Simonti

Science p. 1063, 10.1126/science.ads2658

INFECTIOUS DISEASES

A vaccine for norovirus

Although most humans infected with norovirus recover after an unpleasant few days, susceptible populations, including older adults, can develop severe disease. A vaccine, especially one that is easy to administer, would thus be an important advance for protecting older adult populations. Flitter *et al*. report that an orally delivered vaccine against the norovirus GI.1 variant is safe and elicits robust immune responses in adults between 55 and 80 years of age. Importantly, antibody responses are elicited in the saliva and nasal cavity, potentially offering a first line of defense against mucosal pathogens such as norovirus. These promising clinical trial results support the further development of oral norovirus vaccines, including ongoing studies with bivalent vaccines. —Courtney Malo

Sci. Transl. Med. (2025) 10.1126/scitranslmed.ads0556

IN OTHER JOURNALS

Edited by **Corinne Simonti** *and* **Jesse Smith**

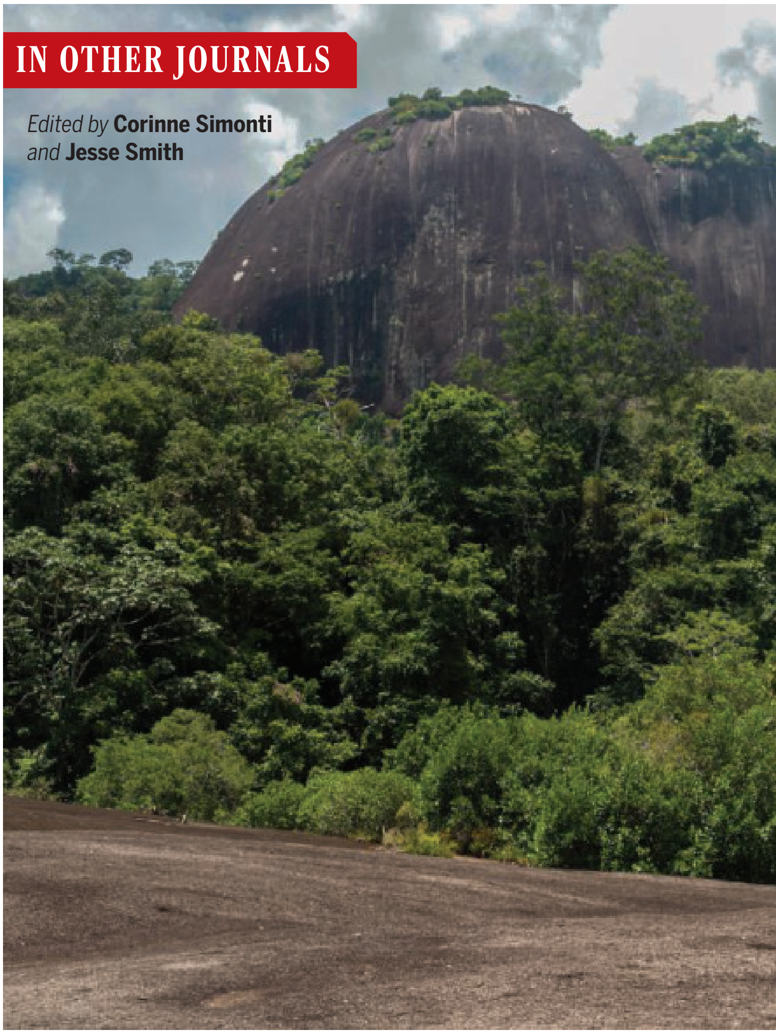

PHOTO: ARIADNE VAN ZANDBERGEN/ALAMY STOCK PHOTO

NEUROSCIENCE

Memory loss long before disease onset

In Alzheimer's disease, amyloid-beta (Aβ) pathology begins to accumulate within several brain regions, particularly the basal frontotemporal cortex, decades before clinical impairment. This brain region supports the ability to distinguish between events occurring at different times. Vanderlip *et al.* therefore tested whether Aβ deposition contributes to deficits in temporal mnemonic discrimination in cognitively unimpaired older adults. They found that individuals with elevated Aβ levels were selectively impaired on temporal, but not object or spatial, mnemonic discrimination. These results suggest that temporal mnemonic discrimination deficits relate to early Aβ deposition in the preclinical stage of Alzheimer's disease, and may be a useful tool to predict future disease progression and cognitive decline. —Peter Stern

J. Neurosci. (2025) 10.1523/JNEUROSCI.1605-24.2025

PHYSIOLOGY

Effects of circadian disruption in utero

Timing of food intake has important consequences for metabolism and weight management. Yao *et al.* found that such effects can even be transferred from mothers to their offspring. The authors exposed pregnant mice to circadian phase shifts (similar to jet lag) or genetic disruption of the circadian clock itself. Even as adult animals, the offspring of these mice were more susceptible than control animals to diet-induced obesity. They also showed disruption of timing of eating, resistance to the hormones leptin and insulin, decreased energy consumption and energy expenditure, and disrupted rhythmic accumulation of metabolites and gene expression in the liver. Thus, in mice, early events experienced by the fetus can influence responses to metabolic stress later in life. —L. Bryan Ray

Cell Metab. (2025)
10.1016/j.cmet.2024.12.002

ENDOMETRIOSIS

A close-up of endometriosis

Endometriosis is a painful chronic condition characterized by the abnormal growth of functional endometrium (uterine lining) outside of the uterine cavity. Although it is very common and can be disabling, its mechanisms remain poorly understood and there are no targeted therapies. To gain insight into the pathogenesis of endometriosis, Liu *et al.* performed single-cell profiling and compared endometrial tissue attached to patients' ovaries with intrauterine endometrial tissue from patients and controls. The authors identified changes associated with the menstrual cycle, as well as characteristic patterns in cell populations and immune cell clusters within the endometrium. They also detected specific alterations in signaling pathways and cellular interactions associated with endometriosis, revealing chronic inflammation that may be amenable to therapeutic interventions. —Yevgeniya Nusinovich

Cell Genom. (2025)
10.1016/j.xgen.2024.100737

HEAVY METALS

Engineered fish detoxify methylmercury

Methylmercury is a highly toxic compound produced by bacteria in waterlogged soils containing mercury. It is readily absorbed by plants and animals and concentrated within food webs, leading to high levels in some fish species. Tepper *et al.* engineered fruit flies and zebrafish to express two genes from bacteria that convert methylmercury to elemental mercury, which is far less toxic and less likely to be absorbed in the digestive tract. In both cases, the engineered animals were more resistant to toxic methylmercury exposure and accumulated less total mercury in their biomass. —Michael A. Funk

Nat. Commun. (2025)
10.1038/s41467-025-56145-w

METALLURGY

Metal mixology at room temperature

High-entropy alloys that consist of five or more principal elements require time-consuming and energy-intensive synthesis methods at high temperatures. Wu *et al.* used a liquid metal, gallium, as a solvent to dissolve metal particles of multiple elements in a commercial vortex mixer. This process produced GaMnFeCoNiZn alloys at room temperature within 6 hours, which is nearly an order of magnitude faster than traditional methods. This liquid metal–assisted processing route is promising for industry-scale production of high-entropy alloys with low energy consumption. —Sumin Jin

Matter (2025)
10.1016/j.matt.2025.101986

ARCHAEOLOGY

Scent of a mummy

The mummification practices in ancient Egypt have transfixed modern chemists because of the extraordinary effectiveness of the preservation techniques using natural materials. Paolin *et al.* sought to classify and distinguish the residual scents of the preservation chemicals used on nine mummies in the collection of the Egyptian Museum in Cairo, ranging from approximately 1700 to over 3000 years old. A sensory panel identified "woody, spicy, and sweet" as the most salient collective odors, although gas chromatography and olfactometry on separated components highlighted "cheesy, waxy, floral, and herbal" odors. It was necessary to deconvolute original materials from pesticides used for contemporary conservation. —Jake S. Yeston

J. Am. Chem. Soc. (2025)
10.1021/jacs.4c15769

CONSERVATION

A patchwork won't work

Continued human population growth has led to biodiversity loss. Our response to this problem has been to establish specific protected areas. However, islands of habitat surrounded by converted lands are not able to facilitate the healthy, connected ecosystems that these species—and humans—require. Greco *et al.* used a large camera trap dataset collected for over 200 species of tropical forest mammals to determine whether the presence of human activities outside such patches influences species richness and occupancy. They found that human presence, even outside protected areas, leads to extinction of sensitive species. These results show that we must take a more holistic approach to landscape preservation and use to maintain species sensitive to human presence and activities. —Sacha Vignieri

PLOS Biol. (2025) 10.1371/journal.pbio.3002976

Human activity adjacent to protected areas like the Central Suriname Nature Preserve still has negative effects on sensitive species within.

RESEARCH ARTICLE SUMMARY

MOLECULAR BIOLOGY

G-quadruplex–stalled eukaryotic replisome structure reveals helical inchworm DNA translocation

Sahil Batra†, Benjamin Allwein†, Charanya Kumar, Sujan Devbhandari, Jan-Gert Brüning, Soon Bahng, Chong M. Lee, Kenneth J. Marians, Richard K. Hite*, Dirk Remus*

INTRODUCTION: Cellular genomes are replicated by large, multisubunit complexes, called replisomes, which orchestrate the unwinding of the parental DNA and synthesis of the daughter strands at replication forks. Cellular replisomes in all domains of life are assembled around ring-shaped hexameric DNA helicases that topologically encircle DNA to drive the processive unwinding of the parental DNA. The eukaryotic replicative DNA helicase, CMG (Cdc45-MCM-GINS), is composed of the ring-shaped heterohexameric MCM ATPase and the noncatalytic cofactors, Cdc45 and GINS. At replication forks, CMG encircles and translocates along the leading strand template using DNA-binding hairpin loops that line its central channel, while sterically excluding the lagging strand template from entering the channel. Notably, CMG-driven DNA unwinding is frequently challenged by physical obstacles in the chromosomal template, including non–B-form DNA secondary structures, such as G-quadruplexes (G4s), which can cause replication stress and pose a threat to genome stability.

RATIONALE: Our previous studies established that G4s can impede replisome progression by inhibiting the CMG helicase. However, the molecular mechanism of DNA translocation by CMG and how G4s might interfere with CMG activity is not understood. Elucidation of these processes is critical to understanding both normal replisome function and the causes of replication stress. To this end, we took advantage of our ability to reconstitute yeast and human replisomes with purified proteins, which allows for a detailed biochemical and structural characterization of replisomes stalled at G4s in the parental DNA template.

RESULTS: We demonstrate that a single G4 can arrest DNA replication by stalling the translocation cycle of the CMG helicase. Our cryo–electron microscopy (cryo-EM) structures of yeast and human CMG stalled at a G4 in the leading strand template reveal that the G4 is fully folded and lodged within the central channel of CMG. Thus, the G4 is effectively sequestered away from G4-resolving helicases inside the stalled replisome, raising questions on potential fork restart mechanisms. We resolved two distinct conformations of G4-stalled CMG. The first closely resembles previously reported structures of CMG bound to normal forked DNA, recapitulating the protein-DNA interactions inside the CMG channel necessary for both DNA translocation and unwinding. Our second structure, by contrast, differs from previously determined CMG conformations and is consistent with an intermediate state along the translocation pathway. Our analysis provides evidence that CMG utilizes a previously uncharacterized mechanism to propel the 3′-to-5′ movement of the replication fork. This mechanism features oscillatory spiral-to-planar transitions of DNA-binding loops inside the CMG central channel, contrasting with the sequential rotary mechanism proposed previously for the homohexameric replicative DNA helicases in bacterial systems.

CONCLUSION: Our work provides definitive physical evidence for how DNA secondary structures can pose formidable barriers to the chromosomal DNA replication machinery. Additionally, our structures of CMG stalled at G4-containing replication forks unexpectedly point to a DNA translocation mechanism that is distinct among hexameric helicases. Further studies will be important for understanding the kinetics of this process and how G4-induced fork arrest may be resolved to allow for the completion of chromosome replication. ■

The list of author affiliations is available in the full article online.
*Corresponding author. Email: remusd@mskcc.org (D.R.); hiter@mskcc.org (R.K.H.)
†These authors contributed equally to this work.
Cite this article as S. Batra *et al.*, *Science* 387, eadt1978 (2025). DOI: 10.1126/science.adt1978

READ THE FULL ARTICLE AT
https://doi.org/10.1126/science.adt1978

G4s stall the eukaryotic replicative helicase. The eukaryotic replisome is assembled around the replicative DNA helicase, CMG. A single G4 can arrest DNA replication by stalling the CMG translocation cycle. Cryo-EM structures of G4-stalled fork protection complex (FPC)–bound CMG reveal a translocation cycle intermediate with a distinct conformation of the MCM presensor 1 and helix 2 insert DNA-binding hairpin loops.

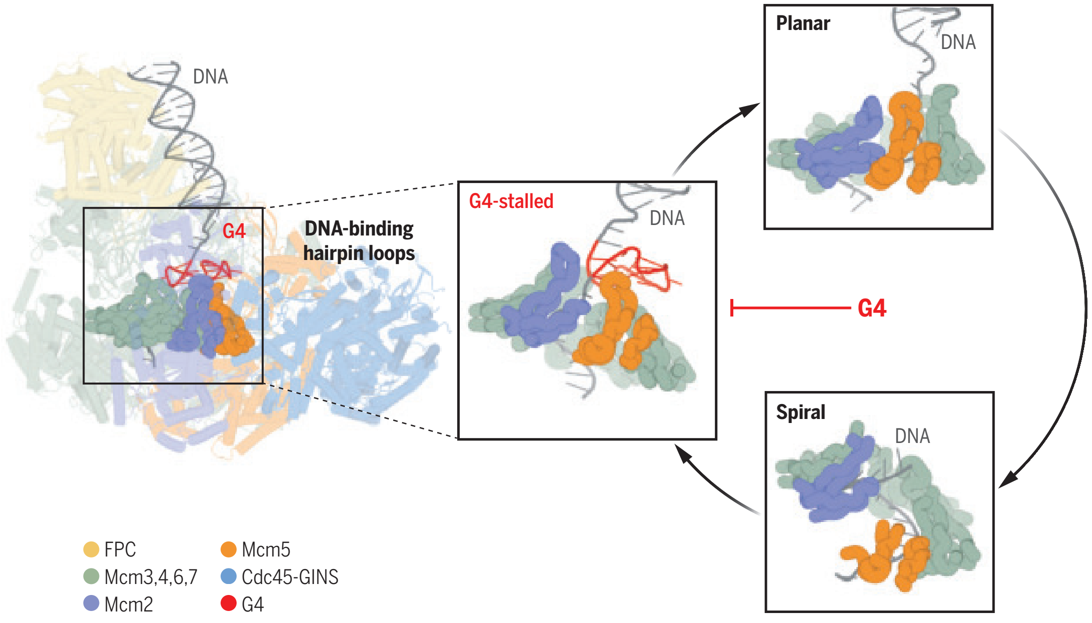

RESEARCH ARTICLE SUMMARY

CROP GENETICS

Historic manioc genomes illuminate maintenance of diversity under long-lived clonal cultivation

Logan Kistler*, Fabio de Oliveira Freitas*, Rafal M. Gutaker, S. Yoshi Maezumi, Jazmín Ramos-Madrigal, Marcelo F. Simon, J. Moises Mendoza F., Sergei V. Drovetski, Hope Loiselle, Eder Jorge de Oliveira, Eduardo Alano Vieira, Luiz Joaquim Castelo Branco Carvalho, Marina Ellis Perez, Audrey T. Lin, Hsiao-Lei Liu, Rachel Miller, Natalia A. S. Przelomska, Aakrosh Ratan, Nathan Wales, Kevin Wann, Shuya Zhang, Magdalena García, Daniela Valenzuela, Francisco Rothhammer, Calogero M. Santoro, Alejandra I. Domic, José M. Capriles, Robin G. Allaby*

INTRODUCTION: Manioc (*Manihot esculenta*), a root crop also called cassava and yuca, is one of the most important staple foods in the world, feeding around a billion people globally. Archaeobotanical and genetic evidence show that it originated in the southwestern Amazon region, and it was widespread throughout the American tropics at the time of European colonization. Manioc's wild progenitor is a short-lived outcrossing perennial species, but manioc is almost exclusively cultivated by vegetative propagation of stem cuttings. It thrives in the fire-shaped ecosystems of seasonally dry forests and edge habitats in South America, where Indigenous farmers first began clonally propagating desirable varieties.

RATIONALE: More than any other group of crop species, our understanding of plant domestication has been shaped by the archaeobotany and genetics of weedy annuals, such as maize and rice. However, many major economic crops are clonal species—e.g., potatoes, yams, sweet potatoes, sugarcane, and others—and we know much less about how clonal cultivation in human crop fields shapes domestication, population genomics, and genome evolution. In this work, we carry out a broad genomic survey of manioc and its wild relatives sampled from herbaria, living collections, on-farm cultivation, and archaeological sites. Using 573 new and previously published genomes, we aimed to understand how clonal reproduction and selection shape the genomic landscape of manioc. We also integrated crop diversity and interviews with traditional farmers in Brazil's Xingu region to better understand traditional strategies for managing and sustaining crop biodiversity.

RESULTS: We found that manioc sampled from around the Americas spanning >100 years carries almost no geographic population structure. That is, genetic makeup is a negligible predictor of geographic origins. This pattern starkly contrasts with that of its wild progenitor and defies basic expectations of biogeography previously demonstrated in many other crops. Most manioc varieties also have close kinship links with other varieties collected hundreds of kilometers away. These patterns reflect the shift to clonal propagation coupled with human-driven strategies for rapidly spreading clonal lineages over great distances, so that local genetic differentiation is overprinted by cultivation and dispersal practices. Manioc is highly heterozygous, and we observe that offspring are more heterozygous than expected in light of their parents' genotypes. This pattern likely reflects selection for global heterozygosity that suppresses the effects of recessive deleterious mutations under clonality. We found that all pairs of manioc worldwide share substantial fractions of their genomes in large identical-by-descent chromosomal haploblocks, a finding that is normally taken as robust evidence for recent common ancestry. However, we use breeding records to show that even unrelated samples carry far more genomic blocks than can be explained by kinship. Demographic simulations show that the shift to clonality and selection for heterozygosity lead to this unexpected pattern.

CONCLUSION: Clonal crop species account for a major fraction of global food production and caloric intake. Our population genomic treatment of manioc—focusing on traditional varieties, wild relatives, and an exhaustive sampling of farming landscapes in the Americas—establishes some previously unrealized expectations for the interplay of agricultural pressures and genomic outcomes under clonal cultivation. ■

The list of author affiliations is available in the full article online.
*Corresponding author. Email: kistlerl@si.edu (L.K.); fabio.freitas@embrapa.br (F.d.O.F.); r.g.allaby@warwick.ac.uk (R.G.A.)

Cite this article as L. Kistler *et al.*, *Science* **387**, eadq0018 (2025). DOI: 10.1126/science.adq0018

READ THE FULL ARTICLE AT
https://doi.org/10.1126/science.adq0018

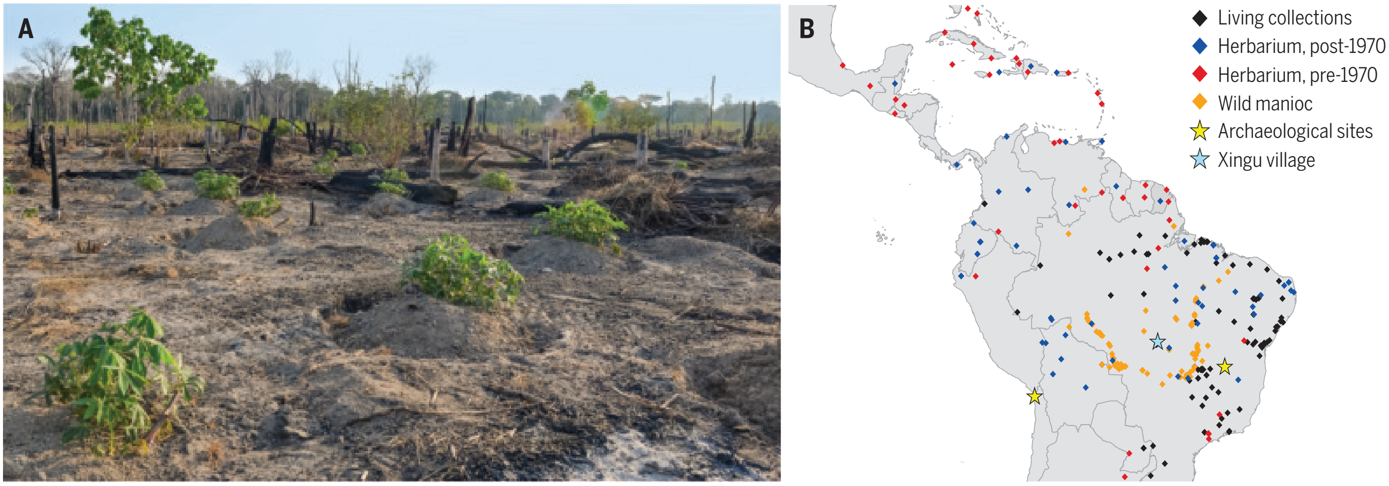

PHOTO: LOGAN KISTLER

Young manioc growing in mounds from stem cuttings, in a newly cleared field that had previously been left to fallow in regrowing forest. (**A**) Upper Xingu region, Mato Grosso, Brazil. (**B**) New archaeological, herbarium, and modern-day samples sequenced for this study. These 282 samples combined with published data yielded 573 total genomes for analysis.

RESEARCH ARTICLE SUMMARY

CORONAVIRUS

Macrophage peroxisomes guide alveolar regeneration and limit SARS-CoV-2 tissue sequelae

Xiaoqin Wei, Wei Qian, Harish Narasimhan, Ting Chan, Xue Liu, Mohd Arish, Samuel Young, Chaofan Li, In Su Cheon, Qing Yu, Gislane Almeida-Santos, Xiao-Yu Zhao, Eric V. Yeatts, Olivia J. Spear, Megan Yi, Tanyalak Parimon, Yinshan Fang, Young S. Hahn, Timothy N.J. Bullock, Lindsay A. Somerville, Mark H. Kaplan, Anne I. Sperling, Yun Michael Shim, Robert Vassallo, Peter Chen, Sarah E. Ewald, Anja C. Roden, Jianwen Que, Dianhua Jiang, Jie Sun*

INTRODUCTION: Severe acute respiratory syndrome coronavirus 2 (SARS-CoV-2) infection causes both acute manifestations and long-term complications. These post acute sequelae (PASC) of SARS-CoV-2 infection or Long Covid have affected more than 60 million individuals worldwide. Similar chronic sequelae have also been observed after other respiratory viral infections, including influenza. Despite advances in antiviral and anti-inflammatory therapies, we lack effective interventions that target tissue regeneration and recovery after severe viral injury to minimize the development of chronic host conditions. Following alveolar damage, the emergence of epithelial progenitors—including transitional progenitor cells highly expressing cytokeratin 8 (KRT8)—is a hallmark of the lung repair process. However, dysregulated persistence of these cells can lead to pathological tissue remodeling and fibrosis, characteristics of post viral chronic lung sequelae. The immunological mechanisms regulating the development and persistence of dysplastic KRT8 cells after infection are not fully understood.

RATIONALE: Macrophages are critical in antiviral immunity, lung inflammation, and tissue repair after viral infection. Peroxisomes, cellular organelles involved in lipid metabolism and cellular redox balance, are often overlooked compared with other organelles such as mitochondria. Working in mouse models of infection, we examined the dynamic changes of macrophage peroxisome compartment in vivo after respiratory viral infection including SARS-CoV-2. We also investigated how peroxisomes regulate macrophage inflammatory and repair function in the lung after viral injury in vivo. Furthermore, we evaluated whether pharmacologically enhancing peroxisome biogenesis could serve as a prorepair therapeutic approach to mitigate acute and chronic host conditions following infection.

RESULTS: Severe COVID-19 significantly remodeled the peroxisome compartment, reducing the number of peroxisomes in mouse lung macrophages, as revealed by bioinformatic and immunofluorescence analyses. We found that increased interferon signaling, especially IFNγ signaling, inhibited peroxisome biogenesis and promoted peroxisome degradation through pexophagy (autophagy of peroxisomes) in macrophages. Mouse models with selective depletion of macrophage peroxisomes demonstrated that peroxisomes were essential for resolving inflammation and promoting alveolar regeneration after severe viral injury. Mechanistically, peroxisomes exhibited cell type–specific modulation of lipid metabolism, enhancing mitochondrial health and supporting macrophage repair programs for the self-renewal of alveolar type 2 (AT2) cells. Macrophage peroxisome dysfunction, however, led to increased inflammasome activation and excessive IL-1β release by means of the Gasdermin D pore. Persistent IL-1β production subsequently caused the accumulation of dysplastic KRT8 transitional epithelial progenitors in the lung, driving chronic tissue pathology and fibrotic remodeling following acute SARS-CoV-2 infection. Chronic peroxisome impairment was observed in the lungs from human patients with PASC pulmonary fibrosis and relevant mouse models. Notably, in our mouse models, pharmacological enhancement of peroxisome biogenesis using sodium 4-phenylbutyrate (4-PBA) restored peroxisome function in macrophages, mitigated lung inflammation and fibrosis, and enhanced alveolar regeneration after viral infection.

CONCLUSION: This study suggests that severe respiratory viral infections can reduce peroxisome biogenesis and promote peroxisome degradation in response to raised interferon levels. Our findings reveal that peroxisomes act as essential regulators of macrophage-mediated lung inflammation resolution and tissue regeneration following viral injury. Thus, peroxisomal dysfunction in macrophages contributes to the development of severe acute morbidity and chronic tissue sequelae post-COVID-19. Targeting peroxisome biogenesis or enhancing peroxisomal metabolic function represents a promising therapeutic approach for mitigating the long-term consequences of respiratory viral infections, with potential for improving health outcomes for patients with PASC. ■

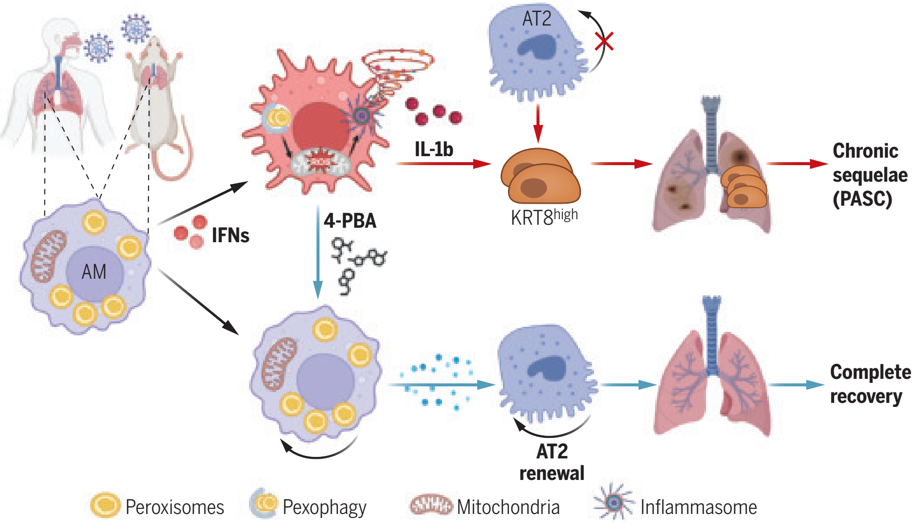

Model of peroxisome function in macrophage-mediated alveolar regeneration after viral injury. Peroxisome activity in alveolar macrophages (AM) is essential for AT2 self-renewal and alveolar repair following viral infection. Dysfunction of macrophage peroxisomes causes excessive inflammasome activation and promotes dysplastic KRT8 transitional cell accumulation, resulting in chronic tissue sequelae post acute infection. 4-PBA treatment facilitates peroxisome biogenesis in macrophages to enhance alveolar regeneration after respiratory viral infection [figure created using BioRender.com.]

The list of author affiliations is available in the full article online.
*Corresponding author. Email: js6re@virginia.edu

Cite this article as X. Wei *et al.*, *Science* **387**, eadq2509 (2025). DOI: 10.1126/science.adq2509

READ THE FULL ARTICLE AT
https://doi.org/10.1126/science.adq2509

RESEARCH ARTICLE SUMMARY

CELL BIOLOGY

A subcellular map of translational machinery composition and regulation at the single-molecule level

Zijian Zhang†, Adele Xu†, Yunhao Bai, Yuxiang Chen, Kitra Cates, Craig Kerr, Abel Bermudez, Teodorus Theo Susanto, Kelsie Wysong, Fernando J. García Marqués, Garry P. Nolan, Sharon Pitteri, Maria Barna*

INTRODUCTION: Ribosomes, the universal molecular machinery for protein synthesis, have been viewed as structurally and functionally uniform entities since their initial characterization over six decades ago. However, accumulating evidence suggests that ribosomes can contain distinct combinations of ribosomal proteins (RPs) and are regulated by ribosome-associated proteins (RAPs). These heterogeneous ribosomal subpopulations are hypothesized to play specialized roles in translational control, contributing to cellular protein homeostasis. However, the field has lacked tools to directly visualize individual ribosomes, characterize their molecular composition, and map their spatial distribution in cells. Understanding how ribosomal diversity impacts translation could unveil new layers of gene expression regulation.

RATIONALE: To bridge this technical gap, we developed two synergistic approaches: ribosome expansion microscopy (RiboExM) and ALIBi (an optogenetic proximity labeling method). RiboExM couples physical expansion of cells with standard confocal microscopy to achieve subribosomal resolution, allowing direct visualization of distinct ribosomal populations and their spatial organization within mammalian cells. ALIBi enables biochemical isolation of ribosomes and associated RAPs and mRNAs from specific subcellular compartments, facilitating quantitative proteomics and transcriptomics analyses. Together, these methods offer complementary insights into ribosomal composition and its functional implications, enabling a comprehensive investigation of subcellular translational machinery at the single-molecule level.

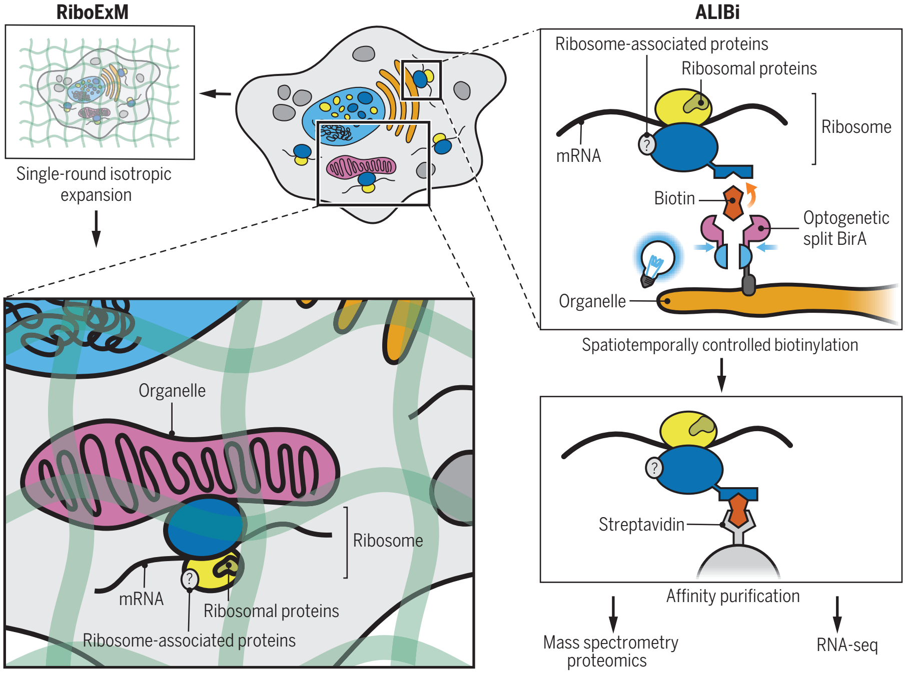

Two complementary methods reveal subcellular heterogeneity of ribosomes and mRNA translation. Ribosome expansion microscopy (RiboExM) enables isotropic single-molecule imaging of ribosomal populations, specialized ribosomes, and associated mRNAs. AviTag-specific Location-restricted Illumination-Enhanced Biotinylation (ALIBi) is an optogenetically controlled technology that allows affinity purification of subcellular ribosome populations for multimodal downstream analysis. Here, we describe the use of these technologies to characterize ribosomes in subcellular space and in neurons.

RESULTS: Using RiboExM, we constructed a single-molecule panorama of the translational machinery in mammalian cells. This map revealed distinctive spatial patterns: Whereas 40*S* subunits were distributed more evenly in the cytoplasm, 60*S* subunits clustered near polysomes and were enriched at the endoplasmic reticulum (ER). ALIBi confirmed the selective enrichment of 60*S* subunits at the ER and also revealed RAPs that were enriched at the ER, including the presumed ribosome biogenesis factor Lsg1. Knocking down Lsg1 disrupted 60*S* enrichment at the ER and altered translation of specific proteins, revealing a mechanism of translational control independent of ER stress. We also applied ALIBi to examine ribosome composition in other subcellular compartments, identifying both well-described and new RAPs as a resource for studying ribosomes associated with specific organelles.

ALIBi and RiboExM enabled discovery of "specialized ribosomes" with unconventional RP compositions. Focusing on the outer mitochondrial membrane (OMM), we visualized the enrichment of RPS25- and RPL29-depleted ribosomes. In addition, RiboExM enabled simultaneous visualization of ribosomes and their associated mRNAs, revealing that specialized ribosomes at the OMM preferentially bind to mRNAs involved in metabolism, specifically those in the vitamin B_{12} utilization pathway. This demonstrates ribosome heterogeneity–mediated translational control in subcellular contexts.

In neurons, RiboExM revealed a functional dichotomy between monosomes and polysomes. Monosomes were enriched in distal neurites at baseline, whereas polysomes formed dynamically in response to external stimuli, suggesting regulation of protein synthesis in neuronal processes.

CONCLUSION: Together, RiboExM and ALIBi constitute a key toolkit for studying ribosomal composition, localization, and function at single-molecule resolution. In this study, we have used these tools to unveil ribosomal heterogeneity and its implications for translational control across cellular compartments and cell types. In general, RiboExM and ALIBi offer opportunities for exploring macromolecular interactions and regulatory mechanisms in cellular biology. The versatility of these methods holds potential for advancing understanding of translational regulation in both physiological and pathological contexts. ■

The list of author affiliations is available in the full article online.
***Corresponding author. Email: mbarna@stanford.edu**
†These authors contributed equally to this work.

Cite this article as Z. Zhang *et al.*, *Science* **387**, eadn2623 (2025). DOI: 10.1126/science.adn2623

READ THE FULL ARTICLE AT
https://doi.org/10.1126/science.adn2623

RESEARCH ARTICLE SUMMARY

MICROBIOTA

Neonatal fungi promote lifelong metabolic health through macrophage-dependent β cell development

Jennifer Hampton Hill, Rickesha Bell, Logan Barrios, Halli Baird, Kyla Ost, Morgan Greenewood, Josh K. Monts, Erin Tracy, Casey H. Meili, Tyson R. Chiaro, Allison M. Weis, Karen Guillemin, Anna E. Beaudin, L. Charles Murtaugh*, W. Zac Stephens*, June L. Round*

INTRODUCTION: Systemic glucose homeostasis depends on the hormone insulin, which is produced solely by pancreatic β cells. Without sufficient insulin, diabetes will ensue. β cell mass expands rapidly after birth, to accommodate the metabolic demands of growing infants. By studying postnatal β cell development, we may uncover novel mechanisms to either bolster this process in individuals who are genetically susceptible to diabetes or stimulate the endogenous replacement of these important cells after their loss.

Coincident with postnatal β cell expansion, the composition of the gut microbiota diversifies in distinct phases, with each new phase dominated by distinct taxa. Acquiring a sufficiently diverse microbiota appears to protect against childhood diabetes; however, the mechanisms involved are not known, and we cannot yet attribute specific mechanisms of disease susceptibility or protection to specific microbes.

RATIONALE: We have previously identified resident microbes that stimulate larval β cell proliferation in zebrafish, but mammals have more restricted β cell proliferation and distinct microbial communities. Specifically, mammalian microbiotas undergo distinct developmental diversification steps, whereby different microbial taxa dominate at different times. Microbiota diversification coincides with a fleeting period of postnatal β cell proliferation, which establishes a sufficient insulin-producing cell population. Therefore, we sought to test the hypothesis that mouse postnatal β cell development is stimulated by specific microbes during defined windows of microbial colonization.

RESULTS: By systematically ablating and restoring the microbiota during defined windows of pre- and postnatal life in mice, we identified a 10-day period before weaning when resident microbes are required to establish normal β cell mass. These observations were replicated using antibiotic and antifungal drugs, indicating that both bacteria and fungi promote host β cells. We also found that fecal samples from human infants, 7 to 12 months of age, robustly stimulated mouse β cell mass, whereas samples from other age groups did not, suggesting that humans also exhibit a window of colonization by β cell–promoting microbes. By comparing microbial communities that could and could not elicit β cell development, we identified specific bacterial and fungal taxa (*Escherichia coli*, *Enterococcus gallinarum*, and *Candida dubliniensis*) that were sufficient to promote murine postnatal β cell expansion. RNA sequencing of islets from germ-free and conventional pups across the critical window revealed a necessary role for microbes in stimulating macrophage infiltration of islets. Among our microbial candidates, we found that *C. dubliniensis* colonization promoted islet macrophages most significantly. Further, ablation of macrophages reversed the pro–β cell effects of *C. dubliniensis*, indicating that macrophages are required to mediate β cell promotion by *C. dubliniensis* in the developing islet. *C. dubliniensis* cell wall modifications were critical components of this islet-fungal signaling axis. We also tested the capacity of *C. dubliniensis* to mitigate diabetes in mouse models and found that not only could it reduce disease prevalence and severity, but it could also promote β cell restoration in adult animals after ablation.

CONCLUSION: Our study identifies a critical window in early life when transient enrichments of specific microbes are necessary to promote pancreatic β cell development. Bacteria and fungi provide important cues that are sufficient to promote this process. However, host sensing of these cues differs according to their microbial origins, highlighting the diverse host-microbe signaling mechanisms that have evolved to support insulin production. We describe a microbiota-mediated macrophage-dependent mechanism that supports recognition of distinct cell wall stimuli from commensal yeast, which may be used as a tool to prevent or reverse β cell loss. ■

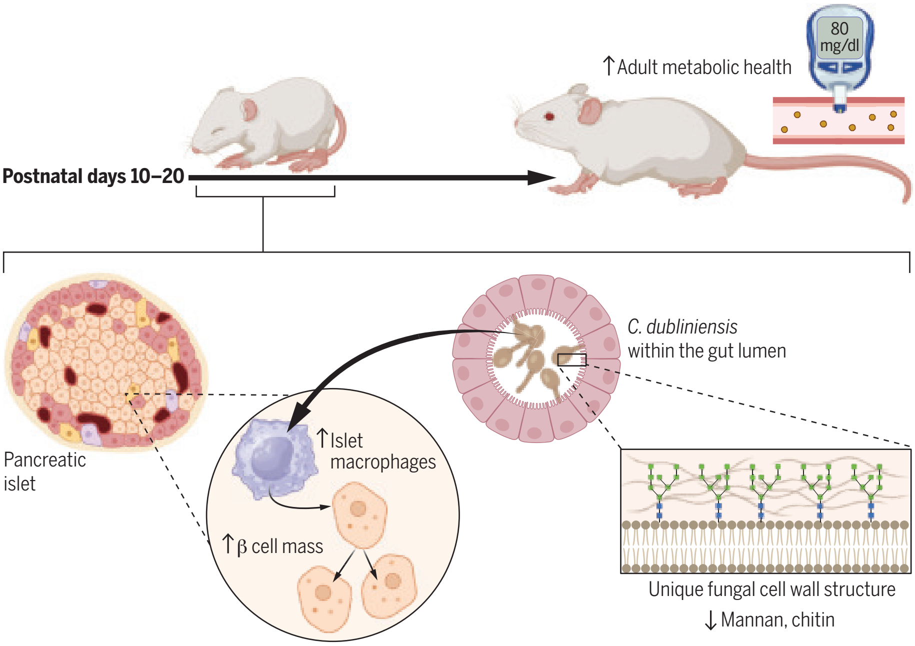

***C. dubliniensis* colonization promotes postnatal development in the pancreas.** Specific microbes promote mouse β cell expansion during a critical postnatal period before weaning (days 10 to 20). Colonization by the fungal commensal *C. dubliniensis* stimulates β cell mass through a macrophage-dependent mechanism. This effect appears to be activated by *C. dubliniensis*' distinctive cell wall structure, which has reduced levels of both mannan and chitin. These early-life processes result in long-term metabolic health. [Created in BioRender. Hill, J. (2024) https://BioRender.com/v02g855]

The list of author affiliations is available in the full article online.
*Corresponding author. Email: june.round@path.utah.edu (J.L.R.); murtaugh@genetics.utah.edu (L.C.M.); zac.stephens@path.utah.edu (W.Z.S.)
Cite this article as J. H. Hill *et al.*, *Science* **387**, eadn0953 (2025). DOI: 10.1126/science.adn0953

READ THE FULL ARTICLE AT
https://doi.org/10.1126/science.adn0953

RESEARCH ARTICLE SUMMARY

FOREST CHANGE

Tropical forests in the Americas are changing too slowly to track climate change

Jesús Aguirre-Gutiérrez* ***et al.***

INTRODUCTION: Tropical land regions are experiencing rapid climate change, with some scenarios for the tropical Americas projecting temperature increases of up to ~4°C and precipitation reductions of close to 20% by 2100. This would expose current species assemblages to climates that they have never experienced before, potentially selecting for future plant communities adapted to such climates but unlike those currently observed. Community responses to climate change will thus likely depend on underlying mechanisms and geographical context. In the face of threats from climate change, it is both critical and urgent to understand the ability of these complex systems to adapt to change and survive. The relationships among environmental conditions, plant performance, and distribution are mediated by species' functional traits. Therefore, a trait-based approach provides a promising framework for predicting the impacts of climate change and resilience across forest ecosystems.

RATIONALE: Climate change is already affecting the survival and distribution of tropical American plant communities. If species respond to climate change through migration, then we would expect montane communities to track changes in climate better than those in the lowland forests because mountains have different climate conditions occurring at shorter distances and thus are potentially easier to migrate across than lowlands. Given exposure to a drying and warming climate, we could expect increased abundance of species exhibiting more drought-tolerance traits. Drought-avoidance traits, notably deciduousness, could also become more prominent in the future as an adaptation to increasing drought.

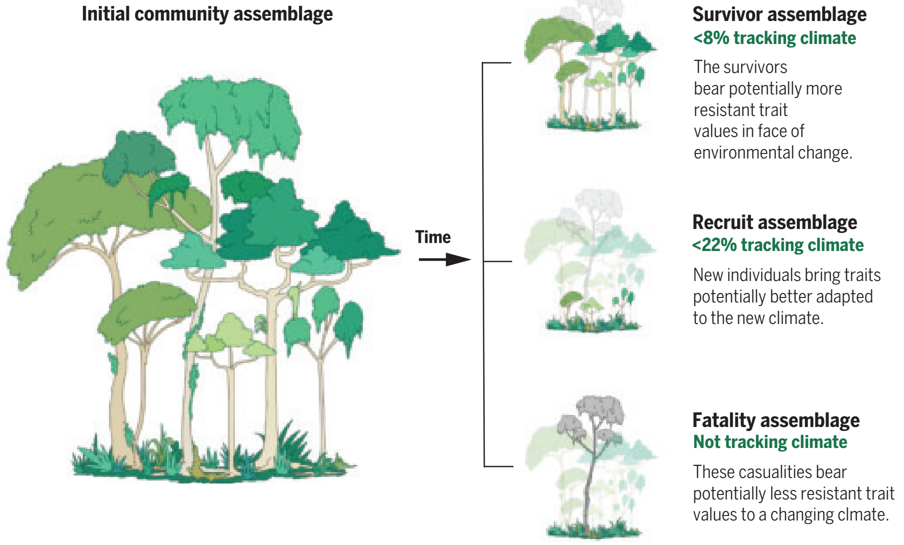

Mechanisms driving changes in community trait composition and climate tracking. Changes in climatic conditions significantly influence tropical forest tree community dynamics, including survival (survivor assemblages), recruitment (recruit assemblages), and mortality (fatality assemblages). Quantifying these community dynamics is crucial for understanding how tropical forests adapt to and track a changing climate. Survivor assemblages consist of trees with traits potentially suited to existing climatic conditions, aiding in incremental climate tracking. Conversely, recruit assemblages are composed of individuals with traits potentially better adapted to emerging climatic conditions, enhancing their ability to thrive under new environmental conditions. By contrast, fatality assemblages represent individuals with less resilient traits, leading to their inability to cope with climatic shifts. Our analysis reveals that survivor assemblages are tracking climate changes at <8% of the expected rate given current climate shifts. Recruit assemblages demonstrate a higher tracking rate, ~22% of the expectation. However, fatality assemblages by definition do not track climate because they consist of individuals that have already perished, likely due to their inadequate adaptation to changing climatic conditions.

It is as yet unclear how shifts in the abundance and distribution of species translate into changes in functional composition and what functional changes have occurred as a response to the onset of a warmer, drier, and more variable climate across the tropical Americas. It is uncertain if these functional shifts match the direction of climate change and, if so, whether the rate of functional trait change keeps pace with climate change or lags behind. Here, we address these knowledge gaps by analyzing tree community trait shifts that have occurred across the past 40 years in tropical forests of the Americas due to the dynamics of survivor, recruit, and fatality tree assemblages. The survivor tree assemblages consist of trees with traits potentially better suited to existing climatic conditions, and the recruit assemblages are composed of individuals with traits adapted to emerging climatic conditions. The fatality assemblages could represent individuals with less resilient traits that cause their inability to cope with climatic shifts. We also quantify if the observed changes in trait composition have been enough to track climate change to date.

RESULTS: Overall, we found that lowland forests show significant and larger changes in more community traits than montane forests. Across forests and for the survivor assemblages, the abundance of deciduous species is increasing, with accompanying increases in leaf photosynthetic capacity and decreases in leaf area and leaf thickness, perhaps as an adaptation to a warmer and dryer climate. However, the recruiting communities in the lowland forests have, on average, exhibited decreases in their abundance of deciduous species, in leaf carbon and nitrogen content, and in wood density. Crucially, most of these traits are changing at only a fraction of the rate required to maintain equilibrium with climate in the full tree community and survivor assemblages. The recruiting communities show the best tracking of a changing climate.

CONCLUSION: Our analysis demonstrates that tree community composition is shifting to track climate change, but tree species composition and functional properties of tropical American forests (and possibly all tropical forests) are increasingly out of equilibrium with local climate. Such disequilibrium likely increases vulnerability to climate change. ■

The complete list of authors and their affiliations is available in the full article online.

*Corresponding author. Email: jeaggu@gmail.com

Cite this article as J. Aguirre-Gutiérrez ***et al.***, ***Science*** **387, eadl5414 (2025). DOI: 10.1126/science.adl5414**

S READ THE FULL ARTICLE AT
https://doi.org/10.1126/science.adl5414

RESEARCH ARTICLES

FOREST CHANGE

Upslope plant species shifts in Mesoamerican cloud forests driven by climate and land use change

Santiago Ramírez-Barahona[1,2]*, Ángela P. Cuervo-Robayo[2,3], Kenneth J. Feeley[4], Andrés Ernesto Ortiz-Rodríguez[1], Antonio Acini Vásquez-Aguilar[5], Juan Francisco Ornelas[5], Hernando Rodríguez-Correa[6]

Global change drives biodiversity shifts worldwide, but these shifts are poorly understood in highly diverse tropical regions. In tropical mountains, plants are mostly expected to migrate upslope in response to warming. To assess this, we analyze shifts in elevation ranges of species in Mesoamerican cloud forests using three decades of species' occurrence records. Our findings reveal a mean upslope shift of 1.8 to 2.7 meters per year since 1979 driven by the upslope retreat of the less thermophilic montane species. These shifts are mostly accompanied by retreating lower and upper edges attributed to varying degrees of species' exposure to deforestation and climate change. Our results highlight the vulnerability of cloud forests under global change and the urgency to increase monitoring of species' responses.

Changes in global surface temperatures and precipitation over the past century (*1*–*3*) are altering the distribution and abundances of many species (*4*–*9*). Migration through range displacement is the most common apparent response of species to these changes (*5*, *10*–*13*). In tropical mountains, plant species are expected to migrate primarily toward higher elevations as a result of a shallow latitudinal temperature gradient (*12*, *14*–*19*), leading to directional changes in community composition with elevation (*4*–*11*, *14*, *20*–*29*). Species can also respond to rapidly changing climates through in situ acclimatization or adaptation (*10*, *12*, *30*). However, these responses may be hindered by land use changes (*31*), biological interactions, or species' life histories (*11*), reducing the areas available for migration or augmenting exposure to climate and thereby increasing the probability of local extinction (*4*, *10*, *12*, *32*).

Documenting contemporary elevation range shifts in highly diverse tropical forests is critical to understanding the extent of species' responses to climate change and anticipating its future impacts. Neotropical cloud forests are especially vulnerable (*17*, *33*–*36*), as their distribution is tightly linked to cloud formation, temperature, relative humidity, and vegetation cover (*15*, *16*, *37*). Mesoamerican cloud forests support the highest concentration of animal and plant diversity in the region but are among the most threatened ecosystems. These forests occupy less than 1% of the region's terrestrial surface and harbor over 6000 vascular plant species (*38*) (18% of plant diversity in the region), of which 2500 to 2800 preferentially inhabit these forests (*39*). Less than 20% of cloud forests are under protection (*37*) and estimates indicate that forest cover has been halved over the past century as a result of deforestation (*36*, *37*). The combination of rapidly changing climates and ongoing deforestation suggests that species' elevational range shifts are already underway across Mesoamerican mountains. Indeed, there is evidence of increases in the relative abundance of lowland, warm-adapted species in mid- to high elevations, a phenomenon known as thermophilization (*20*, *21*, *40*). However, the extent of elevational range shifts in less thermophilic cloud forest plants and its drivers remains largely unexplored, partly due to the lack of appropriate datasets (*13*, *41*).

Ideally, species range shifts should be assessed using systematically surveyed time series datasets (*13*, *41*), but these are unavailable for most tropical regions. In the absence of continuous time series, occurrence data from different time periods can be used to detect elevational shifts and enhance our understanding of species range dynamics in response to global change. We harness three decades worth of occurrence records (*42*), along with climate and land use data, to explore species' elevational shifts in Mesoamerican cloud forests and their potential drivers. By accounting for the spatially and temporarily disorganized structure of occurrence data, we aim to determine: (i) whether elevation shifts are detectable in cloud forest plant species; (ii) whether species' traits and habitat preferences explain variation in the magnitude and direction of these shifts; and (iii) whether these shifts are spatially and temporarily associated with warming, reduced precipitation, and land use conversion.

Elevational shifts in cloud forests

We assessed elevation shifts in 1021 plant species, representing 36% of the plants that preferentially inhabit Mesoamerican cloud forests, chosen for having at least 95% of their occurrence records within the ecoregions covering the distribution of these cloud forests (fig. S1). The selected species encompass a range of functional types (trees, shrubs, herbs, epiphytes, climbers). We retrieved elevation data (meters above sea level) for each species occurrence record (*42*) using a 30-m resolution digital elevation model (*43*). To calculate species' elevation midpoints, as well as upper and lower elevation limits (range edges) through time, we used 10-year rolling means for every year since 1979 (*43*).

We expected shifts in the elevation midpoint of species in response to climate change, particularly warming and decreasing cloud immersion (*16*, *17*, *21*, *44*–*46*). Indeed, a linear mixed model of elevation midpoints as a function of time showed a mean shift of 2.72 ± 0.216 m yr^{-1} that translates into 84.32 ± 6.7 m of upslope shift since 1979 (the models were truncated after 2010 because of data uncertainty) (*43*). Over the same period, linear mixed models showed a mean upslope shift of lower range edges (8.46 ± 0.295 m yr^{-1}) and a mean downslope shift of upper range edges (–6.29 ± 0.321 m yr^{-1}) (Fig. 1A). These trends are likely sensitive to estimation error. Therefore we refitted our models, incorporating estimation error as a covariate (*43*) to examine its effects on elevational shifts (table S1). The error primarily affected baselines (intercepts) rather than rates of shift (slopes) for lower range edges, whereas increasing error resulted in less pronounced midpoint shifts and steeper upper range–edge shifts (Fig. 1A).

Impact of sampling bias and uncertainty

Sampling of cloud forest species has undoubtedly been temporarily and spatially heterogeneous, introducing potential biases to the estimation of species elevation through time. Stochastic, methodological, and sampling errors [e.g., interannual population variability (*22*) as well as undetected species (*22*, *41*)] may partially underlie variability in estimated shifts among species, as the probability of species detection at particular elevations can vary due to species-specific annual collection effort.

---

[1]Departamento de Botánica, Instituto de Biología, Universidad Nacional Autónoma de México (UNAM), Circuito Exterior s/n, Ciudad de México, Mexico. [2]Laboratorio Nacional CONAHCyT de Biología del Cambio Climático, Instituto de Biología, Universidad Nacional Autónoma de México (UNAM), Circuito Exterior s/n, Ciudad de México, Mexico. [3]Departamento de Zoología, Instituto de Biología, Universidad Nacional Autónoma de México (UNAM), Circuito Exterior s/n, Ciudad de México, Mexico. [4]Department of Biology, University of Miami, Coral Gables, FL, USA. [5]Departamento de Biología Evolutiva, Instituto de Ecología, A.C. (INECOL), Carretera antigua a Coatepec No. 351, El Haya, Xalapa, Veracruz, Mexico. [6]Escuela Nacional de Estudios Superiores (ENES) Unidad Morelia, Universidad Nacional Autónoma de México (UNAM), Antigua Carretera a Pátzcuaro 8701 Ex Hacienda de San José de la Huerta, Morelia, Michoacán, Mexico.
***Corresponding author. Email: santiago.ramirez@ib.unam.mx**

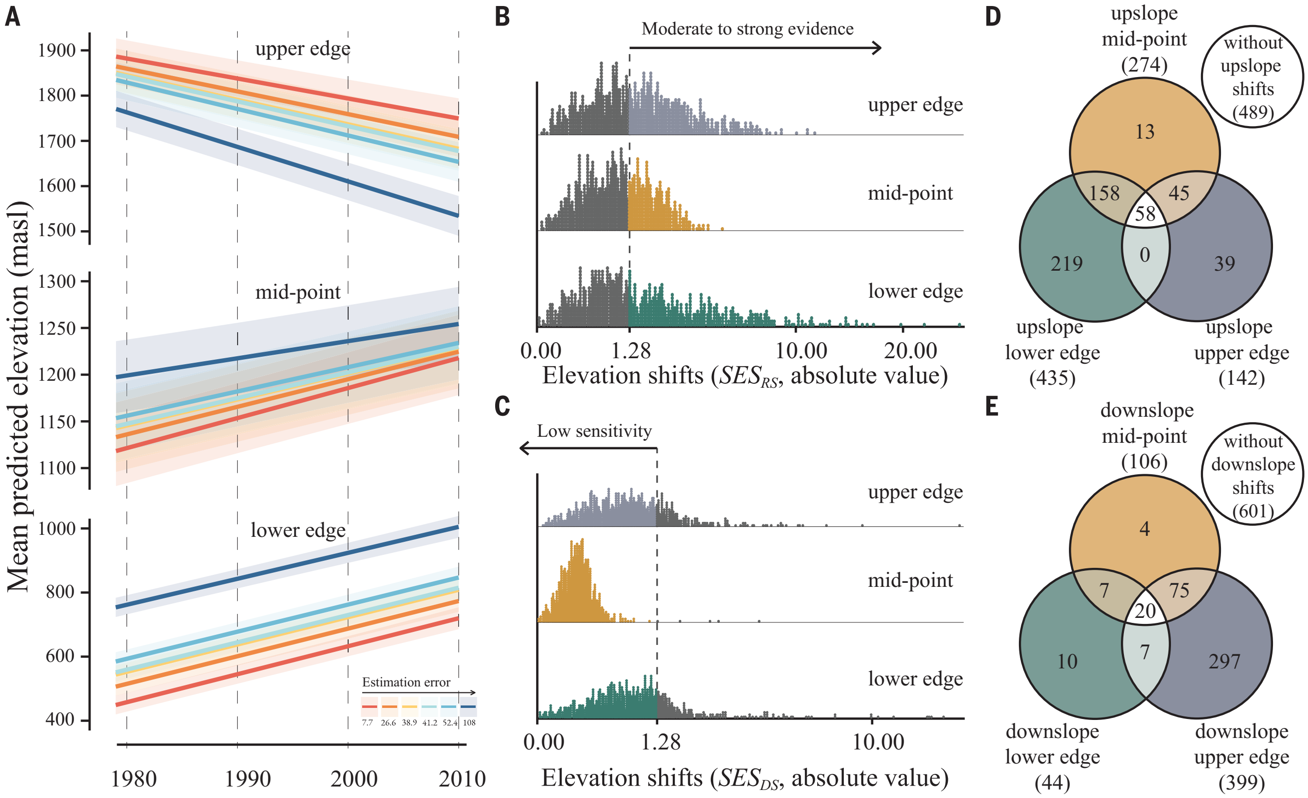

Fig. 1. Elevation shifts across 1021 vascular plant species in Mesoamerican cloud forests over the period 1979 to 2010. (**A**) Mean predicted elevation from linear mixed models of lower edges, midpoints, and upper edges as a function of time and including estimation error as a covariate (e.g., species are grouped depending on the confidence of estimates). Colors indicate predictions for different levels of estimation error based on the quantiles of the error distribution across species. (**B** and **C**) Absolute values of Standardized Effect Sizes (SES) for species' elevation shifts estimated under the (B) resampling and (C) downsampling null models. Dashed lines mark the |1.28| threshold, representing a 90% confidence level for observed elevation shifts. In (B) estimates to the right of the threshold (colored) indicate species with strong evidence for "true" elevational shifts, irrespective of the direction of shifts. In (C) estimates to the left of the threshold (colored) indicate species with low sensitivity to sampling heterogeneity, irrespective of the direction of shifts. (**D**) Venn diagrams depicting the number of species with upslope midpoint shift that also display upslope shifts in upper and lower range edges. (**E**) Venn diagrams depicting the number of species with downslope midpoint shift that also display downslope shifts in upper and lower range edges. Numbers in parenthesis indicate the total number of species with the corresponding shift; number of species without evidence of shifts is depicted in the white (isolated) circles.

Rolling averages are aimed at mitigating some of these effects (*43*), but these still assume that species do not remain undetected regionally for prolonged periods.

If sampling bias underlies the observed upslope species shifts, we should expect consistent changes in sampling coverage through time and across elevation. We found that while occurrence records decrease toward the present, leading to increased estimation error, sampling coverage across elevation has remained constant (fig. S2). To further investigate the impact of estimation error, we fitted linear mixed models of elevation through time to 1000 bootstrap replicates of species' elevation time series (*43*). These models showed that the observed mean upslope shift lies within the range of bootstrap estimates (fig. S3). In 83% of species (843) the bootstraps replicates supported the direction of observed midpoint shifts (upslope or downslope), but with more uncertain magnitudes. In other words, our results indicate that the elevational "center of gravity" of species (*44*–*46*) has indeed changed over time and that estimation error, likely due to sampling biases in the occurrence data (*22*, *45*, *47*), underlies some—but not all—of the observed signal of shifts.

To assess the extent to which individual species have been systematically affected by temporally heterogeneous sampling, we generated random sets of occurrence records (null models) with similar spatiotemporal structures to observed data (fig. S4). These models were designed to generate expectations for elevation shifts given the regional sampling effort per year [resampling (RS) models] and to assess the sensitivity of shifts to yearly variation in collection intensity [downsampling (DS) models] (*43*). For each replicate (1000 for each null model), we fitted linear mixed models of elevation through time and found support for "true" signals of elevation shifts when the observed coefficient differed from the mean of the RS models (strength of evidence), but not from that of the DS models (*43*). Standardized effect sizes (SES) indicate that species' elevation midpoint shifts are generally robust to sampling bias and temporal heterogeneity (Fig. 1, B and C). We estimated an average elevation midpoint shift of 0.67 ± 0.011 m yr^{-1} and of 2.51 ± 0.003 m yr^{-1} across RS and DS replicates, respectively. Occurrence data are likely overestimating the "true" magnitude of elevation midpoint shifts. Collating null models and observed data revealed a more conservative average midpoint shift of 1.84 m yr^{-1}. Using a 90% confidence level ($SES > |1.28|$), our models indicate 37.2% of species (380) had strongly supported midpoint shifts with low sensitivity, of which 274 species showed upslope shifts.

Interpreting range dynamics from occurrence data are inherently uncertain, as strong shifts in upper and lower edges can occur by chance alone (RS lower-edge shift: 2.69 ± 0.007 m yr^{-1}; RS upper-edge shift: −3.03 ± 0.011 m yr^{-1}). Despite this, our null models supported ($SES_{RS} > |1.28|$) upper- and lower-range-edge shifts in 41.0% and 43.7% of species, respectively. Upslope midpoint shifts were

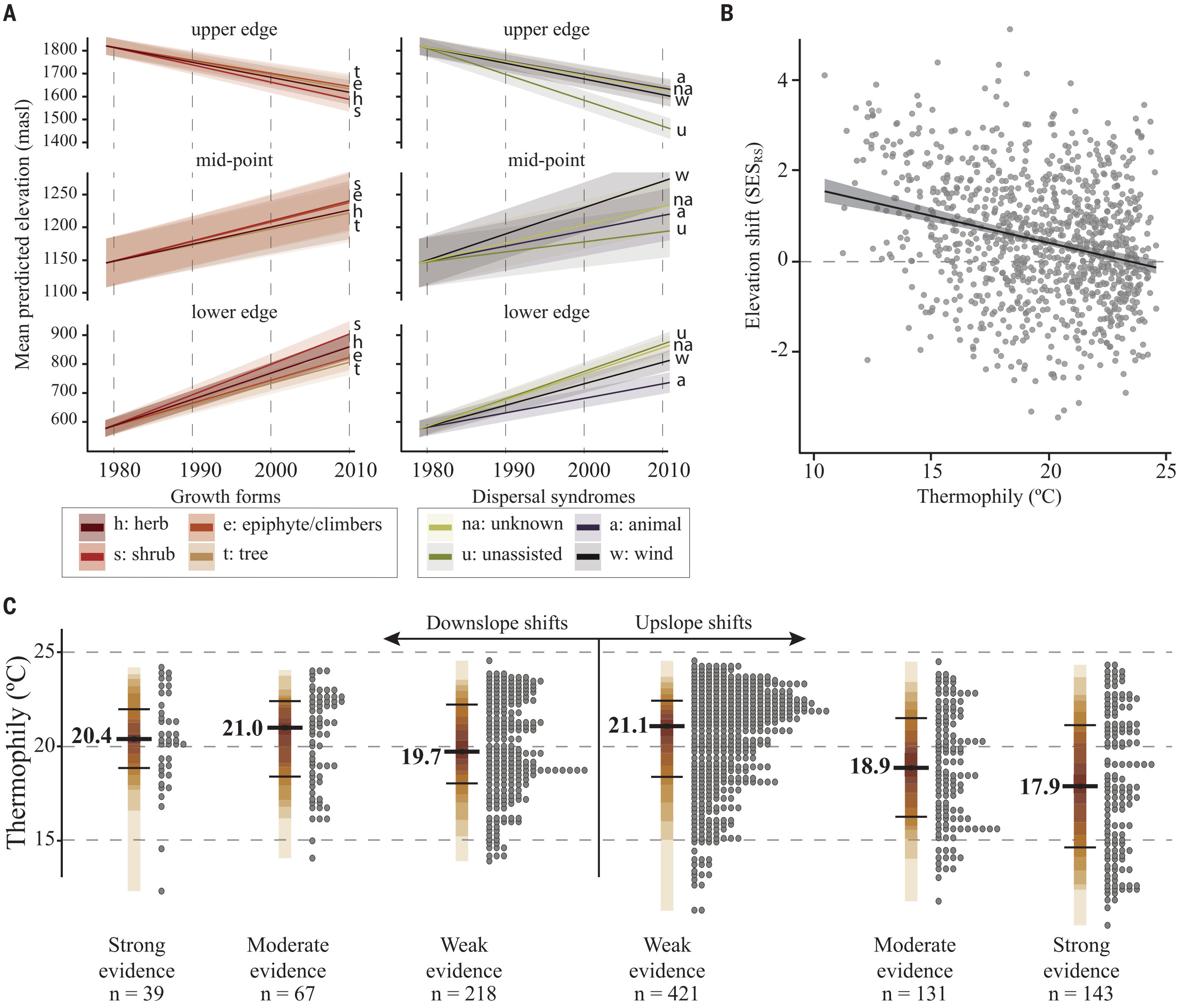

Fig. 2. Species' growth forms, dispersal syndrome, and thermal preferences (thermophily) relate to elevation shifts across 1021 vascular plant species in Mesoamerican cloud forests. (**A**) mean predicted elevation from linear mixed models of lower edges, midpoints, and upper edges as a function of time, including species' growth forms and dispersal syndromes as covariates. Colors indicate slopes predicted for different categories of growth forms and dispersal syndromes based on publicly available data. (**B**) mean predicted elevation shifts from a linear regression of species' standardized effect sizes under the RS null models (SES_{RS}) as a function of species' thermophily ($\beta_1 = -0.12$, $F_{(1,1017)} = 77.1$, $P < 0.001$). (**C**) Estimated thermophily for species categorized according to the strength of evidence for elevation midpoint shifts (SES_{RS}: strong evidence = $SES_{RS} > |1.96|$, moderate evidence = $|1.28| < SES_{RS} > |1.96|$, weak evidence $SES_{RS} < |1.28|$). Gray circles correspond to individual estimates for species, the colored vertical bars represent the density distribution of estimates, and the black vertical bars represent the 0.75, 0.5, and 0.25 quantiles. Inset numbers in bold depict the median thermophily for each category.

more frequently accompanied by retreating lower-range edges rather than by expanding upper range edges (Fig. 1D). Likewise, downslope midpoint shifts were more frequently observed in combination with retreating upper-range edges rather than with expanding lower-range edges (Fig. 1E). However, retreating lower- and upper-range edges are expected as a result of the geometric constraints of mountains (*48*, *49*). Indeed, constructing spatially bounded null models (*43*), we found that upper-range edges shifts relate negatively with elevation by chance alone (*48*), but found no relationship between lower-range edges and elevation (fig. S5). However, we observed steeper downward shifts in upper-range edges than expected by chance alone, suggesting that other factors besides mountain geometry drive these shifts.

Differences in shifts among species

Our data and models show that many species have not shifted their elevation midpoints or have even shifted downslope (*14*, *50*), in contrast to the expectations of warming-driven shifts (*11*, *17*). Great variation in species' responses is expected (*14*, *47*–*51*) and much of this variation is likely due to stochastic processes (e.g., population extinction, colonization). Nonetheless, variations in susceptibility and exposure to global change have been observed among species with different life history traits (*12*, *50*, *52*, *53*). Since species must disperse to track environmental change, we expected

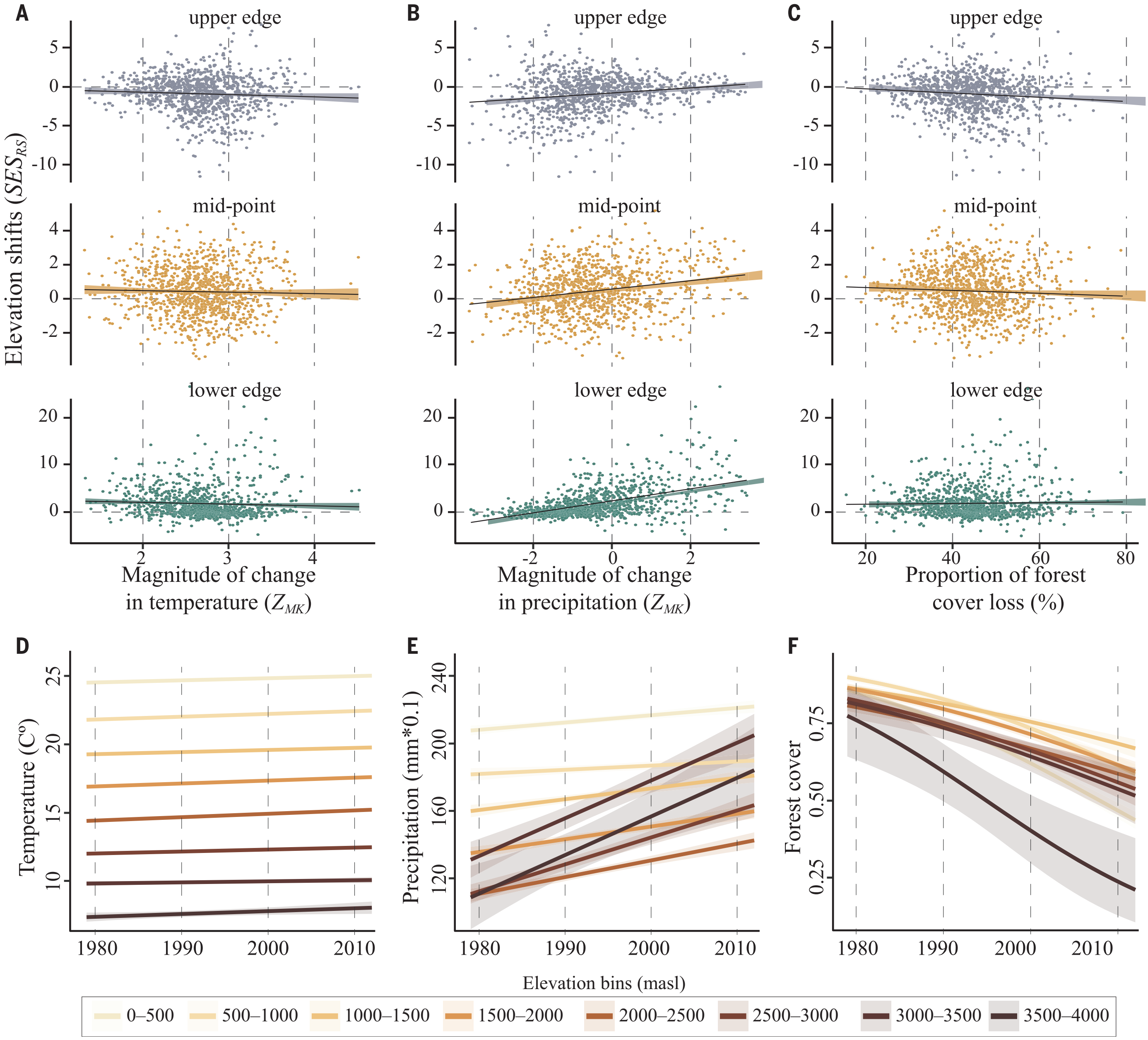

Fig. 3. Anthropogenic drivers of elevation shifts for 1021 vascular plant species in Mesoamerican cloud forests. (**A** to **C**) Mean predicted elevation shifts from a linear regression of species' standardized effect sizes under the RS null models (SES_{RS}) as a function of the magnitude of change in (A) temperature and (B) precipitation, and (C) the proportion of forest loss across Mesoamerica. Changes in temperature and precipitation were estimated using Multivariate Mann-Kendall statistics (Z_{MK}) over the period 1979 to 2010, which are indicators of the degree and consistency of climate change across the region. Forest loss was estimated and summarized for each species as the complement of the proportion of original (baseline) forest cover that remained unaffected over the period 1979 to 2010 (*43*). See table S7 for model statistics. (**D** to **F**) Mean predicted values from linear models for (A) temperature and (B) precipitation as a function of time, including elevation bins as a covariate. f, mean predicted values from a binomial model of forest cover as a function of time, including elevation bins as a covariate. In all models, elevation was defined as a categorical variable with 500-m elevation bins. Elevation is measured in meters above sea level. Model statistics are detailed in tables S4 to S7.

dispersal capacity to correlate positively with more rapid responses (for instance, higher for wind dispersed species than for other dispersal modes). However, successful establishment following dispersal depends on species' growth forms and habitat availability, possibly resulting in slower or lagged responses as a result of factors such as long generation times or low recruitment (*25*). We tested these predictions by assessing shifts among distinct growth forms (trees, shrubs, herbs, epiphytes/climbers) and dispersal syndromes (water, wind, animal, unassisted) (*43*). Despite uncertainty in species' trait data (*43*), a linear mixed model of elevation through time showed slight differences in shifts among growth forms and dispersal syndromes (Fig. 2A and tables S2 and S3): Wind-dispersed species, epiphytes, and shrubs show the steepest midpoint shifts, whereas species with unassisted dispersal (e.g., gravity) and trees show the shallowest midpoint shifts.

Idiosyncratic responses of species can also be attributed to differential sensitivities to biological, ecological, or anthropogenic factors. For example, while the range of some species and their responses may be determined primarily by temperature, the range of others may be determined more by water availability (*14*, *40*). To assess how species' thermal preferences and susceptibility associate with elevation shifts, we assessed variation in midpoint shifts as a function of species' thermophily. We used baseline temperatures from 1979 to 1989 (*43*) to estimate thermophily (i.e., hotter baseline temperatures indicate higher thermophily) and test whether less thermophilic species show more pronounced upslope shifts (*21*). Indeed, we found a negative association between species' thermophily and their observed responses (Fig. 2, B and C): The least thermophilic species had, on average, stronger signals (SES_{RS}) of upslope shifts compared with the most thermophilic species. This indicates that the thermophilization of tropical montane forests is being driven not only by advancing warm-adapted (mostly lowland) species (*20*, *21*), but also by the upslope retreat of less thermophilic montane species, irrespective of differences in thermophily among growth forms and dispersal syndromes (fig. S6).

Anthropogenic drivers of elevation shifts

Increasing temperatures and reduced water availability are considered some of the most adverse effects of climate change on cloud forests (*7*, *15*, *16*, *36*, *54*). These changes show accelerating rates over the last four decades (*1*–*3*), leading to a consistent rise in the elevation at which low-level clouds are formed, a phenomenon known as a "lifting cloud base" (*17*). A lifting cloud base reduces the amount of horizontal precipitation (fog)—a key element in cloud forests' hydrological cycle (*15*, *17*, *37*)—thereby increasing the seasonal vapor pressure deficit and causing hydric stress for many species at the lower edge of their distribution (*14*, *51*, *55*, *56*). Theoretically, this would lead to upslope shifts in species elevation ranges (*12*, *15*, *16*, *57*).

Neotropical cloud forests have experienced a lifting cloud base at rates of 0.84 to 1.64 m yr^{-1} (*17*), which translates into an upward displacement of 25.2 to 49.2 m since the 1980s. These estimates, along with general trends of warming and changing water availability across the region (*1*–*3*, *54*, *58*), align with our analyses of recent climate data. The conservative upslope midpoint shift of cloud forests (57.04 ± 7.4 m) and the mostly retreating lower-range edges fit the expectations of a lifting cloud-base driving these shifts (*7*–*9*, *15*–*17*). Linear models of climate change through time revealed regionally consistent rates of warming across elevational bins, but weaker and less consistent changes in water availability below 3000 m (Fig. 3A and tables S4 to S6). While warming has been ubiquitous across elevation, low- to mid-elevations have likely become less humid due to increasing vapor-pressure deficit and potentially less horizontal precipitation (*17*). We also assessed climate change using nonparametric multivariate Mann-Kendall statistics (*43*) (fig. S7), which can be interpreted as indicators of the magnitude and consistency of exposure to climate change (*59*). Linear models associating species' shifts with estimates of climate change showed a positive association between species' shifts (lower, mid, and upper) and changes to water availability, but not with changing temperatures (Fig. 3, B and C, and table S7). Although annual precipitation imperfectly correlates with the total water budget of cloud forests (*15*), plants are responding positively to increasing water availability in mid to high elevations. This is indicative of warming itself being less important for species' responses than changes to water availability.

The loss of forest cover diminishes the interception of horizontal precipitation by vegetation and increases the thermal instability within forests (*15*–*17*, *36*, *54*, *60*), both of which threaten species persistence in cloud forests (*15*, *34*, *36*, *37*, *52*, *53*). Our models and data showed increasing water availability in both forests and non-forested areas (*43*), but shallower rates of warming in forests compared to non-forested areas (fig. S8). By fitting a binomial model of forest cover as a function of time (*43*), we estimated a decrease in the log odds ratio of $-0.05 \pm 0.001\ \mathrm{yr}^{-1}$; this translates to a 0.28 drop in the probability of forest cover over three decades across Mesoamerica (*36*, *37*). Forest loss also showed variation across elevation, with less pronounced losses at 1000 to 2000 m (Fig. 3A and table S8). Although species may respond positively to lowland disturbances or their cessation (*50*), our data support expanding lower edges only in 30 species (2.9%). Deforestation, besides causing extirpation, likely limits the available areas for migration and occupancy (*37*, *61*, *62*) through direct and indirect impacts on species occurrence (e.g., canopy thinning, changes in microclimate) (*52*, *53*); this aligns with the observation that among dispersal syndromes, unassisted dispersal had the steeper rates of upper-range edge shifts (Fig. 2A). Indeed, upper-range-edge shifts in cloud forest plants showed a negative correlation with estimates of forest cover loss, but this is not the case for midpoint shifts or lower-range-edge shifts (Fig. 3D and table S7).

Conclusions

The general upslope elevation range shifts of cloud forest plants adds to the mounting body of evidence of contemporary shifting biodiversity in response to global change. Occurrence data provide evidence of range shifts in ~40% of the studied taxa (380 out of 1021 species), which represents a small but representative fraction of the plant diversity in Mesoamerican cloud forests. The remaining fraction of species have likely undergone little to no elevation range shifts, prompting the question of whether these would be able to adapt or acclimate to new conditions. Uncovering elevation shifts using an occurrence-based approach proves invaluable for the study of range shifts and has important implications for understanding the impacts of global change on highly diverse and vulnerable tropical montane ecosystems. The mean upslope shift we uncovered is consistent across species' functional types, supporting a scenario where at least one quarter of cloud forest plants are moving upslope, most likely in response to a lifting cloud-base and deforestation. Our data and models—along with their limitations—underscore the urgency of monitoring species' in a region known for large spatial and temporal gaps in species collection (*63*), ideally through the generation of systematic time-series surveys of tropical montane ecosystems.

REFERENCES AND NOTES

1. IPCC, Climate Change 2021: The Physical Science Basis. Contribution of Working Group I to the Sixth Assessment Report of the Intergovernmental Panel on Climate Change (Cambridge Univ. Press, 2021).
2. N. C. Pepin *et al.*, *Rev. Geophys.* **60**, e2020RG000730 (2022).
3. IPCC, Climate change 2013: The Physical Science Basis. Contribution of Working Group I to the Fifth Assessment Report of the Intergovernmental Panel on Climate Change (Cambridge Univ. Press, 2013).
4. C. D. Thomas *et al.*, *Nature* **427**, 145–148 (2004).
5. C. Parmesan, G. Yohe, *Nature* **421**, 37–42 (2003).
6. M. H. C. Neate-Clegg, S. E. I. Jones, O. Burdekin, M. Jocque, Ç. H. Şekercioğlu, *Biotropica* **50**, 805–815 (2018).
7. G. Grabherr, M. Gottfried, H. Paull, *Nature* **369**, 448 (1994).
8. M. Gottfried *et al.*, *Nat. Clim. Chang.* **2**, 111–115 (2012).
9. I. C. Chen, J. K. Hill, R. Ohlemüller, D. B. Roy, C. D. Thomas, *Science* **333**, 1024–1026 (2011).
10. K. J. Feeley, E. M. Rehm, B. Machovina, *Front. Biogeogr.* **4**, 69–84 (2012).
11. G.-R. Walther *et al.*, *Nature* **416**, 389–395 (2002).
12. R. T. Corlett, *Trends Ecol. Evol.* **26**, 606–613 (2011).
13. M. A. Rubenstein *et al.*, *Environ. Evid.* **12**, 7 (2023).
14. J. Lenoir, J. Svenning, *Ecography* **38**, 15–28 (2015).
15. P. Foster, *Earth Sci. Rev.* **55**, 73–106 (2001).
16. C. J. Still, P. N. Foster, S. H. Schneider, *Nature* **398**, 15–17 (1999).
17. S. O. Los, F. A. Street-Perrott, N. J. Loader, C. A. Froyd, *Remote Sens. Environ.* **260**, 112431 (2021).
18. S. E. Metcalfe, S. L. O'Hara, M. Caballero, S. J. Davies, *Quat. Sci. Rev.* **19**, 699–721 (2000).
19. C. Nolan *et al.*, *Science* **361**, 920–923 (2018).
20. B. Fadrique *et al.*, *Nature* **564**, 207–212 (2018).
21. K. J. Feeley, C. Bravo-Avila, B. Fadrique, T. M. Perez, D. Zuleta, *Nat. Clim. Chang.* **10**, 965–970 (2020).
22. C. M. McCain, C. F. Garfinkel, *Curr. Opin. Insect Sci.* **47**, 111–118 (2021).
23. I. C. Chen *et al.*, *Proc. Natl. Acad. Sci. U.S.A.* **106**, 1479–1483 (2009).
24. A. T. Peterson *et al.*, *Sci. Adv.* **1**, e1400071 (2015).
25. D. Jiménez-García, X. Li, A. Lira-Noriega, A. T. Peterson, *Biotropica* **53**, 798–807 (2021).
26. T. Jezkova, J. J. Wiens, *Proc. Biol. Sci.* **283**, 20162104 (2016).
27. K. J. Feeley, J. Hurtado, S. Saatchi, M. R. Silman, D. B. Clark, *Glob. Change Biol.* **19**, 3472–3480 (2013).
28. C. Román-Palacios, J. J. Wiens, *Proc. Natl. Acad. Sci. U.S.A.* **117**, 4211–4217 (2020).
29. K. L. Holzmann, R. L. Walls, J. J. Wiens, *Ecol. Lett.* **26**, 1877–1886 (2023).
30. K. J. Feeley, M. Bernal-Escobar, R. Fortier, A. T. Kullberg, *Plants* **12**, 3142 (2023).
31. E. M. Rehm, K. J. Feeley, *Ecography* **38**, 1167–1175 (2015).
32. O. L. Hajek, A. K. Knapp, A. K. Knapp, *New Phytol.* **233**, 119–125 (2022).

33. O. R. Rojas-Soto, V. Sosa, J. F. Ornelas, *Biodivers. Conserv.* **21**, 2671–2690 (2012).
34. R. Ponce-Reyes *et al*., *Nat. Clim. Chang.* **2**, 448–452 (2012).
35. J. Barlow *et al*., *Nature* **559**, 517–526 (2018).
36. D. N. Karger, M. Kessler, M. Lehnert, W. Jetz, *Nat. Ecol. Evol.* **5**, 854–862 (2021).
37. T. Toledo-Aceves, J. A. Meave, M. González-Espinosa, N. Ramírez-Marcial, *J. Environ. Manage.* **92**, 974–981 (2011).
38. M. Gual-Díaz, A. Rendón-Correa, *Agro productividad* **10**, 3–9 (2017).
39. J. L. Villaseñor, El bosque húmedo de montaña en México y sus plantas vasculares: Catálogo florístico-taxonómico. (Universidad Nacional Autónoma de México, 2010).
40. A. Ordonez, J. W. Williams, J. Svenning, *Nat. Clim. Chang.* **6**, 1104–1109 (2016).
41. M. W. Tingley, S. R. Beissinger, *Trends Ecol. Evol.* **24**, 625–633 (2009).
42. GBIF, GBIF Occurrence Download. (Global Biodiversity Information Facility, 2022); https://doi.org/10.15468/dl.544ewq.
43. Materials and Methods are available as supplementary materials.
44. K. J. Feeley *et al*., *J. Biogeogr.* **38**, 783–791 (2011).
45. K. J. Feeley, *Glob. Change Biol.* **18**, 1335–1341 (2012).
46. B. G. Freeman, Y. Song, K. J. Feeley, K. Zhu, *Ecol. Lett.* **24**, 1697–1708 (2021).
47. C. M. McCain, S. R. B. King, T. M. Szewczyk, *Ecology* **102**, e03300 (2021).
48. P. Elsen, M. Tingley, *Nat. Clim. Chang.* **5**, 772–776 (2015).
49. E. Iseli *et al*., *Nat. Ecol. Evol.* **7**, 405–413 (2023).
50. X. Zhang *et al*., *Environ. Res. Lett.* **14**, 114033 (2019).
51. K. Zu *et al*., *Sci. Total Environ.* **783**, 146896 (2021).
52. J. Lenoir, T. Hattab, G. Pierre, *Ecography* **40**, 253–266 (2017).
53. P. De Frenne *et al*., *Proc. Natl. Acad. Sci. U.S.A.* **110**, 18561–18565 (2013).
54. J. A. Guzmán, Q. H. F. Hamann, G. A. Sánchez-Azofeifa, *Ecol. Indic.* **158**, 111599 (2024).
55. C. H. Bravo-Avila, K. J. Feeley, *Plants* **12**, 2957 (2023).
56. J. Guillemot *et al*., *Glob. Change Biol.* **28**, 2622–2638 (2022).
57. K. J. Feeley, Y. Malhi, P. Zelazowski, M. R. Silman, *Glob. Change Biol.* **18**, 2636–2647 (2012).
58. A. P. Cuervo-Robayo *et al*., *PLOS ONE* **15**, e0209808 (2020).
59. C. Carroll, J. J. Lawler, D. R. Roberts, A. Hamann, *PLOS ONE* **10**, e0140486 (2015).
60. Y. Jang, S.-F. Shen, J.-Y. Juang, C. Huang, M.-H. Lo, *Geophys. Res. Lett.* **49**, 1–10 (2022).
61. M. G. Betts *et al*., *Nature* **547**, 441–444 (2017).
62. M. L. Martínez *et al*., *For. Ecol. Manage.* **258**, 1856–1863 (2009).
63. S. Ramírez-Barahona, A. P. Cuervo-Robayo, S. Magallón, *New Phytol.* **240**, 1659–1672 (2023).
64. S. Ramírez-Barahona, Upslope shifts of species in Mesoamerican montane cloud forests, version 2.1, Zenodo (2025); https://doi.org/10.5281/zenodo.11198971.

ACKNOWLEDGMENTS

We thank J.A.A. Aguirre Liguori for comments on earlier drafts and three anonymous reviewers for constructive comments. **Funding:** This work was funded by the following: Consejo Nacional de Humanidades, Ciencias y Tecnologías (CONAHCyT) grant CF-2019/263962 (S.R.-B., J.F.O., H.R.-C.). **Author contributions:** Conceptualization: S.R.-B. Methodology: S.R.-B. and K.J.F. Data curation and investigation: S.R.-B. and A.P.C.-R. Formal analyses: S.R.-B. Visualization: S.R.-B. Funding acquisition: S.R.-B. J.F.O., and H.R.-C. Writing – original draft: S.R.-B. Writing – review & editing: S.R.-B., A.P.C.-R., K.J.F., J.F.O., A.E.O.-R., A.A.V.-A., and H.R.-C. **Competing interests:** The authors declare no competing interests. **Data and materials availability:** The R code and data supporting the results in the main text are deposited in Zenodo (*64*). The raw geographic occurrence data are available through the Global Biodiversity Information Facility (*42*). **License information:**

SUPPLEMENTARY MATERIALS

science.org/doi/10.1126/science.adn2559
Materials and Methods
Figs. S1 to S8
Tables S1 to S8
References (*65*–*93*)
MDAR Reproducibility Checklist

Submitted 8 December 2023; accepted 8 January 2025
10.1126/science.adn2559

COEVOLUTION

Macroevolutionary divergence of gene expression driven by selection on protein abundance

Alexander L. Cope[1,2,3,4]†, Joshua G. Schraiber[5]†, Matt Pennell[5,6]*

The regulation of messenger RNA (mRNA) and protein abundances is well-studied, but less is known about the evolutionary processes shaping their relationship. To address this, we derived a new phylogenetic model and applied it to multispecies mammalian data. Our analyses reveal (i) strong stabilizing selection on protein abundances over macroevolutionary time, (ii) mutations affecting mRNA abundances minimally impact protein abundances, (iii) mRNA abundances evolve under selection to align with protein abundances, and (iv) mRNA abundances adapt faster than protein abundances owing to greater mutational opportunity. These conclusions are supported by comparisons of model parameters with independent functional genomic data. By decomposing mutational and selective influences on mRNA-protein dynamics, our approach provides a framework for discovering the evolutionary rules that drive divergence in gene expression.

Evolutionary divergence in gene expression is a major contributor to phenotypic divergence (*1*). Accordingly, many studies investigate how evolutionary processes shape patterns of mRNA abundances (*2*–*6*). However, mRNA abundances provide an incomplete picture of gene expression evolution. Studies across of taxa found differences in mRNA abundances need not imply differences in protein abundances (*7*–*11*). Indeed, a fundamental question in molecular biology is how various regulators and molecular mechanisms act in concert to produce the necessary amount of protein of a given gene for a cell to function (*12*, *13*). Despite our improved understanding of the molecular basis of this regulation, we do not fully understand how and why these regulatory mechanisms themselves evolve.

To understand the coevolutionary dynamics of mRNA and protein abundances, we must explain patterns observed across evolutionary timescales. Firstly, steady-state mRNA and protein abundances are tightly correlated within organisms, but this correlation varies among individuals and species (*14*, *15*). Secondly, genetic variants associated with changes in expression of mRNA (expression quantitative trait loci, eQTLs) or proteins (protein quantitative trait loci, pQTLs) are often distinct (*16*–*18*). Thirdly, comparative studies revealed that protein abundances are generally more conserved than mRNA abundances (*7*, *8*, *19*). Fourthly, evolutionary changes at one level of regulation may be offset or buffered by changes at another level of regulation over evolutionary time, resulting in little change in protein abundance (*9*–*11*). This could be due to offsetting changes in transcription and translation (*9*) or between transcription and posttranslational regulation (*10*, *16*). The mechanisms involved in evolutionary buffering may be distinct from the buffering mechanisms that keep protein levels relatively stable in a cell (*20*–*22*).

One explanation of these observations is "compensatory evolution" in which protein abundances, being closer to the phenotype than mRNA abundances, are generally under stabilizing selection. Thus, regulatory mutations that push a protein away from its optimum can fix in the population if they are compensated by other types of regulatory mutations that move the protein abundances back. This model implicitly predicts mRNA abundances should show interspecific divergences similar to neutrality (*23*), inconsistent with abundant comparative evidence that mRNA abundances are constrained (*6*, *24*, *25*). Moreover, as a verbal model, compensatory evolution neither makes any predictions for how much mRNA and protein abundances should diverge from one another nor the relative importance of various evolutionary or regulatory processes in shaping patterns of gene expression.

To make quantitative predictions, we derived a set of novel phylogenetic models rooted in first principles of evolutionary and molecular biology and fit this model to comparative data. By comparing the fit of alternative models using matched transcriptome and proteome datasets from mammalian skin samples taken from 10 species and by examining the values of estimated parameters, our model revealed the sources of divergence in gene expression. We tested our interpretation of the model using functional genomic data from species not among the 10 that we analyzed. These data provide critical out-of-sample tests of our model.

---

[1]Department of Biological Sciences, Vanderbilt University, Nashville, TN, USA. [2]Department of Genetics, Rutgers University, New Brunswick, NJ, USA. [3]Human Genetics Institute of New Jersey, Rutgers University, New Brunswick, NJ, USA. [4]Robert Wood Johnson Medical School, Rutgers University, New Brunswick, NJ, USA. [5]Department of Quantitative and Computational Biology, University of Southern California, Los Angeles, CA, USA. [6]Department of Computational Biology, Cornell University, Ithaca, CA, USA.
***Corresponding author. Email: mpennell@cornell.edu**
†These authors contributed equally to this work.

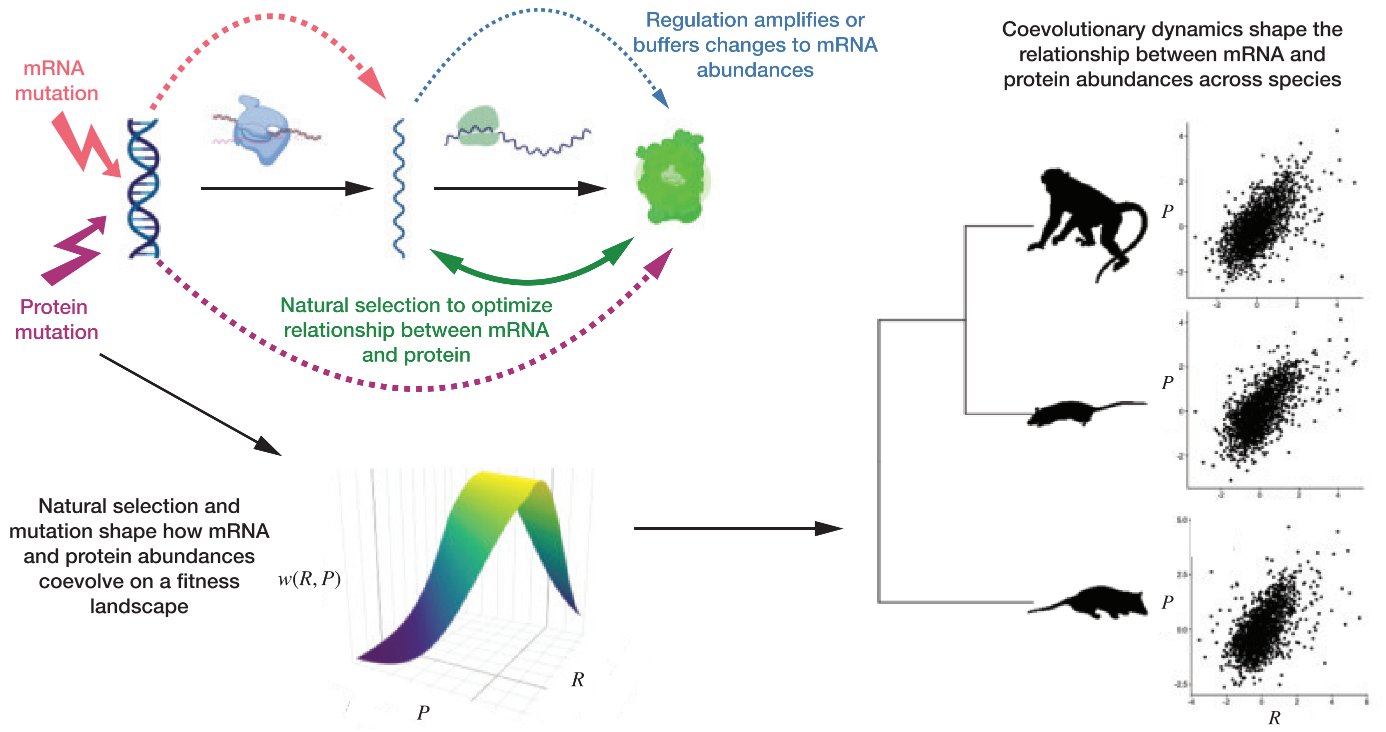

Fig. 1. Conceptual framework of phylogenetic model. Scatter plots show relationship between mRNA and protein abundances for *Macaca mulatta*, *Rattus norvegicus*, and *Monodelphis domestica* (*19*). $w(R,P)$ represents the joint fitness of a given mRNA and protein abundance. Icons for DNA, RNA polymerase, mRNA, ribosome, and protein were obtained from BioRender.com. Images of species were taken from Phylopic (https://www.phylopic.org/).

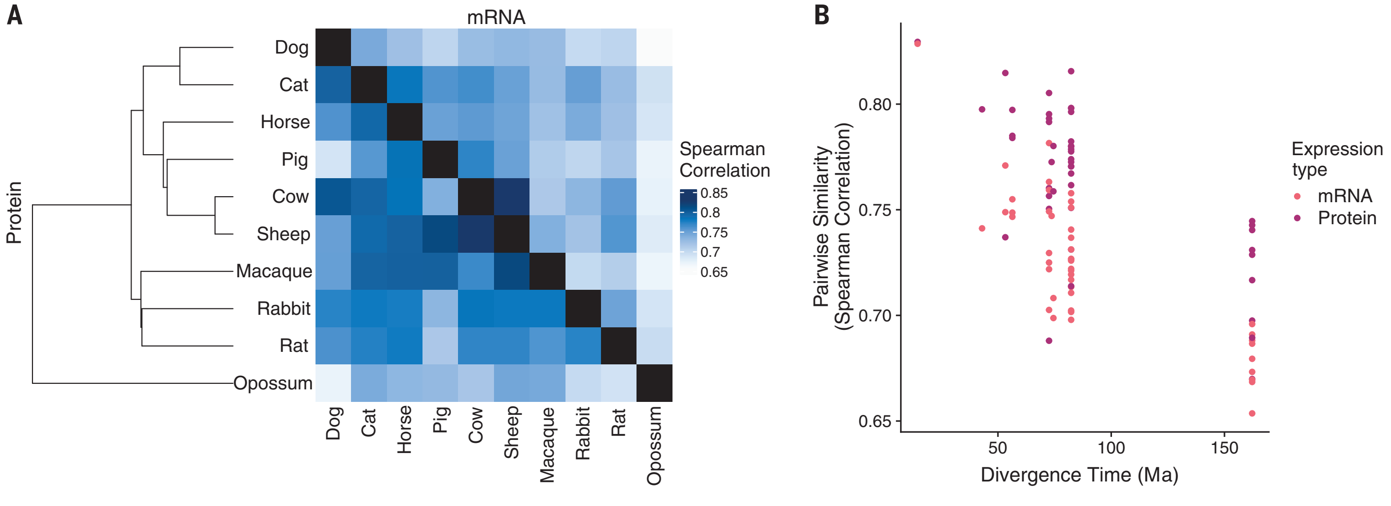

Fig. 2. Comparison of mRNA and protein abundances for 1641 genes across 10 mammals. (**A**) Heatmap showing across-species pairwise comparisons (measured as the Spearman rank correlation) of mRNA (upper triangle) and protein abundances (lower triangle). The phylogenetic tree of the 10 species is included on the lower triangle. (**B**) Pairwise correlations of mRNA and protein abundance as a function of species divergence time. Ma, million years ago.

A macroevolutionary model of mRNA and protein abundance coevolution

Our framework is founded on a mutational model with two possible types of mutations, which are then filtered through natural selection (Fig. 1). Firstly, there are "mRNA mutations" that influence the steady-state mRNA abundance and, in turn, impact the downstream protein steady-state abundances (e.g., mutations that influence transcription or mRNA degradation rates). These mRNA mutations potentially create a mutational coupling between mRNA and protein abundances. Secondly, there are "protein mutations" that impact protein abundance (e.g., mutations that influence protein degradation) but do not directly influence steady-state mRNA abundances in our model.

To model the fitness of given mRNA and protein abundances, we imposed a fitness cost to having mRNA and protein abundances that are mismatched relative to the amount of mRNA

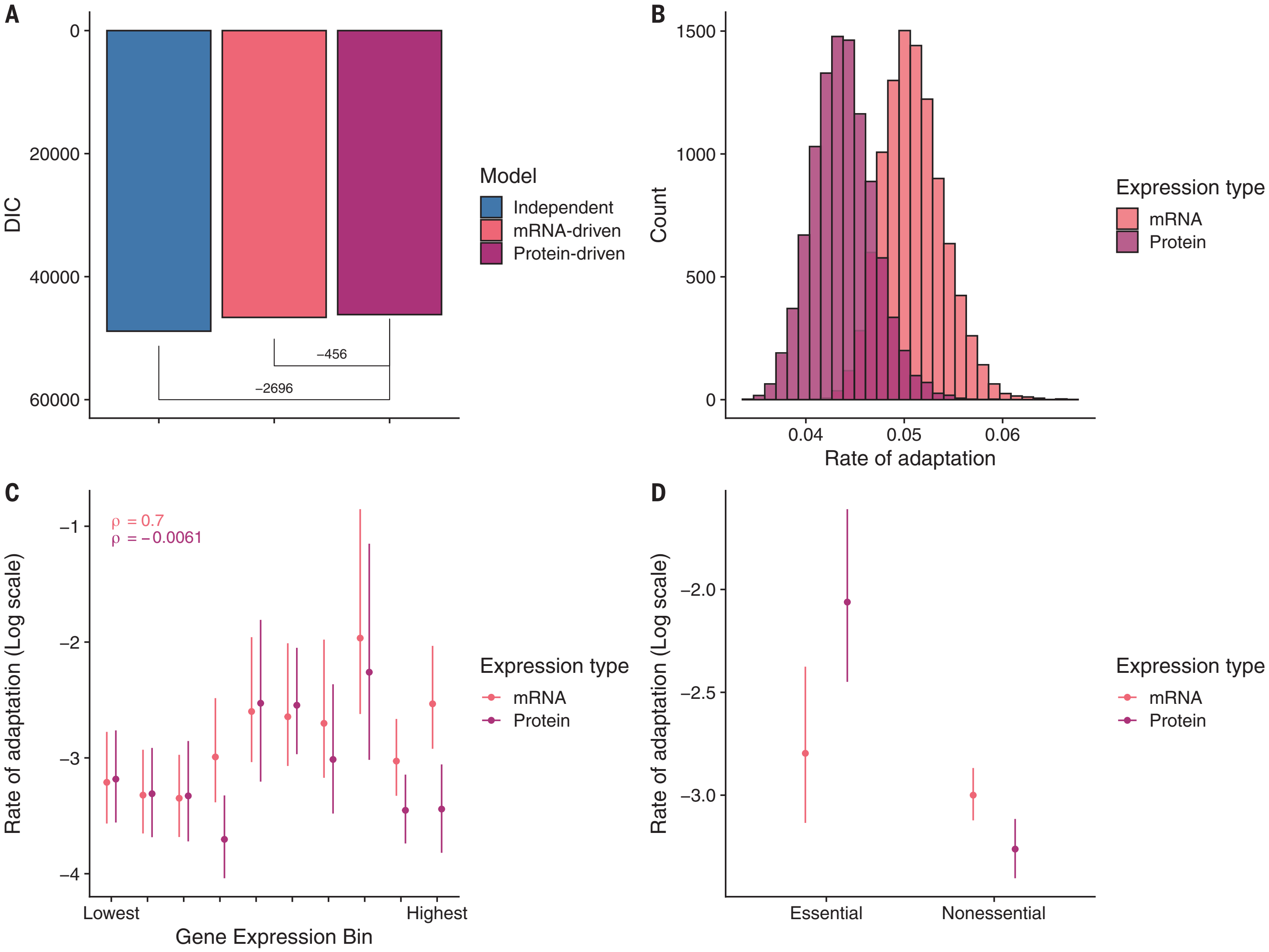

Fig. 3. Comparisons of models and posterior distributions of model parameters from protein-driven model fit. (**A**) Comparison of DIC values for protein-driven, mRNA-driven, and independent models. The protein-driven model has the lowest DIC value, indicating that it is the best of the three models. Brackets indicate the ΔDIC values relative to the protein-driven model. (**B**) mRNA and protein abundance rate of adaptation parameters α_R (mRNA) and α_P (protein), respectively (10,000 posterior samples each). (**C**) Rate of adaptation parameters α_R and α_P across gene expression decile bins (164 to 165 genes per bin). Deciles were determined by using the integrated protein abundance data for humans from PaxDB. Spearman rank correlations are reported. Error bars represent 95% CIs. (**D**) Rate of adaptation parameters across "essential" (264 genes) and "nonessential" (1377 genes) genes in human in vitro cell line, as previously described (*38*). Error bars represent 95% CIs.

required to produce a given amount of protein (*26*, *27*). To capture this, we modeled the optimal mRNA abundance, $\hat{R}$, as a linear function of protein abundance, $\hat{R} = \theta_R + a_R P$, and the optimal protein abundance, $\hat{P}$, as a linear function of mRNA abundance, $\hat{P} = \theta_P + a_P R$. The intercept parameters, θ_R and θ_P, are the optimum abundances of mRNA and protein abundances in the absence of any fitness consequence of having incorrectly tuned mRNA and protein abundances. The slope parameters, a_R and a_P, capture the optimal amount of mRNA required per unit protein and the optimal amount of protein produced per unit mRNA, respectively. Thus, they create an evolutionary coupling between mRNA and protein expression in addition to the mutational coupling arising because mRNA mutations can also impact protein abundances. We incorporated these mutational and fitness models into a strong selection, weak mutation framework (*28*). The impact of cosegregating compensatory mutations can be modeled using an "effective effect size" [section 1.3.5 (*29*)] (*30*). From this, we derived a pair of coupled stochastic differential equations describing the joint evolution of steady-state mRNA and protein abundances subject to mutation and selection. These stochastic differential equations capture the cumulative effects of mutation, selection, and substitution over millions of years.

We found that the compound parameters describing the combined effects of mutation, selection, and drift are important. Firstly, α_R describes the rate of adaptation of the mRNA. Secondly, α_P describes the rate of adaptation of the protein. In both cases, the rate of adaptation is a function of mutational target size, mutational effect size, and the strength of selection [section 1.3 (*29*)]. The downstream effect of mRNA mutations on protein abundance is quantified by the parameter *c*, which reflects the immediate impact of a change in mRNA to protein abundances owing to downstream regulatory mechanisms that buffer or amplify changes in mRNA abundances (*12*, *13*).

The most general model in which all parameters can take arbitrary values is both intractable and difficult to interpret. We focused on three limiting cases of our general model. These cases represent different ends of the spectrum of evolutionary scenarios.

In the first model, we assume that mRNA mutations play an important role on macroevolutionary timescales and that natural selection

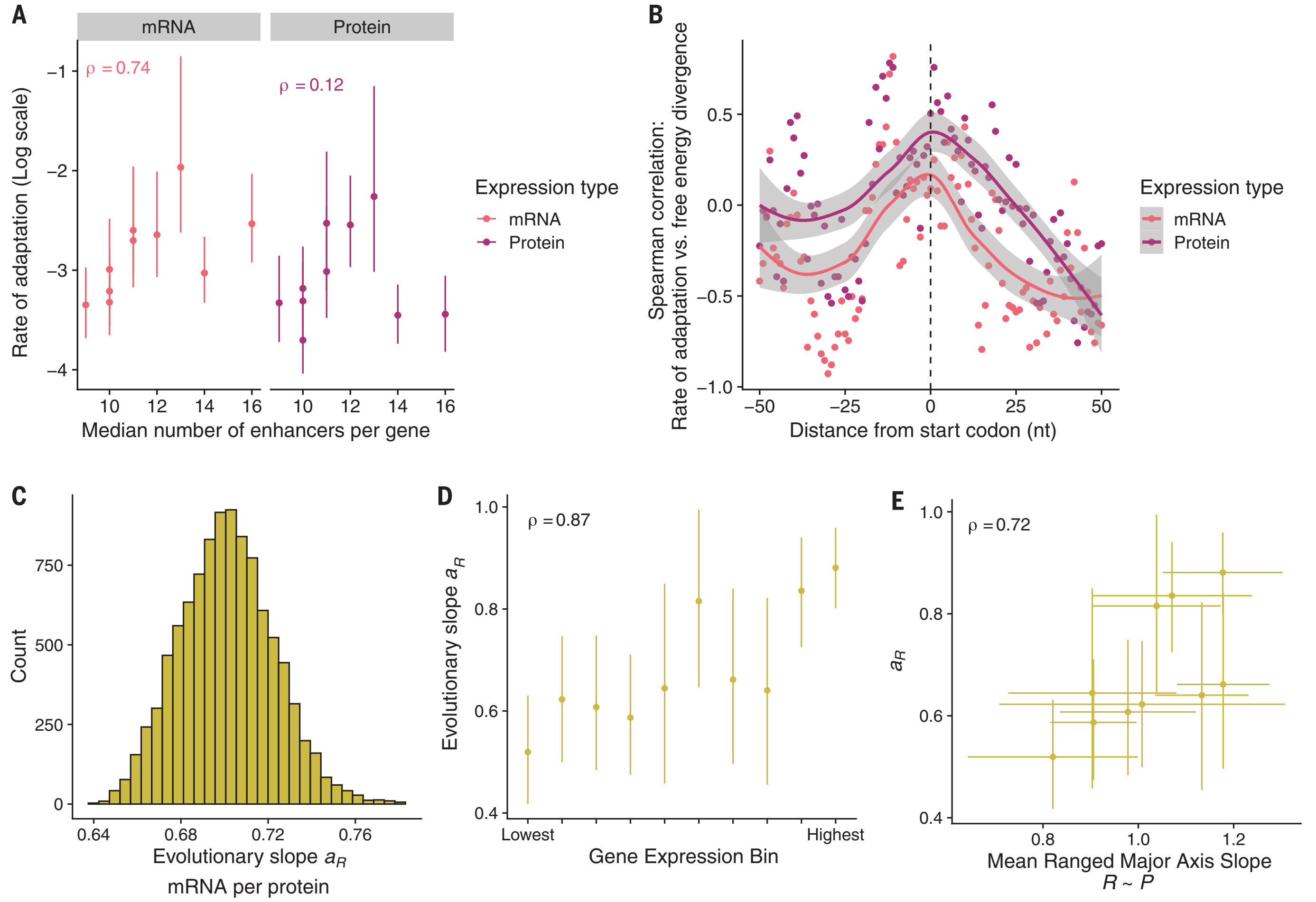

Fig. 4. Validation of model parameter estimates using out-of-sample human functional genomics data. Fits were based on protein-driven model. All error bars represent 95% CIs. Spearman rank correlations are reported. (**A**) The relationship between the median number of enhancers per gene and the rate of adaptation for mRNA and protein abundances. Rate of adaptation estimates are taken from the decile bins based on gene expression. The number of genes per bin with predicted enhancers ranges from 146 to 158 genes. (**B**) Correlation between divergence in mRNA secondary structure (specifically, free energy) near the start codon for human and mouse genes and the rates of adaptation (62 to 87 genes per bin). nt, nucleotide. (**C**) Posterior distribution (10,000 samples) of the evolutionary slope parameter a_R. (**D**) Variation in a_R across gene expression decile bins (164 to 165 genes per bin). (**E**) Comparison of posterior mean for a_R (95% CI) with the across-species mean reduced major axis (RMA) slopes (±1 SD) estimating the relationship between protein and mRNA abundances. Note that RMA slopes were calculated with mRNA (R) as the "dependent" variable.

acting on mRNA abundances is substantially stronger than natural selection acting on those of proteins. Thus, protein abundances are determined by mRNA abundances. We refer to this model as "mRNA-driven evolution."

In the second model, mRNA mutations have a negligible impact on evolutionary changes to protein abundances, with evolutionary changes to mRNA abundances selected to reach the appropriate ratio relative to protein abundances. Here, we set $c = 0$, so that mRNA mutations are fully buffered on macroevolutionary timescales. We refer to this model as "protein-driven evolution."

As a null model, we considered uncoupled evolutionary dynamics of mRNA and protein abundances. We refer to this model as "independent evolution." Under all three models, mRNA and protein abundances may be correlated within and between species; thus, to decide between them, we must test phylogenetic hypotheses rather than compute correlations between mRNA and protein abundances. All models are coupled Ornstein-Uhlenbeck (OU) processes (*31*). Univariate OU processes are widely applied to describe the univariate evolution of mRNA abundances along a phylogeny (*6*, *24*); in this work, we apply coupled OU processes to study gene expression evolution at two different levels simultaneously. To fit our models using a Bayesian approach, we developed a custom Markov chain Monte Carlo (MCMC) machinery using the R package LaplacesDemon (*32*). By using simulations [sections 1.5 and 2.1 (*29*)], we validated our estimation procedure under a range of conditions and found that standard model selection techniques (*33*) can identify the generating scenario. A full derivation of the model can be found in section 1.3 of (*29*).

Evolution of gene expression in mammalian fibroblast skin tissue is determined by selection on protein abundance

We analyzed a recent dataset (*19*) of mRNA and protein abundances measured by RNA sequencing (RNA-seq) and liquid chromatography coupled with data-independent acquisition tandem mass spectrometry, respectively, for 10 species of mammalian skin samples [section 1.2 (*29*)]. These were all measured by the same researchers and by using standardized experimental protocols to minimize the impact of technical variation. The phylogenetic tree [section 1.1 (*29*)] and the correlations between mRNA and protein abundances are shown in Fig. 2A; the pairwise similarity as a function of divergence time is shown in Fig. 2B.

Ten species is a large sample size for paired transcriptomic and proteomic data, but it is small relative to the number of parameters we sought to estimate. To overcome this limitation, we assumed that the steady-state mRNA and protein abundances for each of the 1641 orthologous genes in the dataset were an independent outcome of the same coevolutionary process. As such, we estimated distinct steady-state optima for mRNA and protein abundances of each gene, both functions of the gene-specific parameters θ_R and θ_P; all other parameters were assumed to be equal across genes. Despite variation in the coevolutionary dynamics across genes, simulations revealed our model parameter estimates closely match the mean values across genes [sections 1.5.2 and 2.1 (*29*)].

We found overwhelming support for the protein-driven evolution model (Fig. 3A): the deviance information criterion (DIC) value for the protein-driven model was 456 DIC units lower than the next-best model. Thus, we inferred that mRNA mutations have a negligible impact on protein abundances over long evolutionary timescales in mammalian fibroblasts skin tissue {i.e., c is close to 0; even under the disfavored mRNA-driven model, we estimate c to be 0 [95% credible interval (CI): –0.102 to 0.081]}. Numerous lines of empirical evidence (*12*, *13*, *16*–*18*) suggest that changes to mRNA abundance can be buffered by posttranscriptional mechanisms, although the generality of these mechanisms are poorly understood; our results suggest that mechanistic buffering also influences the macroevolutionary dynamics of steady-state expression. Moreover, we emphasize that our model represents the cumulative effect of mutation and natural selection over millions of years and is compatible with the observation that mRNA abundances can causally impact protein abundances in experiments.

mRNA abundances adapt more rapidly than protein abundances

Examining the parameter estimates from the protein-driven model, we found that the two parameters describing the rate of adaptation, α_R and α_P, have posterior means (on the natural scale) of 0.051 (95% CI: 0.045 to 0.057) and 0.044 (95% CI: 0.038 to 0.050), respectively (Fig. 3B). These estimates correspond to a mean "phylogenetic half-life" (*34*) of 13.651 million years (Myr) (95% CI: 11.994 to 15.177 Myr) for the mRNA abundances and 15.915 Myr (95% CI: 13.753 to 18.132 Myr) for the protein abundances. This means that it takes longer for the proteins to adapt to changes in their optima than it does for mRNA, consistent with previous observations that protein abundances are more similar between species than mRNA abundances (*7*, *8*, *19*).

Multiple lines of evidence indicate natural selection is stronger on highly expressed genes (*35*, *36*). If our model is capturing the proposed evolutionary processes, then adaptation parameters α_R and α_P would be correlated with expression level. To test this prediction, we binned genes into deciles based on an integrated measure of protein abundances in humans taken from PaxDB 5.0 (*37*). We then refit the preferred protein-driven model to the binned data. We found that more highly expressed genes tended to have a higher rate of adaptation for both mRNA and protein abundances, except for the highest expression categories in the case of proteins in which the direction of the trend reversed (Fig. 3C) [section 2.3.2 (*29*)]. We did not calculate P values for these correlations because they are influenced by bin size; we divided the data into gene expression deciles to ensure that we could still estimate parameters within each set of binned genes.

We further validated our inferences by testing whether genes whose functional roles make them likely to be under strong purifying selection indeed have stronger selection terms estimated from our model (Fig. 3D). By using annotations from (*38*), we found that, as predicted by our protein-driven model, the rate of adaptation for protein abundances was significantly higher in essential (α_P = 0.130, 95% CI: 0.0789 to 0.186) versus nonessential genes (α_P = 0.038, 95% CI: 0.033 to 0.044). There was no difference between the selection on mRNA between the essential (α_R = 0.062, 95% CI: 0.040 to 0.087) and nonessential genes (α_R = 0.050, 95% CI: 0.044 to 0.057), consistent with our inference that natural selection on protein levels is the primary driver of gene expression evolution. We also found that the rate of adaptation of haploinsufficient genes is slower than background, which may be caused by their intolerance to mutation [section 2.3.1, in (*29*)].

Genetic architecture is predictive of macroevolutionary trends

An important open question is the extent to which microevolutionary processes shape evolutionary outcomes on long timescales, with many suggesting that there may be only a minimal correlation (*39*). To answer this question using mRNA and protein abundances, we made predictions for how molecular features and functional genomic measurements should relate to our inferred evolutionary parameters based on our modeling framework.

Firstly, we expect the rate of adaptation to scale with mutational input. Although it is difficult to quantify mutational input to mRNA and protein abundances, we used several proxies to assess the predictions of our model. We hypothesized the number of cis-regulatory elements regulating transcription is correlated with mutational target size for mRNA abundances but not protein abundances. Using the EnhancerAtlas2.0 database (*40*), we estimated the number of active enhancers per gene in human keratinocyte cells, the primary cell type found in the epidermis. To control for confounding owing to the absolute value of gene expression, we calculated the median number of enhancers per gene for each expression bin and compared them with the estimated parameter value of each bin. Consistent with our prediction, genes with more enhancers in human keratinocyte cells showed a higher rate of adaptation at the mRNA level (Spearman rank correlation coefficient ρ = 0.74) but not generally at the protein level (ρ = 0.12) (Fig. 4A). Similar results were obtained by using enhancer counts from mice and flies [section 2.3.3 (*29*)], suggesting that the same evolutionary principles apply over longer evolutionary distances. We performed a similar analysis using human eQTL absolute effect sizes estimated from the Gene-Tissue Expression database (*41*) as a proxy for mutational effect size. We found a negative correlation between the eQTL effect sizes and the rates of adaptation [section 2.3.4 (*29*)]. We speculate that this is because eQTLs need to be both common enough and have large enough effects to be detected using genome-wide association study methods. Thus, eQTLs for genes under strong selection would be predicted to have small effects, whereas large-effect eQTLs would preferentially impact genes under weak selection (*42*).

We next examined the mutations that we expect to impact protein abundances but not mRNA abundances. Cells can regulate protein abundance independently of mRNA abundance by tuning mRNA translation, particularly the ability of ribosomes to initiate translation (*43*). Initiation efficiency is regulated by numerous transcript features, including mRNA secondary structure near the coding sequence (CDS) start codon and properties of the 5′ untranslated region (5′UTR). By using estimated mRNA secondary structure ensemble free energies near the CDS start codon for human and mouse, we found that divergence in secondary structure is positively associated with higher rates of adaptation for protein but not mRNA abundance (Fig. 4B) [section 2.3.5 (*29*)]. The correlation between the rate of protein abundance adaptation and divergence of mRNA secondary structure peaks near the start codon, consistent with changes to translation initiation efficiency significantly altering protein abundances (*44*). Furthermore, we found that human genes with less-conserved 5′UTRs [based on the mean phastCons scores comparing sequence alignments to 99 other vertebrates (*45*)] showed higher rates of adaptation in protein abundances (ρ = –0.61) [section 2.3.5 (*29*)]. Our results indicate that the evolution of regulators of mRNA translation plays a substantial role in shaping the evolution of steady-state protein abundances independent of mRNA abundances. Although changes to mRNA translation can also alter mRNA degradation rates and hence act as mutational input to mRNA abundance (*46–48*), our results suggest that changes to mRNA translation generally have a weaker effect on the evolution of steady-state mRNA abundances and are a stronger driver of protein abundance evolution. Further work is needed to better decouple the impact of mRNA translation on mRNA versus protein abundances.

Strong selection to maintain correlations between mRNA and protein abundances

The parameter a_R quantifies the evolutionary relationship between mRNA and protein abundances. We estimated a_R to be 0.701 (95% CI: 0.661 to 0.744; Fig. 4C). Because $a_R < 1$ indicates that an increase in protein abundance by one unit results in an increase in mRNA abundance by less than one unit, the optimal relationship between mRNA and protein abundances is one in which translation acts to amplify steady-state mRNA abundance. Thus, when protein abundances shift due to mutation, drift, and selection, mRNA abundances are selected to shift in the same direction but not to the same extent. When stratifying genes by expression level, we see that a_R increases as a function of gene expression, approaching but not reaching 1 (ρ = 0.87; Fig. 4D). This suggests high expression genes require less amplification of mRNA abundances compared to low expression genes.

Because a_R is shared across genes, it is possible to relate a_R to within-species biophysical models for describing the general relationship between mRNA and protein abundances across genes. Our finding that the optimal relationship between mRNA and protein abundances is one in which translation amplifies mRNA abundances is consistent with previous work examining a biophysical model of reduced amplification for highly expressed genes (*15*). Applying this model to the mRNA and protein data for each species [sections 1.7.4 and 2.3.6 (*29*)], we found a positive correlation between the relationship of per unit changes in mRNA and protein and our estimates of a_R on a per-bin basis (ρ = 0.72; Fig. 4E), supporting our interpretation of a_R as quantifying the amplification of mRNA abundances, including decreasing amplification for highly expressed genes.

To further determine whether our model captures independent biophysical measurements, we used translation efficiency (TE), which quantifies the biophysical relationship between mRNA levels and protein production and is typically estimated by combining ribosome profiling and RNA-seq data to estimate the number of actively translating ribosomes per mRNA (*49*). We found that our per-bin median estimates of the optimum TE (estimated as the ratio of the optimum protein to the optimum mRNA on the logarithmic scale) are highly correlated with empirical TEs estimated from independent human ribosome profiling and RNA-seq data [ρ = 0.95; section 2.3.6 (*29*)] (*50*), showing that our model captures downstream regulatory outcomes. Furthermore, we found that the lengths of 5′UTRs in humans and mice are negatively correlated with a_R [section 2.3.6 (*29*)], indicating that genes with more opportunity for posttranscriptional control are amplified more heavily.

Conclusions

Numerous studies have used phylogenetic models to investigate the evolutionary processes that shaped variation in mRNA abundances among species (*6*). In this work, we infer the processes that shaped the coevolution between mRNA and protein abundances. Doing so required us to derive mechanistic models from first principles to capture the biophysical and evolutionary relationships between these quantities. To assess the generality of our results, there is a need to collect paired mRNA and protein abundance across multiple species and multiple tissues. We suggest that our general modeling framework can serve as the foundation for further investigations into the role of complex processes in shaping patterns of gene expression.

We show that the parameter estimates from these macroevolutionary models are consistent with within-species functional genomic information. In evolutionary biology, it has often been difficult to map the parameters estimated from macroevolutionary to microevolutionary processes (*39*). Our findings imply that, at least for gene regulation, we may be able to understand the general rules that shape evolutionary dynamics across timescales.

REFERENCES AND NOTES

1. G. A. Wray, *Nat. Rev. Genet.* **8**, 206–216 (2007).
2. P. Khaitovich *et al.*, *PLOS Biol.* **2**, E132 (2004).
3. B. Lemos, C. D. Meiklejohn, M. Cáceres, D. L. Hartl, *Evolution* **59**, 126–137 (2005).
4. R. Blekhman, A. Oshlack, A. E. Chabot, G. K. Smyth, Y. Gilad, *PLOS Genet.* **4**, e1000271 (2008).
5. M. S. Hill, P. Vande Zande, P. J. Wittkopp, *Nat. Rev. Genet.* **22**, 203–215 (2021).
6. P. D. Price *et al.*, *Nat. Ecol. Evol.* **6**, 1035–1045 (2022).
7. J. M. Laurent *et al.*, *Proteomics* **10**, 4209–4212 (2010).
8. Z. Khan *et al.*, *Science* **342**, 1100–1104 (2013).
9. C. G. Artieri, H. B. Fraser, *Genome Res.* **24**, 411–421 (2014).
10. S. H. Wang, J. Hsiao, Z. Khan, J. K. Pritchard, *Genome Biol.* **19**, 83 (2018).
11. Z. Y. Wang *et al.*, *Nature* **588**, 642–647 (2020).
12. Y. Liu, A. Beyer, R. Aebersold, *Cell* **165**, 535–550 (2016).
13. C. Buccitelli, M. Selbach, *Nat. Rev. Genet.* **21**, 630–644 (2020).
14. J. J. Li, P. J. Bickel, M. D. Biggin, *PeerJ* **2014**, e270 (2014).
15. G. Csárdi, A. Franks, D. S. Choi, E. M. Airoldi, D. A. Drummond, *PLOS Genet.* **11**, e1005206 (2015).
16. A. Battle *et al.*, *Science* **347**, 664–667 (2015).
17. J. M. Chick *et al.*, *Nature* **534**, 500–505 (2016).
18. E. M. Teyssonnière *et al.*, *Proc. Natl. Acad. Sci. U.S.A.* **121**, e2319211121 (2024).
19. Q. Ba *et al.*, *Sci. Adv.* **8**, eabn0756 (2022).
20. A. Raj, S. A. Rifkin, E. Andersen, A. van Oudenaarden, *Nature* **463**, 913–918 (2010).
21. J. M. Schmiedel *et al.*, *Science* **348**, 128–132 (2015).
22. G. Kustatscher, P. Grabowski, J. Rappsilber, *Mol. Syst. Biol.* **13**, 937 (2017).
23. D. Jiang, A. L. Cope, J. Zhang, M. Pennell, *Mol. Biol. Evol.* **40**, msad169 (2023).
24. J. Chen *et al.*, *Genome Res.* **29**, 53–63 (2019).
25. J. R. Dimayacyac, S. Wu, D. Jiang, M. Pennell, *Genome Biol. Evol.* **15**, evad211 (2023).
26. A. Wagner, *Mol. Biol. Evol.* **22**, 1365–1374 (2005).
27. J. Hausser, A. Mayo, L. Keren, U. Alon, *Nat. Commun.* **10**, 68 (2019).
28. J. H. Gillespie, *Am. Nat.* **121**, 691–708 (1983).
29. See supplementary materials.
30. S. Negm, C. Veller, The effect of long-range linkage disequilibrium on allele-frequency dynamics under stabilizing selection, bioRxiv 2024.06.27.601075 [Preprint] (2024); https://doi.org/10.1101/2024.06.27.601075.
31. K. Bartoszek, J. Pienaar, P. Mostad, S. Andersson, T. F. Hansen, *J. Theor. Biol.* **314**, 204–215 (2012).
32. L. L. C. Statisticat, LaplacesDemon: Complete Environment for Bayesian Inference (2021); https://cran.r-project.org/web/packages/LaplacesDemon/index.html.
33. D. J. Spiegelhalter, N. G. Best, B. P. Carlin, A. Van Der Linde, *J. R. Stat. Soc. Series B Stat. Methodol.* **64**, 583–639 (2002).
34. T. F. Hansen, *Evolution* **51**, 1341–1351 (1997).
35. D. A. Drummond, C. O. Wilke, *Cell* **134**, 341–352 (2008).
36. A. L. Cope, M. A. Gilchrist, *BMC Genomics* **23**, 408 (2022).
37. Q. Huang, D. Szklarczyk, M. Wang, M. Simonovic, C. von Mering, *Mol. Cell. Proteomics* **22**, 100640 (2023).
38. T. Zeng, J. P. Spence, H. Mostafavi, J. K. Pritchard, *Nat. Genet.* **56**, 1632–1643 (2024).
39. J. Rolland *et al.*, *Nat. Ecol. Evol.* **7**, 1181–1193 (2023).
40. T. Gao, J. Qian, *Nucleic Acids Res.* **48**, D58–D64 (2020).
41. F. Aguet *et al.*, *Science* **369**, 1318–1330 (2020).
42. H. Mostafavi, J. P. Spence, S. Naqvi, J. K. Pritchard, *Nat. Genet.* **55**, 1866–1875 (2023).
43. P. Shah, Y. Ding, M. Niemczyk, G. Kudla, J. B. Plotkin, *Cell* **153**, 1589–1601 (2013).
44. G. Kudla, A. W. Murray, D. Tollervey, J. B. Plotkin, *Science* **324**, 255–258 (2009).
45. N. Wieder *et al.*, *Genome Biol.* **25**, 111 (2024).
46. L. Y. Chan, C. F. Mugler, S. Heinrich, P. Vallotton, K. Weis, *eLife* **7**, e32536 (2018).
47. R. Buschauer *et al.*, *Science* **368**, eaay6912 (2020).
48. A. A. Bicknell *et al.*, *Cell Rep.* **43**, 114098 (2024).
49. N. T. Ingolia, S. Ghaemmaghami, J. R. S. Newman, J. S. Weissman, *Science* **324**, 218–223 (2009).
50. S. P. Chothani *et al.*, *Mol. Cell* **82**, 2885–2899.e8 (2022).
51. A. L. Cope, J. G. Schraiber, M. Pennell, applied-phylo-lab/rna-protein-coevolution: processed data and code, Zenodo (2025); https://doi.org/10.5281/zenodo.14893738.

ACKNOWLEDGMENTS

We thank R. Jiang, Q. Wang, M. Guzman, and R. Brem for comments on the manuscript as well as P. Shah and the Pennell, Edge, Mooney, and Rokas lab groups for helpful discussion of this work. F. Machado and J. Uyeda provided advice on our implementation of the MCMC. T. Zheng, J. Spence, H. Mostafavi, and J. Pritchard provided curated data on gene function. **Funding:** This work was supported by the NIH-funded Rutgers INSPIRE IRACDA Postdoctoral Program (grant no. GM093854 to A.L.C.) and NIH grant R35GM151348 to M.P. **Author contributions:** A.L.C., J.G.S., and M.P. conceptualized the project. A.L.C. and J.G.S. developed and implemented the model. A.L.C., J.G.S., and M.P. designed the computational experiments. A.L.C. and J.G.S. performed the computational analyses. A.L.C., J.G.S., and M.P. wrote and edited the manuscript. **Competing interests:** The authors declare that they have no competing interests. **Data and materials availability:** No new data were generated for this study. The publicly available data used in this study are available through the references provided in this manuscript. Processed data, R notebooks, and R scripts for recreating our analyses are deposited in GitHub, available through Zenodo (*51*).

SUPPLEMENTARY MATERIALS

science.org/doi/10.1126/science.ads2658
Materials and Methods
Supplementary Text
Figs. S1 to S16
References (*52–70*)

Submitted 5 August 2024; accepted 24 January 2025
10.1126/science.ads2658

SOLAR CELLS

Graphene-polymer reinforcement of perovskite lattices for durable solar cells

Qing Li[1], Yichu Zheng[2], Haonan Wang[1], Xinyi Liu[1], Miaoyu Lin[1], Xinyuan Sui[1], Xuesong Leng[1], Da Liu[1], Zhanpeng Wei[1], Mengyao Song[1], Dongdong Li[1], Hua Gui Yang[1], Shuang Yang[1]*, Yu Hou[1]*

The lattice deformation and structural evolution of perovskite films in response to electric fields, temperature, and light limit the operational endurance of solar cells. We mechanically reinforced perovskite thin films by integrating a polymer-coupled monolithic single-layer graphene interface that led to a twofold enhancement in modulus and hardness. The synergistic effect of graphene and poly(methyl methacrylate) restricted photoinduced lattice expansion and decreased the deformation ratio from 0.31 to 0.08%, which minimized the structural damage caused by dynamic lattice evolution. Solar cell devices maintained >97% of their initial power conversion efficiency after maximum power point tracking for >3670 hours under full-spectrum air mass 1.5 global (AM 1.5 G) sunlight at 90°C.

Perovskite solar cells (PSCs) have achieved power conversion efficiencies (PCEs) >26% (*1*), but their practical implementation requires improving their stability during operation (*2*, *3*). Efforts to stabilize PSCs include compositional engineering, interface design, and defect passivation (*4*–*12*). However, the longevity of PSCs under working conditions still lags far behind that of the existing industrial silicon solar cells, which can guarantee a <0.5% annual loss for >20 years (*13*).

The fundamental origin of the instability is the soft ionic nature of hybrid perovskites that leads to properties such as giant photostriction, large electrostrictive response, flexoelectricity, anharmonic vibration, and large polaron formation (*14*–*18*). For instance, there is ~0.63% of isotropous lattice expansion in $FA_{0.7}MA_{0.25}Cs_{0.05}PbI_3$ thin film (where FA is formamidinium and MA is methylammonium) after 1-sun illumination for 180 min, whereas the lattice structure of crystalline silicon keeps stationary with a variation ratio <0.001% under 1-sun illumination (*19*). Notwithstanding the potential advantages of stimulus-induced lattice dynamics in device performance (*20*, *21*), it inevitably contributes to lattice deformation, structural evolution, and further device degradation. A very recent study has revealed that the stability issue of PSCs under conditions of cycled light illumination becomes more pronounced than under continuous light irradiation, which underscores the necessity of regulating the stimulus-induced lattice dynamics (*22*).

We designed a mechanical robust interface comprising a monolithic single-layer graphene and poly(methyl methacrylate) (PMMA) coupling interlayer to reinforce the perovskite thin films. Benefitting from graphene's mechanical properties and the polymer's coupling effect, the synergy of both components could notably restrict the photoinduced perovskite lattice expansion by reducing the lattice deformation ratio from 0.31 to 0.08% under illumination, thus minimizing the expansion-induced damage near grain boundaries (GBs). Such interface structure also physically protected the underlying films by inhibiting the lateral interdiffusion of mobile species. Solar cells with the bilayer structure delivered PCEs >24% and maintained >97% of the initial PCE after operation at the maximum power point (MPP) under simulated air mass 1.5 global (AM 1.5 G) irradiation and 90°C for 3670 hours. The outstanding durability of the mechanically reinforced devices highlights their potential to fulfill industrial protocols for large-scale application of PSCs.

Assembly of monolithic graphene–perovskite heterojunctions

The structural deformation of metal halide perovskite varies with changes in operating conditions, such as light illumination and temperature, and will induce local strain accumulation in perovskite polycrystalline films. Many studies have elucidated the adverse impacts of strain on the stability of perovskites (*23*–*25*). In principle, minimizing local stress concentrations is one of the most effective protocols to mitigate the resulting damage.

We fabricated a monolithic graphene–PMMA laminate structure on perovskite surfaces to confine the dynamic structural evolution according to the following considerations: First, graphene is a strong material with an intrinsic tensile strength of 130 GPa and Young's modulus near 1 TPa (*26*, *27*). Second, a monolithic graphene monolayer can impede ionic migration toward charge transport layers. Third, an ultrathin polymeric layer can be used to tightly couple the ionic van der Waals heterointerface. The dynamic evolution of the perovskite lattice under light stimulation is illustrated in Fig. 1A. A graphene-PMMA interface would constrain the structural deformations of the perovskite and cause the adjacent perovskite layer to be harder.

A monolithic monolayer graphene was grown by chemical vapor deposition on copper foil (Fig. 1B and figs. S1 and S2) and transferred by a combination of heat-release-tape lifting and wet-etching processes (see details in the supplementary materials). Before graphene transfer, a 4-nm ultrathin PMMA layer with a glass transition temperature (T_g) of ~105°C, which is above the highest photovoltaic operating temperature of ~85°C, was deposited onto the perovskite to strengthen the interfacial connection and improve adhesion of the graphene layer. Its high uniformity and low surface roughness created a flatter surface for graphene transfer, which minimized defects such as wrinkles and air pockets (*28*, *29*).

Scanning electron microscopy (SEM) images of the $Cs_{0.05}FA_{0.81}MA_{0.14}PbI_{2.55}Br_{0.45}$ perovskite films (denoted as CsFAMA) at different stages of the transfer process revealed the uniformity and full coverage of both the PMMA and graphene layers, with only a few wrinkles appearing on the graphene surface (Fig. 1C). Raman spectra showed the characteristic G band of high-quality monolayer graphene at 1585 cm^{-1} (*30*–*32*) (Fig. 1D). Closer inspection by Raman mapping of a 20-μm–by–10-μm region (Fig. 1E) revealed the uniform monolithic integration of graphene on the perovskite thin films. The centimeter-scale uniformity and integrity of the transferred graphene was demonstrated by water-droplet and contact-angle experiments. The graphene-covered perovskite film became hydrophobic and could sustain the droplet for >120 s without notable color change, unlike the pristine perovskite surface (figs. S3 and S4). However, contact-angle measurements with chlorobenzene revealed fast spreading of solution on graphene-covered perovskite film, which did not impose a negative effect on the subsequent solution deposition of a phenyl-C61-butyric acid methyl ester (PCBM) layer (fig. S5).

We next examined the heterointerface based on focused ion beam lamellas (ITO/perovskite/PMMA/graphene/PMMA/Pt, where ITO is indium tin oxide) by transmission electron microscopy (TEM; Fig. 1F and fig. S6). An additional PMMA layer was deposited on top of the graphene layer to circumvent the overlap of graphene and Pt nanoparticles. The representative high-resolution TEM image shown in Fig. 1G captured a continuous, compact PMMA/graphene/PMMA trilayer architecture, wherein the layered graphite feature could be distinctly recognized with the (002) lattice spacing of ~3.35 Å. The thickness of the PMMA could

---

[1] Key Laboratory for Ultrafine Materials of Ministry of Education, Shanghai Engineering Research Center of Hierarchical Nanomaterials, School of Materials Science and Engineering, East China University of Science and Technology, Shanghai, China. [2] School of Mechatronic Engineering and Automation, Shanghai University, Shanghai, China.
***Corresponding author. Email: syang@ecust.edu.cn (S.Y.); yhou@ecust.edu.cn (Y.H.)**

be controlled by concentration, with ~8 nm for 0.4 mg ml^{-1} and ~4 nm for 0.2 mg ml^{-1} solutions (Fig. 1G and fig. S7), and the device with a PMMA thickness of ~4 nm demonstrated the best efficiency and stability (figs. S8 to S10 and table S1).

Energy-dispersive spectroscopy mapping shown in Fig. 1H further visualized the spatial distribution of Pb, I, Br, In, and Si elements,

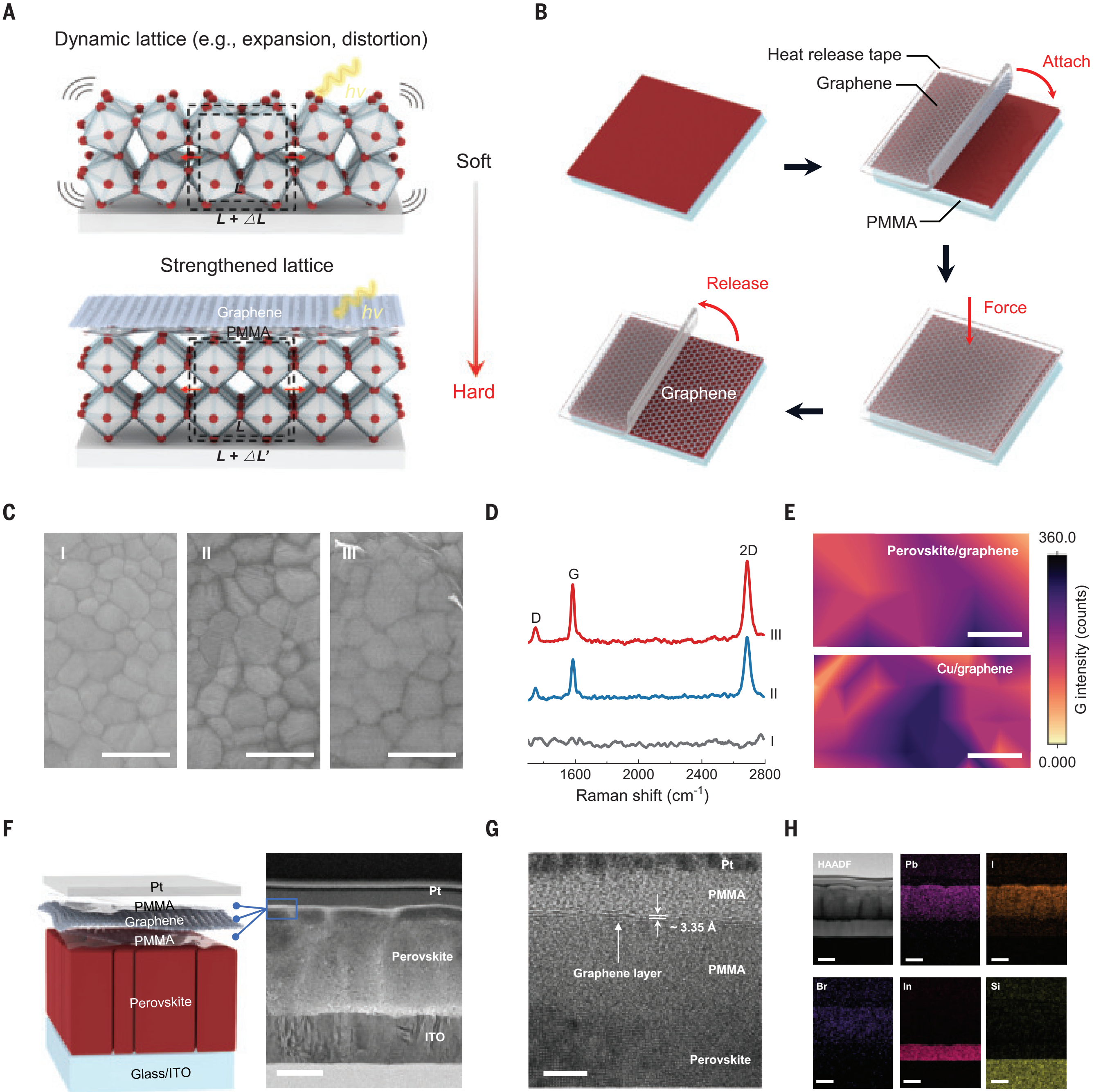

Fig. 1. Fabrication of a monolithic graphene–perovskite heterojunction. (**A**) The alterations in the perovskite lattice structure induced by light radiation exposure. The black dashed rectangles and red arrows indicate expansion measured by a change in length (*L*). (**B**) Schematic diagram of the transfer process of monolayer graphene to the perovskite film surface. (**C**) SEM images of (I) bare perovskite, (II) perovskite/PMMA, and (III) perovskite/PMMA/graphene films. (**D**) Raman spectra of (I) bare perovskite, (II) perovskite/graphene, and (III) perovskite/PMMA/graphene films. Raman spectroscopy was conducted under an excitation wavelength of 532 nm. The G peak, observed at approximately 1580 cm^{-1}, corresponds to the signal of monolayer graphene. D and 2D bands are associated with phonon-defect interactions and a two-phonon double-resonance process, respectively. (**E**) Raman mapping of the G band of a monolayer graphene on Cu foil and a transferred monolayer graphene on top of a perovskite film. (**F**) Device structure and the corresponding cross-sectional TEM image of a perovskite device slice fabricated by focused ion beam. (**G**) High-resolution TEM image of the interface showing the perovskite/PMMA/graphene/PMMA/Pt structure. (**H**) Scanning TEM image and corresponding energy-dispersive spectroscopy mapping of the perovskite/PMMA/graphene/PMMA/Pt structure. A thick PMMA layer was fabricated to better visualize the hybrid interface. Scale bars are 500 nm in (C), 5 μm in (E), 5 nm in (G), and 200 nm in (F) and (H). HAADF, high-angle annular dark-field.

with discernable boundaries of the multiple stacks. One notable observation is that iodine diffused into the bottom PMMA layer yet stopped at the graphene interface, indicating the excellent homogeneity and considerable ionic-blocking function of the graphene monolayer (fig. S11). Similarly, electrochemical impedance spectroscopy of a PMMA/graphene device showed a capacitive vertical line in the low-frequency region, which is an indication of a reflecting boundary for mobile ions (*33*) (fig. S12).

Mechanical reinforcement of perovskite films

Given the mechanical robustness of the coupled graphene monolayer, we performed nanoindentation and tensile strength measurements of perovskite films with different interfaces (*34*–*36*) (Fig. 2A). At a given indentation depth of 100 nm, a loading force approximately double that of the pristine film was required for perovskite films with graphene or PMMA/graphene layers (Fig. 2B), which corresponds to an increase in Young's modulus from 27.4 GPa for the pristine film to 50.3 GPa for the PMMA/graphene sample, as well as an enhancement in hardness from 0.62 GPa for the pristine film to 1.08 GPa for the PMMA/graphene sample (Fig. 2G and tables S2 to S4). Concurrently, the improved recovery of indentation damage

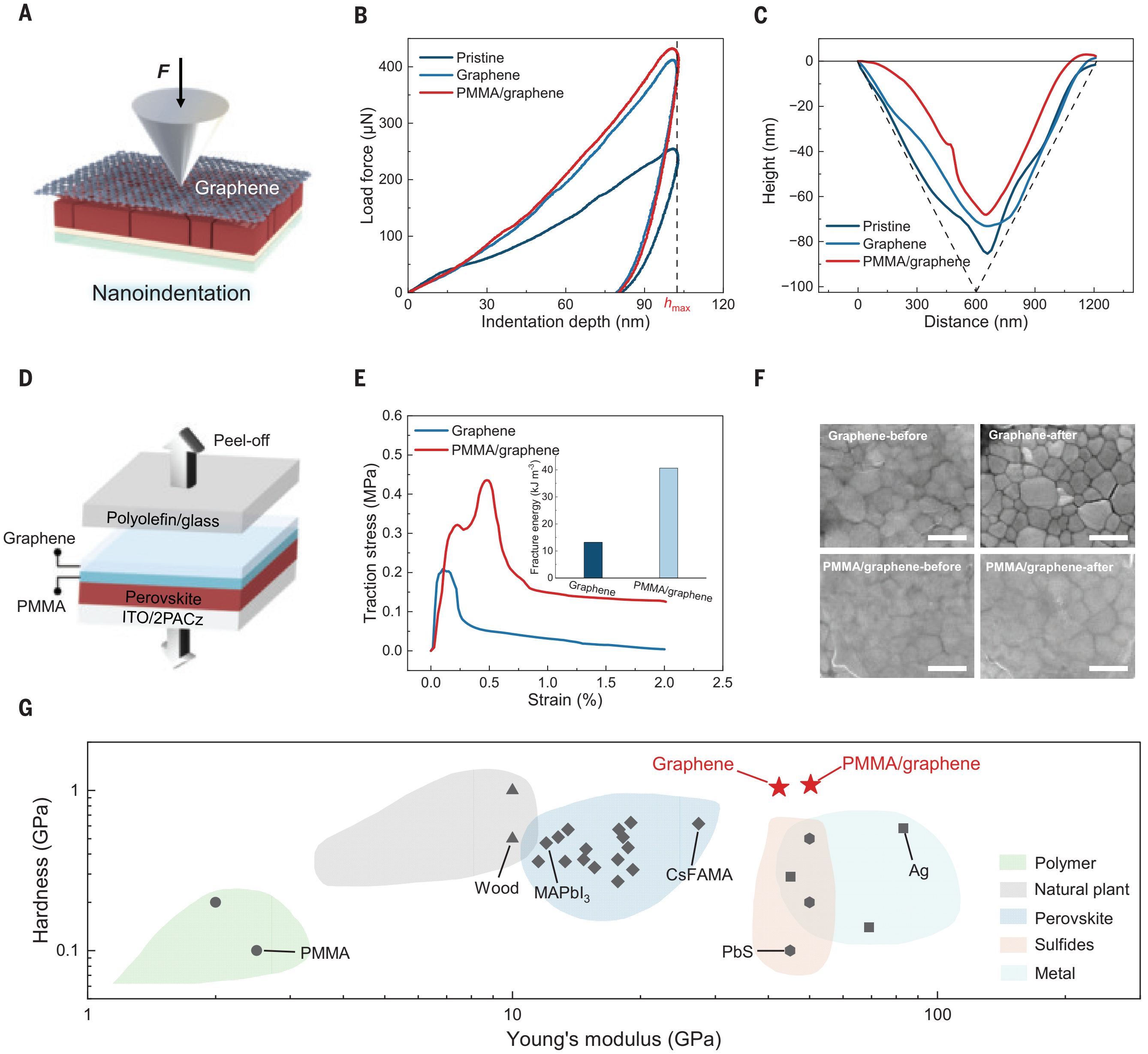

Fig. 2. Mechanical properties of perovskite films. (**A**) Schematic diagram of the nanoindentation measurements. *F*, force. (**B**) Load force–dependent indentation depth curve and (**C**) height profiles of the indented position of perovskite films with different interfaces. The indentation depth was precisely set to be 100 nm, and the continuous variation of load was recorded in real time. The dashed lines indicate the profile corresponding to the initial indentation depth. h_{max}, the maximum indentation depth. (**D**) The structure used for the tensile stress measurements. (**E**) Stress-strain curve of the perovskite films. The inset shows the fracture energies of perovskite films. (**F**) SEM images of perovskite films with graphene or PMMA/graphene interfaces before and after the tensile stress measurements. Scale bars are 500 nm. (**G**) Correlation diagram of Young's modulus versus hardness for common materials.

of the perovskite film with the PMMA/graphene layer confirmed that the heterostructures retained the toughness and rebound resilience of graphene, whereas the pure perovskite films were often fragile and underwent plastic deformation (*37*) (Fig. 2C and fig. S13).

Nanoindentation tests were also performed on perovskite films deposited on flexible polyethylene terephthalate (PET) substrates. Compared with films on rigid ITO substrates, the Young's modulus and hardness were reduced on PET, which is attributed to the softness of the polymer substrate (*38*, *39*). However, despite this substrate effect, the PMMA/graphene layer still shows substantial improvement in Young's modulus and hardness (fig. S14). These results further confirmed that the incorporation of PMMA/graphene enhanced the mechanical robustness of perovskite films, regardless of whether the films were on rigid or flexible substrates.

The progressive evolution of the applied tensile stress-strain relation during the delamination event of devices with the structure ITO/2PACz/perovskite/graphene/polyolefin/glass {Fig. 2D; where 2PACz is [2-(9H-carbazol-9-yl) ethyl]phosphonic acid}, either with or without PMMA, is shown in Fig. 2E (*40*). The PMMA coupling layer improved the interfacial tensile strength of the perovskite/graphene interface from 0.21 to 0.44 MPa, concomitant to an increase in the fracture energies from 13.2 to 40.6 kJ m^{-3}. Inspection of the delaminated devices revealed that delamination initially occurred at the perovskite/graphene interface in this device configuration, but it occurred at the graphene/polyolefin or perovskite/ITO interfaces when the PMMA layer was present (fig. S15). SEM images in Fig. 2F further revealed the persistence of the perovskite/PMMA/graphene interface after tensile testing. Thus, PMMA is both in close contact with graphene and strongly bonded to lead cations on the perovskite surface through its acrylate groups (fig. S16).

Solar cell fabrication and performance

We fabricated solar cells with a typical planar heterojunction architecture of glass/ITO/2PACz/perovskite/PCBM/BCP/Cu (where BCP is bathocuproine) to explore device performance and longevity (Fig. 3A). Current density-voltage (*J-V*) curves and corresponding photovoltaic parameters of solar cell devices are shown in Fig. 3B and table S5. The pristine device based on CsFAMA delivered a short-circuit current density of 24.8 mA cm^{-2}, an open-circuit voltage of 1.15 V, a fill factor of 78.0%, and a PCE of 22.3%. An enhanced PCE of 24.6% was achieved in the target device by using the bilayer architecture composed of the monolithic graphene and PMMA coupling interlayer and is in agreement with the stabilized power output at the MPP (fig. S17). The increase in the average PCE from 20.7 to 23.7% demonstrated the reproducibility of our devices after the introduction of the PMMA/graphene structure (Fig. 3C and fig. S18).

We attributed the enhanced performance of the devices to two factors. First, the PMMA-graphene heterostructure passivated defects, which reduced the charge recombination and prolonged the carrier lifetime (*41*) (figs. S19 to S21). Second, graphene has a lower work function (4.3 to 4.5 eV) than perovskites (4.7 to 4.9 eV). We used Kelvin probe force microscopy to characterize the surface electronic property of the resulting films. We observed a larger surface potential with excellent homogeneity for the target film, which corresponds to a smaller work function at the interface (fig. S22). This shift should improve band alignment and charge transport at the electron transport layer/perovskite interface (fig. S23) and ultimately enhance photovoltaic performance (*42*). We note that our device design was broadly compatible with other perovskite materials. By incorporating the bilayer architecture of PMMA/graphene, we achieved high PCEs of 25.4% in the $FAPbI_3$-based device, 22.15% in the $MAPbI_3$-based device, and 16.0% in the $CsPbI_2Br$-based device (table S5).

The impact of the interfacial structures on device durability was evaluated under operational conditions. By subjecting encapsulated CsFAMA devices to the MPP condition under 1-sun illumination at 90°C (fig. S24), the target device retained >97% of its initial PCE after continuous operation for 3670 hours. The pristine PSC experienced a rapid decay to only 45% of the original PCE within 1298 hours. A tilting stability experiment conducted on a solar cell with only a graphene layer exhibited a PCE decay to 80% of the original value after 1998 hours, and the solar cell with a PMMA layer demonstrated a PCE decay to 85% of the original value after 1586 hours, which underscored the need to reinforce the perovskite/graphene connection apart from the interfacial blocking function (Fig. 3D).

By comparing the operational stability data under 1-sun illumination between 25° and 90°C, we could show that the CsFAMA perovskite in conjunction with the PMMA/graphene interface enabled one of the most stable PSCs that has been reported (table S6). Moreover, when stored in ambient air without encapsulation, the target devices encompassing the water-resilient graphene surface show almost no PCE degradation after 3000 hours, whereas the PCE of the pristine devices decreased to <50% of the initial value after 1800 hours (Fig. 3E).

The photostability of the device was also evaluated under low-vacuum conditions, which have been shown to be more severe than the encapsulation or inert environment (Fig. 3F). After light soaking under ~1.3×10^3 Pa and an open circuit for 1656 hours, the target devices maintained >98% of the original PCE value, whereas the PCE of the pristine devices decreased to 60% of the initial value after 1200 hours. Furthermore, we performed day-night cycling stability tests on PSCs with and without the PMMA/graphene interface and found that the device with the PMMA/graphene interface was also tolerant to this cycling condition (fig. S25). These observations corroborated the ability of our fabrication protocol to improve the tolerance of PSCs to multiple environments.

We then examined the perovskite thin films after disassembly of solar cell devices operated for various durations of time. After operation for 1000 hours, there was a high density of flake-shaped PbI_2-like analog located at the GBs in the pristine perovskite film (figs. S26 to S28). The decomposition products were then rationalized by x-ray diffraction (XRD) measurements, in which the characteristic PbI_2 (001) peak at 12.2° gradually emerged at a prolonged working time of 500 hours. After integrating the PMMA/graphene interface, the PbI_2 products were absent in both SEM and XRD results across the entire duration of the light-soaking process, which is fully consistent with the long-term stability results (fig. S29). Although the specific pathways and dynamics of perovskite degradation cannot be well resolved, depending on several factors such as loading stress or perovskite compositions, the perovskite degradation herein should be initialized from the GBs at the operation timescale of the devices.

Stabilization mechanism

We monitored in real time the structural evolution of half-devices (ITO/2PACz/perovskite/PCBM) under 1-sun illumination with in situ XRD. The samples were not intentionally cooled and came to a temperature of ~45°C after a total illumination time of 50 min. The schematic in Fig. 4A shows the shift of characteristic (001), (002), and (022) diffraction peaks of pristine perovskite half-devices that can be interpreted as the lattice expansion from 6.372 to 6.392 Å for (001), 3.166 to 3.175 Å for (002), and 2.234 Å to 2.240 Å for (022) lattice planes. In contrast to those of the pristine half-devices with a (001) plane expansion of 0.31%, the XRD signals of the perovskite film with a PMMA/graphene interface were insensitive to light and thermal stress, with only a 0.08% variation in (001) lattice spacing (Fig. 4, B and C).

To demonstrate the functions of PMMA and graphene as two basic building blocks, we also conducted in situ XRD on half-devices with either graphene or PMMA alone. The XRD evolution data for these samples under light over time are shown in Fig. 4, D to F. The (001) lattice expansion was estimated to be 0.22% for the perovskite film with graphene and 0.26%

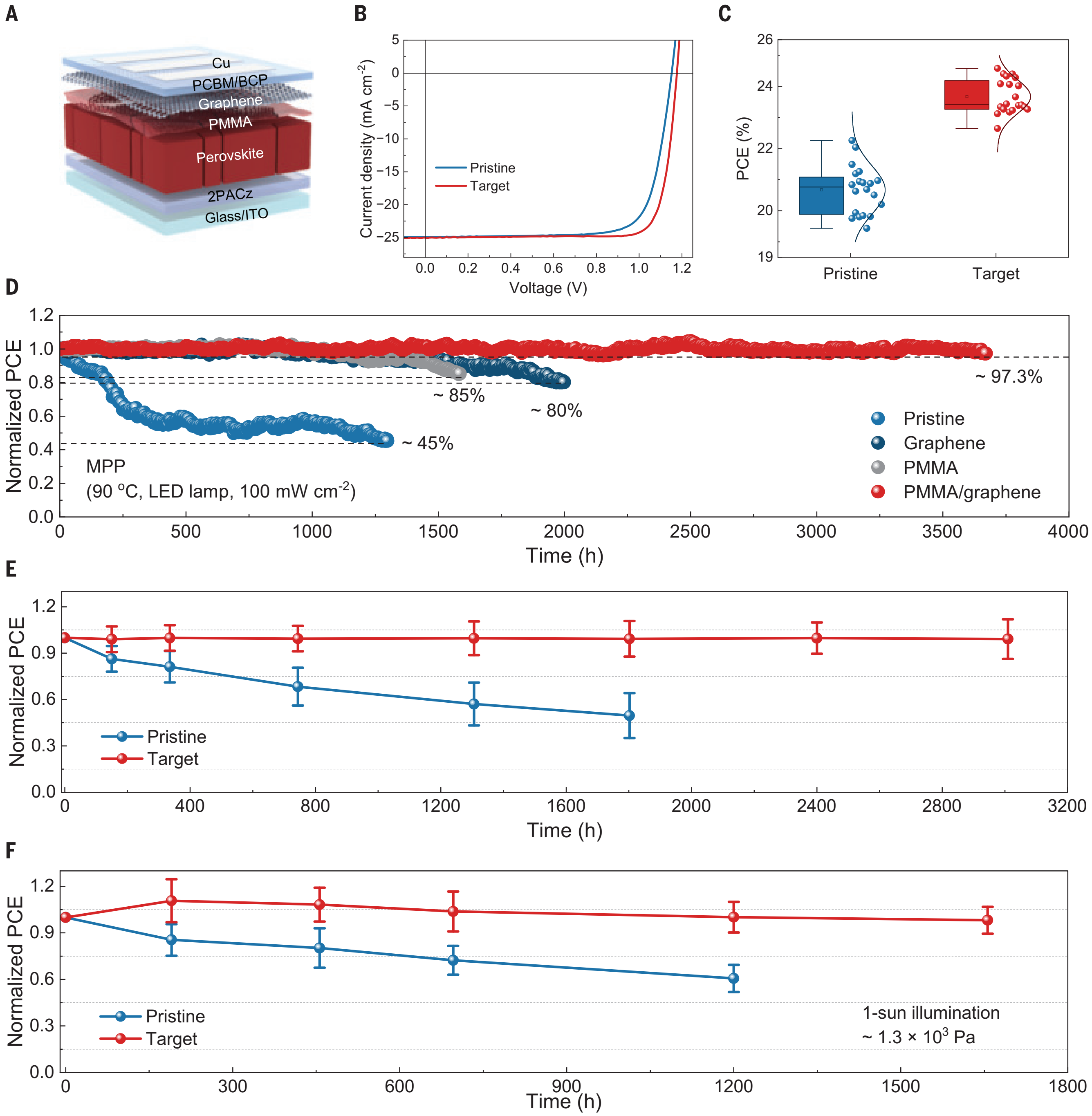

Fig. 3. Photovoltaic performance and device stability. (**A**) Device structure of the PSC based on a bilayer architecture composed of single-layer graphene and a polymeric coupling interlayer. (**B**) *J-V* curves for pristine and target PSCs. All *J-V* curves were measured under AM 1.5 G illumination with a reverse scan rate of 0.15 V s^{-1}. (**C**) PCE distribution of pristine and target devices. The center line represents the median, box limits are upper and lower quartiles, and whiskers are minimum and maximum values. (**D**) Long-term operational stability of devices with various interfacial structures, assessed by tracking their MPP under continuous 1-sun illumination at 90°C. LED, light-emitting diode. (**E**) Long-term stability of the encapsulated devices stored in ambient conditions. Error bars indicate standard deviations. (**F**) Vacuum stability of pristine and target devices measured at open circuit under 1-sun illumination with a pressure of 1.3 × 10^3 Pa. Error bars indicate standard deviations.

for the film with PMMA alone (table S7). These results emphasize the synergistic nature of the stabilization mechanism with PMMA and graphene. After switching off the light, a gradual recovery of lattice constants was observed for all samples within 5 hours. Grazing-incidence wide-angle x-ray scattering (*43*) provided further evidence of the isotropic nature of the photomechanical effect according to the similar expansion ratio of perovskite lattice in both in-plane and out-of-plane orientations (fig. S30).

In situ Raman spectroscopy is extremely sensitive to lattice vibrations and local strain, and we measured the low-frequency vibrations (<60 cm^{-1}) that are predominantly associated with the lead iodide network (*44*–*46*) (fig. S31). After switching on the light, the intensity of the

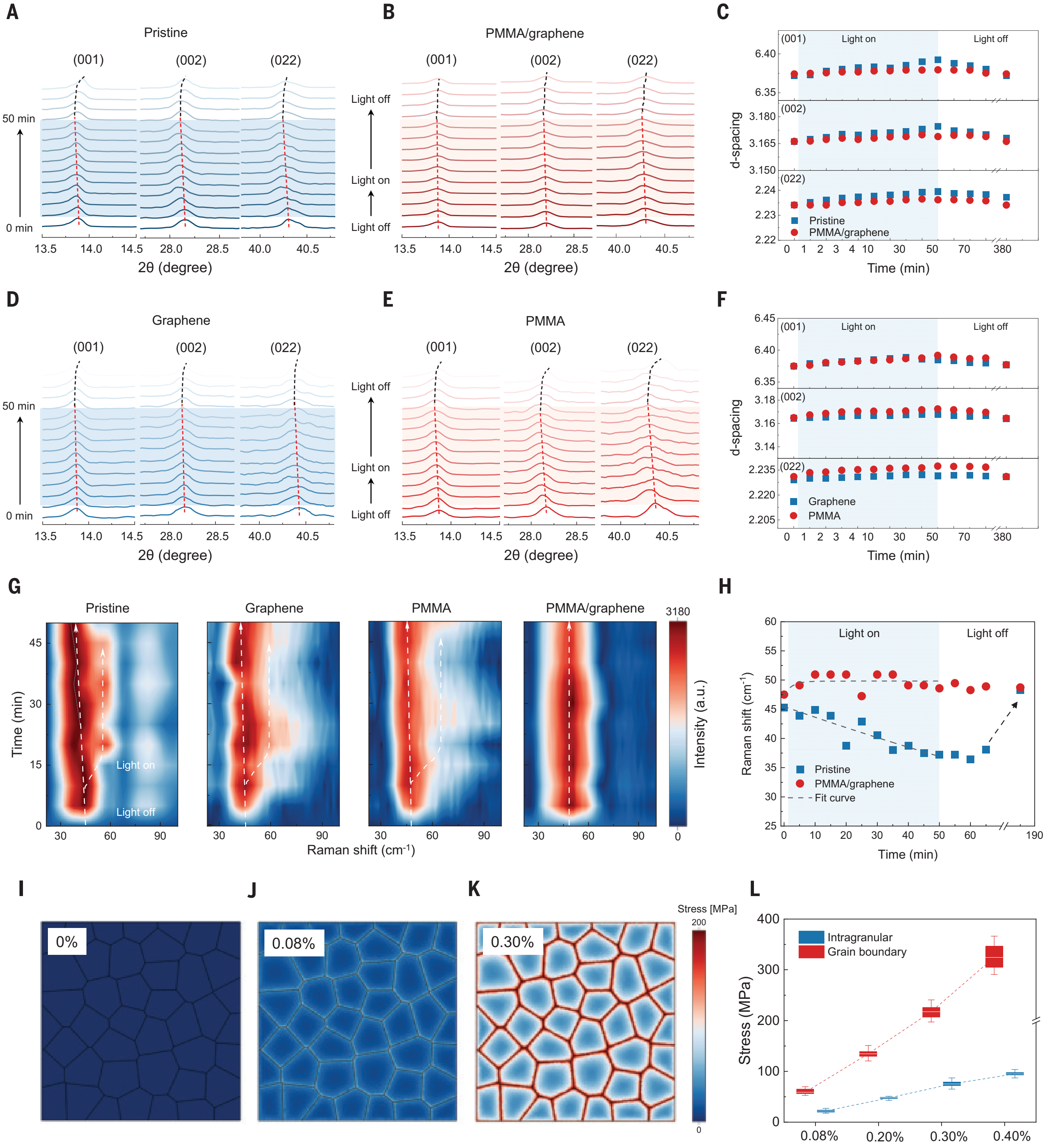

Fig. 4. Microstructure evolution of perovskite thin films. In situ XRD patterns of half-devices with various interface structures under white LED light irradiation for (**A**) pristine, (**B**) PMMA/graphene, (**D**) graphene, and (**E**) PMMA. (**C** and **F**) Variation in the d value of (001), (002), and (022) reflections as determined by the XRD analysis for (C) pristine and PMMA/graphene and (F) graphene and PMMA. The temperature was about 45°C during the illumination time. (**G**) In situ Raman spectra of half-devices with various buffer layers under white LED light illumination. The characteristic peak observed at 45 cm^{-1} corresponds to the vibration mode of the metal halide octahedra of metal halide perovskites. The white dashed lines indicate the evolutionary trend of the most prominent peak. a.u., arbitrary units. (**H**) Evolution of the lead halide octahedral modes derived from Raman spectra upon light illumination. The device structure for in situ XRD and Raman measurements is ITO/2PACz/perovskite/PCBM, with a PCBM layer thickness of 10 nm. (**I** to **K**) Stress simulation results of perovskite polycrystalline films under different crystal expansions: 0% (I), 0.08% (J), and 0.30% (K). (**L**) Stress statistics of the intragranular region and GB. The center line represents the median, box limits are upper and lower quartiles, and whiskers are minimum and maximum values.

Raman signal centered at 45 $\mathrm{cm^{-1}}$ increased by a factor of 10 for the pristine perovskite film. Such variation in Raman modes agrees with previous results that suggest that the well-defined cubic $\mathrm{FAPbI_3}$ structure is less Raman active but becomes active with high scattering intensity under stress that reduces lattice symmetry (*47*, *48*). Extending the light exposure to around 20 min widened the vibrational peaks with non-Gaussian geometry, which then split into two components for the pristine perovskite film: a strong feature that gradually shifted from 38.1 to 36.6 $\mathrm{cm^{-1}}$ at 50 min and a weak feature located at 56.3 $\mathrm{cm^{-1}}$ (fig. S32).

We interpreted the intrinsic softening of the main Raman modes to be the result of tensile strain in conjunction with lattice expansion, as disclosed by XRD. Phase segregation has been identified as one important degradation mechanism in many perovskite systems with multiple cations or halides. However, our in situ photoluminescence measurements revealed no evidence of phase segregation under ultraviolet light exposure and an even higher temperature of 90°C (fig. S33). The Raman signal of perovskite films with PMMA/graphene remained almost stationary over the entire light soaking, confirming that the lattice deformation was virtually eliminated by the interface (Fig. 4, G and H).

After switching the light off, structural reversibility was also observed in the Raman spectra within 3 hours (fig. S34). Furthermore, in situ Raman analyses of samples containing either graphene or PMMA alone demonstrated a broadening of the vibrational peaks (Fig. 4G) that resembled the broadening of the pristine sample peaks, which was consistent with the XRD results. Thus, graphene or PMMA alone cannot restrict the dynamic deformation of the lead-iodine octahedra of perovskites under illumination. Because of the limited duration of in situ experiments, we have not yet observed the irreversible decomposition residuals of the perovskite at this timescale. Nonetheless, the large discrepancy in lattice deformation as well as its impact on the degradation pathway cannot be neglected when attempting to understand the stabilization mechanism of the PMMA/graphene interface.

To further elucidate the influence of lattice expansion, we conducted a numerical simulation to analyze the stress and strain distribution in perovskite films. The topological structure of perovskite grains was included in the finite element model with a uniform grain deformation ratio of 0, +0.08, and +0.30%. The detailed procedure is described in the supplementary text. The geometric expansion of grains makes the entire film crowded, with a large compression at the boundary region (Fig. 4, I to K, and fig. S35). Thus, stress gradients appeared with actinomorphic distribution and reached their maximum near GB regions, where the stress was about five times that of the grain center (Fig. 4L). The increase in the expansion ratio from 0.08 to 0.30% led to an increase in overall stress level in the film, in which the stress near GBs increased from ~50 to 200 MPa. Previous studies have shown that strain is often detrimental to perovskite structure because it exacerbates the ionic migration or defect formation (*49*). Thus, a higher expansion ratio of the perovskite lattice would be expected to induce larger strain at the GB region and result in faster degradation (figs. S36 and S37).

We operated conductive atomic force microscopy (c-AFM) measurements to spatially resolve the impact of light illumination on carrier transport in perovskite films. The schematic setup of the c-AFM is shown in fig. S38. The surface topology and local dark current were simultaneously acquired by a Pt-Cr cantilever equipped with a current-to-voltage preamplifier. A prominent current discrepancy between the intra- and intergranular regions was captured in the pristine perovskite film: The mean dark currents are estimated to be about 500 and 350 pA at the GB and interior, respectively (Fig. 5A). Light soaking for 20 hours widened the conductive region of the GB, with a full width at half maximum of about 0.08 to 0.18 μm, which implies that the undesired electronic "GB-like" regions are substantially expanded, albeit these parts do not belong to the real GB (figs. S39 and S40).

A statistical analysis of the current maps shown in Fig. 5B illustrates the emergence of an additional conducting component centered at about 0.72 nA that corresponded to the signals from enlarged GBs. Hence, illumination did not just affect the conductivity at the GB surface but also involved the near-GB region, which was closely associated with the photomechanical strain upon lattice expansion. After inclusion of a PMMA/graphene interface, a minimal dark current at GBs was observed that should originate from the combined effects of the defect passivation by the interlayer and the accumulation of relatively thick PMMA at the concave GB (*50*) (Fig. 5C and fig. S41).

Moreover, the overall value and distribution of the dark current with respect to both grain interior and boundary were well sustained after light soaking (Fig. 5D). Additionally, light exposure for 20 hours resulted in a decrease in photocurrent near the GBs, whereas the current within the grain interiors mostly remained (fig. S42). This result suggests that lattice expansion caused by light exposure accumulates stress at the GBs, which degrades charge transport capacity in these regions and potentially affects device performance under prolonged illumination. This contrasting trend in electronic characteristics of these samples emphasizes the necessity of suppression of the photomechanical effect in stabilizing perovskite devices. We measured the evolution of dark currents of full solar cell devices and observed good consistency between the microscopic and macroscopic variation of dark currents, which confirmed the reliability of the current-mapping results (Fig. 5, E and F).

The evolution of dark currents was closely related to the defect formation. We used thermal admittance spectroscopy to probe the trap density of states (tDOS) in these solar cells. After subjecting the pristine device to light exposure for 20 hours, there was a nearly threefold increase in the density of shallow trap states (0.3 to 0.5 eV) (Fig. 5G). Recent defect spectroscopy studies have determined that these shallow trap states predominantly originate from iodine-related defects (*51*, *52*), which are energetically stabilized near the perovskite surface or GBs (*53*). We infer that the shallow states enriched at GBs should be responsible for the increased shunt current seen in current maps. In comparison, the tDOS of the target device remained stationary upon illumination (Fig. 5H), which is consistent with the c-AFM results that showed that the reinforcement of perovskite films can minimize GB damage and suppress the dark current in devices.

Discussion

Our work identified that lattice deformation under environmental stress is an important factor in GB damage and structural degradation of perovskite polycrystalline films that has been long neglected in this field. We show that such soft lattice dynamics can be suppressed by the synergistic effect of a PMMA-coupled monolithic graphene interface, which endows the perovskite films with mechanical properties of high modulus, large hardness, rebound resilience, intimate interconnection, and physical protection.

Both graphene and PMMA are necessary for mechanical reinforcement of the perovskite layer, in which the graphene serves as a reinforcing substrate and PMMA acts as a bonding medium. Experimental observations of the dynamic structural evolution coupled with results from computational models demonstrate the utility of the hybrid interface for controlling lattice deformation as well as lateral ionic migration under working conditions. As a result, the hybrid interface enables long-term stabilization of highly efficient perovskite devices under various environments, such as under light soaking, high temperature, ambient air, and vacuum.

Because the perovskite materials are inherently fragile, the presence of intimately coupled and tough graphene in this approach is expected to address the issue of stress-induced damage and crack propagation in flexible devices. With the development of two-dimensional materials, this strategy would be compatible with large-area graphene transfer and has been

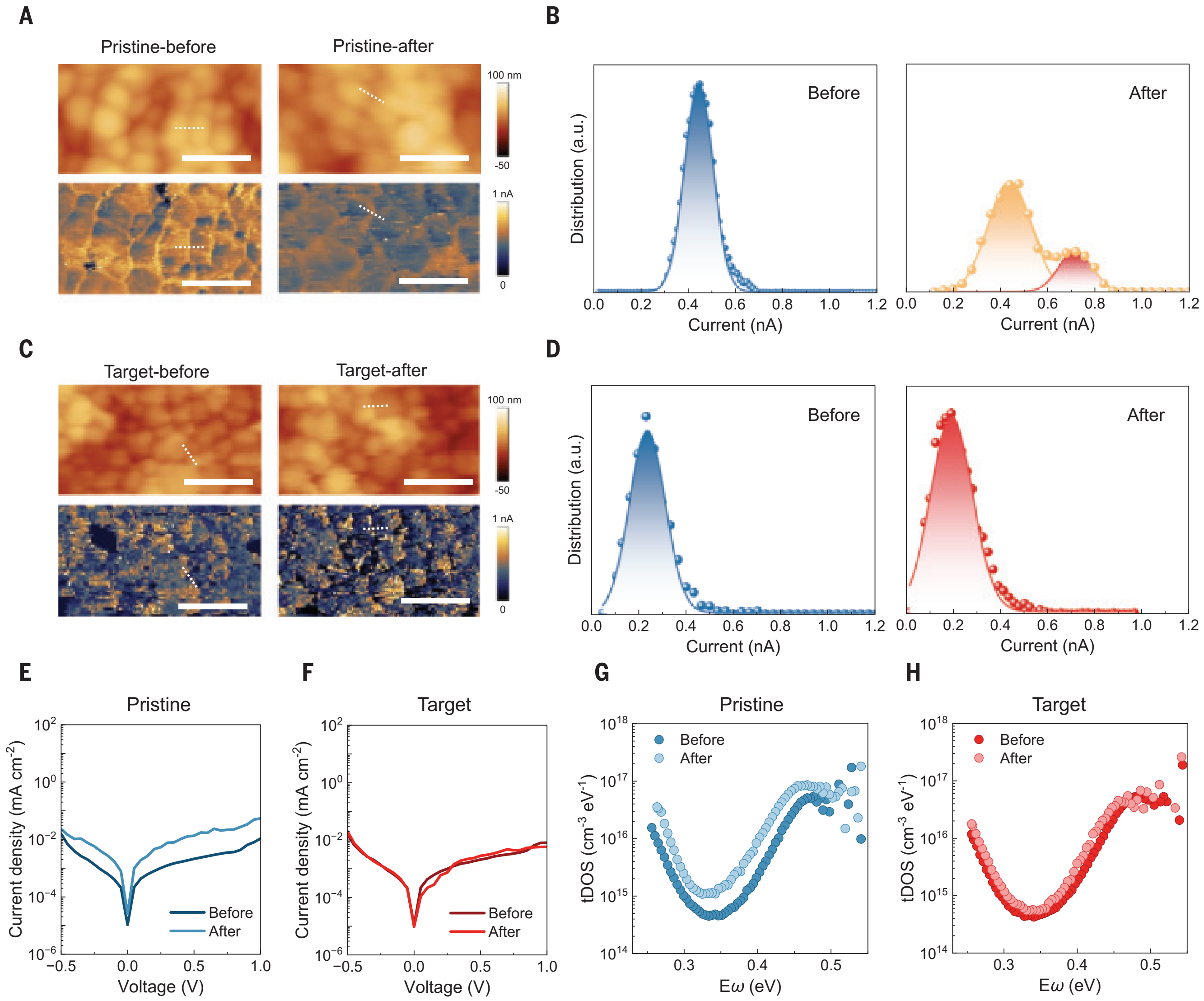

Fig. 5. Photoelectric properties of perovskite thin films. (**A** and **C**) AFM height images (top) and current maps (bottom) and (**B** and **D**) current distribution diagrams of the pristine and target films on ITO substrates before and after white LED irradiation for 20 hours. The current maps were scanned by a Pt-Cr cantilever tip at a scan rate of 0.3 Hz and a dc bias of 2.6 V under dark conditions. The white dotted lines in (A) and (C) indicate the profile crossing through two adjacent grains. All scale bars are 500 nm. (**E** and **F**) Dark *J-V* curves and (**G** and **H**) tDOS of pristine and target devices before and after light irradiation for 20 hours. Eω, demarcation energy depends on characteristics of the measured traps.

applied in the fabrication of centimeter-sized perovskite devices (fig. S43). Our work provides a fundamental understanding of dynamic structural damage in PSCs under practical operation and opens more possibilities for overcoming stability issues for further industrial production and application of perovskite devices.

REFERENCES AND NOTES

1. National Renewable Energy Laboratory, Best research-cell efficiencies; https://www.nrel.gov/pv/assets/pdfs/best-research-cell-efficiencies.pdf [accessed June 2024].
2. R. Guo *et al*., *Nat. Energy* **6**, 977–986 (2021).
3. Y. Jiang *et al*., *Joule* **4**, 1087–1103 (2020).
4. N. J. Jeon *et al*., *Nature* **517**, 476–480 (2015).
5. Q. Jiang *et al*., *Nature* **611**, 278–283 (2022).
6. D. B. Khadka *et al*., *Nat. Commun.* **15**, 882 (2024).
7. X. Leng *et al*., *Energy Environ. Sci.* **17**, 4295–4303 (2024).
8. Z. Liang *et al*., *Nature* **624**, 557–563 (2023).
9. W.-T. Wang *et al*., *Nature* **632**, 294–300 (2024).
10. Y. Wang *et al*., *Science* **365**, 687–691 (2019).
11. X. Lin *et al*., *Nat. Energy* **7**, 520–527 (2022).
12. J. Peng *et al*., *Nature* **601**, 573–578 (2022).
13. T. Saga, *NPG Asia Mater.* **2**, 96–102 (2010).
14. B. Chen *et al*., *Nat. Mater.* **17**, 1020–1026 (2018).
15. T. Debnath *et al*., *Nat. Commun.* **12**, 2629 (2021).
16. K. Miyata, T. L. Atallah, X.-Y. Zhu, *Sci. Adv.* **3**, e1701469 (2017).
17. L. Shu *et al*., *Nat. Mater.* **19**, 605–609 (2020).
18. Y. Zhou *et al*., *Nat. Commun.* **7**, 11193 (2016).
19. H. Tsai *et al*., *Science* **360**, 67–70 (2018).
20. B. Guzelturk *et al*., *Nat. Mater.* **20**, 618–623 (2021).
21. K. Miyata *et al*., *Sci. Adv.* **3**, e1701217 (2017).
22. Y. Shen *et al*., *Nature* **635**, 882–889 (2024).
23. J. Jiang *et al*., *Nat. Photonics* **16**, 575–581 (2022).
24. D. Liu *et al*., *Nat. Mater.* **20**, 1337–1346 (2021).
25. D. J. Xue *et al*., *Nat. Commun.* **11**, 1514 (2020).
26. C. Lee, X. Wei, J. W. Kysar, J. Hone, *Science* **321**, 385–388 (2008).
27. G. López-Polín *et al*., *Nat. Phys.* **11**, 26–31 (2014).
28. Y. Song, W. Zou, Q. Lu, L. Lin, Z. Liu, *Small* **17**, e2007600 (2021).
29. W. Zhu *et al*., *Nano Lett.* **12**, 3431–3436 (2012).
30. A. Eckmann *et al*., *Nano Lett.* **12**, 3925–3930 (2012).
31. T. Huang *et al*., *eScience* **2**, 319–328 (2022).
32. J.-B. Wu, M.-L. Lin, X. Cong, H.-N. Liu, P.-H. Tan, *Chem. Soc. Rev.* **47**, 1822–1873 (2018).
33. W. Peng *et al*., *ACS Energy Lett.* **3**, 1477–1481 (2018).
34. S. Chen *et al*., *Joule* **4**, 2661–2674 (2020).
35. S. Hong *et al*., *Nature* **582**, 511–514 (2020).
36. W. Jiang *et al*., *eScience* **4**, 100203 (2024).
37. X. Li *et al*., *Nat. Mater.* **22**, 1175–1181 (2023).
38. T. Y. Tsui, G. M. Pharr, *J. Mater. Res.* **14**, 292–301 (1999).
39. R. Saha, W. D. Nix, *Acta Mater.* **50**, 23–38 (2001).
40. T. Duan *et al*., *Science* **384**, 878–884 (2024).
41. S. Liu *et al*., *Nature* **632**, 536–542 (2024).
42. X. Zheng *et al*., *Nat. Energy* **5**, 131–140 (2020).
43. R. Quintero-Bermudez *et al*., *Nat. Mater.* **17**, 900–907 (2018).
44. J. Ibaceta-Jaña *et al*., *Phys. Chem. Chem. Phys.* **22**, 5604–5614 (2020).
45. M. Liao, B. Shan, M. Li, *J. Phys. Chem. Lett.* **10**, 1217–1225 (2019).
46. N. Phung *et al*., *Joule* **6**, 2152–2174 (2022).
47. Y. Chen *et al*., *Nature* **577**, 209–215 (2020).
48. J. A. Steele *et al*., *ACS Nano* **11**, 8072–8083 (2017).

49. J. Zhao *et al.*, *Sci. Adv.* **3**, eaao5616 (2017).
50. Y. Shi *et al.*, *Adv. Mater.* **30**, e1800251 (2018).
51. Z. Ni *et al.*, *Nat. Energy* **7**, 65–73 (2021).
52. X. Ren *et al.*, *Nat. Mater.* **23**, 810–817 (2024).
53. S. G. Motti *et al.*, *Nat. Photonics* **13**, 532–539 (2019).

ACKNOWLEDGMENTS

Funding: This work was funded by the National Ten Thousand Talent Program for Young Top-notch Talent; National Natural Science Foundation of China (22379044, 52203330, 12304109); Science and Technology Commission of Shanghai Municipality (21DZ1207101, 23520710700); Key Program of the National Natural Science Foundation of China (22239001); International (Regional) Cooperation and Exchange Projects of the National Natural Science Foundation of China (51920105003); Shanghai Pilot Program for Basic Research (22TQ1400100-5); "Dawn" Program of Shanghai Education Commission (22SG28); Shanghai Municipal Natural Science Foundation (22ZR1418000); Shanghai Sailing Program (22YF1410000, 22YF1413100); Postdoctoral Research Foundation of China (2021M701190); Fundamental Research Funds for the Central Universities (JKD01241607, JKVD1241041); Shanghai Engineering Research Center of Hierarchical Nanomaterials (18DZ2252400); and Shanghai Frontiers Science Center of Optogenetic Techniques for Cell Metabolism (Shanghai Municipal Education Commission). **Author contributions:** Conceptualization: Q.L., H.W., S.Y., Y.H.; Methodology: Q.L., Y.Z., H.W., X.Liu, X.S., Z.W., M.S., D.Li, S.Y., Y.H.; Investigation: Q.L., Y.Z., X.Leng, S.Y., Y.H.; Visualization: Q.L., Y.Z., H.W., X.Liu, M.L., X.S., S.Y., Y.H.; Funding acquisition: H.G.Y., S.Y., Y.H.; Project administration: H.G.Y., S.Y., Y.H.; Supervision: H.W., X.Liu, D.Liu, X.Leng, Z.W., H.G.Y., S.Y., Y.H.; Writing – original draft: Q.L., Y.Z., X.Liu, D.Liu; Writing – review & editing: Q.L., Y.Z., H.G.Y., S.Y., Y.H. **Competing interests:** The authors declare that they have no competing interests. They also do not have any patent applications or pending or granted patents to disclose. **Data and materials availability:** All data are available in the main text or the supplementary materials.

SUPPLEMENTARY MATERIALS

science.org/doi/10.1126/science.adu5563
Materials and Methods
Supplementary Text
Figs. S1 to S43
Tables S1 to S7
References (*54*–*86*)

Submitted 11 November 2024; accepted 7 January 2025
10.1126/science.adu5563

SPECTROSCOPY

Ultrafast on-demand exciton formation in a single-molecule junction by tailored terahertz pulses

Kensuke Kimura[1]*, Ryo Tamaki[2,3], Minhui Lee[1,4], Xingmei Ouyang[5,6], Satoshi Kusaba[2]†, Rafael B. Jaculbia[1,7], Yoichi Kawada[8], Jaehoon Jung[9], Atsuya Muranaka[5], Hiroshi Imada[1,10]*, Ikufumi Katayama[2,11]*, Jun Takeda[1,2]*, Yousoo Kim[1,4,7,10]*

The ultrafast manipulation of molecular states by charge transfer is essential for characterizing and controlling molecular dynamics. In this study, we demonstrated exciton formation in a single molecule through ultrafast electron tunneling processes between a molecule and a metal tip of a scanning tunneling microscope (STM) using a phase-controlled terahertz (THz) pulse. The pronounced luminescence of the well-defined molecular system under the distinct carrier-envelope phase of the THz pulse revealed that sequential state-selective electron-tunneling processes to the frontier molecular orbitals promoted ultrafast exciton formation in the molecule at the STM junction. Furthermore, ultrafast control of exciton formation was achieved using phase- and delay-controlled THz pulse pairs, providing a route for the regulation of molecular dynamics and the emergence of new molecular functions.

Charge transfer between a metal and a molecule is fundamental to various fields of science and technology, including electrochemical reactions, oxidation and reduction reactions on catalytic surfaces, photoelectric conversions, and device interfaces (*1*–*3*). Charge transfer produces intermediates such as charged states, vibrationally excited states, electronically excited states (excitons), and trions, the dynamics of which profoundly influence the functionalities of molecules (*2*–*7*). Given their short lifetimes, the on-demand generation of intermediates by ultrafast charge manipulation is essential for tracking and controlling their dynamics, yet it is still challenging to regulate intermediates on their intrinsic timescales.

The intense electric fields of few-cycle optical pulses enable the control of molecular states through ultrafast charge manipulation (*8*–*12*). In particular, terahertz (THz) field–driven tunneling at a nanogap electrode, caused by strong distortions in the tunneling barrier due to electromagnetic field oscillations, is an intriguing technique for the precise ultrafast control of electrons (*13*–*33*). By applying this technique to a tunneling junction of a scanning tunneling microscope (STM), field-driven electron tunneling through isolated molecules and its modulation due to the molecular motion have been observed (*14*, *15*). However, the on-demand exciton formation has not yet been achieved because it requires the sequential control of the charged states through electron injection into the lowest unoccupied molecular orbital (LUMO) and its removal from the highest occupied molecular orbital (HOMO) on an ultrafast timescale. Because the sequential and bidirectional tunneling processes result in a net zero current, it remains challenging for THz-STM to realize and evaluate the sequential electron tunneling required for the ultrafast manipulation of the quantum states of a molecule.

In this work, we demonstrated on-demand exciton formation in a molecule using a waveform-tailored THz pulse. To elucidate the mechanism of exciton formation by field-driven tunneling through a molecule, we combined luminescence spectroscopy with field-driven tunneling current measurements because photons emitted during energy dissipation processes provide crucial insights into quantum conversions (*34*–*47*). We conducted THz-field–driven scanning tunneling luminescence (THz-STL) measurements (*32*) on a Pd(II) phthalocyanine (PdPc) molecule (*34*) adsorbed onto a NaCl film grown on an Ag(111) surface (see Fig. 1A and figs. S1 and S2 for a more detailed description of the instrument setup). By using waveform-tailored THz pulses, we clarified that exciton formation occurred through sequential state-selective electron-tunneling processes induced by the positive and negative components within one cycle of the THz pulse.

Electron transport through a single molecule triggered by a THz pulse

Figure 1B shows an STM image of PdPc molecules adsorbed on a three- and four-monolayer (ML)–thick NaCl film grown on an Ag(111) surface. To determine the transport channels of a PdPc molecule, we measured the differential conductance ($dI_{\mathrm{DC}}/dV_{\mathrm{DC}}$) spectrum of PdPc/NaCl(3ML)/Ag(111), where I_{DC} is the DC tunneling current and V_{DC} is the DC sample voltage (Fig. 1C). The $dI_{\mathrm{DC}}/dV_{\mathrm{DC}}$ spectrum exhibited two resonant tunneling peaks: the negative ion resonance (NIR) at V_{DC} = 1.0 V and the positive ion resonance (PIR) at –2.4 V, which are assigned to the resonant tunneling through the

---

[1]Surface and Interface Science Laboratory, RIKEN Cluster for Pioneering Research, Wako, Saitama, Japan. [2]Department of Physics, Graduate School of Engineering Science, Yokohama National University, Yokohama, Kanagawa, Japan. [3]Kanagawa Institute of Industrial Science and Technology (KISTEC), Ebina, Kanagawa, Japan. [4]Department of Applied Chemistry, School of Engineering, The University of Tokyo, Bunkyo-ku, Tokyo, Japan. [5]Molecular Structure Characterization Unit, RIKEN Center for Sustainable Resource Science, Wako, Saitama, Japan. [6]Emergent Soft Matter Function Research Group, RIKEN Center for Emergent Matter Science, Wako, Saitama, Japan. [7]Center for Quantum Conversion Research, Institute for Basic Science, Gwangju, Republic of Korea. [8]Central Research Laboratory, Hamamatsu Photonics K.K., Hamamatsu, Shizuoka, Japan. [9]Department of Chemistry, University of Ulsan, Ulsan, Republic of Korea. [10]Department of Chemistry, Gwangju Institute of Science and Technology, Gwangju, Republic of Korea. [11]Semiconductor and Quantum Integrated Electronics Research Center, Institute for Multidisciplinary Sciences, Yokohama National University, Yokohama, Japan.
***Corresponding author. Email: kensuke.kimura@riken.jp (K.K.); himada@riken.jp (H.I.); katayama-ikufumi-bm@ynu.ac.jp (I.K.); jun@ynu.ac.jp (J.T.); ykim@riken.jp (Y.Ki.)**
†Present address: Department of Physics, Tokyo Metropolitan University, Hachioji, Tokyo, Japan.

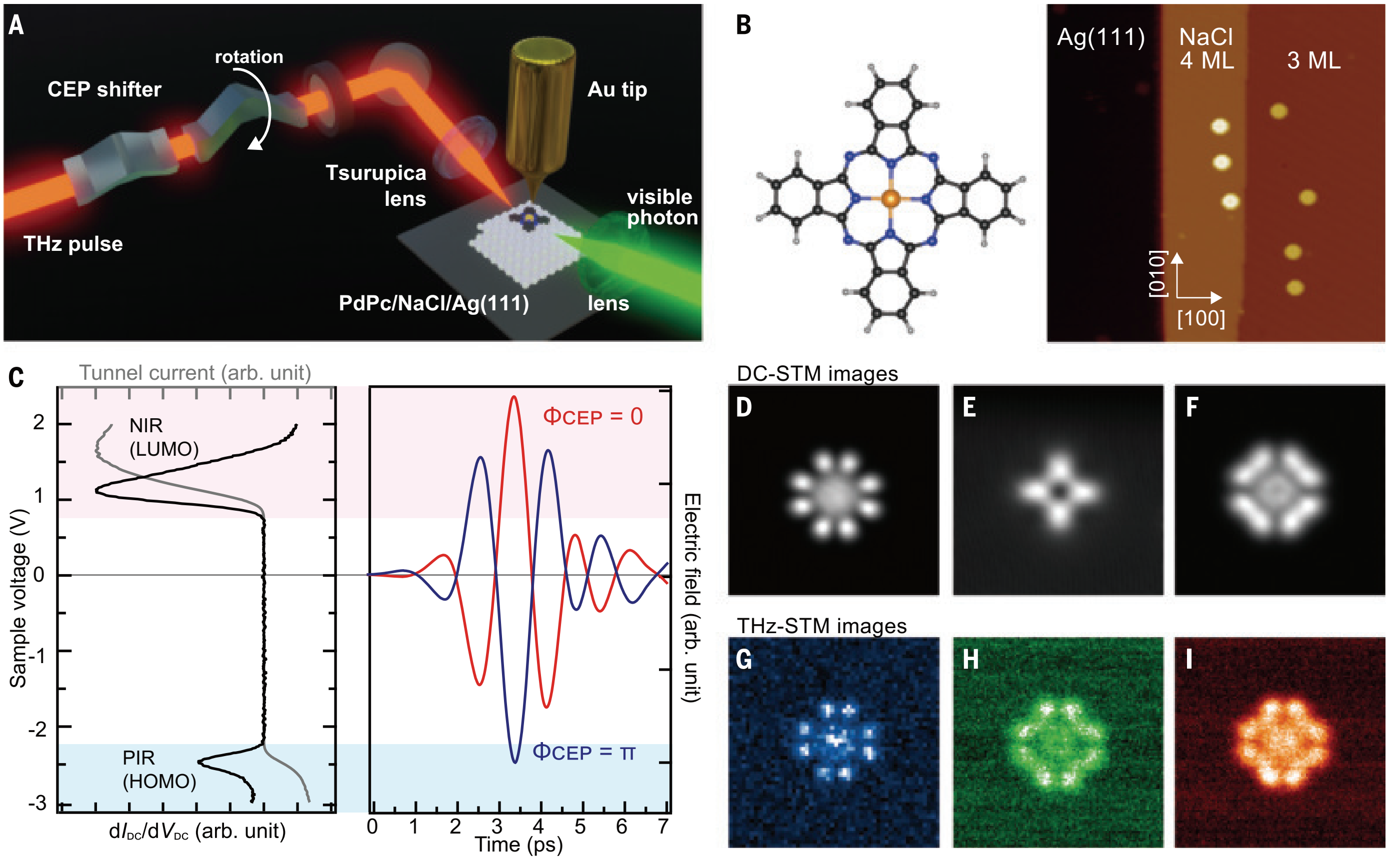

Fig. 1. THz-STM measurements on PdPc/NaCl/Ag(111). (**A**) Schematic illustration of the THz-STL setup. (**B**) Left, molecular structure of PdPc. Orange indicates Pd; black, C; blue, N; and gray, H. Right, STM image of PdPc/NaCl/Ag(111) (V_{DC} = 1.0 V, I_{DC} = 10 pA, 75 × 75 nm^2). White arrows indicate the [100] and [010] directions of NaCl film, and the cross-axis of PdPc is aligned with these directions. (**C**) Left, dI_{DC}/dV_{DC} spectrum of PdPc/NaCl(3ML)/Ag(111) (black). The gray line shows the I_{DC}-V_{DC} curve. The feedback loop was turned off at V_{DC} = 1.0 V and I_{DC} = 10 pA (defined as Δz = 0; see the materials and methods for details). Right, temporal profile of a single-cycle THz pulse. Red indicates Φ_{CEP} = 0; blue, $\Phi_{CEP} = \pi$. In the case of the THz waveform at $\Phi_{CEP} = \pi$, when the voltage applied by the negative main peak (V_{THz}) is larger than the threshold voltage of the PIR peak, the voltages applied by the positive subpeaks are also larger than the threshold voltage of the NIR peak. (**D** to **F**) Constant height DC-STM images of PdPc/NaCl(3ML)/Ag(111) (4 × 4 nm^2). In (D), V_{DC} = −2.5 V; in (E), V_{DC} = 0.5 V; in (F), V_{DC} = 1.0 V. (**G** to **I**) THz-STM images of PdPc/NaCl(3ML)/Ag(111) (4 × 4 nm^2). In (G), $\Phi_{CEP} = \pi$, E_{THz} = −80 V/cm, V_{DC} = −1.7 V, and Δz = −0.2 nm, obtained by a lock-in amplifier (see fig. S7 for details). The repetition rate (f_{rep}) of the THz pulse was 49 MHz. In (H), $\Phi_{CEP} = \pi$, E_{THz} = −72 V/cm, f_{rep} = 49 MHz, V_{DC} = 0 V, and Δz = −0.3 nm. In (I), Φ_{CEP} = 0, E_{THz} = 48 V/cm, f_{rep} = 49 MHz, V_{DC} = 0 V, and Δz = −0.3 nm.

LUMO and the HOMO, respectively (*34*, *42*). This assignment was supported by the V_{DC} dependence of the STM images (Fig. 1, D to F). The spatial distributions of the LUMO and the HOMO were observed at V_{DC} = 1.0 V (Fig. 1F) and −2.5 V (Fig. 1D), respectively. A cross-structure appeared at V_{DC} = 0.5 V in the gap region between these peaks (Fig. 1E) (*48*).

Figure 1, G to I, shows THz-STM images of a PdPc molecule obtained at different nearfield carrier envelope phase (CEP) values of the THz pulse (Φ_{CEP}). Here, Φ_{CEP} of 0 rad is defined as applying a maximum positive THz electric field (E_{THz}), and $\Phi_{CEP} = \pi$ corresponds to a negative E_{THz} (see fig. S3 for details). An evaluation of the voltage applied by the THz pulse to the STM junction (V_{THz}) is shown in fig. S4, where E_{THz} = 47.2 V/cm corresponds to V_{THz} = 2.0 V in this study. When positive E_{THz} was applied to the PdPc molecule (Φ_{CEP} = 0) with V_{DC} set to 0 V, a positive THz-field–driven current (I_{THz}) was detected. The fourfold symmetric distribution of the LUMO is visualized in Fig. 1I, similar to the DC-STM image obtained with positive V_{DC} (Fig. 1F). The threshold V_{THz} for visualizing the LUMO was nearly equivalent to that of V_{DC} (fig. S5); therefore, it is concluded that the peak top of the positive main peak of the THz pulse opened the transport channel through the NIR, and the LUMO was visualized in the THz-STM image. Conversely, when a negative E_{THz} was applied ($\Phi_{CEP} = \pi$), both a net positive I_{THz} (fig. S6) and the spatial distribution of the LUMO were also observed in the THz-STM image (Fig. 1H), similar to the case of Φ_{CEP} = 0 (Fig. 1I), although a sufficiently negative E_{THz} of −72 V/cm (V_{THz} = −2.9 V) to visualize the HOMO was applied to the PdPc molecule. This result was rationalized by the single-cycle waveform of the THz pulse and the asymmetric features of the PdPc/NaCl/Ag(111) transport channels (Fig. 1C). Because the dI_{DC}/dV_{DC} peak position of the NIR is closer to the Fermi level than that of the PIR, and the intensity of the NIR peak is larger than that of the PIR peak, electron transport through the NIR is more likely to occur than through the PIR, resulting in a net positive I_{THz}.

To confirm the validity of this interpretation, we measured a THz-STM image at $\Phi_{CEP} = \pi$ with simultaneously applied negative V_{DC} (Fig. 1G and fig. S7). In this measurement, $V_{THz}(t) + V_{DC}$ was applied to the STM junction, where V_{DC} served as an offset voltage (fig. S7A). Using a lock-in technique, we isolated the pure THz-STM image (fig. S7C) from the THz-STM image with a DC offset (fig. S7B). We observed the eight-lobe structure originating from the HOMO in the THz-STM image (Fig. 1G). These

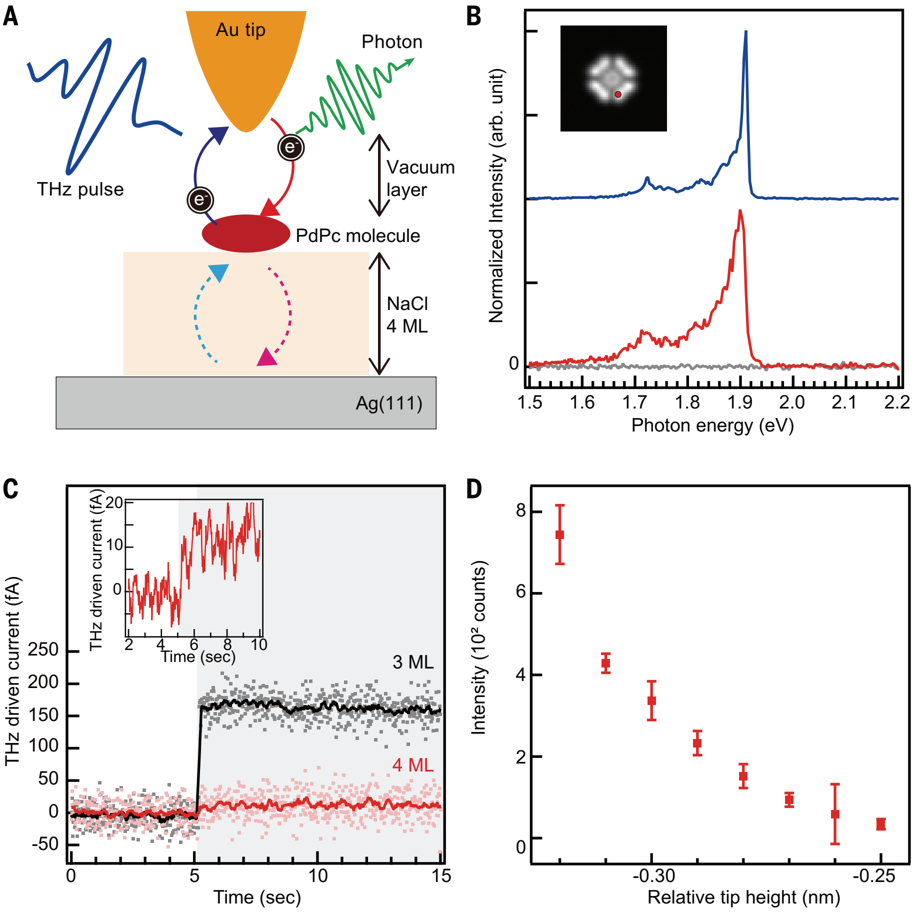

Fig. 2. Single-molecule THz-STL measurements on PdPc/NaCl/Ag(111). (**A**) Schematic illustration of THz-STL measurements on PdPc/NaCl(4ML)/Ag(111). Black circles represent electrons. (**B**) DC-STL (blue, V_{DC} = −2.5 V, I_{DC} = 10 pA) and THz-STL spectra of PdPc/NaCl(4ML)/Ag(111) ($\Phi_{CEP} = \pi$, E_{THz} = −60 V/cm, f_{rep} = 49 MHz, V_{DC} = 0 V, and Δz = −0.31 nm). Red indicates THz on; gray indicates THz off. The red circle in the inset DC-STM image (4 × 4 nm^2) shows the tip position during luminescence measurements. (**C**) Current trace measurements of PdPc on NaCl 4 ML (red) and 3 ML (black). THz pulses were irradiated after 5 s (shaded area). Solid lines show smoothed data. The inset figure magnifies the data of NaCl(4ML) ($\Phi_{CEP} = \pi$, E_{THz} = −60 V/cm, f_{rep} = 49 MHz, V_{DC} = 0 V, and Δz = −0.31 nm). (**D**) Tip height dependence of luminescence intensities ($\Phi_{CEP} = \pi$, E_{THz} = −50 V/cm, and f_{rep} = 10 MHz). Exposure time (t) was 120 s. The error bars were obtained by calculating the SDs of five repeated measurements.

results suggest that both positive and negative transient currents can be induced by the THz pulse with $\Phi_{CEP} = \pi$ and V_{DC} = 0 V, but the negative component vanishes because of the time-averaged I_{THz} detection. This interpretation implies that the molecular state is sequentially changed by THz-field–driven tunneling and that an exciton can be formed by electron injection into the LUMO and its removal from the HOMO. Further investigation is required to fully describe the overall field-driven tunneling processes through the molecule.

THz-field–driven single-molecule electroluminescence measurements

STL has been used to characterize electron transport accompanying many-body state transitions in a molecule because it provides abundant spectroscopic information on photon intensity, energy, polarization, and conversion efficiency (*34*–*47*). Therefore, THz-STL measurements were performed on PdPc to elucidate the electron transport mechanism hidden in the time-averaged measurements (Fig. 2A). Because a thicker NaCl film gives stronger luminescence intensity because of the suppression of molecule-metal coupling (*39*), we prepared a 4-ML-thick NaCl film for the THz-STL measurements (the dI_{DC}/dV_{DC} spectrum of PdPc/NaCl(4ML)/Ag(111) is given in fig. S8). Figure 2B shows the THz-STL spectra obtained when the THz pulse of $\Phi_{CEP} = \pi$ was either irradiated to the STM (red spectrum) or blocked (gray spectrum) with V_{DC} = 0 V alongside the DC-STL spectrum (blue). Several sharp peaks appeared at ~1.9 eV in the red spectrum, whereas no peaks were observed in the gray spectrum. The energy of the main peak in the THz-STL spectrum is identical to that of the DC-STL spectrum (blue), so we attributed the observed luminescence to the fluorescence from the singlet exciton (S_1) in PdPc (*34*). The peak width of the THz-STL spectrum is greater than that of the DC-STL spectrum. This result can be explained by differences in the tip-sample distance and the oscillation of the THz electric field. Because the tip height during the THz-STL measurement is ~3 Å closer to the molecule compared with the DC-STL measurement, it is expected that the energy decay of the exciton becomes faster, resulting in a broader peak width (*45*). In contrast to the static electric field during the DC-STL measurements, the THz electric field oscillation can vary the exciton energy through the Stark effect and transient changes in the molecular and NaCl structures (*15*, *49*). These effects also contribute to the broadening of the luminescence peak width.

During THz-STL measurements of a PdPc molecule on NaCl(4ML), the I_{THz} value was ~10 fA (red line in Fig. 2C), which was ~17 times smaller than that of PdPc on NaCl(3ML) (black line in Fig. 2C). In addition, the luminescence intensity depended on the tip height (Fig. 2D), indicating that precise control of the tunneling junctions is required to form an exciton in a molecule. Because the thickness of the vacuum layer (tip-sample distance) is 3 to 4 Å smaller than the thickness of the NaCl(4ML) film (1.12 nm), and considering the tip height of ~0.7 nm based on our previous works (*41*, *47*), it is expected that the tunneling probability between the tip and the molecule (vacuum layer) is several orders of magnitude larger than that between the molecule and the metal substrate (NaCl layer) in our THz-STL measurements. Therefore, back-and-forth electron transport between the tip and the molecule (solid arrows in Fig. 2A) is responsible for exciton formation. These results highlight that the combination of optical measurements with THz-STM is essential for investigating the sequential field–driven tunneling to form an exciton that cannot be detected by I_{THz} measurements because of the net-zero current.

Exciton formation mechanism by sequential THz-field–driven tunneling

In addition to the precise control of the tunneling junction, controlling the CEP of the THz pulse can influence exciton formation. To fully understand the role of CEP, we investigated its effect on the THz-STL spectra. Figure 3A presents a series of THz-STL spectra measured at different CEP values. The integrated luminescence intensities of the fluorescence are plotted as a function of CEP in Fig. 3B, which shows that the luminescence intensity reaches its maximum at Φ_{CEP} value of ~7π/6. Although distinct luminescence signals were

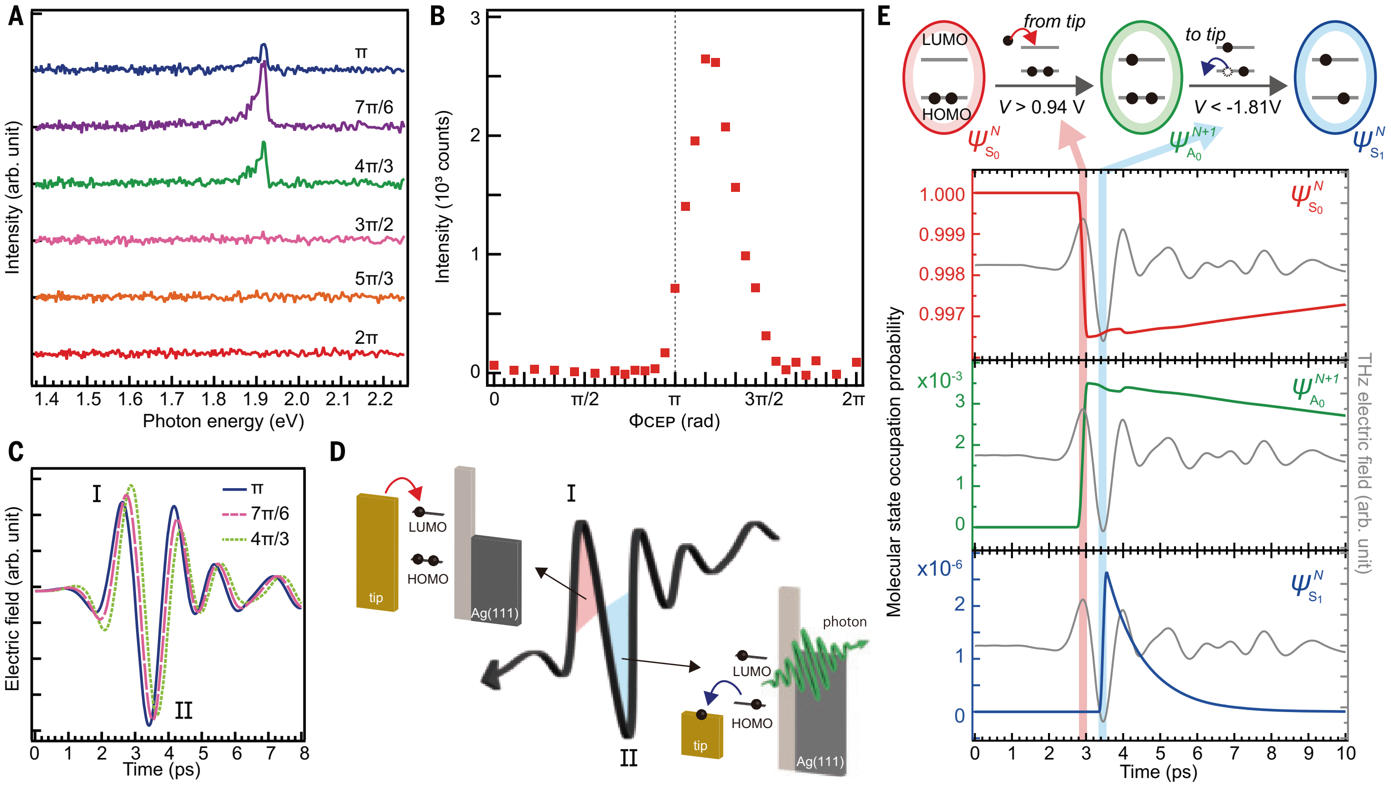

Fig. 3. Exciton formation mechanism by THz-field–driven tunneling. (**A**) Series of THz-STL spectra with changing Φ_{CEP} from π to 2π (E_{THz} = −56 V/cm at $\Phi_{CEP} = \pi$, f_{rep} = 49 MHz, V_{DC} = 0 V, Δz = −0.28 nm, and t = 120 s). (**B**) Φ_{CEP} dependence of luminescence intensities (E_{THz} = −56 V/cm at $\Phi_{CEP} = \pi$, f_{rep} = 49 MHz, V_{DC} = 0 V, Δz = −0.28 nm, and t = 120 s). (**C**) Φ_{CEP} dependence of temporal profiles of single-cycle THz pulses. $\Phi_{CEP} = \pi$ (blue solid line), $7\pi/6$ (pink dashed line), and $4\pi/3$ (green dotted line). (**D**) Schematic images of the exciton formation mechanism. (I) An electron is injected into the LUMO of PdPc from the tip by the positive subpeak of THz pulse (pink area). (II) The electron is removed from the HOMO to form S_1 by the negative main peak of THz pulse (light blue area), and photons are emitted from the molecule (green arrow). Gold and silver columns in energy diagrams represent the density of states of the tip and Ag(111), respectively. Black spheres represent electrons. (**E**) Theoretical considerations of the exciton formation mechanism. Top, schematic illustrations of the proposed exciton formation mechanism. The $\psi^{N+1}_{A_0}$ state (green) is formed by electron injection into the LUMO of $\psi^N_{S_0}$ (red) at V > 0.94 V. Then, the $\psi^N_{S_1}$ state (blue) is formed by electron removal from the HOMO of $\psi^{N+1}_{A_0}$ at V < −1.81 V. Bottom, time evolution of the molecular state occupation probabilities of $\psi^N_{S_0}$ (red), $\psi^{N+1}_{A_0}$ (green), and $\psi^N_{S_1}$ (blue) at $\Phi_{CEP} = 7\pi/6$. The gray line shows the waveform of THz pulse used in the calculation (see fig. S10 for additional discussion).

observed at Φ_{CEP} values close to π (negative E_{THz}), no luminescence signals appeared at Φ_{CEP} values close to 0 (positive E_{THz}).

The THz pulses with $\Phi_{CEP} = 0$ and $\Phi_{CEP} = \pi$ apply the same magnitude of V_{THz} but with opposite polarities, indicating that the field-driven electrons are expected to have the same energy at these CEPs. Therefore, if the localized plasmons or inelastic tunneling electrons, as reported in DC-STL works (*35*, *37*), were the main contributors to the THz-STL, then the fluorescence would be expected to appear at both $\Phi_{CEP} = 0$ and $\Phi_{CEP} = \pi$. However, no luminescence signal was observed around Φ_{CEP} = 0, suggesting that the contribution of exciton formation by a plasmon or inelastic tunneling can be negligible. Instead, exciton formation by sequential electron injection into the LUMO and removal from the HOMO is responsible for the luminescence signals observed in our measurements (*37*, *41*–*43*).

To elucidate the exciton formation mechanism in detail, we examined the CEP dependence of the THz waveforms (Fig. 3C). When the CEP is rotated in the positive direction from $\Phi_{CEP} = \pi$, the intensity of the negative main peak at nearly 3.5 ps (labeled as II in Fig. 3C) decreases and the intensity of the positive subpeak at around 2.5 ps (labeled as I in Fig. 3C) increases, indicating that the positive subpeak (I) is also important for the exciton formation. Therefore, we propose the following primary exciton formation mechanism by the THz pulse: (I) An electron is injected into the LUMO from the tip by the positive subpeak (pink) to form a negatively charged state, and (II) an electron is removed from the HOMO to the tip by the main negative peak (light blue), resulting in the formation of S_1, as illustrated in Fig. 3D.

To substantiate this interpretation, we evaluated many-body transitions using numerical values obtained from density functional theory (DFT) and time-dependent DFT calculations (Fig. 3E and fig. S9) (*42*). We express the molecular state as ψ^N_a, where N represents the number of electrons in the neutral PdPc molecule, and a denotes the electronic state of the molecule, such as the singlet ground state (S_0), the cationic ground state (C_0), the anionic ground state (A_0), and S_1. Therefore, the proposed mechanism in Fig. 3D is expressed as $\psi^N_{S_0} \rightarrow \psi^{N+1}_{A_0} \rightarrow \psi^N_{S_1}$. The sample voltages required to induce (I) $\psi^N_{S_0} \rightarrow \psi^{N+1}_{A_0}$ and (II) $\psi^{N+1}_{A_0} \rightarrow \psi^N_{S_1}$ transitions were 0.94 and −1.81 V, respectively (Fig. 3E and fig. S9). This asymmetry in the threshold voltages is due to the positions of the HOMO and LUMO energy levels with respect to the Fermi level of the substrate. The sequential many-body transitions (I) and (II) required for exciton formation cannot occur during DC-STL because the polarity of V_{DC} does not change during DC-STL measurements.

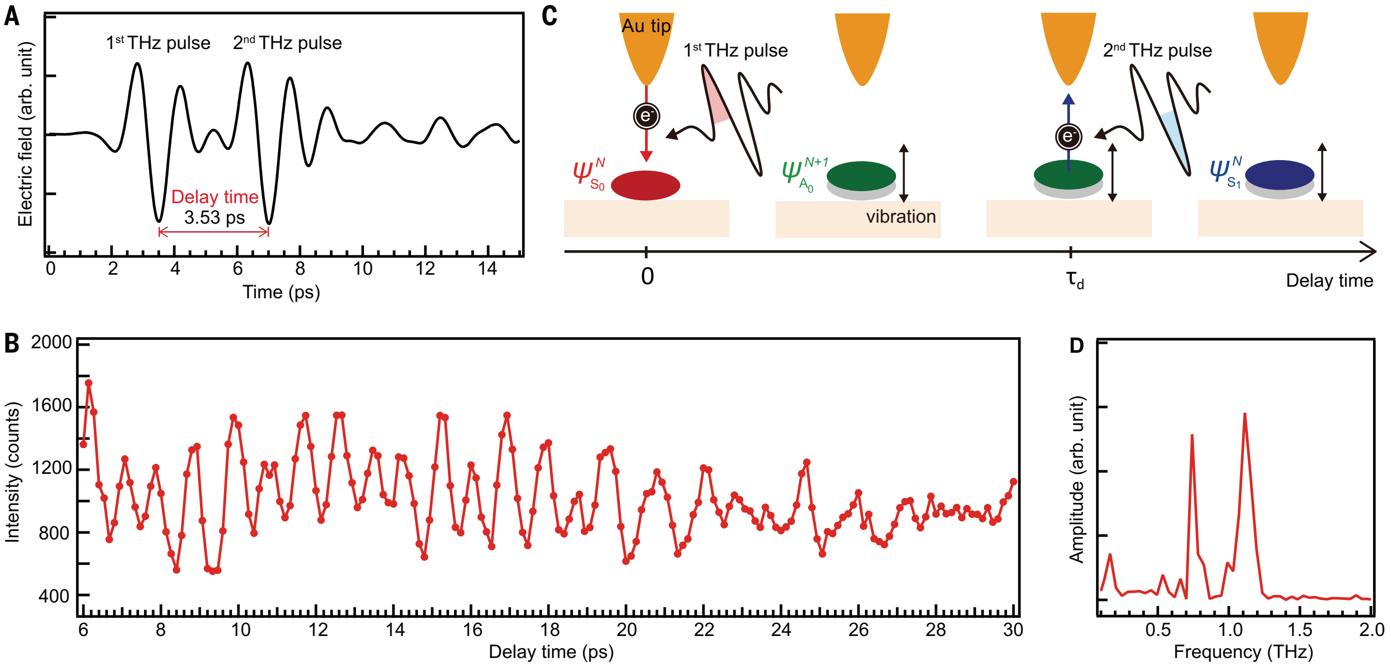

Fig. 4. Dynamic control of exciton formation by THz pulse pair. (**A**) Temporal profiles of the THz pulse pair with delay time (τ_d) of 3.53 ps ($\Phi_{CEP} = 7\pi/6$). (**B**) Delay time dependence of luminescence intensities ($\Phi_{CEP} = 7\pi/6$, $E_{THz} = -61$ V/cm, $f_{rep} = 9.8$ MHz, $V_{DC} = 0$ V, $\Delta z = -0.32$ nm, and $t = 120$ s). (**C**) Step-by-step schematic illustration of the additional excitation process in the THz pulse pair experiment. At $t = 0$ ps, an electron is injected into the molecule in the $\psi^{N}_{S_0}$ state (red) to form the $\psi^{N+1}_{A_0}$ state (green). The charge injection induces molecular vibrations. At $t = \tau_d$, an electron is removed from the $\psi^{N+1}_{A_0}$ state and the $\psi^{N}_{S_1}$ state (blue) is created. (**D**) Fourier spectrum of the delay time dependence in (B).

By contrast, a THz pulse can apply both positive and negative transient voltages to the molecule, making this exciton formation mechanism feasible in THz-STL measurements. When Φ_{CEP} is rotated from π to 2π, the magnitude of the positive subpeak increases, which is advantageous to induce transition (I). However, the magnitude of the negative main peak decreases due to the Φ_{CEP} rotation, which is disadvantageous to induce transition (II). We conclude that this trade-off results in the maximum luminescence intensity at $\Phi_{CEP} = 7\pi/6$ in Fig. 3B.

The proposed exciton formation mechanism and CEP dependence were examined through kinetic model simulations by setting up the rate equations of the molecular states considering the threshold voltages for many-body transitions (see figs. S10 to S14 for details). Figure 3E shows the calculated time evolution of the occupation probabilities of the molecular states when the THz pulse of $\Phi_{CEP} = 7\pi/6$ was applied to the STM junction. The time evolution revealed that $\psi^{N+1}_{A_0}$ was formed from $\psi^{N}_{S_0}$ by the positive subpeak (I) of the THz pulse (pink area in Fig. 3E) with a probability of ~10^{-3}. Subsequently, $\psi^{N}_{S_1}$ was formed by electron removal through the negative main peak (II) (light blue area) with a probability of ~10^{-3} (resulting in a total probability of ~2.5×10^{-6}). The created $\psi^{N}_{S_1}$ radiatively decayed to $\psi^{N}_{S_0}$, contributing to the fluorescence signals observed in the THz-STL spectra. This kinetic model simulation also reproduced the Φ_{CEP} dependence of luminescence intensity (figs. S11 and S12), supporting the validity of our model simulation and assumptions. We emphasize that sequential and state-selective electron tunneling processes were achieved due to the tailor-made THz waveform, resulting in on-demand exciton formation. Furthermore, the luminescence intensity depended on the lateral tip position above the molecule (fig. S15), further supporting the importance of state-selective electron tunneling to the molecular orbitals for exciton formation.

Ultrafast control of exciton formation by THz pulse pair

According to the kinetic model simulation results in Fig. 3E, the population probability of $\psi^{N+1}_{A_0}$ remained at ~3.5×10^{-3} after the arrival of a THz pulse and decayed gradually over a certain lifetime (green line in Fig. 3E). Therefore, $\psi^{N}_{S_1}$ can potentially be formed effectively from $\psi^{N+1}_{A_0}$ by using an additional THz pulse before the relaxation of $\psi^{N+1}_{A_0}$. On the basis of this scenario, exciton formation could be coherently regulated on the timescale of the $\psi^{N+1}_{A_0}$ lifetime by using a pair of THz pulses with coordinated timing. To explore this possibility, two successive THz pulses were prepared by splitting the pump laser pulses used for THz generation (Fig. 4A). The THz-STL spectra were measured while varying the delay time (τ_d) between the two THz pulses (fig. S16), and the luminescence intensities are plotted as a function of τ_d in Fig. 4B. High-frequency oscillations with large amplitudes were observed (Fig. 4B), and their amplitudes gradually decreased with increasing delay time. In addition, the overall luminescence intensity decayed to ~900 counts as the delay time increased (Fig. 4B).

Similar to the exciton formation by a single THz pulse discussed in Fig. 3E, individual THz pulses within a pulse pair can form excitons through the sequential tunneling (see fig. S14 for details). In addition to this exciton formation mechanism, we propose that the THz pulse pair opens a new pathway for exciton formation (Fig. 4C). Given that the lifetime of $\psi^{N+1}_{A_0}$ is estimated to be 10 to 100 ps depending on the thickness of the NaCl film and the tip-sample distance in our setup (2), we hypothesize that $\psi^{N+1}_{A_0}$ is formed by the first THz pulse and remains intact until the arrival of the second pulse. Subsequently, an electron is removed from the HOMO by the second THz pulse, forming $\psi^{N}_{S_1}$. As simulated in fig. S14, with increasing time intervals between the two THz pulses, the occupation probability of $\psi^{N}_{S_1}$ (and, consequently, the luminescence intensity) decreases due to the decay of $\psi^{N+1}_{A_0}$. The overall attenuation of the baseline luminescence intensity was determined by performing the fitting of the experimental result (see fig. S17 and the supplementary text for details). Thus, we conclude that there are two distinct exciton formation mechanisms in the pulse pair experiment.

The large high-frequency oscillations shown in Fig. 4B can be attributed to molecular vibrations (*14*). When the distance between the molecule and tip decreases because of the vibrational motion excited by the first pulse (*14*), the probability of electron tunneling induced by the second pulse increases, facilitating exciton formation and constructively increasing the luminescence intensity (Fig. 4C). By contrast, a longer tip-molecule distance reduces the luminescence intensity. The oscillation frequencies were determined to be 0.75 and 1.1 THz by Fourier transform (Fig. 4D). Our DFT calculations revealed the presence of molecular vibrational modes perpendicular to the surface in the low-frequency region (<2 THz), which are coupled with the displacement of Na and Cl ions (see figs. S18 to S20 and movies S1 to S5). These molecular vibrational modes influence the efficiency of exciton formation by modulating the tip-molecule distance, making them responsible for the oscillation observed in the luminescence intensities (Fig. 4B). We conclude that the oscillations in the THz pulse pair experiment arise from vibrational dynamics caused by the interfacial interactions between the molecule and the substrate. Because of the longer lifetime of the charged states compared with that of the exciton in the STM nanocavity (*2*, *45*), we successfully achieved coherent control over the dynamics and correlations of the molecular states, enabling ultrafast on-demand exciton formation. These results demonstrated that THz-STL provides a powerful experimental platform for the real-time investigation of charged state dynamics at the atomic scale.

Conclusions

We have demonstrated ultrafast exciton formation in a single molecule through charge exchange induced by a waveform-tailored THz pulse. Conductance and luminescence measurements of a well-defined molecular system revealed that sequential and state-selective electron tunneling to the frontier molecular orbitals, driven by the positive and negative components of the THz pulse, is responsible for the ultrafast exciton formation in the molecular junction. In this work, THz photons were upconverted into visible photons mediated by electron tunneling to the molecular orbitals. We anticipate that our results will be transferable to nanoscale optoelectronic devices using molecules (*50*, *51*).

Because of the ultrafast temporal resolution of THz-STL, we envision that fundamental quantum photonics, such as energy transfer in molecular systems previously studied using DC-STL (*34*, *35*), can be further explored on their intrinsic length and timescales. Furthermore, we predict that the quantum efficiency of energy transfer can be controlled by using a THz pulse to induce ultrafast fluctuations in molecules (*1*, *15*). The combination of the versatile functions of THz-STL provides a distinctive and powerful experimental platform for investigating ultrafast exciton dynamics at the single-molecule level.

We have also achieved ultrafast coherent control of exciton formation mediated by charge transfer between the molecule and the metal tip. By controlling the timing of charge manipulation with THz pulse pairs, the dynamics and correlations of the charged states can be explored in detail. Because the number of electrons in a molecule cannot be desirably altered by ultrafast photoexcitation in conventional molecular photoscience, the study of charge-induced molecular dynamics remains an unexplored field. Our research on exciton formation through charge injection and extraction offers precise control over molecular dynamics with ultrafast temporal resolution, highlighting the importance of charge states. For instance, by combining this technique with spectroscopic methods such as photoluminescence (*45*–*47*) and Raman spectroscopy (*52*–*55*), pump-probe spectroscopy can be implemented at the ultimate spatiotemporal resolution to track the dynamics of minute structural changes upon charging, which have so far been observed statically using an atomic force microscope (*56*). Our approach paves the way for studying ultrafast charged-state dynamics at the single-molecule level, driving progress in molecular science that integrates molecular electronics, photonics, and chemical reactions on catalytic systems.

REFERENCES AND NOTES

1. H. Imahori, Y. Kobori, H. Kaji, *Acc. Mater. Res.* **2**, 501–514 (2021).
2. K. Kaiser, L.-A. Lieske, J. Repp, L. Gross, *Nat. Commun.* **14**, 4988 (2023).
3. Y. Kobayashi *et al.*, *J. Phys. Chem. C Nanomater. Interfaces* **127**, 746–758 (2023).
4. H. Uoyama, K. Goushi, K. Shizu, H. Nomura, C. Adachi, *Nature* **492**, 234–238 (2012).
5. B. C. Stipe, M. A. Rezaei, W. Ho, *Science* **280**, 1732–1735 (1998).
6. Y. Kim, T. Komeda, M. Kawai, *Phys. Rev. Lett.* **89**, 126104 (2002).
7. A. Singh *et al.*, *Phys. Rev. Lett.* **117**, 257402 (2016).
8. A. Schiffrin *et al.*, *Nature* **493**, 70–74 (2013).
9. Y. Kawakami *et al.*, *Nat. Commun.* **11**, 4138 (2020).
10. T. Higuchi, C. Heide, K. Ullmann, H. B. Weber, P. Hommelhoff, *Nature* **550**, 224–228 (2017).
11. M. Garg, K. Kern, *Science* **367**, 411–415 (2020).
12. M. Garg *et al.*, *Nat. Photonics* **16**, 196–202 (2022).
13. T. Rybka *et al.*, *Nat. Photonics* **10**, 667–670 (2016).
14. T. L. Cocker, D. Peller, P. Yu, J. Repp, R. Huber, *Nature* **539**, 263–267 (2016).
15. D. Peller *et al.*, *Nature* **585**, 58–62 (2020).
16. T. L. Cocker *et al.*, *Nat. Photonics* **7**, 620–625 (2013).
17. K. Yoshioka *et al.*, *Nat. Photonics* **10**, 762–765 (2016).
18. V. Jelic *et al.*, *Nat. Phys.* **13**, 591–598 (2017).
19. K. Yoshioka *et al.*, *Nano Lett.* **18**, 5198–5204 (2018).
20. S. Yoshida *et al.*, *ACS Photonics* **6**, 1356–1364 (2019).
21. S. E. Ammerman *et al.*, *Nat. Commun.* **12**, 6794 (2021).
22. J. Allerbeck *et al.*, *ACS Photonics* **10**, 3888–3895 (2023).
23. Y. Luo *et al.*, *Phys. Rev. B* **102**, 205417 (2020).
24. M. Müller, N. Martín Sabanés, T. Kampfrath, M. Wolf, *ACS Photonics* **7**, 2046–2055 (2020).
25. M. Abdo *et al.*, *ACS Photonics* **8**, 702–708 (2021).
26. S. Sheng *et al.*, *Phys. Rev. Lett.* **129**, 043001 (2022).
27. S. Sheng *et al.*, *Nat. Phys.* **20**, 1603–1608 (2024).
28. L. Bobzien *et al.*, *APL Mater.* **12**, 051110 (2024).
29. C. Roelcke *et al.*, *Nat. Photonics* **18**, 595–602 (2024).
30. I. Katayama, K. Kimura, H. Imada, Y. Kim, J. Takeda, *J. Appl. Phys.* **133**, 110903 (2023).
31. M. Müller, *Prog. Surf. Sci.* **99**, 100727 (2024).
32. K. Kimura *et al.*, *ACS Photonics* **8**, 982–987 (2021).
33. L. Wang, Y. Xia, W. Ho, *Science* **376**, 401–405 (2022).
34. S. Cao *et al.*, *Nat. Chem.* **13**, 766–770 (2021).
35. H. Imada *et al.*, *Nature* **538**, 364–367 (2016).
36. Y. Zhang *et al.*, *Nature* **531**, 623–627 (2016).
37. H. Imada *et al.*, *Phys. Rev. Lett.* **119**, 013901 (2017).
38. B. Doppagne *et al.*, *Science* **361**, 251–255 (2018).
39. L. Zhang *et al.*, *Nat. Commun.* **8**, 580 (2017).
40. A. Rosławska *et al.*, *Nano Lett.* **18**, 4001–4007 (2018).
41. K. Kimura *et al.*, *Nature* **570**, 210–213 (2019).
42. K. Miwa *et al.*, *Nano Lett.* **19**, 2803–2811 (2019).
43. S. Jiang *et al.*, *Phys. Rev. Lett.* **130**, 126202 (2023).
44. J. Doležal *et al.*, *ACS Nano* **16**, 1082–1088 (2022).
45. J. Doležal, A. Sagwal, R. C. de Campos Ferreira, M. Švec, *Nano Lett.* **24**, 1629–1634 (2024).
46. H. Imada *et al.*, *Science* **373**, 95–98 (2021).
47. M. Imai-Imada *et al.*, *Nature* **603**, 829–834 (2022).
48. A. Grewal, C. C. Leon, K. Kuhnke, K. Kern, O. Gunnarsson, *ACS Nano* **17**, 13176–13184 (2023).
49. S. Fatayer *et al.*, *Nat. Nanotechnol.* **13**, 376–380 (2018).
50. S. Du, K. Yoshida, Y. Zhang, I. Hamada, K. Hirakawa, *Nat. Photonics* **12**, 608–612 (2018).
51. J. Shi *et al.*, *Nat. Nanotechnol.* **17**, 1288–1293 (2022).
52. R. Zhang *et al.*, *Nature* **498**, 82–86 (2013).
53. J. Lee, K. T. Crampton, N. Tallarida, V. A. Apkarian, *Nature* **568**, 78–82 (2019).
54. R. B. Jaculbia *et al.*, *Nat. Nanotechnol.* **15**, 105–110 (2020).
55. Y. Luo, A. Martin-Jimenez, R. Gutzler, M. Garg, K. Kern, *Nano Lett.* **22**, 5100–5106 (2022).
56. S. Fatayer *et al.*, *Science* **365**, 142–145 (2019).
57. K. Kimura *et al.*, Data for: Ultrafast on-demand exciton formation in a single-molecule junction by tailored terahertz pulses, Zenodo (2024); https://doi.org/10.5281/zenodo.1321896658.

ACKNOWLEDGMENTS

We thank Y. Hasegawa, Y. Shimizu, and E. Kazuma for technical support with tip fabrication and Y. Arashida, S. Yoshida, and K. Miwa for helpful discussions. K.K. was supported by the RIKEN Special Postdoctoral Researchers Program. J.J. was supported by a JSPS Invitational Fellowship. The numerical calculations were performed with the use of the HOKUSAI supercomputer system at RIKEN. All experiments were conducted at RIKEN. **Funding:** This work was supported by Grant-in-Aid for Scientific Research (S) JP20H05662 (H.I., I.K., J.T., and Y.Ki.); Grant-in-Aid for Transformative Research Areas (A) JP23H03979 (K.K.); Grant-in-Aid for Transformative Research Areas (A) JP21H05412 (K.K.); Grant-in-Aid for Early-Career Scientists JP21K14593 (K.K.); Grant-in-Aid for Scientific Research (S) JP22H04967 (K.K., H.I., and Y.Ki.); Grant-in-Aid for Scientific Research (A) JP20H00326 (H.I., I.K., J.T., and Y.Ki.); National Research Foundation of Korea Grant NRF-2021R1A2C1009191 (J.J.); Grant-in-Aid for Scientific Research (B) JP20H02728 (A.M.); Mitsubishi Foundation Grant 202110024 (J.T.); and the AMADA Foundation (J.T.). **Author contributions:** Conceptualization: K.K., H.I., I.K., J.T., Y.Ki.; Funding acquisition: K.K., J.J., A.M., H.I., I.K., J.T., Y.Ki.; Investigation: K.K., R.T., M.L.; Methodology: K.K., R.T., X.O., S.K., R.B.J., Y.Ka., J.J., A.M.; Project administration: J.T., Y.Ki.; Supervision: H.I., I.K., J.T., Y.Ki.; Visualization: K.K., R.T., M.L.; Writing – original draft: K.K., R.T., M.L.; Writing – review & editing: X.O., S.K., R.B.J., Y.Ka., J.J., A.M., H.I., I.K., J.T., Y.Ki. **Competing interests:** The authors declare no competing interests. **Data and materials availability:** All data needed to evaluate the conclusions in the paper are available in the main text or the supplementary materials. Data for all figures presented in this study are available from Zenodo (*57*).

SUPPLEMENTARY MATERIALS

science.org/doi/10.1126/science.ads2776
Materials and Methods
Supplementary Text
Figs. S1 to S20
References (*58*–*85*)
Movies S1 to S5

Submitted 6 August 2024; resubmitted 9 January 2025
Accepted 28 January 2025
10.1126/science.ads2776

ORGANIC CHEMISTRY

Catalytic remodeling of complex alkenes to oxonitriles through C=C double bond deconstruction

Zengrui Cheng[1]†, Kaimeng Huang[1,2]†, Chen Wang[1]†, Lili Chen[1]†, Xinyao Li[3], Zhibin Hu[1], Xinyuan Shan[4], Peng-Fei Cao[4], Haofeng Sun[5], Wei Chen[6], Chenhao Li[2], Ziyao Zhang[1], Hui Tan[1], Xue Jiang[1], Guikai Zhang[7], Zhongying Zhang[7], Min Lin[2], Liang Wang[8], Anmin Zheng[6,9], Changjiu Xia[2]*, Teng Wang[4], Song Song[1], Xingtian Shu[2], Ning Jiao[1,10]*

Deconstructive transformation of carbon-carbon double bonds (C=C) is a pivotal strategy in synthetic chemistry and drug discovery. Despite the substantial advances in olefin metathesis and ozonolysis for natural product synthesis through C=C double-bond cleavage, the catalytic remodeling of complex molecules through C=C double-bond deconstruction has been underdeveloped. We report a heterogeneous copper-catalyzed C=C double-bond cleavage, which enables the remodeling of complex molecules by converting the carbons on either side of the C=C double bond to carbonyl and cyano groups, respectively. In particular, this method provides an efficient protocol to conveniently transform terpenoids, glycals, steroids, and bioactive molecules to privileged scaffolds with underexplored chemical space.

Natural products are important chemical sources for drug discovery, and about 50% of new drugs have originated from natural products or their analogs (*1*–*3*). Well-known cases include artemisinin and finasteride, both derived through the cleavage of carbon-carbon double bonds (C=C) from artemisinic acid and androstenedione, respectively (Fig. 1A) (*4*, *5*). These cases demonstrate that the structural remodeling of C=C bond in complex molecules plays an important role in synthetic chemistry and drug discovery (*6*, *7*). Over the past decades, several high-profile methods for C=C double bond cleavage have been disclosed (*8*–*15*). However, except for some mild metathesis and ozonolysis, these approaches were hardly used in the remodeling of complex molecules because of the harsh conditions or limited functional group compatibility.

In contrast to olefin metathesis and oxidative cleavage methods that facilitate the formation of new C=C double bonds and carbonyl groups, the nitrogenation of C=C double bonds is equally crucial in constructing important nitrogen-containing compounds. For example, the well-developed aziridination and difunctionalization of C=C double bonds offer effective approaches for synthesizing nitrogen-containing compounds with the alkenyl skeleton unchanged (*16*–*26*). Very recently, Kwon and coworkers reported an elegant and mild aminodealkenylation reaction through C(sp^3)–C(sp^2) bond cleavage of the alkenyl skeleton of bioactive compounds (Fig. 1B) (*27*), which enables efficient skeleton remodeling (*28*–*32*) of pharmaceuticals, peptides, and nucleosides, avoiding the multistep transformation. Despite the prospective utility, the deconstructive nitrogenation of C=C double bond in natural and bioactive compounds is still underdeveloped because of the presence of multiple reactive sites and various functional groups in complex molecules. In addition, the cleavage of electron-deficient C=C double bonds exhibit low reactivity and is rarely reported (Fig. 1C) (*33*).

In this work, we present the design of a recyclable heterogeneous copper catalyst (CuO/*h*-TS-1) for the aerobic nitrogenation of C=C double bonds, enabling the synthesis of high-value nitrogen- and oxygen-containing compounds (Fig. 1D). In particular, in this study we converted various C=C bonds, including electron-deficient alkenes and C=C bonds in complex molecules that were inaccessible with a previous 2,2,6,6-tetramethylpiperidin-1-oxyl (TEMPO)–catalyzed method (*11*), into C=O and C≡N bonds, and we provide an innovative remodeling methodology of natural products and complex bioactive molecules—including terpenes, glycals, and steroids—through C=C double bond cleavage.

Reaction development

As an ongoing interest of ours in developing nitrogenation and oxygenation strategies through C–C bond cleavage (*34*, *35*), we aimed to remodel complex molecules through C=C double-bond cleavage to construct oxonitriles. However, our previously reported TEMPO-catalyzed method (*11*) exhibits three notable shortcomings: (i) the difficulty of addition of electrophilic azido radical to the electron-deficient alkenes (*36*, *37*); (ii) poor compatibility, hindering the skeletal remodeling of complex olefins such as steroids and terpenoids; and (iii) substantial consumption of unrecyclable catalysts. To tackle these problems, we hypothesized that an efficient catalyst should possess the ability to initiate and activate azido radical and should avoid acting as a radical scavenger (for example, TEMPO). Hence, we focused our efforts on screening transition-metal catalysts that meet these criteria for this reaction.

Our research commenced with the aerobic nitrogenation of the electron-deficient alkene **1** (table S1). As expected, the organocatalysts such as TEMPO and NHPI (*N*-hydroxyphthalimide) that act as both radical initiators and terminators could not catalyze the cleavage of **1** to oxonitrile **2** in the presence of azidotrimethylsilane ($TMSN_3$) and O_2 (table S1, entries 1 and 2). With $CoCl_2$, $MnBr_2$, $CuCl_2$, $FeCl_2$, or CuO as the catalyst, low yields of **2** were obtained (entries 3 to 7). Nano-sized CuO particles [diameter (d) < 50 nm] exhibited higher catalytic efficiency compared with bulk CuO (table S1, entry 7 versus entry 8). These results indicated that increasing the dispersion of the active centers is beneficial to improve the activity of the catalyst. Encouraged by previous studies on bimetallic molecular sieves (*38*–*41*), we designed and synthesized a series of transition-metal catalysts dispersed on three-dimensional zeolite substrates (table S1). The yield of **2** increased to 64% with CuO/TS-1 as the catalyst (table S1, entry 9). The iron-, cobalt-, or manganese oxide–loaded TS-1 could not catalyze the reaction (table S1, entries 10 to 12). No reaction occurred with the unloaded TS-1 or hierarchical TS-1 (*h*-TS-1) zeolite catalyst (table S1, entries 13 and 14). The copper oxide–loaded hierarchical TS-1 (CuO/*h*-TS-1, 6.5 mg, molar ratio of Cu/Si of 4/100) showed the best catalytic activity to deliver **2** in 76% yield (table S1, entry 17). The yield decreased to 30% when a physical mixture of CuO nanoparticles and *h*-TS-1 support was used as the catalyst (table S1, entry 21). The oxidative cleavage of **1** also occurred smoothly even with 0.2 mol % of CuO/*h*-TS-1 as the catalyst (table S1, entry 22).

Catalytic remodeling of complex molecules

The privileged scaffolds in natural products, because of their distinctive chemical diversity and biological relevance, have consistently occupied a foundational position in drug

---

[1] State Key Laboratory of Natural and Biomimetic Drugs, Chemical Biology Center, School of Pharmaceutical Sciences, Peking University, Beijing, China. [2] State Key Laboratory of Catalytic Materials and Reaction Engineering, Research Institute of Petroleum Processing, SINOPEC, Beijing, China. [3] Department of Chemistry, College of Sciences, Shanghai Engineering Research Center of Organ Repair, Shanghai University, Shanghai, China. [4] College of Chemistry, State Key Laboratory of Organic-Inorganic Composites, Beijing University of Chemical Technology, Beijing, China. [5] Key Laboratory of Precision and Intelligent Chemistry, University of Science and Technology of China, Hefei, China. [6] State Key Laboratory of Magnetic Resonance and Atomic and Molecular Physics, Innovation Academy for Precision Measurement Science and Technology, Chinese Academy of Sciences, Wuhan, China. [7] Beijing Synchrotron Radiation Facility, Institute of High Energy Physics, University of Chinese Academy of Sciences, Beijing, China. [8] Key Lab of Biomass Chemical Engineering of Ministry of Education, College of Chemical and Biological Engineering, Zhejiang University, Hangzhou, China. [9] Interdisciplinary Institute of NMR and Molecular Sciences, School of Chemistry and Chemical Engineering, Wuhan University of Science and Technology, Wuhan, China. [10] Changping Laboratory, Beijing, China.
*Corresponding author. Email: jiaoning@pku.edu.cn (N.J.); xiachangjiu.ripp@sinopec.com (C.X.)
†These authors contributed equally to this work.

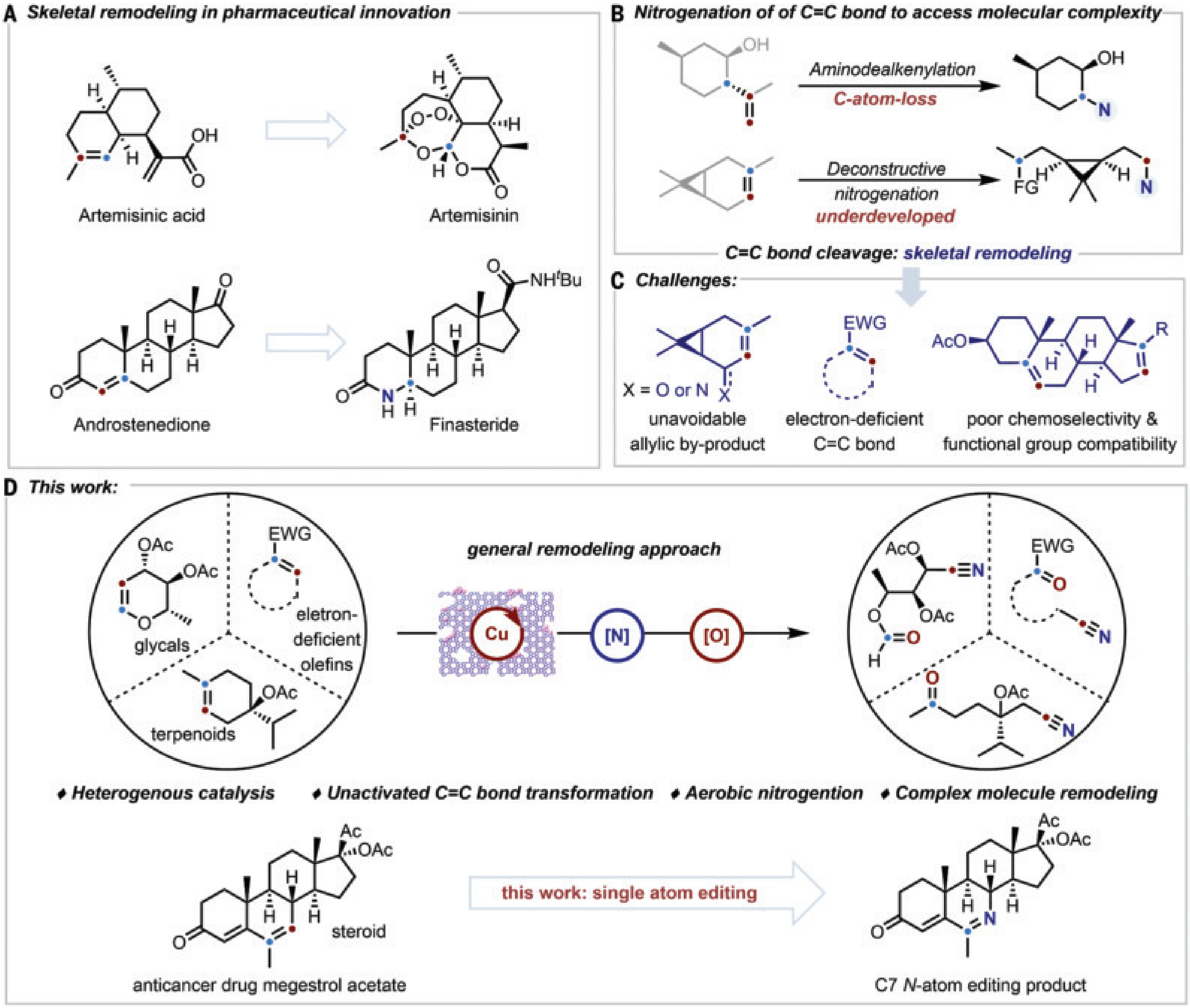

Fig. 1. Cleavage of C=C double bonds. (**A**) Skeletal remodeling through C=C double-bond cleavage in synthetic chemistry and drug discovery. (**B**) Nitrogenation of C=C double bonds with skeletal remodeling. (**C**) The challenges of remodeling complex molecules through C=C double-bond deconstruction. (**D**) This work. Heterogeneous CuO/*h*-TS-1 catalyzed aerobic nitrogenation of olefins.

discovery (*42*, *43*). However, these natural compounds often present attributes such as an abundance of sp^3-hybridized carbon atoms and oxygen atoms, along with numerous hydrogen bond acceptors and donors, juxtaposed with a relative paucity of nitrogen atoms (*3*). Despite the crucial role that nitrogen atoms play in medicinal chemistry, developing methodologies to incorporate nitrogen-containing groups into such scaffolds remains a major challenge (*44*).

Nitrogen-containing group-modified steroids exhibit enhanced properties—including antimicrobial, antiviral, anti-inflammatory, and anticancer activity—compared with the original compounds (*45*). With the optimal conditions in hand, we focused our attention toward the aerobic nitrogenation of steroids containing C=C double bonds. This protocol suppressed the undesirable allylic oxidation at the C-7 position (*46*, *47*) and selectively produced a series of valuable B-ring 5,6-secosteroids (**3** to **7**) that are inaccessible with traditional methods (Fig. 2A). The structure of **5** was confirmed by means of x-ray crystallography. Bioactive molecules or their derivatives were cleaved under our conditions in moderate yields (Fig. 2B, **8** to **10**). Abiraterone acetate was selectively converted to 16,17-seco derivative without interference from the pyridyl group. However, under the prior TEMPO-catalyzed conditions, these steroids exhibited very low reaction efficiency.

Although previous approaches have predominantly focused on modifying the side chains and peripheral A or D rings of steroids, core skeletal modification, especially by means of single-atom editing, is a largely unmet challenge (*29*, *31*). To demonstrate the practicality of aerobic nitrogenation reactions, the HegG2 inhibitor medroxyprogesterone acetate was converted into oxonitrile **11** in 80% yield at 5 mmol scale. After the hydrolysis and Hofmann rearrangement, **11** was rapidly converted to **13**, which was the product of the nitrogen atom exchange of medroxyprogesterone acetate at the C7 position.

This approach was applied in remodeling terpenoids that possess C=C double bonds

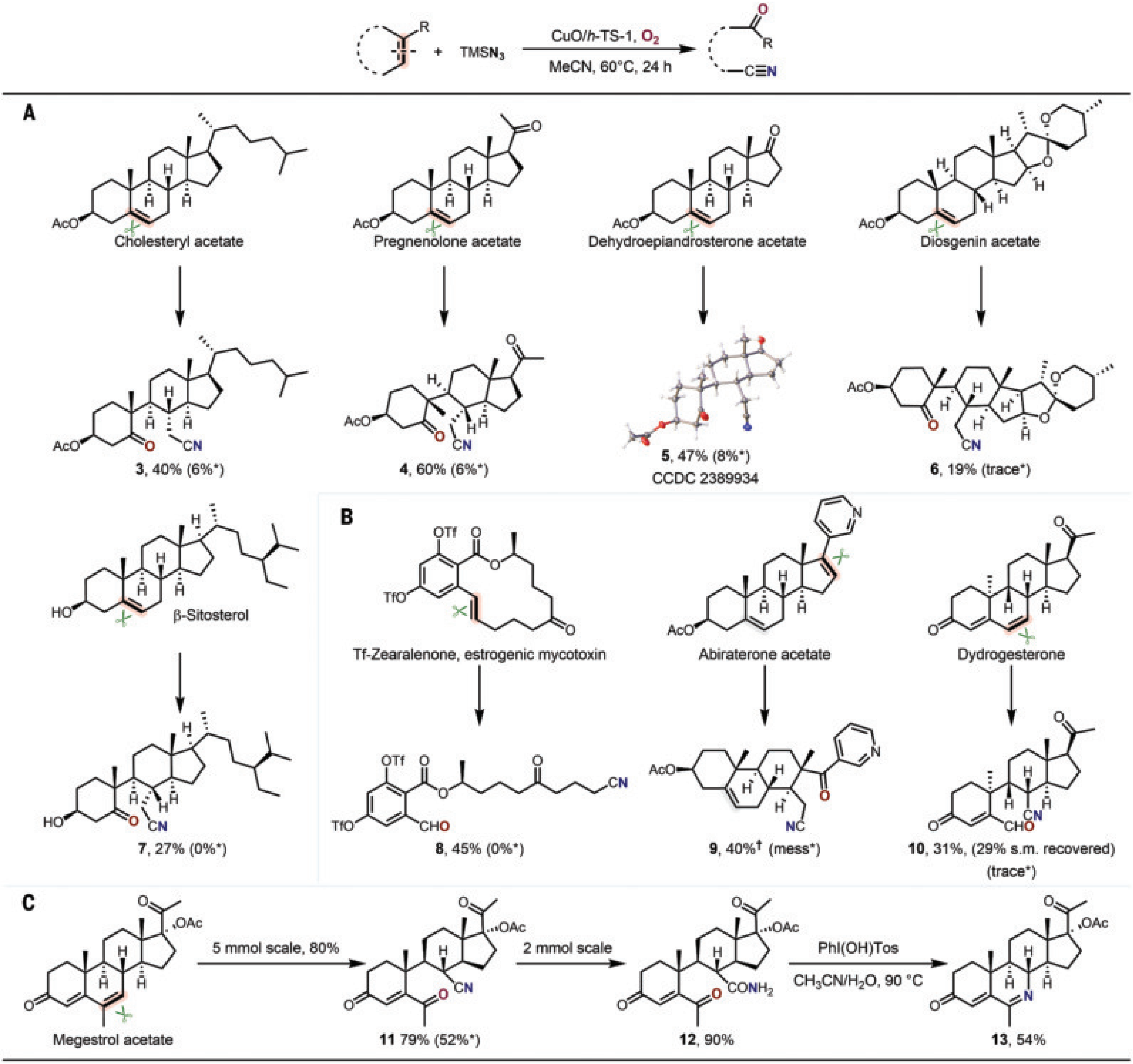

Fig. 2. Steroid modification. (**A**) Deconstructive aerobic nitrogenation of steroids. (**B**) Deconstructive aerobic nitrogenation of bioactive molecules. (**C**) Gram-scale preparation and atom exchange of megestrol acetate. General reaction conditions for C=C double-bond cleavage: The solution of olefin (0.3 mmol), TMSN$_3$ (0.6 mmol), and CuO/*h*-TS-1 (6.5 mg) in MeCN was stirred at 60°C under O$_2$ atmosphere. Isolated yields. *The yields under previous TEMPO catalysis are provided for comparison. †The reaction was conducted at 80°C. Experimental details are provided in the supplementary materials.

(Fig. 3). The oxidative cleavage of (1*S*, 6*R*)-(+)-3-carene yielded a *cis*-cyclopropane **14** in 41% yield. Similarly, derivatives of (1*R*)-(+)-α-pinene and (1*R*)-(−)-nopol, which contain a cyclobutane, underwent cleavage to yield diverse chiral cyclobutane structures, accommodating hydroxyl, azide, ester, and amide functionalities (**15** and **21** to **24**). Furthermore, the cleavage of (−)-α-cedrene facilitated the synthesis of a complex bicyclo[3.3.0]octane skeleton (**16**), demonstrating the protocol's efficacy in generating chiral cyclopropanes, cyclobutanes, and cyclopentanes with varied functional groups. When (*R*)-(−)-terpine-4-ol acetate and derivatives thereof were subjected to standard conditions, oxonitriles featuring a chiral quaternary carbon center were obtained in moderate yields (**17** to **19**). The cyclic and exocyclic double bonds in (1*R*, 4*E*, 9*S*)-(−)-β-caryophyllene were simultaneously cleaved to afford trans-substituted cyclobutane derivative **20**. These instances underscore that complex terpenoid compounds are viable substrates for this methodology, heralding new avenues for diversifying the structural frameworks of complex molecules. In most cases, the TEMPO-catalyzed method is ineffective for these unactivated olefins present in natural products.

Recognizing the crucial role of the cyano group in drug design, the nitrogenation of the terminal isobutenyl group in terpenoid structures was investigated (*48*, *49*). The acyclic alkyl nitrile products (**25** to **29**) were prepared from the cleavage of one or two C=C double bonds in compounds such as osthole; (*S*)-(−)-β-citronellol and its acetate, nerol; and α-bisabolol derivatives. The cleavage of one or two double bonds of myrac alcohol and its corresponding ester derivative was selectively controlled by the hydroxy group to afford products **30**, **31**, and **31′**, respectively. In addition, glycals (such as 3,4,6-tri-*O*-acetyl-D-glucal, 3,4,6-

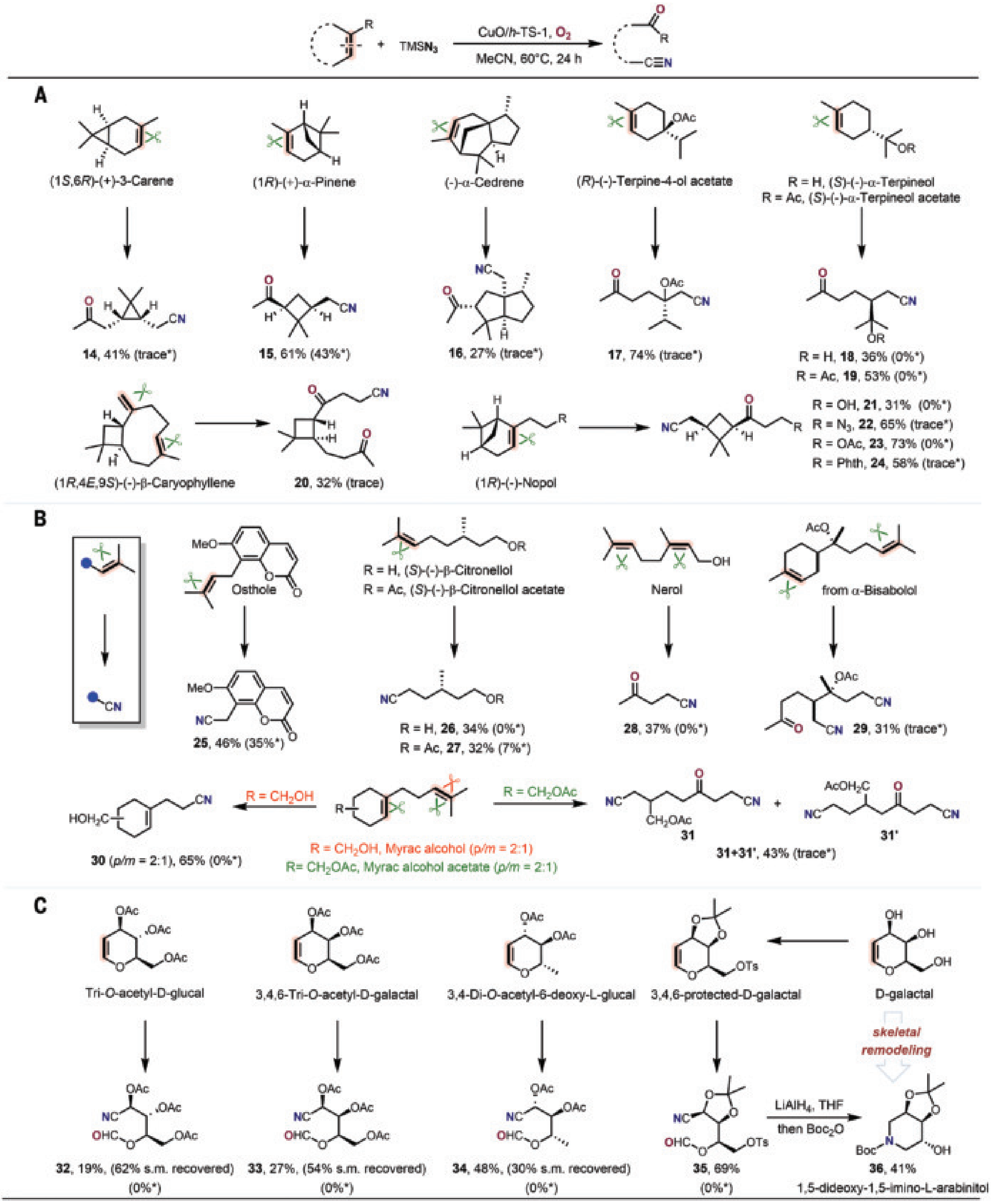

Fig. 3. Terpenoid modification. (**A**) Deconstructive aerobic nitrogenation of terpenoids. (**B**) Cyanation modification of terminal isobutene motifs in natural product derivatives. (**C**) Deconstructive aerobic nitrogenation of glycals. General reaction conditions for C=C bond cleavage: The solution of olefin (0.3 mmol), $TMSN_3$ (0.6 mmol), and CuO/*h*-TS-1 (6.5 mg) in MeCN was stirred at 60°C under O_2 atmosphere. Isolated yields. *The yields under previous TEMPO catalysis are provided for comparison. Detailed reaction conditions are provided in the supplementary materials.

tri-*O*-acetyl-D-galactal, and 3,4-di-*O*-acetyl-6-deoxy-L-glucal) could be converted to cyano-substituted formates (**32** to **34**) with starting materials recovered. However, the transformation of glycals is entirely unachievable under TEMPO-catalysis. The present protocol could efficiently remodel D-galactal into 1,5-dideoxy-1,5-imino-L-arabinitol **36** through the C=C bond–cleaved intermediate **35** (Fig. 3C). This methodology underscores the versatility of cyano group incorporation in terpenoid and glycal chemistry, paving the way for innovative approaches in bioactive molecule design.

Olefin scope of deconstructive nitrogenation

Besides complex molecules, the present method was also successfully applied in the remodeling of simple olefins (Fig. 4). For trisubstituted cyclic olefins, the ring size or functional groups such as phenyl, halogen, ether, or carbonyl showed little influence on the reaction efficiencies, and a series of electron-deficient olefins were smoothly converted to oxonitriles (**2** and **37** to **44**) in good yields under the standard conditions. The cleavage of phenyl cyclohexene or even larger cyclic olefins proceeded to deliver long-chain oxonitriles (**45** to

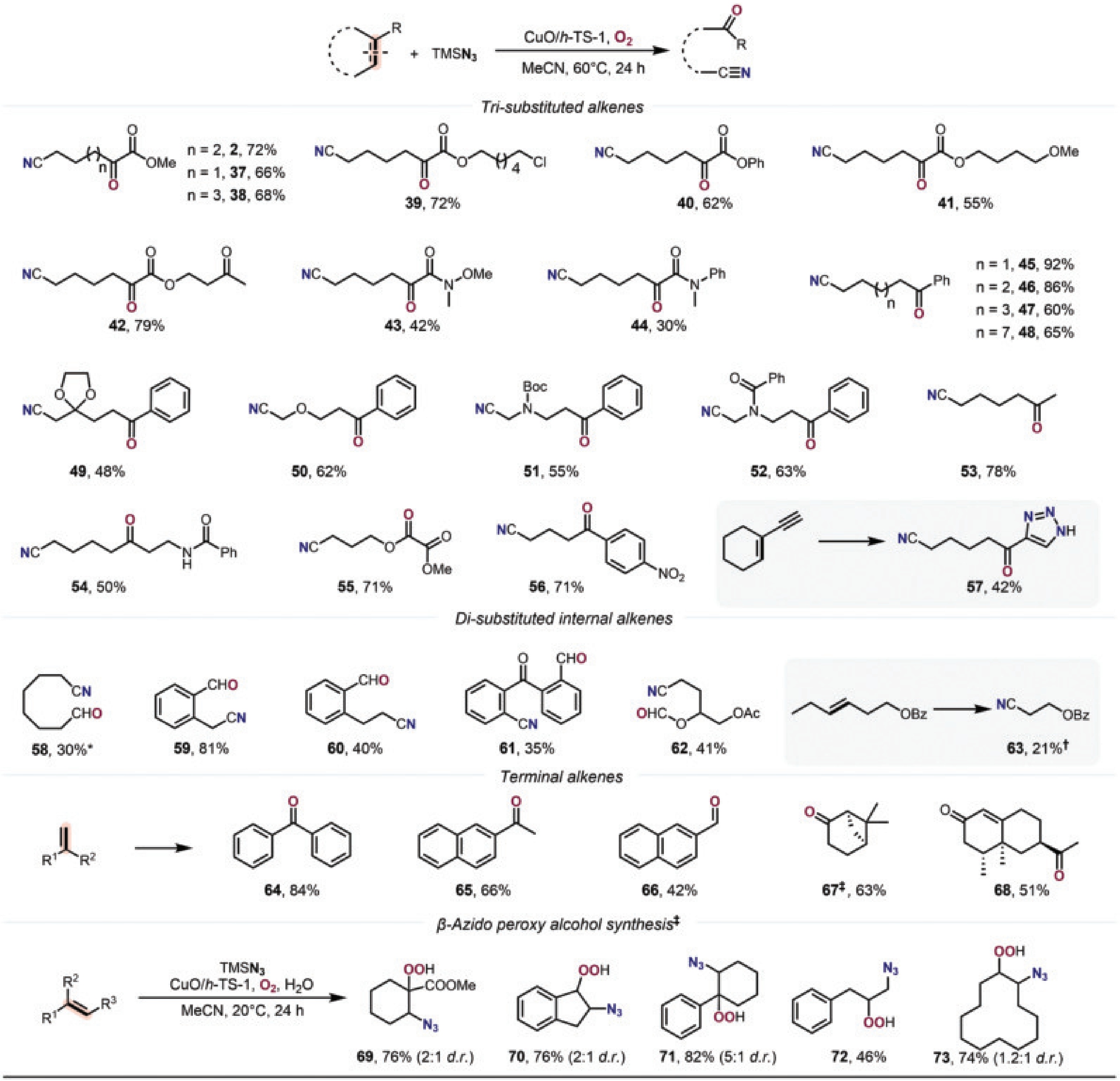

Fig. 4. Olefin scope of heterogeneous catalytic aerobic nitrogenation. General reaction conditions: The solution of olefin (0.3 mmol), TMSN$_3$ (0.6 mmol), and CuO/*h*-TS-1 (6.5 mg) in MeCN (2 mL) was stirred under oxygen atmosphere at 60°C for 24 hours. Isolated yields. *The reaction was carried out at room temperature for 48 hours. †The reaction was carried out at 80°C for 24 hours. ‡The azide-peroxidation of olefins. Reaction conditions: The solution of olefin (0.3 mmol), TMSN$_3$ (0.6 mmol), H$_2$O (3 mmol), and CuO/*h*-TS-1 (6.5 mg) in MsseCN (2 mL) was stirred under oxygen atmosphere at 20°C for 24 hours. Isolated yields.

48) in good yields. Besides, the acid-sensitive ketal group on the cyclohexene scaffold was well tolerated to deliver product **49** in moderate yield. Moreover, dihydropyrans, *N*-protected 1,2,3,6-tetrahydropyridines, and alkyl-substituted cyclohexenes (**50** to **55**) were cleaved smoothly. Electron-deficient aryl-substituted cyclopentene underwent cleavage to deliver compound **56** in 71% yield. The CuO/*h*-TS-1 could simultaneously catalyze the deconstruction of a C=C double bond followed by click reaction of the C≡C triple bond to afford tetrazole **57** in 42% yield.

Next, the cleavage of disubstituted olefins such as cyclooctene, indene, dihydronaphthalene, and 5-dibenzosuberenone produced oxonitriles

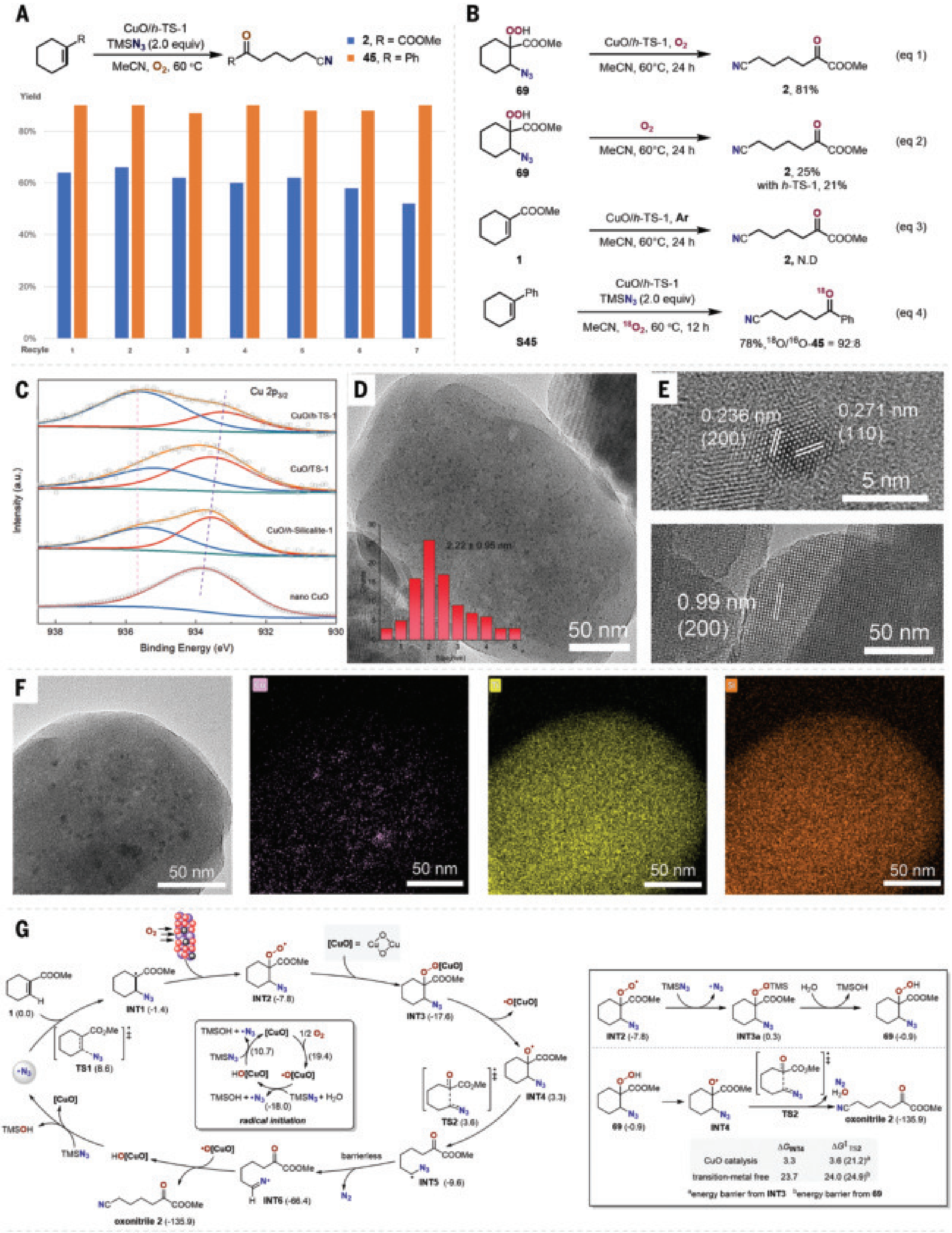

	ΔG_INT4	ΔG‡_TS2
CuO catalysis	3.3	3.6 (21.2)[a]
transition-metal free	23.7	24.0 (24.9)[b]

[a]energy barrier from INT3 [b]energy barrier from 69

Fig. 5. Mechanistic studies. (**A**) Recycling experiments. (**B**) Control experiments to determine the main influencing factors and isotope labeling experiment. (**C**) XPS spectra of Cu-containing catalysts. (**D** and **E**) TEM images of CuO/*h*-TS-1 with different magnification. (**F**) TEM– energy-dispersive x-ray spectroscopy mapping images of CuO/*h*-TS-1 particles. (**G**) Proposed mechanism based on DFT-calculated energy profiles for the aerobic nitrogenation of substrate **1**. Energies are given in kilocalories per mole with respect to substrate **1**.

(**58** to **61**) under standard conditions. 3,4-Dihydro-2*H*-pyran derivative was cleaved to cyano-substituted formate ester **62**. The inactive linear aliphatic olefin was converted to the corresponding product **63** with lower yield owing to poor regioselectivity. In addition to cyclic olefins, the present catalytic system was also applied in the cleavage of terminal olefins to afford ketones or aldehydes with high efficiency (**64** to **68**). Moreover, when the reaction was carried out at 20°C in the presence of water, the C=C double bond of olefin **1** was not cleaved, but β-azido peroxy alcohol **69** was obtained in 76% yield. This strategy thereby provides an efficient approach to β-azido peroxy alcohols (**70** to **73**).

Additionally, another advantage of this protocol is that the CuO/*h*-TS-1 catalyst could be recycled without substantial loss in the yields after running multiple cycles. For the oxidative cleavage reaction of methyl cyclohex-1-ene-1-carboxylate and 1-phenyl cyclohexene, the catalyst CuO/*h*-TS-1 was reused seven times without obvious deterioration in catalytic activity (Fig. 5A). The content of copper in the solvent was measured with inductively coupled plasma atomic emission spectroscopy (ICP-AES) after each cycle, indicating that almost no copper (<1 part per million) was lost from CuO/*h*-TS-1 (supplementary materials).

Some control experiments were conducted to investigate the mechanism (Fig. 5B). β-Azido peroxy alcohol **69** was converted to oxonitrile **2** in the presence of CuO/*h*-TS-1 and *h*-TS-1 catalyst in 81 and 21% yield, respectively. In addition, **69** could be partially converted into product **2** under O_2 without catalyst (Fig. 5B, eq 1 and eq 2). These results indicated that the CuO/*h*-TS-1 also played a major promotive role in the transformation of β-azido peroxy alcohol. The oxidative cleavage reaction cannot occur under argon atmosphere (Fig. 5B, eq 3). An isotope-labeling experiment was carried out under $^{18}O_2$, and ^{18}O-**45** was obtained in 78% yield, clearly indicating that $^{18}O_2$ served as the oxygen source in this reaction (Fig. 5B, eq 4).

To better understand the catalytic performance of CuO/*h*-TS-1, multiple characterization experiments were conducted to comprehensively reveal the dispersion and the chemical state of Cu-based species (preparation and characterization details are provided in the supplementary materials). For comparison, we also synthesized *h*-TS-1, CuO/*h*-S-1, and CuO/TS-1. The oxidation state of Cu was estimated by means of x-ray photoelectron spectroscopy (XPS) analysis (Fig. 5C). For the Cu 2p spectra, CuO/*h*-S-1, CuO/TS-1, and CuO/*h*-TS-1 all show two main peaks at ~935 and 955 eV, with spin-orbit splitting separation and with 20 eV corresponding to Cu $2p_{3/2}$ and $2p_{1/2}$, respectively, which confirms that the Cu-containing species in different samples are predominantly in a +2 oxidation state. The $Cu2p_{3/2}$ BE peaks of these loaded catalysts are quite similar to the peak of nano CuO. The O 1s spectrum of CuO/*h*-S-1 can be fit by two peaks at ~533 and ~532.2 eV, which correspond to the Si–O–Si and adsorbed oxygen species, respectively (fig. S9A). The absence of characteristic peaks of CuO in O 1s may arise from the low content of CuO, which was also confirmed with the x-ray diffraction (XRD) pattern in which no crystalline Cu species were detected for CuO/*h*-TS-1 (fig. S10).

In addition, we used transmission electron microscopy (TEM) to directly investigate the dispersion of CuO nanoparticles inside *h*-TS-1 (Fig. 5, C to F). The TEM images of different magnifications show that there are no bulk CuO crystals or large CuO nanoparticles. The abundance of open intracrystalline mesopores in *h*-TS-1 likely favors the mass diffusion inside the zeolite. The high-resolution TEM (Fig. 5E) shows the presence of CuO (200) and (110) planes with interplanar *d*-spacing of 0.236 and 0.271 nm, respectively, because the 0.99 nm lattice fringe corresponds to the (200) crystal face of *h*-TS-1. Moreover, as illustrated with the element mapping images in Fig. 5F, both Si and Ti species are evenly distributed in the zeolite particles and are thus in accord with the results from XPS and TEM. Consequently, the highly dispersed CuO particles in mesopores in CuO/*h*-TS-1 might have a positive effect on the azido radical initiation and catalytic activity, which is consistent with the screening results in the cleavage of **1** by CuO/*h*-TS-1 catalyst (table S1, entry 17). To further verify the mechanism, we carried out several experiments using electron paramagnetic resonance (EPR) with 5,5-dimethyl-1-pyrroline *N*-oxide (DMPO) as the trapping agent. Some weak signals of azido radical were detected when $TMSN_3$ was heated under oxygen atmosphere, and the concentration of azido radical was enhanced by the addition of copper catalyst (figs. S12 and S13).

Density functional theory (DFT) calculations suggest that the reaction proceeds through a crucial Cu-assisted O–O bond cleavage step (Fig. 5G) (*50*). The **INT2** was generated through azido radical addition and oxygen capture, subsequently combined with [CuO] catalyst to form **INT3**. The **INT3** can be further fragmented to provide **INT4**, along with the formation of [CuO]O• species. The consequent C–C cleavage process through transition-state **TS2** required a free-energy barrier of 21.2 kcal/mol from **INT3**, suggesting that the C–C bond cleavage to form **INT5** was a rate-determining step. Next, the α-azido radical induced the thermal azido N–N bond cleavage with N_2 release through a barrierless transition state, which was a highly exergonic process to afford **INT6**. The final hydrogen abstraction was facilitated by [CuO]O• species to yield the product **2**, along with [CuO]OH species, which could further oxidize $TMSN_3$ to afford azido radical to complete the catalytic circle. Therefore, CuO played dual roles as an efficient catalyst for the generation of azido radical and a promoter for O–O bond homolysis and C–C bond cleavage. The β-azido peroxy alcohol intermediate was obtained through oxidation of $TMSN_3$ by **INT2**, followed by hydrolysis. The consequent C–C bond cleavage of β-azido alcohol by means of **TS2** required a free-energy barrier of 24.9 kcal/mol from **69**, indicating a disfavored pathway in comparison with the CuO-catalytic pathway (fig. S15).

This chemistry provides a powerful protocol to build compound libraries with expanded chemical space and substantially enlarges the frontier of synthetic chemistry and drug discovery.

REFERENCES AND NOTES

1. A. L. Harvey, *Drug Discov. Today* **13**, 894–901 (2008).
2. J. W.-H. Li, J. C. Vederas, *Science* **325**, 161–165 (2009).
3. A. G. Atanasov, S. B. Zotchev, V. M. Dirsch, C. T. Supuran, International Natural Product Sciences Taskforce, *Nat. Rev. Drug Discov.* **20**, 200–216 (2021).
4. Z.-X. Jiang, J.-Q. Ye, L. Jiang, Y.-S. Zhao, *Steroids* **70**, 690–693 (2005).
5. Z. Amara *et al*., *Nat. Chem.* **7**, 489–495 (2015).
6. S. Wang, G. Dong, C. Sheng, *Chem. Rev.* **119**, 4180–4220 (2019).
7. T. Rodrigues, D. Reker, P. Schneider, G. Schneider, *Nat. Chem.* **8**, 531–541 (2016).
8. S. G. Van Ornum, R. M. Champeau, R. Pariza, *Chem. Rev.* **106**, 2990–3001 (2006).
9. A. Ruffoni, C. Hampton, M. Simonetti, D. Leonori, *Nature* **610**, 81–86 (2022).
10. A. H. Hoveyda, A. R. Zhugralin, *Nature* **450**, 243–251 (2007).
11. T. Wang, N. Jiao, *J. Am. Chem. Soc.* **135**, 11692–11695 (2013).
12. J. Wang, H. Lu, Y. He, C. Jing, H. Wei, *J. Am. Chem. Soc.* **144**, 22433–22439 (2022).
13. X. Qiu *et al*., *Nature* **597**, 64–69 (2021).
14. G. C. Vougioukalakis, R. H. Grubbs, *Chem. Rev.* **110**, 1746–1787 (2010).
15. R. R. Schrock, A. H. Hoveyda, *Angew. Chem. Int. Ed.* **42**, 4592–4633 (2003).
16. L. Legnani, G. Prina-Cerai, T. Delcaillau, S. Willems, B. Morandi, *Science* **362**, 434–439 (2018).
17. M. Ošeka *et al*., *Chem* **7**, 255–266 (2021).
18. D. E. Holst, D. J. Wang, M. J. Kim, I. A. Guzei, Z. K. Wickens, *Nature* **596**, 74–79 (2021).
19. Q.-Q. Cheng *et al*., *Nat. Catal.* **3**, 386–392 (2020).
20. A. J. Musacchio *et al*., *Science* **355**, 727–730 (2017).
21. J. Gui *et al*., *Science* **348**, 886–891 (2015).
22. N. Fu, G. S. Sauer, A. Saha, A. Loo, S. Lin, *Science* **357**, 575–579 (2017).
23. Y. Yang, S.-L. Shi, D. Niu, P. Liu, S. L. Buchwald, *Science* **349**, 62–66 (2015).
24. J. L. Jat *et al*., *Science* **343**, 61–65 (2014).
25. T. Piou, T. Rovis, *Nature* **527**, 86–90 (2015).
26. T. M. Monos, R. C. McAtee, C. R. J. Stephenson, *Science* **361**, 1369–1373 (2018).
27. Z. He, J. A. Moreno, M. Swain, J. Wu, O. Kwon, *Science* **381**, 877–886 (2023).
28. S. H. Kennedy, B. D. Dherange, K. J. Berger, M. D. Levin, *Nature* **593**, 223–227 (2021).
29. J. C. Reisenbauer, O. Green, A. Franchino, P. Finkelstein, B. Morandi, *Science* **377**, 1104–1109 (2022).
30. J. Woo *et al*., *Science* **376**, 527–532 (2022).
31. M. Kamitani *et al*., *Science* **379**, 484–488 (2023).
32. J. Jurczyk *et al*., *Science* **373**, 1004–1012 (2021).
33. M. J. Koh, T. T. Nguyen, H. Zhang, R. R. Schrock, A. H. Hoveyda, *Nature* **531**, 459–465 (2016).
34. J. Liu *et al*., *Science* **367**, 281–285 (2020).
35. Y.-F. Liang, N. Jiao, *Acc. Chem. Res.* **50**, 1640–1653 (2017).
36. F. Parsaee *et al*., *Nat. Rev. Chem.* **5**, 486–499 (2021).
37. M. Shee, N. D. P. Singh, *Chem. Soc. Rev.* **51**, 2255–2312 (2022).

38. J. M. Thomas, R. Raja, G. Sankar, R. G. Bell, *Nature* **398**, 227–230 (1999).
39. L. Liu, A. Corma, *Chem. Rev.* **123**, 4855–4933 (2023).
40. C. P. Gordon *et al.*, *Nature* **586**, 708–713 (2020).
41. M. B. Gawande *et al.*, *Chem. Rev.* **116**, 3722–3811 (2016).
42. A. L. Harvey, R. Edrada-Ebel, R. J. Quinn, *Nat. Rev. Drug Discov.* **14**, 111–129 (2015).
43. M. E. Welsch, S. A. Snyder, B. R. Stockwell, *Curr. Opin. Chem. Biol.* **14**, 347–361 (2010).
44. R. Singh, G. Panda, *Tetrahedron* **69**, 2853–2884 (2013).
45. M. M. Heravi, V. Zadsirjan, *RSC Adv.* **10**, 44247–44311 (2020).
46. E. J. Horn *et al.*, *Nature* **533**, 77–81 (2016).
47. Y. Jiang, S. Chen, Y. Chen, A. Gu, C. Tang, *J. Am. Chem. Soc.* **146**, 2769–2778 (2024).
48. F. F. Fleming, L. Yao, P. C. Ravikumar, L. Funk, B. C. Shook, *J. Med. Chem.* **53**, 7902–7917 (2010).
49. D. C. Blakemore *et al.*, *Nat. Chem.* **10**, 383–394 (2018).
50. X. Sun *et al.*, *J. Am. Chem. Soc.* **137**, 6059–6066 (2015).

ACKNOWLEDGMENTS

We thank J. Peng and S. Shi in this group for reproducing the results of **40**, **42**, **48**, and **50**. **Funding:** Financial support from the National Key R&D Program of China (2021YFA1501700), the NSFC (22293014, 22131002, and 22161142019), Changping Laboratory, the New Cornerstone Science Foundation through the New Cornerstone Investigator Program, and the XPLORER PRIZE are greatly appreciated. **Author contributions:** Z.C., K.H., C.X., and N.J. conceived and designed the experiments. Z.C., K.H., C.W., and L.C. carried out most of experiments; X.L. conducted the DFT calculations. Z.C., K.H., C.W., L.C., X.L. Z.H., X.S., P.-F.C., H.S., W.C., C.L., Zi.Z., H.T., X.J., G.Z., Zh.Z., M.L., L.W., A.Z., C.X., T.W., S.S., X.S., and N.J. analyzed data. Z.C., K.H., C.W. L.C., X.L. X.S., T.W., S.S., C.X., and N.J. wrote the paper. N.J. directed the research. **Competing interests:** N.J., Z.C., K.H., C.W., and L.C. are inventors on a patent application (CN202510186755.3) held by Peking University. All authors declare no other competing financial interests. **Data and materials availability:** Cambridge Crystallographic Data Centre (CCDC) nos. 2389934 (compound **5**) contain the supplemental crystallographic data for this paper. These data can be obtained free of charge from www.ccdc.cam.ac.uk/data_request/cif, by emailing data_request@ccdc.cam.ac.uk, or by contacting the CCDC. All other data are available in the main text or the supplementary materials.

SUPPLEMENTARY MATERIALS

science.org/doi/10.1126/science.adq8918
Materials and Methods
Supplementary Text
Figs. S1 to S15
Tables S1 to S13
Spectral Data
References (*51*–*82*)

Submitted 5 June 2024; accepted 20 December 2024
10.1126/science.adq8918

BIODIVERSITY

Rapid butterfly declines across the United States during the 21st century

Collin B. Edwards[1,2]*, Elise F. Zipkin[3], Erica H. Henry[1,2], Nick M. Haddad[3,4], Matthew L. Forister[5], Kevin J. Burls[6], Steven P. Campbell[7], Elizabeth E. Crone[8], Jay Diffendorfer[9], Margaret R. Douglas[10], Ryan G. Drum[11], Candace E. Fallon[6], Jeffrey Glassberg[12,13], Eliza M. Grames[14], Rich Hatfield[6], Shiran Hershcovich[15], Scott Hoffman Black[6], Elise A. Larsen[16], Wendy Leuenberger[3], Mary J. Linders[2], Travis Longcore[17,18], Daniel A. Marschalek[19], James Michielini[20], Naresh Neupane[16], Leslie Ries[16], Arthur M. Shapiro[20], Ann B. Swengel†, Scott R. Swengel†, Douglas J. Taron[21], Braeden Van Deynze[2], Jerome Wiedmann[22], Wayne E. Thogmartin[23], Cheryl B. Schultz[1]

Numerous declines have been documented across insect groups, and the potential consequences of insect losses are dire. Butterflies are the most surveyed insect taxa, yet analyses have been limited in geographic scale or rely on data from a single monitoring program. Using records of 12.6 million individual butterflies from >76,000 surveys across 35 monitoring programs, we characterized overall and species-specific butterfly abundance trends across the contiguous United States. Between 2000 and 2020, total butterfly abundance fell by 22% across the 554 recorded species. Species-level declines were widespread, with 13 times as many species declining as increasing. The prevalence of declines throughout all regions in the United States highlights an urgent need to protect butterflies from further losses.

The loss of vertebrate and plant species has been well documented (*1*–*3*), but recent attention has shifted to losses of the most diverse taxonomic group on the planet: insects (*4*–*7*). Insect declines are particularly distressing because of the ubiquitous role that they play in ecological processes—including pollination, cycling of nutrients from dead organisms and dung, and pest control—and as food sources for multiple taxa (*4*, *8*, *9*). Despite their considerable diversity and biomass, both of which contribute to their ecological and economic importance, insects are substantially understudied (*10*). As such, the scope and scale of their declines are poorly documented.

Of all insect groups, butterflies are the most extensively monitored. In the United States (US), butterflies have been the focus of volunteer-based and expert science monitoring programs since 1975, with dozens of local-to-regional programs now monitoring butterfly populations (*11*). Efforts to analyze these monitoring data have focused on estimating trends within limited geographic regions (typically a single state) and/or from a single monitoring program (*12*–*17*). The patchwork nature of existing studies renders it difficult to determine whether disparities reflect differences in geographic regions or monitoring programs and to identify the extent to which localized species patterns are consistent across their ranges. A unified analysis of trends at a national scale can guide the enormous tasks associated with insect conservation and management and is a necessary first step in pinpointing the causes of broad-scale butterfly declines (*18*).

We assembled a comprehensive dataset of systematic, decades-long butterfly monitoring within the contiguous US (i.e., the lower 48 states and Washington, DC) from 2000 to 2020 (Fig. 1A). Data sources included every available multispecies butterfly monitoring program of state, regional, and national scale in the contiguous US, as well as several that target individual species, totaling 35 programs (table S1). These monitoring programs differ in their data collection methods, and one of the key challenges that we addressed in our analyses was integrating the available data while appropriately accounting for heterogeneity across programs. Data for 12.6 million individual butterflies comprising 554 species were accumulated from 76,957 surveys of 2478 unique locations.

Using these data, we (i) calculated the trend in total butterfly abundance across the contiguous US and (ii) estimated species-level trends in abundance for 342 individual species with sufficient data [(*19*); fig. S1 and table S2]. To

---

[1]School of Biological Science, Washington State University, Vancouver, WA, USA. [2]Washington Department of Fish and Wildlife, Olympia, WA, USA. [3]Department of Integrative Biology; Ecology, Evolution, and Behavior Program, Michigan State University, East Lansing, MI, USA. [4]Kellogg Biological Station, Michigan State University, Hickory Corners, MI, USA. [5]Department of Biology; Program in Ecology, Evolution, and Conservation Biology, University of Nevada, Reno, NV, USA. [6]Xerces Society for Invertebrate Conservation, Portland, OR, USA. [7]Albany Pine Bush Preserve Commission, Albany, NY, USA. [8]Department of Evolution and Ecology, University of California, Davis, CA, USA. [9]US Geological Survey Geosciences and Environmental Change Sciences Center, Denver, CO, USA. [10]Department of Environmental Studies and Environmental Science, Dickinson College, Carlisle, PA, USA. [11]US Fish and Wildlife Service – Center for Pollinator Conservation, Bloomington, MN, USA. [12]North American Butterfly Association, Morristown, NJ, USA. [13]Department of Biosciences, Rice University, Houston, TX, USA. [14]Department of Biological Sciences, Binghamton University, Binghamton, NY, USA. [15]Butterfly Pavilion, Westminster, CO, USA. [16]Department of Biology, Georgetown University, Washington, DC, USA. [17]Institute of the Environment and Sustainability, University of California, Los Angeles, CA, USA. [18]The Urban Wildlands Group, Los Angeles, CA, USA. [19]Department of Biological and Clinical Sciences, University of Central Missouri, Warrensburg, MO, USA. [20]Center for Population Biology, University of California, Davis, CA, USA. [21]Chicago Academy of Sciences–Peggy Notebaert Nature Museum, Chicago, IL, USA. [22]Ohio Lepidopterists, Columbus, OH, USA. [23]US Geological Survey Upper Midwest Environmental Sciences Center, La Crosse, WI, USA.
***Corresponding author. Email: edwards.evoeco@gmail.com**
†Independent researcher.

account for spatial variation and align with broad-scale conservation decision-making, we aggregated our data into seven geographic regions based on the US Fish and Wildlife Service regions. Using generalized additive models (*20*), we estimated regional temporal trends in butterfly abundance for 301 species for which we had adequate data (table S3), restricting our analyses to extent-of-occurrence polygons estimated for each species [i.e., species ranges; (*21*)], and included covariates to account for species phenology (timing of activity; fig. S2) and survey effort. We then calculated range-wide trends using abundance-weighted averages of regional trends. For an additional 41 species, we had insufficient data to parse out variation across regions but sufficient data to fit simpler models. Accordingly, we estimated abundance trends using a single range-wide model for each of these species. To ensure the quality of each species estimate, two or more butterfly experts reviewed data summaries, model predictions, and regional trends; we removed species for which model fits were deemed unreasonable (14 species; initial species-level analyses had included 356 species).

In sum, butterflies are declining

Total butterfly abundance (all individuals of all species) decreased across the contiguous US at a rate of 1.3% annually [95% confidence interval: −2.3%, −0.2%], for a cumulative 22% decline in overall abundance between 2000 and 2020 (Fig. 1B). Of the seven geographic regions, six had declines in total butterfly abundance ranging from 0.2 to 2.3% annually (cumulative 5 to 37% declines) over the two decades (table S4). The Pacific Northwest was the only region with an estimated increase in total butterfly abundance (0.5% annually, cumulative 10% increase), but this increase was driven by the highly irruptive *Nymphalis californica* (California tortoiseshell), which accounted for 8.7% of observations in this region. The removal of this species from the analysis led to effectively constant abundance in the Pacific Northwest (revised estimate: 0.1% annual decline, cumulative 2% decline). By contrast, removing the most prevalent species in every region did not qualitatively alter our estimated decline in total butterfly abundance across the contiguous US (revised estimate: 1.1% annual decline, cumulative 19% decline).

Our national-scale findings paint the most complete—and concerning—picture of the status of butterflies across the country in the early 21st century. Previously published studies in US states or regions using subsets of the available data have reported similar annual declines of 1.6% in 11 states in the western US (*16*), 2.0% in Ohio (*13*), 3.8% in Illinois (*15*), and 0.72% across the contiguous US using a single data source (*17*). Only one study found an increase in abundance (1.2% in Massachusetts) over

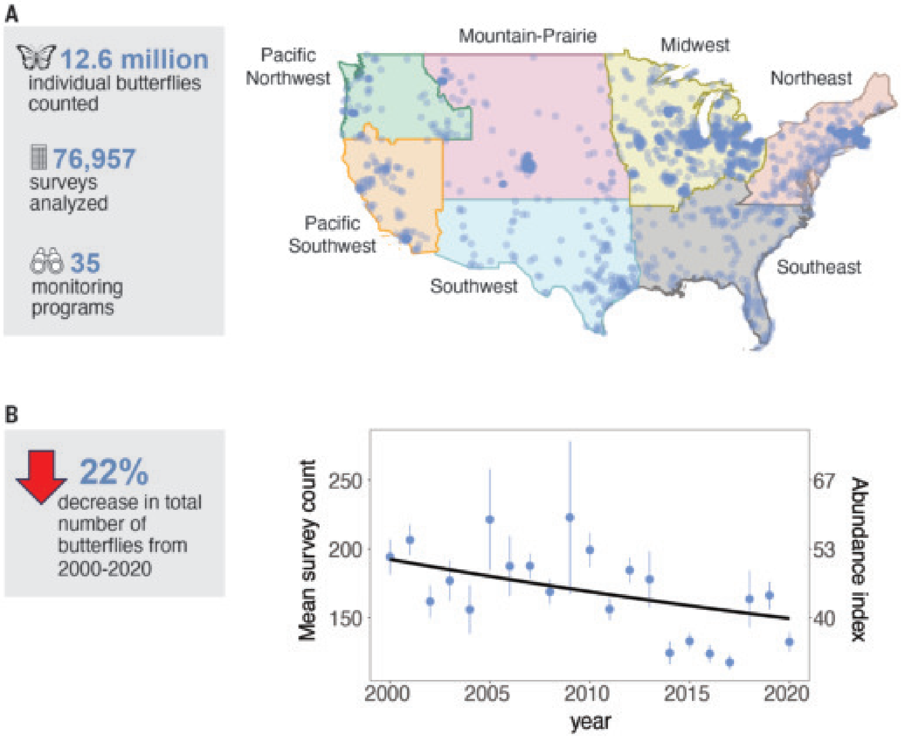

Fig. 1. Data from more than 76,000 monitoring events across the contiguous US reveal a 22% decline in total butterfly abundance from 2000 to 2020. (**A**) We divided the data into the seven US Fish and Wildlife Service regions, which were used for estimating regional trends. The transparent blue points on the map show the 2478 unique survey locations. (**B**) Solid blue points show the average number of butterflies recorded per survey for each year of our study; vertical lines show ±1 SE. The number of surveys per year is available in table S10. The black line shows our estimated abundance index (a relative measure of total butterfly abundance) derived from a fitted generalized additive model of total annual butterfly abundance that accounts for regional variation, seasonality, differences in effort and monitoring program, and site-to-site variation. Targeted surveys (10,511 surveys representing intensive efforts to monitor individual species of conservation concern) were not included in the analysis of total butterfly abundance to prevent overrepresentation of rare and at-risk species.

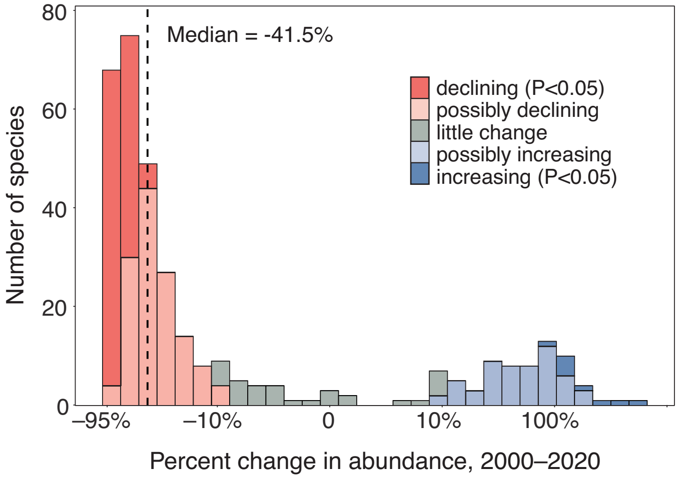

Fig. 2. Approximately 13 times as many butterfly species declined as increased in abundance across the contiguous US from 2000 to 2020. Species with rates of change that significantly differed from zero ($P < 0.05$) are labeled "declining" and "increasing," respectively; remaining species that changed by at least plus or minus 10% from 2000 to 2020 were labeled as "possibly increasing" and "possibly declining," respectively. The median species declined in abundance by 41.5% across the study period. Percent changes are shown on a log (base 10) scale to improve readability; this scaling "stretches" the plot near 0%, leading to the observed apparent bimodality (see fig. S5 for linear presentation).

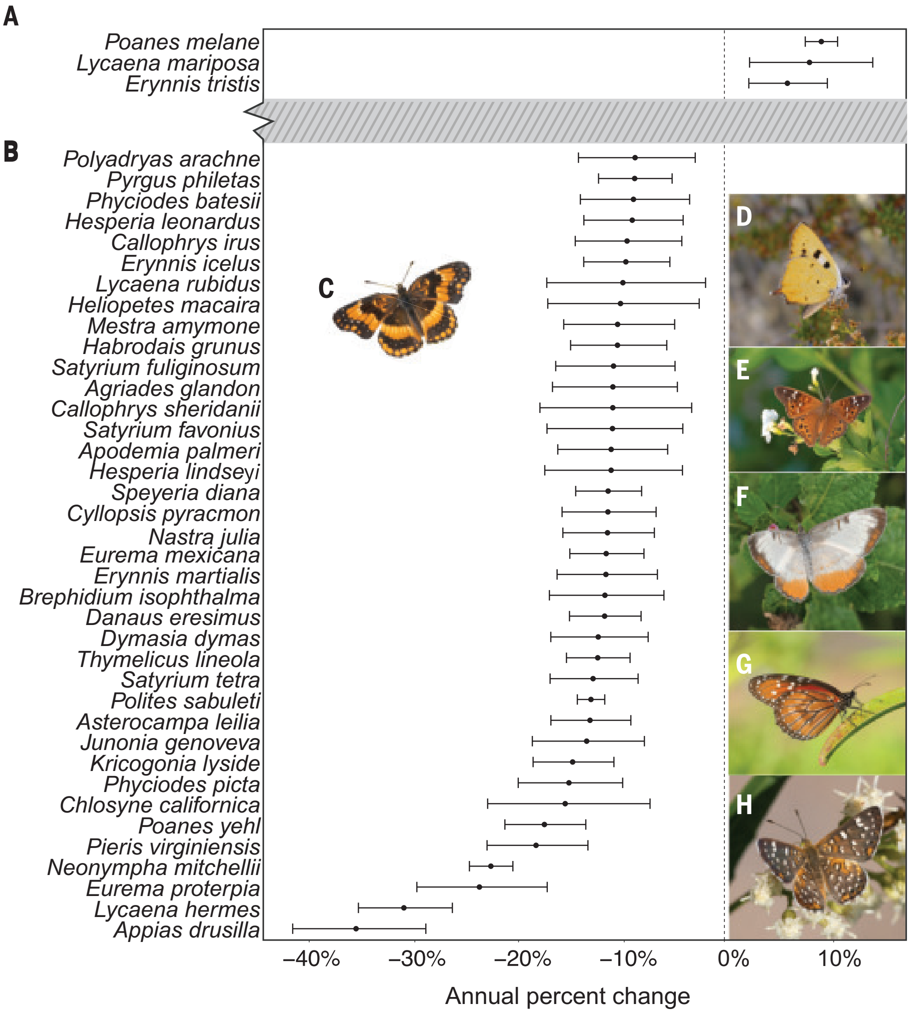

Fig. 3. Species with significant changes in abundance were predominantly declining. Of the increasing and declining species (significant annual change, $P < 0.05$), we show (**A**) the most extreme one-third of increasers (three of nine species) and (**B**) the most extreme third of decliners (38 of 114 species). Solid black points show the estimated annual change in abundance; intervals show 95% confidence intervals. The gray bar represents the remaining 301 (of 342) species fit with species-level models (results not shown), which had intermediate growth rates. (**C** to **H**) Photos of six of the most rapidly declining species: (C) *Chlosyne californica*, (D) *Lycaena hermes*, (E) *Asterocampa leilia*, (F) *Mestra amymone*, (G) *Danaus eresimus*, and (H) *Apodemia palmeri*. [Photo credits: J.G.]

similar time frames (*14*). Here, we establish the regional and continental patterns of butterfly declines by including data from all the systematic monitoring programs used in these targeted studies, in addition to many other programs. Our results for the US are consistent with declines reported globally (*5*), and especially in Europe (*7*, *13*).

Declines are common across species, whereas increases are rare

The change in the total number of butterflies between 2000 and 2020 was driven by the rapid decline of many individual species. Thirteen times as many species declined as increased (defined as significant plus or minus change at $P < 0.05$; Figs. 2 and 3). Over our two-decade study period, 33% of individual butterfly species (114 of 342) showed significantly declining trends in abundance ($P < 0.05$; Fig. 2 and table S5). Conversely, only 3% of species increased (nine species with $P < 0.05$). The median species had an annual decline of 2.6%, which resulted in a cumulative decline of 41.5% after two decades. Many species showed extreme declines in abundance: 107 species declined by more than 50%, including 22 species that declined by more than 90% ($P < 0.05$). Despite our expansive butterfly monitoring database, we were unable to conclusively identify abundance changes for many species; we found $P > 0.05$ for all species with cumulative changes in abundance between −42 and +91%. However, when focusing on the magnitude of trends, declines remained far more prevalent than increases. More than two-thirds of all species (245 of 342) had estimated cumulative decreases of more than 10%, whereas only one-fifth of species (65 species) had a cumulative increase greater than 10%. We defined those species with at least plus or minus 10% cumulative change over the study period and $P > 0.05$ as "possibly increasing" (56 species) or "possibly declining" (131 species), respectively (Fig. 2). Declines were present across all butterfly families, with 60 to 75% of species declining or possibly declining within each family (table S6).

Most species present in multiple regions showed geographically variable trends. Of the 192 species for which we estimated more than one regional trend, only 69 had estimated declines across all modeled regions, and only eight had estimated increases across all modeled regions. In addition to the nine species, 56 species that were not significantly increasing overall had significant increases in one or more regions ($P < 0.05$), which suggests that these species have "refuges" that may prevent range-wide declines, at least in the short term.

If traits were highly correlated with species trends, we could prioritize species groups for conservation action in the absence of species-specific monitoring data. We analyzed seven key traits selected on the basis of their observed relevance to population change in past studies (*19*). Species with more positive trends were associated with longer wing length [linear mixed effects model, $\chi^2(1) = 7.89$, $P = 0.005$], overwintering in a non-egg life stage [$\chi^2(4) = 9.54$, $P = 0.049$], preferences for moist habitats [$\chi^2(1) = 6.45$, $P = 0.011$], host plant generalists rather than specialists [$\chi^2(1) = 4.27$, $P = 0.04$], and association with human-dominated habitat [$\chi^2(1) = 12.05$, $P < 0.001$] (table S7). The other variables we examined—voltinism and canopy affiliation—had no discernible effects. Despite some significant associations, the examined traits provided limited ability to predict species outcomes. A full model that included all traits explained only 9% of the variation in species trends, and controlling for phylogeny removed any apparent support for the effect of traits (table S8). Our results do not preclude meaningful relationships between traits and trends at a more granular level, for example, across populations in specific landscapes. However, our findings make clear that at this broad geographic scale and species-level resolution, traits are not an effective proxy for species performance and cannot be used as a replacement for species-specific analyses in national-scale conservation planning.

Species declines are prevalent in all US regions

Declines were prevalent across all regions in the contiguous US, with every region containing

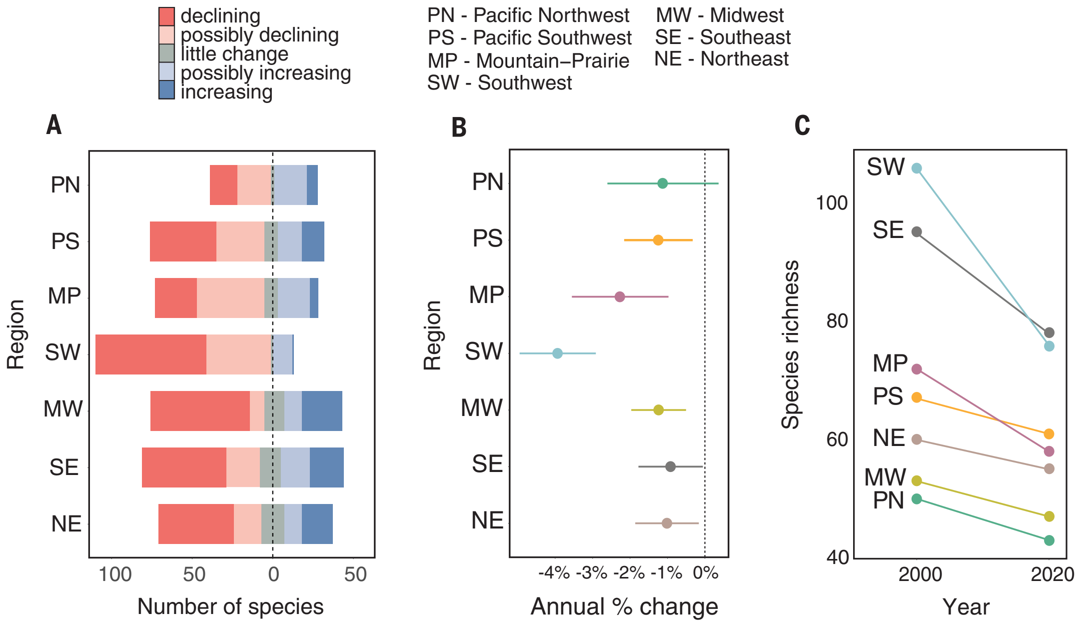

Fig. 4. Declines in individual species abundance and species richness are prevalent across geographic regions. (**A**) Species-level trends by region. Species with rates of change that significantly differed from zero ($P < 0.05$) are labeled "declining" and "increasing," respectively; remaining species that changed by at least plus or minus 10% from 2000 to 2020 are labeled as "possibly increasing" and "possibly declining," respectively. (**B**) Average species annual percent change for each region and associated 95% confidence intervals were derived from a linear mixed model that included a random effect of butterfly family and weighted species by the inverse of associated uncertainty. (**C**) Changes in the estimated species richness index (i.e., the count of "likely observable" species) from 2000 to 2020 in each region.

more declining than increasing species (Fig. 4, A and B, and table S9). The median species annual change in each region (−1.2 to −4.0%) led to cumulative declines of 21 to 55% over the study period. Declines were most severe in the Southwest, consistent with other findings that butterflies in the contiguous US are disproportionately declining in arid and hot climates (*16*, *17*). Among all increasing species, two-thirds had larger extent-of-occurrence areas in Mexico than in the US and Canada combined, and thus our trend estimates primarily characterize the northern portion of these species' ranges.

Between 2000 and 2020, butterfly species richness fell in every region by as much as 28% or 30 species (Fig. 4C). Our measure of species richness is a calculated annual metric of the number of "likely observable" species in each region that accounts for variable monitoring efforts across regions and years [(*19*); fig. S3]. Our index also accounts for the phenomenon that a sufficiently rare species is unlikely to be encountered even before it declines, whereas a sufficiently common species is still likely to be encountered even after moderate declines.

With climate change, butterfly species in North America may find the southern limits of their ranges becoming too warm while the northern limits of their range become more hospitable (*14*, *22*). We tested this prediction through comparisons of regional trends of species that were present in pairs of regions, one to the north and one to the south, that share a common east-west border. For three out of four region pairs, species had higher trends in abundance in the northern region (Northeast versus Southeast: F_1 =15.14, $P < 0.001$, trend in abundance 0.016 higher in the Northeast; Midwest versus Southeast: $F_1 = 10.18$, $P = 0.002$, trend in abundance 0.015 higher in the Midwest; Mountain-Prairie versus Southwest: $F_1 = 6.86$, $P = 0.012$, trend in abundance 0.017 higher in Mountain-Prairie). We did not see an effect of latitude on the Pacific coast (Pacific Southwest versus Pacific Northwest: $F_1 = 0.04$, $P = 0.848$, trend in abundance 0.001 higher in the Pacific Northwest), possibly because elevational differences play a larger role in determining climate in these regions. Still, improved species performance in more northerly regions was not sufficient to reverse species declines, given that median species trends in northern regions were still negative.

Improved monitoring: A call to action

We conducted the definitive assessment of butterfly trends across the contiguous US for the first two decades of the 21st century and found declines at every scale: reductions in total numbers of butterflies, falling species richness, and large decreases in many individual species. Our continental analysis integrated across monitoring programs in which local or short-lived fluctuations in abundance could be different from regional or continental trends. Our synthesis was made possible because of the many individual datasets collected primarily by volunteer scientists. The combined dataset provides a powerful base for assessing spatially expansive trends and a foundation for future analyses to address key questions about the nature and causes of declines across individual species and butterflies at large.

Of the approximately 650 butterfly species with extent-of-occurrence polygons overlapping the contiguous US, only 85% (554 species) were recorded anywhere in our data and only 53% (342 species) were sufficiently represented for species-level analyses. Even among those analyzed, we lacked the power to detect significant trends for most species. Thus, it is possible that many more butterflies are being lost than is estimable because species with limited data are already rare, with small population sizes living in specialized habitats. Further, whole geographic regions are poorly represented in our data. For example, North and South Dakota together contained only five of our >2000 survey sites, for an average of one site per 75,000 km^2 compared with one survey per 340 km^2 in Illinois. The 11 states for which there are standardized, decades-long monitoring programs provide a template that could be used across other states and around the world (table S1). Digitizing historical butterfly records could also offer new insights by unlocking decades worth of data, because more than 90% of insect collections have yet to be made available for analysis (*23*). The future of butterflies depends in part on an up-to-date understanding of each species' status, which necessitates the most complete data possible and a coordinated effort to integrate those data into meaningful analyses.

Potential causes of butterfly declines and steps for the future

The scope and scale of butterfly declines suggest multiple and broadly acting threats, including habitat loss, climate change, and pesticide use [(*6*); fig. S4]. Insecticides have been identified as leading causes of butterfly declines in recent analyses in the midwestern US and California (*24*, *25*). Detailed analyses linking insecticide use to insect mortality can inform regulatory action, including imposing restrictions on neonicotinoid insecticides, as was done in the European Union. Other approaches to reduce pesticide use, such as integrated pest management and diversified cropping, can improve habitats for butterflies and other insects on working lands [e.g., (*26*, *27*)].

Combating habitat loss requires land protection and restoration. Targeted habitat management has successfully reversed the decline of at-risk butterfly species [e.g., (*28*)] and has been linked to local increases in abundances for six of our declining species (*29*). Restoring native landscapes, even in areas where only small spaces are available such as hedgerows, roadsides, and backyards, has great potential for increasing the amount of suitable habitat for butterflies and other insects (*30*).

Butterfly declines have been linked to rising temperatures and changing climates in the US and other countries (*16*, *22*, *31*, *32*). Concordantly, we found that species generally had stronger declines in more southernly parts of their ranges. Additionally, the two regions with the most negative median species trends—the Southwest and the Mountain-Prairie regions (Fig. 4B)—contain 8 of the 10 driest US states and many of the most rapidly warming climate divisions (*33*). Slowing climate change necessitates national and international efforts. However, local-scale actions can mitigate the effects of climate change on individual populations. For example, implementing broadly beneficial conservation actions such as native habitat preservation and restoration can increase abundance trends even in the face of climate change (*29*), and species-specific interventions such as managed relocation (*34*), genetic rescue (*35*), and conservation of local variability in habitat structure and type (*36*) can aid in the protection of highly threatened species.

Butterflies have the potential for rapid population growth under the right circumstances, making species recovery possible—even from very small population sizes (*28*). Expansive efforts in conservation planning and action for insects could prevent widespread future losses and create and maintain the environments in which butterflies and other at-risk species can thrive.

REFERENCES AND NOTES

1. R. Dirzo *et al.*, *Science* **345**, 401–406 (2014).
2. G. Ceballos *et al.*, *Sci. Adv.* **1**, e1400253 (2015).
3. G. Ceballos, P. R. Ehrlich, P. H. Raven, *Proc. Natl. Acad. Sci. U.S.A.* **117**, 13596–13602 (2020).
4. D. Goulson, *Curr. Biol.* **29**, R967–R971 (2019).
5. R. van Klink *et al.*, *Science* **368**, 417–420 (2020).
6. D. L. Wagner, E. M. Grames, M. L. Forister, M. R. Berenbaum, D. Stopak, *Proc. Natl. Acad. Sci. U.S.A.* **118**, e2023989118 (2021).
7. M. S. Warren *et al.*, *Proc. Natl. Acad. Sci. U.S.A.* **118**, e2002551117 (2021).
8. J. F. Tooker, K. A. Pearsons, *Curr. Opin. Insect Sci.* **46**, 50–56 (2021).
9. E. M. Grames, G. A. Montgomery, C. Youngflesh, M. W. Tingley, C. S. Elphick, *Ecol. Lett.* **26**, 658–673 (2023).
10. P. Cardoso, T. L. Erwin, P. A. V. Borges, T. R. New, *Biol. Conserv.* **144**, 2647–2655 (2011).
11. D. Taron, L. Ries, in *Butterfly Conservation in North America: Efforts to Help Save our Charismatic Microfauna*, J. C. Daniels, Ed. (Springer, 2015), pp. 35–57.
12. G. A. Breed, S. Stichter, E. E. Crone, *Nat. Clim. Chang.* **3**, 142–145 (2013).
13. T. Wepprich, J. R. Adrion, L. Ries, J. Wiedmann, N. M. Haddad, *PLOS ONE* **14**, e0216270 (2019).
14. J. P. Michielini, E. B. Dopman, E. E. Crone, *Ecol. Lett.* **24**, 249–257 (2021).
15. N. B. Kucherov, E. S. Minor, P. P. Johnson, D. Taron, K. C. Matteson, *PLOS ONE* **16**, e0257889 (2021).
16. M. L. Forister *et al.*, *Science* **371**, 1042–1045 (2021).
17. M. S. Crossley *et al.*, *Glob. Change Biol.* **27**, 2702–2714 (2021).
18. P. Cardoso, S. R. Leather, *Insect Conserv. Divers.* **12**, 263–267 (2019).
19. Materials and methods are available as supplementary materials.
20. P. Rothery, D. B. Roy, *J. Appl. Stat.* **28**, 897–909 (2001).
21. E. M. Grames *et al.*, Data from: Integrated range maps for North American butterflies derived from expert opinion and relative predicted habitat suitability, Figshare (2024). https://doi.org/10.6084/m9.figshare.22747928.
22. V. Shirey, N. Neupane, R. Guralnick, L. Ries, *Glob. Change Biol.* **30**, e17205 (2024).
23. N. S. Cobb *et al.*, *PeerJ* **7**, e8086 (2019).
24. B. Van Deynze, S. M. Swinton, D. A. Hennessy, N. M. Haddad, L. Ries, *PLOS ONE* **19**, e0304319 (2024).
25. M. L. Forister *et al.*, *Biol. Lett.* **12**, 20160475 (2016).
26. N. L. Haan, B. G. Iuliano, C. Gratton, D. A. Landis, in *The Future of Agricultural Landscapes, Part II*, vol. 64 of Advances in Ecological Research Series, D. A. Bohan, A. J. Vanbergen, Eds. (Academic Press, 2021), pp. 191–250.
27. J. R. Pecenka, L. L. Ingwell, R. E. Foster, C. H. Krupke, I. Kaplan, *Proc. Natl. Acad. Sci. U.S.A.* **118**, e2108429118 (2021).
28. R. E. Bonoan, E. E. Crone, C. B. Edwards, C. B. Schultz, *J. Insect Conserv.* **25**, 499–510 (2021).
29. C. B. Edwards *et al.*, *J. Appl. Ecol.* **61**, 2455–2469 (2024).
30. C. Haaland, R. E. Naisbit, L. F. Bersier, *Insect Conserv. Divers.* **4**, 60–80 (2011).
31. A. M. Franco *et al.*, *Glob. Change Biol.* **12**, 1545–1553 (2006).
32. E. R. Zylstra *et al.*, *Nat. Ecol. Evol.* **5**, 1441–1452 (2021).
33. R. S. Vose *et al.*, *J. Appl. Meteorol. Climatol.* **53**, 1232–1251 (2014).
34. J. J. Hellmann, R. Grundel, C. Hoving, G. W. Schuurman, *Curr. Opin. Insect Sci.* **17**, 92–97 (2016).
35. A. R. Whiteley, S. W. Fitzpatrick, W. C. Funk, D. A. Tallmon, *Trends Ecol. Evol.* **30**, 42–49 (2015).
36. J. J. Lawler *et al.*, *Conserv. Biol.* **29**, 618–629 (2015).
37. C. B. Edwards *et al.*, Data and code for "Butterflies are declining rapidly in the United States during the 21st century", Version 1, Figshare (2024). https://doi.org/10.6084/m9.figshare.27934629.
38. E. H. Henry *et al.*, Data for "Twenty years (2000 - 2020) of butterfly monitoring data across the contiguous United States", Version 1, Figshare (2024). https://doi.org/10.6084/m9.figshare.27934602.

ACKNOWLEDGMENTS

The data in this study are derived from thousands of hours of volunteer monitoring efforts; we thank the volunteer scientists for their dedicated efforts and willingness to contribute to science. We specifically thank the North American Butterfly Association (NABA); Massachusetts Butterfly Club (a chapter of NABA); Cascades Butterfly Project-North Cascades National Park Service Complex; Cascade-Siskiyou National Monument Butterfly Monitoring Program; Colorado Butterfly Monitoring Network; Illinois Butterfly Monitoring Network; Reiman Gardens' Iowa Butterfly Survey Network; Michigan Butterfly Monitoring Network; Missouri Butterfly Monitoring Network; MPG Ranch Butterfly Monitoring Program; Nevada Butterfly Monitoring Network; New Mexico Butterfly Monitoring Network; Ohio Lepidopterists; The Orange County Butterfly Monitoring Program, run by the Irvine Ranch Conservancy (IRC); PRISSM (Partnership of Regional Institutions for Sage Scrub Monitoring); Wisconsin Butterfly Monitoring Network; and Texas Butterfly Monitoring Network. In addition, we thank the following individuals who were instrumental in conducting surveys or curating data for individual species: A. Mills, C. Menke, G. Fitzpatrick, T. Wilder, B. Merkle, C. Crooker, R. Schallmann, R. Lovich, M. Patterson, D. Pickering, and P. Severns. We thank V. Shirey for assistance in using Pollardbase data, T. Wepprich for serving in our expert review process, and M. Belitz for providing code review on parts of our analyses. We thank J. Baron and the staff of the US Geological Survey (USGS) John Wesley Powell Center for supporting and facilitating our work. We thank D. Singh and C. Maffei for their insightful comments during the development of this project. We thank M. Newman for assistance in creating our figures. We thank three anonymous reviewers for their thoughtful comments on the manuscript. L.R. is affiliated with the National Science Foundation (NSF) under the Intergovernmental Personnel Act. The National Science Foundation provided support for this project through its Independent Research and Development Program. The findings and conclusions in this article are those of the authors and do not necessarily represent the views of the National Science Foundation, US Fish and Wildlife Service, or Washington Department of Fish and Wildlife. Any use of trade, firm, or product name is for descriptive purposes only and does not imply endorsement by the US government. This work is a product of the Status of Butterflies working group funded by the USGS John Wesley Powell Center for Analysis and Synthesis. **Funding:** This work was funded by Department of the Navy Cooperative Agreements N68711-04-LT-A0017, N68711-05-LT-A0012, N62473-06-LT-R0011, N62473-07-LT-R0013, N62473-08-2-0011, N62473-11-2-2304, N62473-12-2-2101, N62473-15-2-0002, and N62473-19-2-0009 (T.L.); Department of Defense Strategic Environmental Research and Development Program (SERDP) RC-2700 (E.E.C., C.B.S.); National Science Foundation DEB-2114793 (M.L.F.), DEB-2225092 (E.M.G.), OIA-2019528 (M.L.F., E.M.G.), and DEB-1954406 (E.F.Z.); San Diego Association of Governments (SANDAG) contract nos. 5005783, 5001442, and 5004388 (D.A.M.); US Fish and Wildlife Service (USFWS) Center for Pollinator Conservation grant FWS-F24AC00472-00 (C.B.S.); the USGS Ecosystems Land Change Science Program (J.D.); USGS grant no. G21AC10369-00 (E.F.Z., L.R., W.E.T.); the USGS John Wesley Powell Center for Analysis and Synthesis Working Group on Status of Butterflies with joint funding from USGS and USFWS, grant G22AS00192 (C.B.S., E.E.C., W.E.T.); the USGS National Land Imaging Program (J.D.); and the USGS Species Management Research Program (W.E.T.). Washington State University provided support while writing the manuscript (C.B.E.). **Author contributions:** Conceptualization: C.B.E., E.F.Z., E.H.H., N.M.H., M.L.F., E.E.C., J.D., R.G.D., E.A.L., L.R., W.E.T., C.B.S., S.H.B.; Data collection: E.H.H., M.L.F., K.J.B., J.D., L.R., A.M.S., C.B.S., S.P.C., A.B.S., S.R.S., T.L., R.H., D.A.M., J.G., J.W., S.H., M.J.L., D.J.T.; Data curation: C.B.E., E.H.H., M.L.F., R.G.D., E.M.G., E.A.L., T.L., L.R., A.M.S., C.B.S., S.P.C., A.B.S., S.R.S., T.L., R.H., D.A.M., J.G., J.W., S.H., D.J.T.; Analysis development: C.B.E., E.F.Z., N.M.H., M.L.F., K.J.B., E.E.C., J.D., M.R.D., E.M.G., E.A.L., W.L., L.R., B.V.D., W.E.T., C.B.S.; Analysis implementation: C.B.E., E.E.C.; Expert review of results or code: E.H.H., N.M.H., M.L.F., K.J.B., E.E.C., M.R.D., C.E.F., E.A.L., W.L., J.M., B.V.D., W.E.T., C.B.S., D.A.M., J.G., S.H.B.; Funding acquisition and project administration: E.H.H., E.E.C., R.G.D., W.E.T., C.B.S., S.H.B.; Writing – original draft: C.B.E., E.F.Z., N.M.H., M.L.F.; Writing – review & editing: C.B.E., E.F.Z., E.H.H., N.M.H., M.L.F., K.J.B., E.E.C., J.D., M.R.D., R.G.D., C.E.F., E.M.G., E.A.L., W.L., T.L., J.M., L.R., B.V.D., A.M.S., W.E.T., C.B.S., S.P.C., D.A.M., J.G., D.J.T., S.H.B., N.N. **Competing interests:** The authors declare that they have no competing interests. **Data and materials availability:** Data and code are available at Figshare (*37*). Geographic information, aside from region (e.g., latitude, longitude, state), has been removed from butterfly observations in the 35 individual data sources to protect conservation efforts. Site and survey identifiers frequently contained geographic information and have been anonymized to protect conservation efforts. More geographically granular butterfly data and protocols for requesting updated or nonanonymized data for 19 of the monitoring programs are available at Figshare (*38*).

SUPPLEMENTARY MATERIALS

science.org/doi/10.1126/science.adp4671
Materials and Methods
Fig. S1 to S5
Tables S1 to S10
References (*39*–*76*)

Submitted 29 March 2024; accepted 10 January 2025
10.1126/science.adp4671

CELL BIOLOGY

Protein codes promote selective subcellular compartmentalization

Henry R. Kilgore[1]†*, Itamar Chinn[2,3]†, Peter G. Mikhael[2,3]†, Ilan Mitnikov[2,3]†, Catherine Van Dongen[1], Guy Zylberberg[2,3], Lena Afeyan[1,4], Salman F. Banani[1,5], Susana Wilson-Hawken[1,6], Tong Ihn Lee[1], Regina Barzilay[2,3]*, Richard A. Young[1,4]*

Cells have evolved mechanisms to distribute ~10 billion protein molecules to subcellular compartments where diverse proteins involved in shared functions must assemble. In this study, we demonstrate that proteins with shared functions share amino acid sequence codes that guide them to compartment destinations. We developed a protein language model, ProtGPS, that predicts with high performance the compartment localization of human proteins excluded from the training set. ProtGPS successfully guided generation of novel protein sequences that selectively assemble in the nucleolus. ProtGPS identified pathological mutations that change this code and lead to altered subcellular localization of proteins. Our results indicate that protein sequences contain not only a folding code but also a previously unrecognized code governing their distribution to diverse subcellular compartments.

Groups of proteins involved in shared functions must assemble to fulfill their physiological functions (*1*). For example, the fidelity of gene transcription hinges on the assembly of more than a hundred different proteins at regulatory elements (*2*, *3*). Selective protein-protein and protein–nucleic acid interactions are thought to be the predominant driving force leading to the assembly of specific proteins at locations where they carry out diverse functions (*4*–*7*). Shape complementarity among structurally stable portions of proteins has dominated models of protein assembly, but there is now considerable evidence that large assemblies of proteins with shared functions also occur through weak multivalent noncovalent interactions (*8*–*15*). Nearly all cellular functions involve formation of such assemblies, which have been described as condensates, aggregates, puncta, hubs, and nonmembrane-bound compartments (Fig. 1A). In a recent study, we used small chemical probes to demonstrate that different condensates can harbor distinct internal chemical environments, suggesting that such assemblies have different solvent properties (*16*). It is thus possible that protein molecules that assemble selectively with others in a condensate do so, in part, as a consequence of their compatibility with the internal solvating environment of that compartment (*17*–*20*). Integration of contributions from specific interactions (e.g., DNA-protein binding, protein-protein interactions) and nonspecific interactions (e.g., transient noncovalent interactions) is challenging to model, but protein language models provide a means to incorporate diverse contributions. If such a protein language model could be developed, it would have important implications for our understanding of cellular function and dysfunction by providing evidence of a protein code distributed throughout amino acid sequences that can guide selective distribution to subcellular compartments.

Evidence for shared protein codes in condensate compartments

To learn whether collections of proteins that assemble into specific condensate compartments have shared protein codes, we adapted an evolutionary scale protein transformer language model (ESM2) to predict protein assembly into distinct compartments (*21*, *22*). The transformer architecture of ESM2 allows for simultaneous relationships between all amino acids in an input sequence to be learned, providing a general strategy to detect protein codes embedded in the amino acid sequence of a protein. We focused our studies on a set of 5480 human protein sequences that have been annotated for 12 condensate compartments using the UniProt (Universal Protein Resource) (*23*) and CD-CODE (Crowdsourcing Condensate Database and Encyclopedia) (*24*) databases (Fig. 1B). The compartment identities of the proteins in these databases were determined with various experimental techniques and curated by experts in compartment annotation. Compartment-annotated whole-protein sequences were used as input. A neural network classifier was jointly trained with ESM2 to develop a model, termed ProtGPS, which computes the independent probability of a protein being found within each of the 12 different condensate compartments (Fig. 1C). The area under the receiver operator curve (AUC-ROC) showed that protein compartments could be predicted with remarkable accuracy (0.83 to 0.95) across the 12 different compartments (Fig. 1D). The performance of the ProtGPS model indicates that it detects patterns in the protein sequence that differentiate these condensate compartments.

We attempted to identify features that might contribute to selective compartmentalization, although extraction of the nonlinear patterns or principles learned by a machine learning classifier is a well-known challenge (*25*), owing in part to neural network architecture, to the complexity of pattern information, and to the lack of "language" to describe learned patterns outside of conventional physicochemical properties. The types of sequence features that enable transit across intracellular membranes were not immediately evident in the sets of proteins that that are found together in these compartments (fig. S1). We did observe that proteins in some compartments shared physicochemical properties such as isoelectronic point (pI) and hydrophobicity (fig. S2 and table S1). We also note that the high performance of the protein language model depended on information learned from inclusion of multiple members of protein families and that when these families were not fully represented in the training set, the performance was only somewhat better than a random forest or linear regression model (fig. S2 and table S1). This suggests to us that inclusion of multiple protein family members is informative in optimizing protein language model performance, although inclusion of this information presents some risk of overfitting. Certain amino acids were more informative to differentiate proteins found in separate compartments (fig. S3). We found little evidence to suggest that a protein distribution code can be represented with a small number of components (fig. S4). We anticipate that advances in machine learning and chemical pattern description will enable additional insights into the features learned by ProtGPS that enable its level of performance.

Guided generation of novel protein sequences for compartment selectivity

To further validate that ProtGPS has learned protein codes associated with condensate localization, we sought to design novel protein sequences that, when produced in cells, would selectively assemble into a compartment of interest. To test this idea, we initially designed protein sequences using an autoregressive greedy search (GS) algorithm (*26*) and generated eight novel proteins designed to assemble selectively into nucleoli (table S2). However, these proteins failed to assemble selectively into nucleoli (fig. S5). The failure of our initial efforts to generate proteins that selectively compartmentalize in nucleoli motivated the design of another approach that might be more successful. With GS and ProtGPS, protein sequences are generated without consideration of the chemical

---

[1]Whitehead Institute for Biomedical Research, Cambridge, MA, USA. [2]Computer Science and Artificial Intelligence Laboratory, Massachusetts Institute of Technology (MIT), Cambridge, MA, USA. [3]Abdul Latif Jameel Clinic for Machine Learning in Health, MIT, Cambridge, MA, USA. [4]Department of Biology, MIT, Cambridge, MA, USA. [5]Department of Pathology, Brigham and Women's Hospital, Harvard Medical School, Boston, MA, USA. [6]Computational and Systems Biology Program, MIT, Cambridge, MA, USA.

***Corresponding author. Email: hkilgore@wi.mit.edu (H.R.K.); regina@csail.mit.edu (R.B.); young@wi.mit.edu (R.A.Y.)**

†These authors contributed equally to this work.

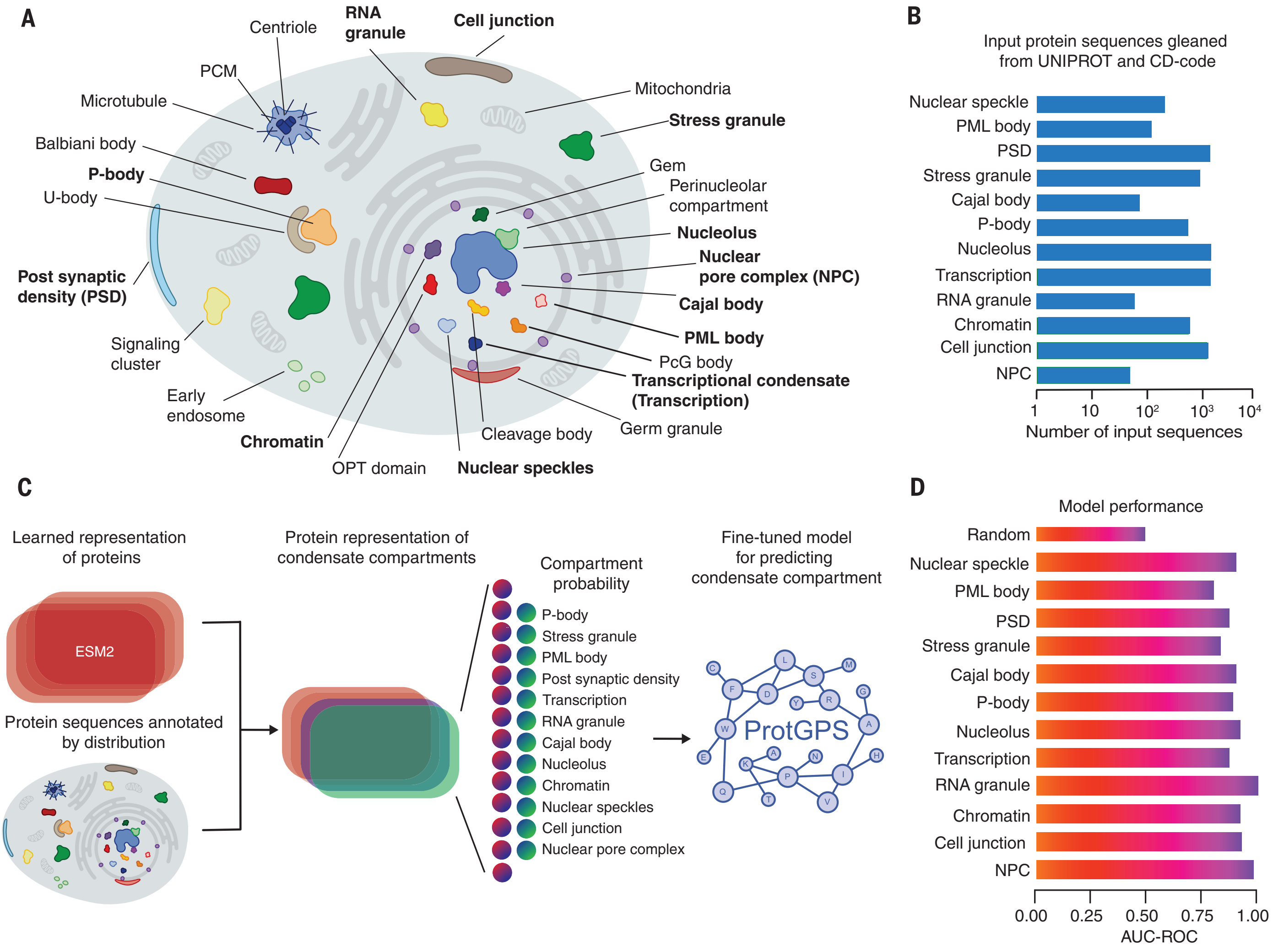

Fig. 1. ProtGPS classifies protein compartment with high performance. (**A**) Graphical depiction of some cellular compartments found in eukaryotic cells; compartments labeled in boldface were studied in this work. OPT domain, Oct1/PTF/transcription domain; P-body, processing body; PcG body, polycomb group body; PCM, pericentriolar material; PML body; promyelocytic leukemia body; U-body, uridine-rich small nuclear ribonucleoprotein–containing body. (**B**) Bar graph showing the number of protein sequences gathered from UniProt and the CD-CODE database used in the development of ProtGPS. (**C**) Schematic showing the approach toward developing ProtGPS. (**D**) Bar graph showing the area under the receiver-operator curve (AUC-ROC) for classification of withheld test data (15% of total) with ProtGPS.

space of proteins found in nature. We sought to create an approach that could overcome this limitation by applying a concept borrowed from medicinal chemistry, in which it is common to consider whether a molecule shares desirable physicochemical properties with others (*27*, *28*), namely, sampling from a protein chemical space with specific properties. To apply these concepts toward protein generation, we sought to constrain generation to (i) sequences in the chemical space (*29*) learned by ESM2; (ii) sequences that are intrinsically disordered (*30*), because these are less likely to introduce competing folded states and are associated with condensates (*31*, *32*); and (iii) sequences that should localize to the intended compartment. In practice, this approach integrates the starting protein sequence (mCherry) and its properties into the search for new peptide sequences that are natural, disordered, and have a compartment classification of 0.95 or greater for the target compartment. Thus, we used additional features of protein chemical space and intrinsic disorder for our Markov chain Monte Carlo (MCMC) algorithm (Fig. 2A).

We then used the MCMC algorithm to perform guided generation of proteins that would selectively assemble into a condensate compartment when appended to mCherry protein, which would allow us to follow protein distribution. The chemical properties of mCherry were therefore necessarily integrated into the resulting newly generated protein, which would then allow us to compare partitioning of the new protein with mCherry alone. We first generated proteins that were designed to selectively partition into nucleoli (*9*), which were selected because they are large, well-studied bodies with distinctive morphologies and possess unambiguous marker proteins (Fig. 2A). Ten 100 amino acid–long protein sequences targeted to nucleoli were generated (Fig. 2A, figs. S6 and S7, and tables S3 and S4). For each protein, a plasmid was constructed that encoded the generated protein attached to an N-terminal nuclear localization sequence and a C-terminal mCherry protein. Each of the proteins was expressed in human cells together with the nucleolus marker NPM1-meGFP, and cells expressing both a test protein (mCherry) and the condensate marker (meGFP) were isolated by using flow cytometry. Imaging of cells revealed that four of 10 proteins designed to assemble into nucleoli (NUC1 to 10) showed readily visible enrichment in

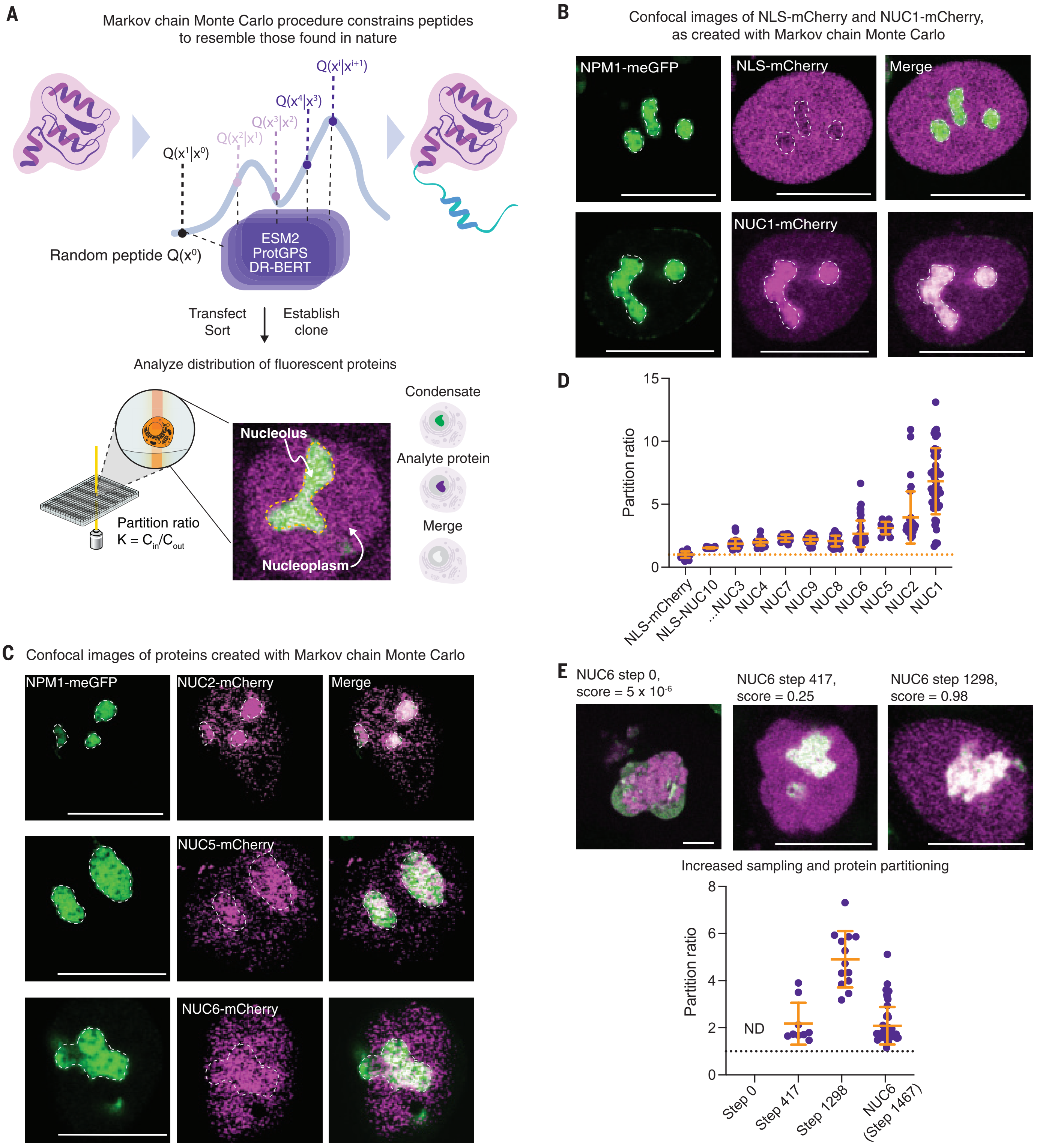

Fig. 2. Generative modeling creates novel proteins that concentrate in a desired condensate. (**A**) Schematic showing the use of Markov chain Monte Carlo to generate proteins and assay them in live cells (MCMC) (more details provided in supplementary materials). (**B**) Live-cell image of a colon cancer cell (HCT-116) tagged at the endogenous NPM1 locus with meGFP and expressing a nucleolus targeted protein NUC1-mCherry. NPM1, nucleophosmin 1; NLS, nuclear localization signal. Scale bars, 10 μm. (**C**) Live-cell confocal micrographs of NUCX-mCherry proteins in HCT-116 cells expressing NPM1-meGFP from the endogenous locus cells. Scale bars, 10 μm. (**D**) Dot plots showing the measured partition ratios of NUCX ($K_x = I_{nucleolus}/I_{nucleoplasm}$) proteins relative to the NLS-mCherry control protein; dotted line is the average value of NLS-mCherry protein (tables S5 and S6 and figs. S8 to S10 provide more information). K, partition ratio; $I_{nucleolus}$, intensity of light in the compartment; $I_{nucleoplasm}$, intensity of light in the nucleoplasm. (**E**) Live-cell images and quantification showing the relationship of measured partition ratios ($K_x = I_{nucleolus}/I_{nucleoplasm}$) into the nucleolus by proteins on the NUC6-mCherry trajectory to its computed probability of partitioning.

nucleolar compartments (NUC1, 2, 5, and 6) (Fig. 2, B and C, and figs. S8 to S12), and a more detailed partitioning analysis indicated that the remaining six NUC proteins exhibited more mild enrichment compared with the mCherry control [Fig. 2D; figs. S8 to S12; tables S5 and S6; and supplementary materials (SM), materials and methods].

We next tested the ability of the MCMC algorithm to guide generation of proteins that would partition into nuclear speckles, which are condensates formed by the mRNA splicing apparatus. Using the approach described for the NUC proteins, 10 proteins designed to assemble into nuclear speckles (SPL proteins) were generated and individually expressed in human cells together with SRSF2-meGFP, a marker of nuclear speckles. Imaging of cells revealed that none of the 10 sequences for SRSF2-asociated nuclear speckles became clearly concentrated in nuclear speckles, but two of the generated proteins, SPL2 and SPL3, accumulated in cytoplasmic puncta together with SRSF2-meGFP (figs. S6, S12, and S13; tables S5

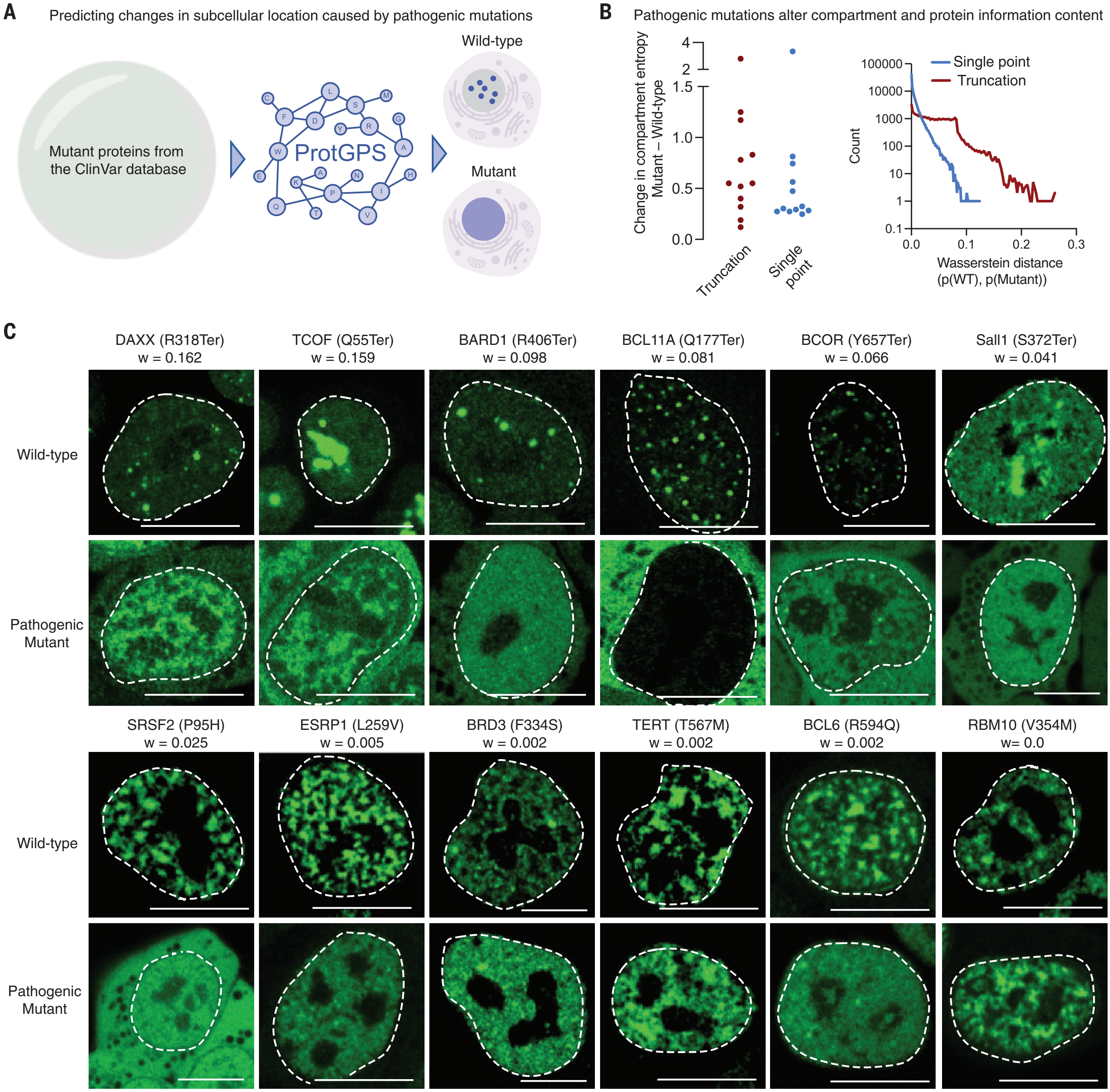

Fig. 3. Pathogenic mutations are predicted to alter protein compartmentalization. (**A**) Schematic of information flow; pathogenic ClinVar mutants caused by single-point or truncation mutations were classified with ProtGPS to determine whether the detected protein code was changed in the pathogenic variant. (**B**) (Left) Dot plot showing the Shannon entropy change in compartment prediction due to single-point or truncation mutation. (Right) Histogram showing the Wasserstein distance between the wild-type and mutant protein compartment probabilities. (**C**) Live-cell images of mESCs ectopically expressing wild-type and truncated pathogenic variants fused to meGFP; Wasserstein distance is given for each mutant as w. Scale bars, 10 μm.

and S6; and SM, materials and methods). It thus appears that SPL2 and SPL3 gained the ability to associate with the SRSF2 speckle protein in a cytoplasmic condensate but lost the ability to migrate into the nucleus, where speckles normally form. This behavior is analogous to the effect of mutations in the splicing regulator RBM20, which cause this nuclear speckle protein to accumulate in cytoplasmic puncta and concentrate other splicing proteins (*33*, *34*). These results with NUC and SPL proteins indicate that the MCMC algorithm can guide generation of proteins that selectively partition into a target compartment; but the algorithm was not fully successful in doing so, suggesting that additional training data and analytical approaches will be necessary for improved performance. Sensitivity analysis conducted on the MCMC generative process suggested that increased sampling could lead to improvements in enrichment but also found that the process was nonlinear and can lead to reduced performance, as seen for the final version selected for NUC6 (Fig. 2E and fig. S14). Generative modeling of new protein sequences is a challenging task, whose success rate can vary from <0.01 to ~70% because of the specific modeling goal, the algorithms used to generate protein sequences, and the criteria used to define success or failure (*35*–*38*).

Pathogenic mutations can alter protein codes

Mutations can create pathogenic effects by altering a protein's function or altering a protein's subcellular compartmental distribution. Because ProtGPS can accurately predict the subcellular compartmentalization of normal proteins, it might be able to identify pathogenic mutations that cause a change in the subcellular location of a mutant protein. To test this possibility, we turned to the ClinVar (*39*) database, a public archive of a vast number of human variations classified for diseases. Data were collected for 205,182 mutations, and ProtGPS was used to predict whether the changes in amino acid sequences alter the subcellular distribution of the mutant proteins (Fig. 3A). We used two approaches, first examining how changes in amino acid sequence affect ProtGPS predictions and then testing experimentally whether mutations predicted by ProtGPS to affect protein distribution can do so.

To characterize the relationship between mutations and changes in ProtGPS predictions, we used approaches applied in information theory. ProtGPS is trained on wild-type sequences and then uses learned patterns to score proteins for their likelihood of distributing to compartments. Mutations affect sequence and can be seen as a change in the information content of the sequence. Any change is thus expected to result in some change in the scoring of mutant protein compared with the wild-type. Furthermore, any changes in scoring are likely to reflect an increase in uncertainty of the prediction because mutations effectively remove information that went into the prediction for the wild-type baseline. To test this, we computed the change in Shannon entropy (*40*, *41*)—an information theory measurement of uncertainty—of the 12 condensate compartments for wild-type versus mutant proteins to ask whether mutations alter the certainty of compartment assignment for a protein (SM, materials and methods). We conducted the analysis for the truncation mutations (83,211)—which we assumed would have major effects—separately from that for the single-point mutations (121,971), which we assumed would have much smaller effects. We found that the Shannon entropy is consistently higher with mutant proteins compared with the normal proteins across all compartments, indicating that mutations are associated with decreased certainty in compartment assignment, with truncations producing larger effects than point mutations (Fig. 3B). A similar analysis was performed for individual proteins; changes in the scores between a wild-type protein and its mutant counterpart can be measured by using Wasserstein distance (*42*–*44*), a metric of dissimilarity between two probability distributions. We found that pathogenic truncation mutations, when compared with single-point mutations, tend to show larger Wasserstein distances (Fig. 3B), but both types of mutations are affecting the scores for compartmentalization. These Wasserstein distances cannot be fully explained by a model of mutations affecting well-recognized features of proteins, such as short linear motifs, residues subjected to posttranslational modifications, or buried residues that might contribute to protein stability (figs. S16 and S20, and tables S7 to S9). These measures indicate that within this collection of pathogenic proteins, sequence variation may alter the predicted compartments of proteins in ProtGPS, suggesting that some mutant proteins may no longer partition selectively into compartments in the same manner as their normal counterparts.

To test experimentally whether pathogenic mutations predicted by ProtGPS to change protein distribution information content did so, we prepared cells ectopically expressing wild-type and pathogenic mutant proteins tagged with a fluorescent marker protein. We selected for study 20 pathogenic mutations (10 truncation and 10 single-point mutations) in proteins involved in a broad range of biological functions and diseases, whose normal cellular compartmentalization was well-known and that scored across the range of Wasserstein distances (0.162 to 0.000) (table S10). We then generated a panel of cell lines stably expressing each protein from a doxycycline-inducible expression cassette, treated cells with doxycycline, and conducted live-cell confocal microscopy analysis. Differences in the subcellular localization between normal and mutant proteins would appear as changes in the fluorescence patterns displayed in micrographs. We noted that signals for all the normal proteins occurred in the subcellular locations where they are known to reside. When comparing images of normal proteins with their mutant counterparts, we found striking differences in compartment appearance for almost all truncation mutation proteins and less-striking but clear differences in compartment appearance for point mutation proteins, except for RBM10 (V354M), which scored with a Wasserstein distance of 0 (Fig. 3C, fig. S21, and table S10). Thus, it appeared that proteins calculated to have a large Wasserstein distance tended to exhibit more dramatic changes in compartment appearance, although this relationship was imperfect (figs. S21 and S22). The effects of truncation mutations on nuclear localization sequences could not account for these results (Fig. 3C, fig. S22, and table S10). These results support the notion that ProtGPS can detect changes in protein codes resulting from pathogenic mutations that are demonstrable in an experimental setting.

Discussion

Our studies suggest that proteins have evolved to harbor at least two types of codes, one for folding and another for intracellular compartmentalization. Deep-learning algorithms such as AlphaFold2, RoseTTAFold, Chroma, EvoDiff, ESMfold, and others have learned the relationships between linear amino acid sequence and three-dimensional structure (*22*, *37*, *45*–*49*). Here, we describe ProtGPS, which can predict a protein's selective assembly into specific condensate compartments in cells. ProtGPS with the MCMC algorithm also showed reasonable success in generating novel proteins that selectively partition into the targeted condensate compartments. The complexity of the underlying physicochemical rules for both protein folding and protein localization have proven difficult to parse when using human interpretable approaches, and these deep-learning approaches therefore provide valuable predictive and analytical tools for the study of protein structure and function.

Previous studies of protein compartmentalization have already described versions of amino acid codes for some compartments. Blobel and Sabatini proposed a seminal version of amino acid sequence–encoded information with their discovery of a signal peptide sequence for translocation to the endoplasmic reticulum (*50*, *51*). For the membrane-bound nucleus, there are well-known nuclear localization sequences that facilitate the transport of protein from the cytoplasm to the nucleus (*52*–*54*). More recently, models were used to identify patterns in protein sequences associated with specific compartments, especially those bounded by a membrane, but these did not sample a broad range of compartments and lacked generative experiments (*55*–*57*). For nonmembrane compartments, here called condensates, there is recent evidence of patterned amino acid sequence features that can engender selective assembly of certain proteins into transcriptional and nucleolar condensates (*58*–*62*). Disease-related human genetic mutations have been shown to affect protein localization and provide additional experimental evidence for a protein code that contributes to compartmentalization (*62*–*64*). These observations are consistent with the concept of a protein code that promotes the selective distribution of proteins into specific compartments. Furthermore, there is recent evidence of distinctive chemical environments within condensates, suggesting that these compartments have different solvent properties (*16*, *61*, *65*). Thus, the patterns of amino acid sequences in proteins would be expected to both promote specific folding behaviors and to favor residence in compartments compatible with their solvent properties.

Patterns of amino acid sequences that occur in proteins, such as hydrophobic surface patches and blocks of charged residues or repeats, appear overall to be highly constrained in biology (*66*–*72*), and we suggest that this is due, in part, to the requirements for both proper folding and subcellular distribution. In our efforts to develop ProtGPS as a guide for generating novel protein sequences that promote selective subcellular distribution, we found that protein sequences sampled from collections of natural proteins were more successful at concentrating in the desired compartment than those generated without this consideration. Analogous to the medicinal chemist's aspiration to increase drug-like attributes such as on-target specificity and low off-target effects when developing small-molecule therapeutics, designing proteins to preferentially distribute in biochemically relevant regions of the targeted cell population might improve upon their therapeutic properties (*16*, *65*, *73*). In addition, exploring the chemical space of proteins naturally present in specific biological compartments may provide a valuable guide to the generation of optimal chemical matter directed to target proteins in specific compartments. Indeed, there are widely used and efficacious anticancer therapeutics that concentrate in transcriptional condensates at oncogenes (*73*) owing to the chemical environment of those compartments (*16*, *65*). It is evident that similar considerations will apply to the design of protein therapeutics. We suggest that further understanding of the chemical environment established by amino acid patterns in proteins will lead to more efficacious disease therapeutics.

We conclude that ProtGPS can predict a protein's selective assembly into specific condensates and guide generation of novel protein sequences whose cellular compartmentalization can be experimentally validated. We anticipate that future studies will advance this field by improving compartment annotation, modeling nested compartments, performing large-scale tests of generated proteins, developing robust techniques for measuring compartmentalization in vivo, deploying alternative machine learning approaches, and further exploring the effects of pathogenic mutations.

REFERENCES AND NOTES

1. S. F. Banani, H. O. Lee, A. A. Hyman, M. K. Rosen, *Nat. Rev. Mol. Cell Biol.* **18**, 285–298 (2017).
2. S. A. Lambert *et al.*, *Cell* **172**, 650–665 (2018).
3. P. Cramer, *Nature* **573**, 45–54 (2019).
4. S. Jena *et al.*, *Chem. Soc. Rev.* **51**, 4261–4286 (2022).
5. E. L. Huttlin *et al.*, *Nature* **545**, 505–509 (2017).
6. K. Luck *et al.*, *Nature* **580**, 402–408 (2020).
7. L. J. Walport, J. K. K. Low, J. M. Matthews, J. P. Mackay, *Chem. Soc. Rev.* **50**, 12292–12307 (2021).
8. Y. Shin, C. P. Brangwynne, *Science* **357**, eaaf4382 (2017).
9. M. Feric *et al.*, *Cell* **165**, 1686–1697 (2016).
10. S. Alberti, A. A. Hyman, *Nat. Rev. Mol. Cell Biol.* **22**, 196–213 (2021).
11. J.-M. Choi, A. S. Holehouse, R. V. Pappu, *Annu. Rev. Biophys.* **49**, 107–133 (2020).
12. B. Tsang, I. Pritišanac, S. W. Scherer, A. M. Moses, J. D. Forman-Kay, *Cell* **183**, 1742–1756 (2020).
13. W.-K. Cho *et al.*, *Science* **361**, 412–415 (2018).
14. B. R. Sabari *et al.*, *Science* **361**, eaar3958 (2018).
15. F. B. Sheinerman, R. Norel, B. Honig, *Curr. Opin. Struct. Biol.* **10**, 153–159 (2000).
16. H. R. Kilgore *et al.*, *Nat. Chem. Biol.* **20**, 291–301 (2024).
17. Y. Yu, J. Wang, Q. Shao, J. Shi, W. Zhu, *Sci. Rep.* **6**, 19500 (2016).
18. A. Ben-Naim, *Biopolymers* **29**, 567–596 (1990).
19. A. M. Klibanov, *Nature* **409**, 241–246 (2001).
20. N. Prabhu, K. Sharp, *Chem. Rev.* **106**, 1616–1623 (2006).
21. A. Chandra, L. Tünnermann, T. Löfstedt, R. Gratz, *eLife* **12**, e82819 (2023).
22. Z. Lin *et al.*, *Science* **379**, 1123–1130 (2023).
23. UniProt Consortium, *Nucleic Acids Res.* **49**, D480–D489 (2021).
24. N. Rostam *et al.*, *Nat. Methods* **20**, 673–676 (2023).
25. S. Kruschel *et al.*, Challenging the Performance-Interpretability Trade-off: An Evaluation of Interpretable Machine Learning Models. arXiv:2409.14429 [cs.LG] (2024).
26. J.-E. Shin *et al.*, *Nat. Commun.* **12**, 2403 (2021).
27. C. Lipinski, A. Hopkins, *Nature* **432**, 855–861 (2004).
28. M. Beckers, N. Fechner, N. Stiefl, *J. Chem. Inf. Model.* **62**, 6002–6021 (2022).
29. P. Kirkpatrick, C. Ellis, *Nature* **432**, 823 (2004).
30. N. Ananthan, F. John Malcolm, L. Simon, M. Sergei, *Structure* **32**, 1260–1268.e3 (2023).
31. A. S. Holehouse, B. B. Kragelund, *Nat. Rev. Mol. Cell Biol.* **25**, 187–211 (2024).
32. R. van der Lee *et al.*, *Chem. Rev.* **114**, 6589–6631 (2014).
33. Y. Zhang *et al.*, *JCI Insight* **8**, e170001 (2023).
34. J. Kornienko *et al.*, *Nat. Commun.* **14**, 4312 (2023).
35. B. L. Hie *et al.*, *Nat. Biotechnol.* **42**, 275–283 (2024).
36. A. H.-W. Yeh *et al.*, *Nature* **614**, 774–780 (2023).
37. J. L. Watson *et al.*, *Nature* **620**, 1089–1100 (2023).
38. N. R. Bennett *et al.*, *Nat. Commun.* **14**, 2625 (2023).
39. M. J. Landrum *et al.*, *Nucleic Acids Res.* **46**, D1062–D1067 (2018).
40. C. E. Shannon, *Bell Syst. Tech. J.* **27**, 379–423 (1948).
41. A. Lesne, *Math. Structures Comput. Sci.* **24**, e240311 (2014).
42. L. V. Kantorovich, *Manage. Sci.* **6**, 366–422 (1960).
43. C. Villani, in *Optimal Transport: Old and New*, vol. 338 of *Grundlehren der mathematischen Wissenschaften*, A. Chenciner, J. Coates, S.R.S. Varadhan, Eds. (Springer, 2009), pp. 93–111.
44. V. M. Panaretos, Y. Zemel, *Annu. Rev. Stat. Appl.* **6**, 405–431 (2019).
45. J. B. Ingraham *et al.*, *Nature* **623**, 1070–1078 (2023).
46. S. Alamdari *et al.*, Protein generation with evolutionary diffusion: sequence is all you need. bioRxiv 2023.09.11.556673 [Preprint] (2023). https://doi.org/10.1101/2023.09.11.556673.
47. S. L. *et al.*, *Nat. Biotechnol.* **2024** (2024).
48. R. Krishna *et al.*, *Science* **384**, eadl2528 (2024).
49. J. Jumper *et al.*, *Nature* **596**, 583–589 (2021).
50. G. Blobel, D. D. Sabatini, *J. Cell Biol.* **45**, 130–145 (1970).
51. D. D. Sabatini, G. Blobel, *J. Cell Biol.* **45**, 146–157 (1970).
52. E. M. De Robertis, R. F. Longthorne, J. B. Gurdon, *Nature* **272**, 254–256 (1978).
53. C. Dingwall, S. V. Sharnick, R. A. Laskey, *Cell* **30**, 449–458 (1982).
54. J. Lu *et al.*, *Cell Commun. Signal.* **19**, 60 (2021).
55. H. Kobayashi, K. C. Cheveralls, M. D. Leonetti, L. A. Royer, *Nat. Methods* **19**, 995–1003 (2022).
56. Y. Jiang *et al.*, *Comput. Struct. Biotechnol. J.* **19**, 4825–4839 (2021).
57. V. Thumuluri, J. J. Almagro Armenteros, A. R. Johansen, H. Nielsen, O. Winther, *Nucleic Acids Res.* **50**, W228–W234 (2022).
58. K. L. Saar *et al.*, *Nat. Commun.* **15**, 5418 (2024).
59. A. Patil *et al.*, *Cell* **186**, 4936–4955.e26 (2023).
60. H. Lyons *et al.*, *Cell* **186**, 327–345.e28 (2023).
61. M. R. King *et al.*, *Cell* **187**, 1889–1906.e24 (2024).
62. M. A. Mensah *et al.*, *Nature* **614**, 564–571 (2023).
63. S. F. Banani *et al.*, *Dev. Cell* **57**, 1776–1788.e8 (2022).
64. J. Lacoste *et al.*, *Cell* **187**, 6725–6741.e13 (2024).
65. H. R. Kilgore, R. A. Young, *Nat. Chem. Biol.* **18**, 1298–1306 (2022).
66. A. I. Podgornaia, M. T. Laub, *Science* **347**, 673–677 (2015).
67. D. Repecka *et al.*, *Nat. Mach. Intell.* **3**, 324–333 (2021).
68. A. J. Faure *et al.*, *Nature* **634**, 995–1003 (2024).
69. J. M. Smith, *Nature* **225**, 563–564 (1970).
70. T. Hayes *et al.*, *Science* **387**, eads0018 (2025).
71. S. Romero-Romero, S. Lindner, N. Ferruz, *Cold Spring Harb. Perspect. Biol.* **15**, a041471 (2023).
72. H. Garcia-Seisdedos, C. Empereur-Mot, N. Elad, E. D. Levy, *Nature* **548**, 244–247 (2017).
73. I. A. Klein *et al.*, *Science* **368**, 1386–1392 (2020).
74. P. G. Mikhael, H. R. Kilgore, I. Chinn, I. Mitnikov, Code and Data for "Protein Codes Promote Selective Subcellular Compartmentalization," Version v1, Zenodo (2024); https://doi.org/10.5281/zenodo.14795445.
75. H. R. Kilgore *et al.*, Data for "Protein Codes Promote Selective Subcellular Compartmentalization," Figshare (2024); https://doi.org/10.6084/m9.figshare.25726581.

ACKNOWLEDGMENTS

We thank C. Lilliehook, A. Dall'Agnese, M. Gallagher, Y. Petri, J. Yang, S. Moreno, and J. Wohlwend for helpful comments, and C. Rausch and Warbler Creative for graphical artwork. **Funding:** This work was supported by NIH GM144283 (R.A.Y.), CA155258 (R.A.Y.), NSF PHY2044895 (R.A.Y.), the St. Jude Transcription Collaborative (R.A.Y), the Whitehead Innovation Initiative (H.R.K., C.V.D., T.I.L., and R.A.Y.), Damon Runyon Cancer Research Foundation Fellowship 2458-22 (H.R.K.), the DTRA Discovery of Medical Countermeasures Against New and Emerging (DOMANE) Threats program (I.C., P.G.M., I.M., and R.B.), the MIT Jameel Clinic for Machine Learning in Health (I.C., P.G.M., I.M., and R.B.), Quanta Computing (I.C., P.G.M., I.M., and R.B.), the Centurion Foundation (I.C., P.G.M., I.M., and R.B.), the Brigham and Women's Hospital Clinical Pathology Residency Program (S.F.B.), and NIH National Cancer Institute (NCI) T32 CA251062-02 (S.F.B.). **Author contributions:** Conceptualization: H.R.K., R.A.Y.; Methodology: H.R.K., I.C., P.G.M., I.M.; Investigation: H.R.K., I.C., P.G.M., I.M., C.V.D., S.F.B., L.A., S.W.-H.; Visualization: H.R.K., R.A.Y.; Funding acquisition: R.B., R.A.Y.; Project administration: H.R.K., R.B., R.A.Y.; Supervision: H.R.K., R.B., R.A.Y.; Writing – original draft: H.R.K., I.C., P.G.M., I.M., R.A.Y.; Writing – review & editing: H.R.K., I.C., P.G.M., I.M., T.I.L., R.A.Y. **Competing interests:** R.A.Y. is a founder and shareholder of Camp4 Therapeutics, Omega Therapeutics, Dewpoint Therapeutics, and Paratus Sciences, and has consulting or advisory roles at Precede Biosciences and Novo Nordisk. R.B. has consulting or advisory roles at Dewpoint Therapeutics, J&J, Amgen, Outcomes4Me, Immunai, and Firmenich. H.R.K. is a consultant of Dewpoint Therapeutics. I.C. and I.M. are founders and shareholders of Voltaris. H.R.K., R.A.Y., I.C., P.G.M., I.M., and R.B. are inventors on patent application 63/634,125 submitted by Whitehead Institute that covers protein codes involved in cellular distribution. All other authors declare that they have no competing interests. **Data and materials availability:** Code and model weights used in this analysis are available at Zenodo (*74*) and GitHub (https://github.com/pgmikhael/protgps). Source data are available at Figshare (*75*). Reagents used are available upon reasonable request. **License information:** Copyright © 2025 the authors, some rights reserved; exclusive licensee American Association for the Advancement of Science. No claim to original US government works. https://www.science.org/about/science-licenses-journal-article-reuse

SUPPLEMENTARY MATERIALS

science.org/doi/10.1126/science.adq2634
Materials and Methods
Supplementary Text
Figs. S1 to S22
Tables S1 to S10
References (*76*–*112*)
MDAR Reproducibility Checklist

Submitted 5 May 2024; resubmitted 7 November 2024
Accepted 28 January 2025
Published online 6 February 2025
10.1126/science.adq2634

ARTIFICIAL MUSCLES

Mandrel-free fabrication of giant spring-index and stroke muscles for diverse applications

Mengmeng Zhang[1], Shaoli Fang[1]*, Wenting Cai[2], Chi Huynh[3], Fatma Göktepe[4], Jiyoung Oh[1], Zhong Wang[1], Ishara Ekanayake[1], Özer Göktepe[4], Ray H. Baughman[1]*

Methods for making high-spring-index polymer fiber or yarn muscles have required expensive fabrication by wrapping around a mandrel, which limits their practical applications. We demonstrate an inexpensive mandrel-free method for making polymer muscles that can have a spring index of >50 and a contractile tensile stroke exceeding 97%. This method enables the spring index to be varied along a muscle's length by varying the plying twist, resulting in muscles that transition between homochiral and heterochiral when either heated or cooled. We demonstrate use of these polymer muscles for robots and environmentally driven comfort-adjusting jackets. This mandrel-free method was used to make high-spring-index carbon nanotube yarns for mechanical energy harvesters, self-powered strain sensors, and solvent-driven and electrochemically driven artificial muscles.

Polymer fibers and nanofiber yarns made by coiling twisted yarns have been of interest for diverse applications, such as artificial muscles (*1*–*6*), twistocaloric refrigerators (*7*, *8*), mechanical energy harvesters (*9*, *10*), elastic conductors (*11*, *12*), batteries (*13*, *14*), and supercapacitors (*15*, *16*). This coiling provides extremely high elasticity and a diversity of other useful properties (*17*, *18*), because yarn elongation enables conversion of coiling twist (called writhe) to yarn twist (called twist). This twist conversion upon stretching in an electrolyte densifies a charge-injected carbon nanotube (CNT) yarn, which decreases its capacitance by temporarily destroying electrochemical double layers. This capacitance decrease increases yarn voltage versus a counter electrode, so that mechanical energy can be harvested as electricity (*9*, *10*). Similarly, the volume increase produced by electrochemically injecting charge into a coiled CNT yarn causes the conversion of yarn twist to yarn coiling, which can result in powerful large-stroke actuation (*2*). The conversion of yarn writhe to yarn twist when stretching a coiled polymer fiber decreases polymer entropy, thereby enabling refrigeration when the stretch is released (*7*, *8*). These property changes are for a homochiral yarn, in which writhe and twist have the same chirality.

The yarn's functionality and mechanical properties depend on the spring index (*7*, *10*, *19*, *20*), which is the ratio of the yarn-center to yarn-center coil diameter to the diameter of the component fiber. The most common method for making a homochiral coiled yarn or fiber is called self-coiling, because twist is inserted under a sufficiently high tensile load that complete coiling occurs without snarling (*1*). Nevertheless, the spring index of a self-coiled polymer fiber is typically <1.7 (*1*), which cannot provide large muscle strokes. For many applications, such as large-stroke artificial muscles (*21*, *22*) and muscle-driven morphing structures (*23*), a spring index of >2 is required.

To realize a large spring index muscle by mandrel coiling, which is achieved by helically wrapping a twisted fiber or yarn around a mandrel (*24*–*27*), would require a mandrel volume that is giant compared with the volume of the produced mandrel-coiled muscle. This is a problem for mandrel coiling, as this process requires mandrel dissolution, and thus the creation of a substantial waste stream.

The mechanical energy delivered by a coiled artificial muscle decreases on increasing this spring index. For many applications, the coiled polymer muscle's tensile stroke is more important than the delivered mechanical energy, and this stroke increases with increasing spring index (*28*, *29*). One application is the use of high-spring-index coiled muscles in comfort-adjusting jackets, which automatically increases the jacket's insulation by opening large thermally insulating pores as the ambient temperature becomes uncomfortably cold (*30*, *31*). The muscle stroke needed to open these pores in response to small ambient temperature changes must be large (*31*). If a contacting mandrel is retained in a high-spring-index fiber, much of the muscle's work capacity would be used to deform the mandrel (*32*).

Mandrel-free fabrication of high-spring-index homochiral polymer fibers or yarns

We developed a mandrel-free process, wherein the final product high-spring-index coiled structure can optionally comprise either a single fiber or a single yarn. The term "yarn length" (or "fiber length") means the length within the coiled structure. This mandrel-free method involves inserting twist into the individual fibers at a level below the twist that causes coiling, and then plying these twisted fibers to create coils for each ply (movie S1). Thermally annealing the torsionally and positionally tethered plied fiber largely freezes the coils of the plied fibers (figs. S1 to S3). During plying, each fiber serves as a mandrel for other fibers (Fig. 1, A and B). A second thermal anneal is then applied to nontethered ply-extracted fibers so that they realize an equilibrated, uniformly coiled, increased spring index structure with reduced intercoil separation (Fig. 1, C and D) (*33*). This is because relaxation to a lower-energy coiled structure is no longer constrained by neighboring plies. These ply-extracted coiled (PEC) fibers before and after the second thermal anneal are called pre-PEC fibers and PEC fibers, respectively.

Although this mandrel-free process is useful for various polymer fibers, we focus on polyurethane fibers (fig. S4) and nylon-6 fishing-line fibers. When the plied nylon-6 fibers were first thermally annealed, they were torsionally and positionally tethered in vacuum at 120°C for 2.5 hours. Unless otherwise mentioned, a twist density of 5.0 turns/cm under an 18.5 MPa load was used for nylon fiber twist to maximize the spring index of PEC fibers (fig. S5). Tensile stresses are normalized to the fiber's cross-sectional area after fiber twist and before plying, or to *n* times this area when *n* fibers are plied.

The spring index can be increased by increasing the number of plies (fig. S6). However, when the ply number exceeds 5, close

---

[1] Alan G. MacDiarmid NanoTech Institute, University of Texas at Dallas, Richardson, TX, USA. [2] Department of Chemistry and Biochemistry, Texas State University, San Marcos, TX, USA. [3] Lintec of America, Inc., Nano-Science & Technology Center, Plano, TX, USA. [4] Textile Engineering Department, Çorlu Engineering Faculty, Tekirdağ Namık Kemal University, Tekirdağ, Turkey.
***Corresponding author. Email: ray.baughman@utdallas.edu (R.H.B.); sfang@utdallas.edu (S.F.)**

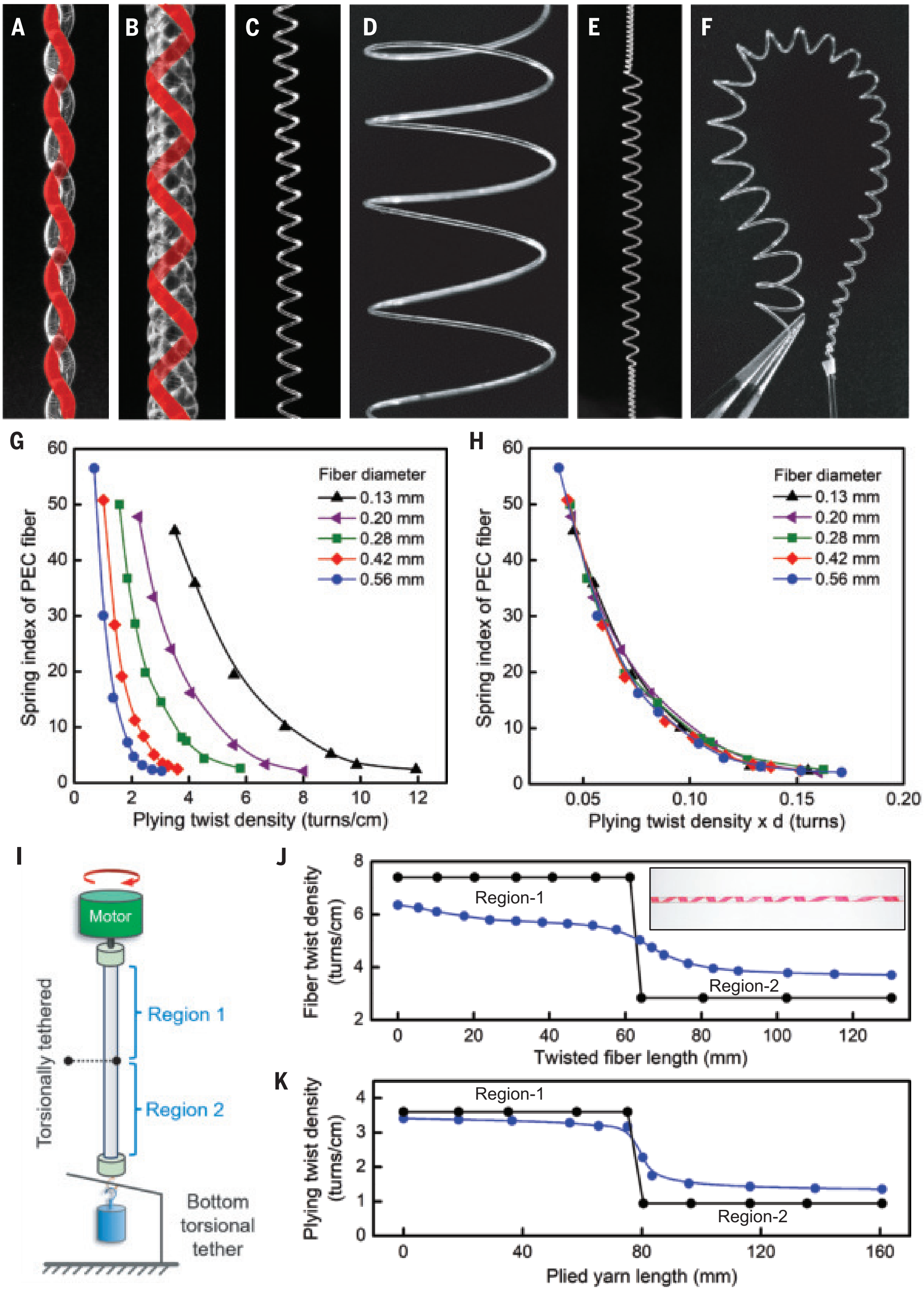

Fig. 1. Mandrel-free fabrication and optical microscope images of plied and PEC fibers made from 0.28-mm-diameter nylon-6 fibers. Images of single-fiber-colorized (**A**) two-ply and (**B**) four-ply fibers, with plying twist densities of 4.5 and 4.0 turns/cm, respectively. Images of PEC fibers having spring indexes of: (**C**) 7.7, (**D**) 45.2, and (**E**) 2.6 at the ends and 9.6 in the middle, and (**F**) which monotonically increase from 2.4 to 18.1. The dependencies of the spring indexes of PEC fibers on (**G**) the plying twist density and (**H**) the product of plying twist density and precursor fiber diameter (*d*). The fibers used in (G) and (H) were twisted to the same fiber bias angle of ~26° under a tensile stress of 18.5 MPa. During plying twist, the applied tensile stress for these different-diameter fibers was the same as used for fiber twist. (**I**) Illustration of our simplest fiber-region-separated twist method for making multi-twist-level fibers, where the bottom tether is continuously maintained, and the middle tether is applied only during the final twist insertion in region 1. (**J**) The length dependence of fiber twist before (black circles) and after midpoint tethering release (blue circles) for a fiber that initially has a uniform twist (2.83 turns/cm) and has been further twisted by midpoint tethering in region 1. (Inset) Optical microscope image of a central region of this fiber (from 54.7 to 68.0 mm) after removal of the midpoint tether (where the variation in bias angle was made visible by marking the nontwisted fiber with a straight red line). (**K**) The twist density during plying along the length of a two-ply yarn with a midpoint tether (black circles) and after removal of the midpoint tether (blue circles).

packing of the fibers in the plied structure requires one fiber (or possibly alternating segments of all plies) to be in the center, so uniform coiling of all fibers does not occur (fig. S7). The second thermal anneal temperature can be optimized (between the first thermal anneal temperature and the fiber's melting point) to further increase the spring index of PEC fibers (fig. S8) (*33*) and was also used to fabricate a multi-spring-index coiled fiber by using region-selected thermal anneal (fig. S9). This second thermal anneal was also used to increase the spring index of a self-coiled fiber, although the increase in spring index was much smaller than for pre-PEC fibers when using similar thermal annealing processes (fig. S10).

A more effective method to increase the spring index is to reduce the plying twist density, because a low plying twist density provides the long length per coil needed for high-spring-index transformed fibers. For precursor fibers with diameters ranging from 0.13 to 0.56 mm, the spring index of two-ply-extracted PEC fibers increased with decreasing plying twist density (Fig. 1G), when the fiber bias angle, the load during fiber twist and yarn plying, and the first and second thermal anneal processes were the same (fig. S11). Although the dependence of spring index, coil bias angle, and length per coil (normalized to fiber diameter) on plying twist density strongly depends on the precursor fiber diameter, these parameters remained the same when the product of plying twist density and precursor fiber diameter was kept constant (Fig. 1H and figs. S12 and S13). These correlations are explained in the supplementary materials (*33*). Under these constant fabrication conditions, we can predict and control the spring index of PEC fibers having any diameter between 0.13 and 0.56 mm from the results for one fiber with a diameter in this range. When the tensile load during plying was increased from 18.5 to 64.6 MPa, the spring index of the PEC fibers negligibly changed (fig. S14). This dependence of the torsional deformation during plying on the product of plying twist density and fiber diameter is like the dependence of a twisted fiber's bias angle on the product of twist density and fiber diameter during fiber twist (*34*–*37*).

A single fiber or yarn with multiple twist levels

To make a fiber having twist densities that vary along its length, we used a fiber-region-separated twist method, which includes inserting an initial twist into the entire fiber, torsionally tethering separated regions, and then inserting or removing a given twist from fiber regions that are not torsionally tethered (Fig. 1I).

We demonstrate the use of this fiber-region-separated twist method to provide a single fiber having different twist densities in two different fiber regions. Initially, 2.83 turns/cm of twist was inserted into a 0.28-mm-diameter, 130-mm-long fiber, and then the midpoint of this fiber was torsionally tethered, and an additional twist of 4.57 turns/cm was inserted between the fiber's nontethered end and its midpoint. The top and bottom regions of this fiber are called region 1 and region 2, respectively (Fig. 1J). The twist densities in region 1 and region 2 are 7.40 and 2.83 turns/cm, respectively. After removing the midpoint torsional tether, part of the twist in the highly twisted region transferred to the low-twist region. The twist density was indicated by the observed fiber bias angle (fig. S15), as these two parameters are approximately linearly corelated (fig. S5A).

Much more complicated distributions of fiber twist can be introduced by using multiple tethering points during twist insertion, or twist insertion and twist removal, for different fiber regions and then removing all of these internal tethers. The aforementioned fiber twist method was also used for profiling plying twist (Fig. 1K), where different plying twists were introduced in different regions of a two-ply yarn. After applying plying twists of 0.94 and 3.60 turns/cm, respectively, to region 2 and region 1, the midpoint torsional tether was removed, enabling some of the plying twist to transfer from the highly twisted plied segment to the less twisted plied segment (Fig. 1K and fig. S16). Given that plying twist density affects the spring index (Fig. 1G), the resulting PEC fiber has a wide distribution of spring indexes along its length.

By applying this process to more-than-two-plied yarn segments, we made PEC fibers having various coil geometries. For example, Fig. 1E shows a PEC fiber in which both ends have the same small spring index (SI: 2.6), while the middle segment has a large spring index (SI: 9.6). Figure 1F shows an intentionally-bent PEC fiber having gradually increased spring indexes from one end (SI: 2.4) to the opposite end (SI: 18.1). It is difficult to make the abovementioned coiled structures with the mandrel-coiling method, because the needed variable mandrel diameter would make it impossible to remove the mandrel-coiled fiber from the mandrel unless the mandrel were dissolved. This ability to profile the spring index of a muscle in diverse ways will enable quite different actuation for various segments of the muscle's length (*38*), which can be usefully deployed for robotic applications (*3*, *39*).

An especially interesting case is when the spring indexes are large and variation in spring index between neighboring coils is sufficient for successive coils to interpenetrate, so the length of the contracted muscle essentially equals the fiber diameter. We previously demonstrated this interpenetration capability by annealing a short polymer fiber in the helical corridor of a flat plate (*35*), but this process is expensive and not applicable for a very long fiber. However, using our fiber-region-separated twist method, a PEC muscle having a continuous gradient in spring index can be made that inverts coil chirality when either heated or cooled (movie S2).

Mandrel-free fabrication and performance of high-spring-index homochiral CNT yarns

This mandrel-free process can also be used for making high-spring-index CNT yarns for diverse applications. However, instead of using low-temperature anneals, we used our incandescent tension anneal process (ITAP) (*40*, *41*) to set the plied CNT yarn structure. Before plying, each CNT yarn was twisted to a twist density just below coil initiation for the applied tensile stress. The tensile-loaded twisted CNT yarns were then plied together until just below the plying twist where the plied yarns begin coiling (*10*). Afterward, they were set by ITAP in an inert environment at ~3000°C for 1 min by electric pulse heating. The ITAP was only used once for setting the plied structure, because ITAP already provides well-separated coils. Thereafter, individual CNT yarns were extracted from the plied structure. Figure 2A shows scanning electron microscope (SEM) images of the untreated two-ply CNT yarn, the plied yarn after ITAP, and one of the yarns extracted from the ITAP-treated plied yarn.

We alternatively used solvent treatment to set the tethered plied structure. There is no need for further solvent treatment of the ply-extracted yarn, as this yarn is already uniformly coiled. Ethanol adsorption and evaporation eliminate the internal torque within CNT yarn that causes major yarn untwist when tethering is removed (*42*). Figure 2B shows the solvent-treated two-ply yarn and a yarn extracted from this plied yarn. For a ply-extracted CNT yarn derived from the same untreated two-ply yarn, the spring index and the coil bias angle of the ITAP-treated yarn were smaller than for the solvent-treated yarn. This is because the ITAP treatment more completely freezes this plied structure than does solvent treatment.

We evaluated application of solvent-treated CNT yarns as self-powered strain sensors and energy harvesters (fig. S17), which were previously investigated only for small-spring-index self-coiled (*9*) or plied (*10*) twistron yarns, which both require torsional tethering during operation and do not enable mechanical energy harvesting or sensing for giant applied strains. Figure 2C shows that the open-circuit voltage and capacitance decrease are both large and approximately linearly depend on percent elongation for both two- and four-ply extracted CNT yarns (fig. S18), which sense strains up to 80% and 120%, respectively. For a wide frequency range from 0.1 to 5 Hz, the output voltage of the CNT yarn strain sensor has very small hysteresis and little change for a given strain (fig. S19) (*33*). Additionally, the spring index for our solvent-treated ply-extracted yarns can be increased to much higher values, which would enable sensing over a much higher strain range, although the voltage change per strain change would be reduced. These mandrel-free fabricated high-spring-index yarns enable sensing to a higher strain than other previously investigated twistron-based strain sensors (fig. S19) (*33*). This means that they are very useful for deformation sensing for robotic applications that previously used capacitive, resistive, piezoelectric, or triboelectric sensors (*43*, *44*).

Given that ITAP partially welds together some of the yarn's nanotubes and provides higher tensile strength than does solvent treatment (*40*, *45*), we characterized solvent-driven and electrochemically driven actuation for the ITAP-produced CNT yarns (Fig. 2, D and E, and fig. S20). Although the contractile work capacity was not high, the maximum contractile stroke reached peaks of at least 21.0%.

Muscle performance of PEC polymer fibers

A high tensile load is always needed for a self-coiled fiber to provide the separation between

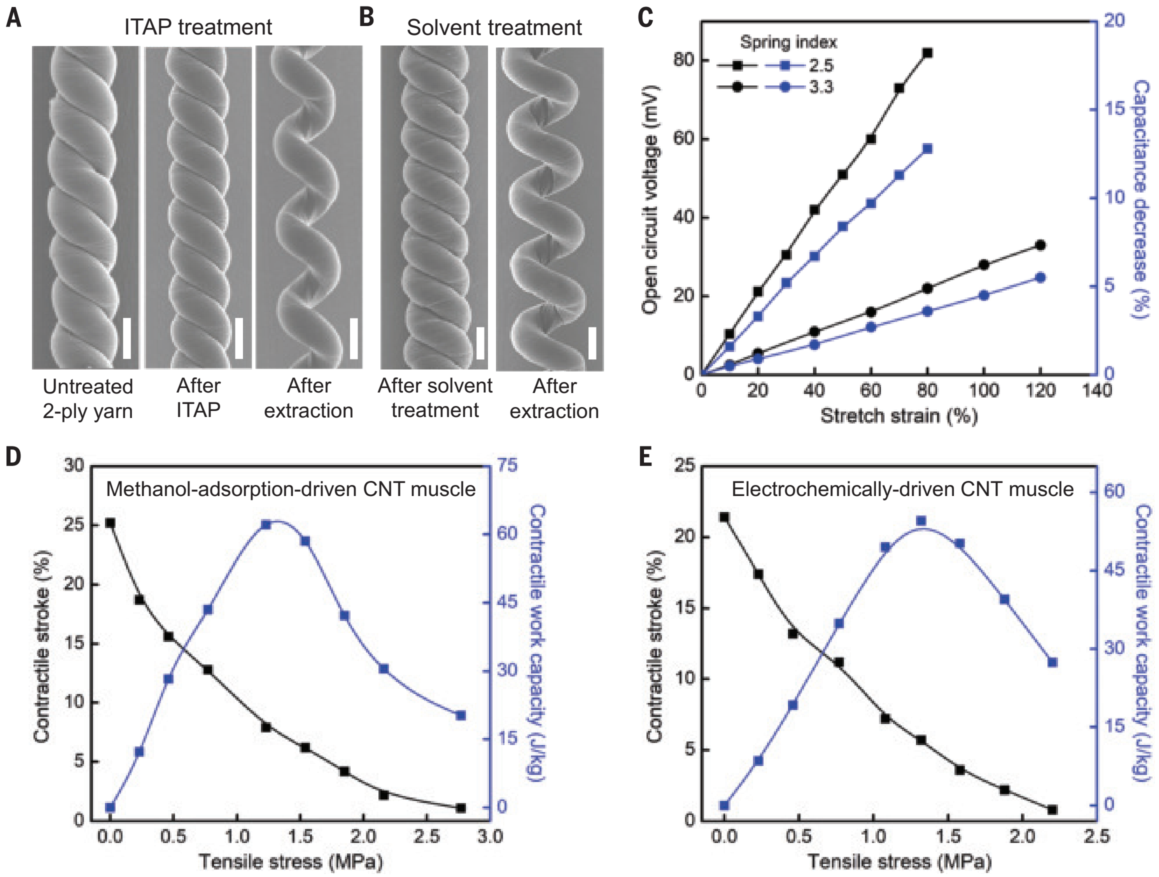

Fig. 2. Mandrel-free fabrication and performance of high-spring-index CNT yarns. (**A**) SEM images of untreated two-ply CNT yarn, plied yarn after ITAP, and a yarn extracted from the ITAP-treated plied yarn. Scale bars: 100 μm. (**B**) SEM images of a two-ply yarn after solvent (ethanol) treatment and a yarn extracted from this plied yarn. Scale bars: 100 μm. (**C**) The dependence of generated open-circuit voltage and resulting capacitance decrease on the tensile strain for self-powered CNT yarn strain sensors when sinusoidally stretched at 1 Hz. Before the high-spring-index CNT yarns were extracted from plied yarns, ethanol adsorption and evaporation were used to set their plied structures. The spring indexes for the two-ply-extracted and the four-ply-extracted CNT yarns were 2.5 and 3.3, respectively. Both the ply-extracted CNT yarn and the Pt-mesh-wrapped buckypaper counter electrode were in 0.1 M LiCl/10 wt % poly(vinyl alcohol) gel electrolyte, which prevented interelectrode shorting. (**D**) The dependence of contractile stroke and work capacity on the tensile stress for methanol-adsorption-driven actuation. Methanol liquid (5 μl/cm) was dropped on the CNT yarn muscle for each contraction and then evaporated for muscle elongation. (**E**) The dependence of contractile stroke and work capacity on the tensile stress for electrochemically driven actuation in 0.2 M tetrabutylammonium hexafluorophosphate (TBA·PF$_6$) in propylene carbonate. The applied 0.02-Hz square-wave voltage between the CNT muscle working electrode and the counter electrode (a Pt-mesh-wrapped buckypaper) was −3.25 V. The two-ply-extracted CNT yarns (SI: 1.3) used in (D) and (E) were fabricated with the ITAP method for setting the two-ply yarn.

neighboring coils required for contraction, which limits the use of self-coiled fibers for important applications (*1*, *46*), especially those requiring large strokes and small loads (*28*). Consequently, self-coiled fibers are useless for highly flexible textile structures, as textile flexibility means that high loads cannot be applied, so the muscle stroke is near zero. A higher load for these self-coiled fibers during thermal anneal cannot be used to set them into a structure that has noncontacted periodic coils, because the regular coiled structure disappears when this higher load is applied during anneal (fig. S21). In contrast, as the plied structure has a large intercoil separation for each component fiber, a large muscle stroke was obtained for PEC fibers without applying a tensile load (figs. S22 and S23). Additionally, we found that the twist load and twist density during fiber twist insertion can be used to optimize PEC muscle actuation at both high and low temperatures (fig. S24).

Figure 3A shows that the tensile actuation of homochiral PEC muscles having different spring indexes is fully reversible for the investigated wide temperature range from −30° to 105°C. For a temperature change from 25° to 80°C, the ~20.7% contraction of a ~5.2 spring index PEC muscle (lifting a load providing a 0.5 MPa tensile stress) was maintained for >1800 heating-and-cooling cycles (Fig. 3B).

The effect of the second anneal temperature on the actuation of PEC fibers was investigated in order to maximize the strokes for given actuation temperature changes (fig. S25). However, given that a very high second thermal anneal temperature causes permanent fiber untwist, it drastically decreases the muscle's contractile work capacity (*1*). Unless otherwise mentioned, the second anneal temperature was 148°C. However, a different second thermal anneal temperature can be used to optimize the stroke and delivered work for specific application needs.

Figure 3, C and D, compares the contractile stroke and contractile work capacity of self-coiled and PEC fibers for thermal actuation between 25° and 93°C. These results indicate that the gravimetric work capacities of the self-coiled muscles are much larger than for PEC muscles, whereas self-coiled muscles have much smaller strokes. However, for applications (such as comfort-adjusting clothing) in which the needed work capacity is small but

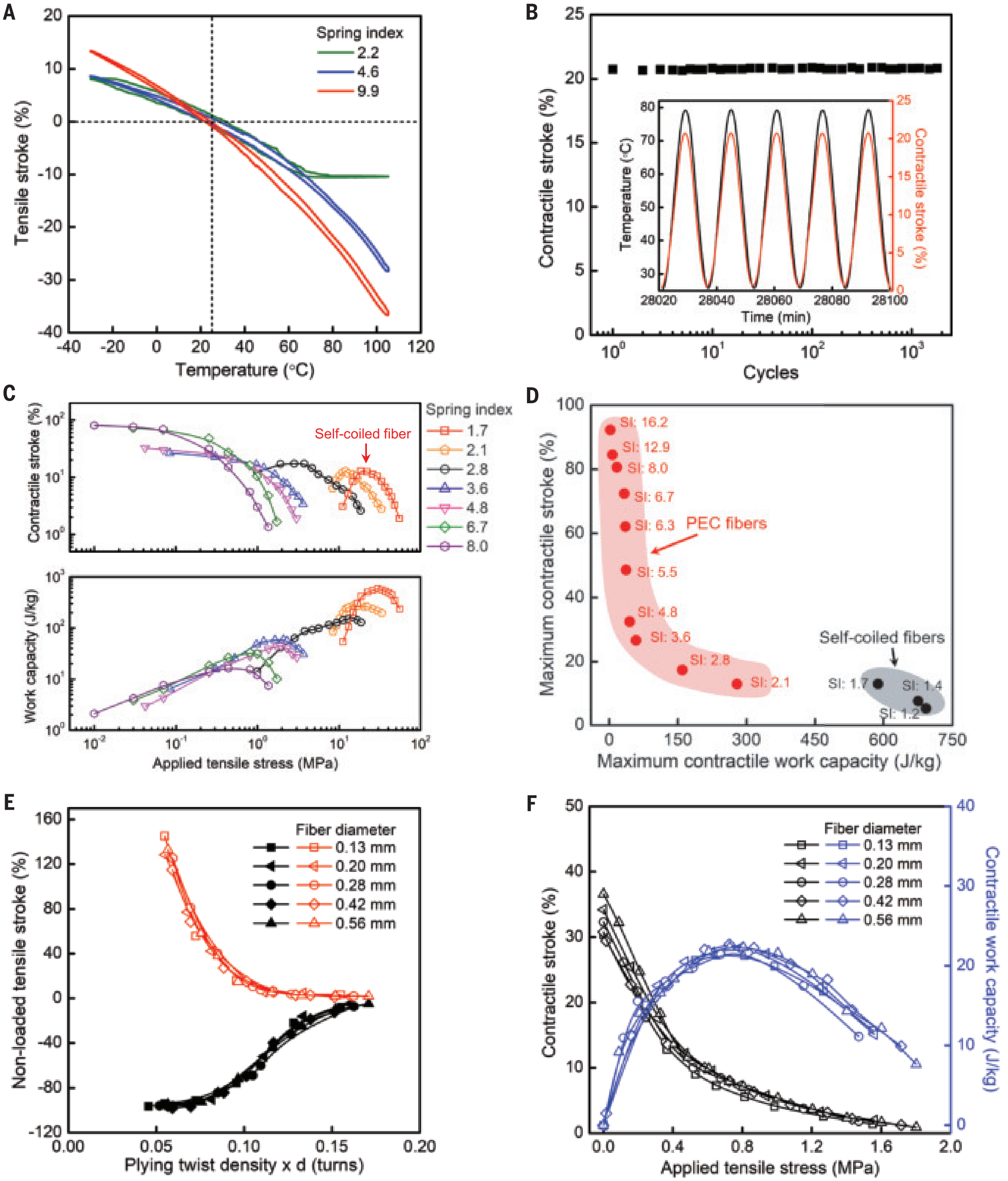

Fig. 3. Muscle performance of two-ply-extracted high-spring-index PEC nylon-6 fibers. (**A**) The temperature dependencies of tensile strokes for PEC muscles having spring indexes of 2.2, 4.6, and 9.9, when the temperature change rate was 1°C/min. The tensile loads applied to these fibers were 4.6, 0.25, and 0.25 kPa, respectively. When the temperature exceeded ~68°C, the flat region of tensile stroke for the muscle (SI: 2.2) was caused by neighboring coils fully contacting. (**B**) A PEC muscle's (SI: 5.2) tensile stroke during 1800 heating-cooling cycles over an ~20-day period when under a 0.5-MPa load. The temperature change rate was 10°C/min, and the investigated temperature range was between 25° and 80°C. The time per one heating-cooling cycle was ~15.6 min. (Inset) The time dependence of temperature and contractile stroke during the last five heating-cooling cycles. (**C**) The dependence of contractile stroke and gravimetric contractile work capacity of PEC fibers and a self-coiled fiber on the applied tensile stress for actuation between 25° and 93°C. Before plying, each individual 0.28-mm-diameter fiber was twist inserted to 5.7 turns/cm under a tensile stress of 18.5 MPa. (**D**) Comparison of maximum contractile strokes and maximum contractile work capacities for PEC fibers and self-coiled fibers. (**E**) The dependencies of the nonloaded tensile strokes of PEC fibers on the product of plying twist density and precursor fiber diameter. The actuation temperatures for muscle contraction and expansion were from 25° to 105°C and from 25° to −15°C, respectively. (**F**) For different-fiber-diameter PEC muscles having the same spring index (~4.5), the dependencies of contractile stroke and contractile work capacity on applied tensile stress was largely independent of precursor fiber diameters for actuation between 25° and 93°C. The fibers used in (E) and (F) were twist inserted to the same fiber bias angle of ~26° under a tensile stress of 18.5 MPa. During plying twist, the applied tensile stress for these different-diameter fibers was the same as used for fiber twist.

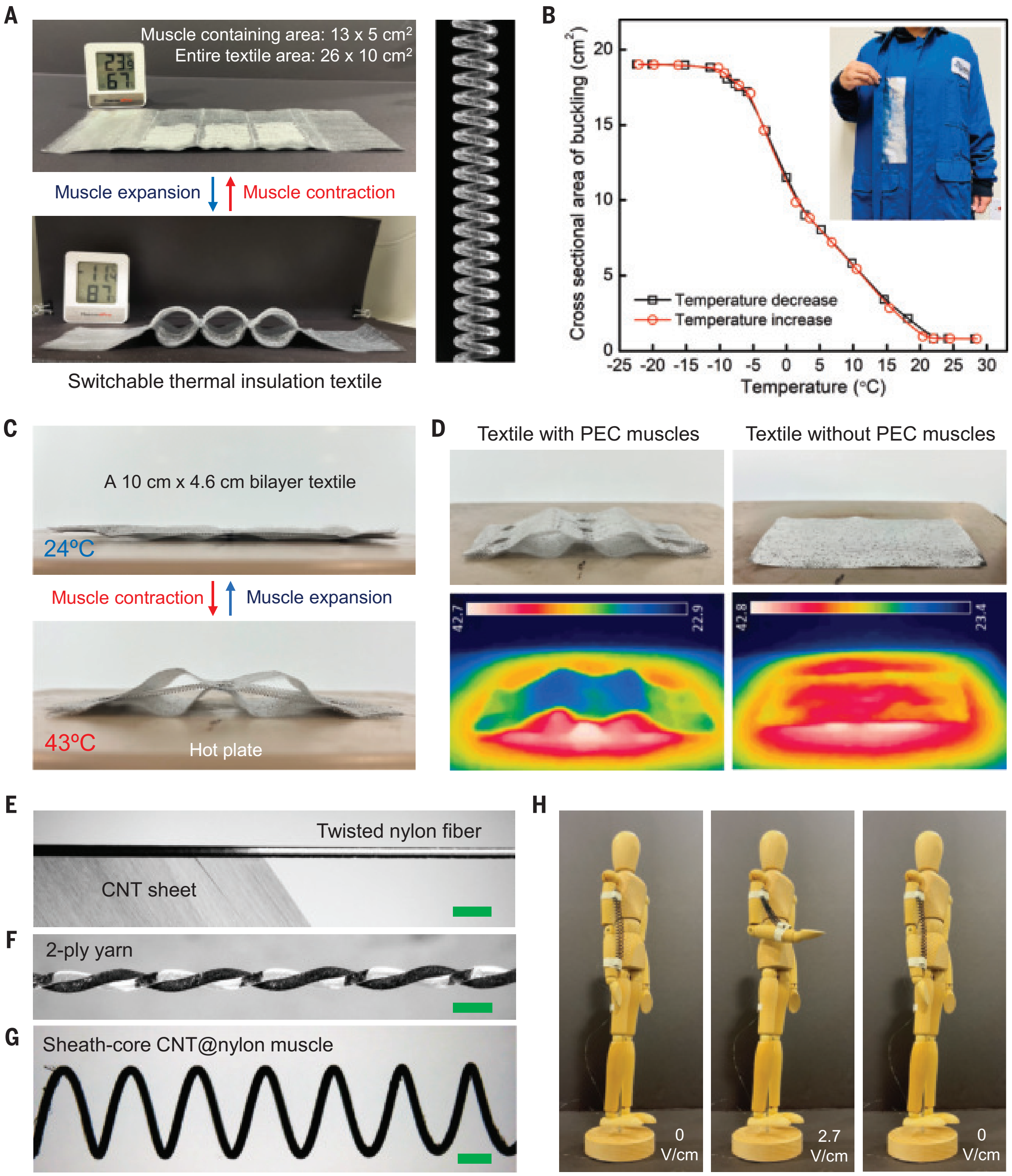

Fig. 4. Applications of PEC polymer fibers. (**A**) Photographs of a bilayer textile, with 21 homochiral PEC fibers sewn (white areas) on both exterior textile layers, when at 23°C (top) and when cooled to −11°C (bottom). The image on the right shows a PEC fiber (SI: ~4.5) used for this textile. (**B**) The dependence of the total interior cross-sectional area of three buckling sections of (A) on the environmental temperature. (Inset) Photograph showing our textile (A) incorporated between the layers of a comfort-adjusting coat. (**C**) Photographs of an actuated bilayer textile in which two homochiral PEC fibers (with 3.5-cm nonactuated length) were sewn midway between textile layers of the actuated sections, when at 24°C (top) and when on a 43°C hot plate (bottom). (**D**) Photographs (top) and corresponding infrared thermal images (bottom) of the bilayer textile from (C) and a bilayer textile without PEC fibers when on a 43°C hot plate. (**E**) A 5.0 turns/cm twisted 0.28-mm-diameter nylon fiber being wrapped with a single-layer CNT sheet. (**F**) A two-ply yarn in which only one ply was CNT wrapped. Before plying, each fiber had a 5.0 turns/cm twist. (**G**) A sheath-core CNT@nylon fiber (SI: 14.0) made from a two-ply yarn (F) having 3.0 turns/cm plying twist under 32 MPa load. Scale bars for (E), (F), and (G): 1 mm. (**H**) The use of two 84.5-mg-weight, 7.7-cm-long, high-spring-index sheath-core CNT@nylon muscles (SI: 6.2; precursor fiber diameter: 0.56 mm) for driving the bending of a 5-cm-long robotic arm. When the arm bent ~90° (middle photograph), the applied voltage per fiber length was 2.7 V/cm and resulting temperature was ~85°C. Nonconstraining 0.025-mm-diameter Pt wires were used for muscle connection.

large muscle strokes are required for small temperature changes (*28*, *29*), these data show that PEC muscles have major advantages. The spring index of PEC fibers can be chosen to provide both the needed stroke and work capacity for this and other applications.

Given that plying twist density mainly dominates the spring index of a PEC muscle (Fig. 1G), and the spring index strongly affects the muscle's tensile stroke, we also characterized the dependence of nonloaded tensile stroke during temperature increase and decrease for two-ply–extracted PEC muscles on the plying twist density (fig. S26A). Because a higher spring index provides a larger stroke, a lower plying twist density (corresponding to a higher spring index) provides a larger stroke for a constant-diameter precursor fiber. When the product of the plying twist density and precursor fiber diameter was kept constant, the effect of the fiber diameter on muscle tensile actuation was eliminated (Fig. 3E) (*33*). These results are useful for muscle applications, because they provide a general guideline for relating fabrication conditions and muscle performance. For these different diameter PEC fibers, the fiber bias angle, the load during fiber twist and yarn plying, and the first and second thermal annealing processes were kept the same.

Figure S26B shows that PEC fibers made from different precursor diameter fibers provided about the same tensile strokes when their spring indexes were the same. When the product of plying twist density and precursor fiber diameter was ~0.12 turns, the contractile stroke and work capacity of PEC muscles with the same spring index (~4.5) were essentially independent of the precursor fiber diameter for an applied tensile stress of 0 to 1.8 MPa (Fig. 3F). Additionally, our mandrel-free fabricated PEC muscles exhibited high consistency when the fabrication conditions were the same (fig. S27 and table S1) (*33*). In comparison to the mandrel-coiled muscles, our mandrel-free fabricated muscles provided a slightly higher maximum contractile stroke and slightly larger maximum work capacity (fig. S28) (*33*).

Applications of mandrel-free high-spring-index polymer PEC muscles

We describe textiles that increase thermal insulation when the outside temperature is either above or below the desired temperature. This ability is critically important when these switchable-insulation textiles are used for applications other than comfort-adjusting clothing, such as for thermal insulation of buildings or underwater or space structures.

For demonstration of PEC muscle use in comfort-adjusting clothing, we incorporated high-spring-index PEC muscles into the exterior of both layers of a bilayer textile. We sewed these PEC muscles on the outer fabric surface of each textile layer by using additional thread (fig. S29). This avoids the possible interference of the weaving process on muscle actuation and enables the use of diverse types of bilayer textiles and localization of morphing areas in any textile region. Figure 4A and movie S3 show this high morphing of a PEC-muscle-actuated bilayer textile. Figure 4B shows the giant fully reversible increase in the cross-sectional area of three intersheet insulating pores (from near-zero at 25°C to 19 cm^2 at −12°C) for complete morphing of our muscle-powered textile. In addition, as the fibers that we used for our mandrel-free method are those used for fishing line, there should be no problem with washability for our textile.

For thermal insulation at high temperatures, our PEC muscles were placed between two layers of a bilayer textile. As shown in Fig. 4C, giant pores reversibly opened when the bilayer textile was placed on a 43°C hot plate, whereas it was planar and low in thermal insulation at 24°C (movies S4 and S5). Infrared thermal images show that a flat bilayer sheet without PEC muscles conducts the hot temperature through the sheet structure, but the bilayer sheet containing PEC muscles becomes thermally insulating (so its top surface remains near room temperature) (Fig. 4D). Given the bilayer textile's response to overly cold or hot temperatures, a stack of two bilayer textiles (or many such two bilayer textiles that provide opposite temperature responses) can be deployed to provide switchable insulation at both targeted cold and hot temperatures for controlling temperatures in buildings or in underwater or space structures (*33*).

Figure S30 shows that a PEC muscle, having a monotonically increasing spring index from one end to the opposite end, propagated along a tube as a crawling robot having an average displacement of 25% of its length per heating-cooling cycle. It is desirable for most robotic applications to electrically drive a polymer muscle by directly heating it (*47*, *48*), instead of driving it by using a heated environment. We demonstrated the use of electrical heating to directly drive a PEC muscle that was fabricated from a twisted nylon-6 fiber that was layer-by-layer wrapped with ~15 layers of forest-drawn electrically conducting CNT sheets before plying (Fig. 4E and movie S6). A two-ply yarn was used, and for visual clarity, only one of the plied nylon fibers was wrapped with CNT sheets (Fig. 4F). However, all plied nylon fibers in practical examples would be individually coated with CNTs, and the precursor plied yarns are useful from two to five ply. A high-spring-index sheath-core CNT@nylon PEC fiber muscle (SI: 14.0) was obtained (Fig. 4G), as a low plying twist density (3.0 turns/cm) was used. The dependence of contractile stroke on the applied voltage per fiber length is shown for this sheath-core CNT@nylon PEC muscle (fig. S31). Also, our mandrel-free high-spring-index sheath-core CNT@nylon muscles were operated at a frequency of >1 Hz, and a 14.6% stroke was obtained at a cycle frequency of 0.5 Hz (fig. S32) (*33*). In addition, we demonstrated the use of two sheath-core PEC muscles to drive the bending of a robotic arm (Fig. 4H and movie S7). This sheath-core structure provides a practical strategy for precisely controlling contractile stroke for robotic applications (movies S8 and S9).

Conclusions

Our inexpensive mandrel-free process provides an important way to address applications where large strokes are required, but the delivered work can be small. Our technology enables the muscle's spring index, and corresponding tensile stroke, to be continuously varied in any desired manner over the muscle's entire length, merely by changing the plying twist density during manufacture. Using this method, we made continuously varied spring index muscles whose segments can contract to near-zero length and then expand by switching between homochiral and heterochiral geometries when either heated or cooled.

Other key robotic applications require precisely controllable muscle strokes dependent on the input electricity, either for thermally or electrochemically driven actuation. We used CNT-wrapped polymer fibers to manufacture high-spring-index electrothermally driven sheath-core CNT@nylon muscles to provide this capability, although other conductor-coated fibers could also be used. Although our demonstrations have focused on nylon-6 fibers and CNT yarns, our mandrel-free process is generically applicable to diverse fibers and yarns. Mandrel-free-fabricated high-spring-index CNT yarns were demonstrated for mechanical energy harvesters, self-powered high-strain-range sensors, and both solvent-driven and electrochemically driven artificial muscles that can be used in robotics.

REFERENCES AND NOTES

1. C. S. Haines *et al*., *Science* **343**, 868–872 (2014).
2. H. Chu *et al*., *Science* **371**, 494–498 (2021).
3. D. R. Higueras-Ruiz, M. W. Shafer, H. P. Feigenbaum, *Sci. Robot.* **6**, eabd5383 (2021).
4. C. Lang *et al*., *Nat. Nanotechnol.* **17**, 752–758 (2022).
5. L. Dong *et al*., *Sci. Adv.* **8**, eabq7703 (2022).
6. S. M. Mirvakili, I. W. Hunter, *Adv. Mater.* **30**, 1704407 (2018).
7. R. Wang *et al*., *Science* **366**, 216–221 (2019).
8. R. Wang, X. Zhou, W. Wang, Z. Liu, *Chem. Eng. J.* **417**, 128060 (2021).
9. S. H. Kim *et al*., *Science* **357**, 773–778 (2017).
10. M. Zhang *et al*., *Nat. Energy* **8**, 203–213 (2023).
11. Z. F. Liu *et al*., *Science* **349**, 400–404 (2015).
12. J. S. Marion *et al*., *Adv. Mater.* **34**, e2201081 (2022).
13. J. M. Lee *et al*., *Nano Energy* **85**, 106034 (2021).
14. L. Ye *et al*., *Nature* **626**, 313–318 (2024).
15. C. Choi *et al*., *Adv. Energy Mater.* **6**, 1502119 (2016).
16. W. Son *et al*., *Nat. Commun.* **10**, 426 (2019).
17. G. M. Spinks, *Adv. Mater.* **32**, e1904093 (2020).
18. X. Zhou, S. Fang, X. Leng, Z. Liu, R. H. Baughman, *Acc. Chem. Res.* **54**, 2624–2636 (2021).
19. M. Kanik *et al*., *Science* **365**, 145–150 (2019).

20. S. Li *et al.*, *Nat. Commun.* **13**, 1331 (2022).
21. J. Mu *et al.*, *Science* **365**, 150–155 (2019).
22. X. Hu *et al.*, *Proc. Natl. Acad. Sci. U.S.A.* **121**, e2412288121 (2024).
23. P. S. Matharu, A. P. Singh, Y. Song, U. Gandhi, Y. Tadesse, *J. Polym. Sci.* **62**, 2071–2093 (2024).
24. X. Leng *et al.*, *Mater. Horiz.* **8**, 1538–1546 (2021).
25. Y. Cui, D. Li, C. Gong, C. Chang, *ACS Nano* **15**, 13712–13720 (2021).
26. S. Aziz *et al.*, *Adv. Mater.* **35**, e2212046 (2023).
27. M. Smith, V. Cacucciolo, H. Shea, *Science* **379**, 1327–1332 (2023).
28. F. Göktepe, O. Göktepe, R. H. Baughman, M. Zhang, J. Oh, *Adv. Mater. Technol.* **9**, 2301971 (2024).
29. V. Sanchez, C. J. Walsh, R. J. Wood, *Adv. Funct. Mater.* **31**, 2008278 (2021).
30. B. Ridley, J. Chang, S. Maikranz, Coiled actuator system and method, U.S. Patent no. US 10793979 B2 (2020).
31. B. Ridley, S. Griffith, S. Maikranz, J. Chang, P. Lynn, System and method for thermally adaptive materials, U.S. Patent no. US 10793981 B2 (2020).
32. W. Son *et al.*, *Adv. Funct. Mater.* **34**, 2312033 (2024).
33. Materials and methods are available as supplementary materials.
34. S. Aziz, G. M. Spinks, *Mater. Horiz.* **7**, 667–693 (2020).
35. C. S. Haines *et al.*, *Proc. Natl. Acad. Sci. U.S.A.* **113**, 11709–11716 (2016).
36. S. Neukirch, G. H. M. Van Der Heijden, *J. Elast.* **69**, 41–72 (2002).
37. J. Sun, J. Zhao, *IEEE Trans. Robot.* **38**, 779–796 (2022).
38. Z. Hu, Y. Zhang, H. Jiang, J. A. Lv, *Sci. Adv.* **9**, eadh3350 (2023).
39. C. Lamuta *et al.*, *Adv. Mater. Technol.* **4**, 1900260 (2019).
40. J. Di *et al.*, *Adv. Mater.* **28**, 6598–6605 (2016).
41. J. Di, S. Fang, C. S. Haines, N. Li, R. H. Baughman, Incandescent tension annealing processes for strong, twist-stable carbon nanotube yarns and muscles, US Patent no. US 10837130 B2 (2020).
42. S. Li *et al.*, *Compos. Sci. Technol.* **72**, 1402–1407 (2012).
43. J. Xiong, J. Chen, P. S. Lee, *Adv. Mater.* **33**, e2002640 (2021).
44. A. Pal, V. Restrepo, D. Goswami, R. V. Martinez, *Adv. Mater.* **33**, e2006939 (2021).
45. Z. Wang *et al.*, *Adv. Mater.* **34**, e2201826 (2022).
46. Z. Zhu, J. Di, X. Liu, J. Qin, P. Cheng, *Matter* **5**, 1092–1103 (2022).
47. J. Zhang *et al.*, *IEEE Trans. Robot.* **35**, 761–781 (2019).
48. J. Wang, D. Gao, P. S. Lee, *Adv. Mater.* **33**, e2003088 (2021).

ACKNOWLEDGMENTS

Funding: Navy grants ONR/STTR N68335-18-C-0368, ONR N00014-22-1-2569, and ONR N00014-23-1-2183; Air Force Office of Scientific Research grant FA9550-21-1-0455; and Robert A. Welch Foundation grant AT-0029. **Author contributions:** Conceptualization: R.H.B., M.Z.; Funding acquisition: R.H.B.; Investigation: M.Z., S.F., W.C., I.E.; Methodology: R.H.B., M.Z., S.F., W.C., C.H., F.G., J.O., Z.W., I.E., Ö.G.; Project administration: R.H.B.; Supervision: R.H.B., M.Z.; Visualization: R.H.B., M.Z., S.F., W.C., J.O., I.E.; Writing – original draft: R.H.B., M.Z., S.F., F.G., Ö.G.; Writing– review & editing: R.H.B., M.Z., S.F. **Competing interests:** M.Z., R.H.B., S.F., J.O., Z.W., F.G., and Ö.G. are among the inventors of US provisional patent application no. 63/482,858, submitted by the Board of Regents of the University of Texas System (for the University of Texas at Dallas), which covers the design, fabrication, performance, and applications of ply-extracted muscles. The remaining authors declare that they have no competing interests. **Data and materials availability:** All data are available in the manuscript or the supplementary materials. Carbon nanotube forests were provided by Lintec of America under a material agreement with the University of Texas at Dallas. Correspondence and requests for materials should be addressed to R.H.B.

SUPPLEMENTARY MATERIALS

science.org/doi/10.1126/science.adr6708
Materials and Methods
Supplementary Text
Figs. S1 to S32
Table S1
References (*49*–*61*)
Movies S1 to S9

Submitted 11 July 2024; accepted 17 January 2025
10.1126/science.adr6708

ORGANIC CHEMISTRY

Oxidative amination by nitrogen atom insertion into carbon-carbon double bonds

Yannick Brägger†, Ann-Sophie K. Paschke†, Nima Nasiri, Bence B. Botlik, Francesco Felician, Bill Morandi*

The synthesis of nitrogen-containing molecules through carbon–nitrogen (C–N) bond formation is critical for the discovery and preparation of medicines, agrochemicals, and materials. Here, we report the direct insertion of a nitrogen atom into unactivated carbon-carbon double bonds to access aza-allenium intermediates, which can be converted either into nitriles or amidine products, depending on the initial alkene substitution pattern. This operationally simple and highly functionally compatible reaction works on a wide range of unactivated alkenes. PIFA, a commercially available and inexpensive hypervalent iodine reagent, is key to this reactivity. Our mechanistic proposal is supported by chemical trapping experiments, which concomitantly demonstrate the utility of our method to access valuable *N*-heterocycles. Additionally, our method can be used as a general strategy for synthesizing amides and amines, as well as ^{15}N-labeled molecules.

Nitrogen-containing molecules constitute one of the most important classes of compounds in the pharmaceutical, agrochemical, and materials industries, with e.g., more than 80% of recent top-selling drugs featuring at least one nitrogen atom (*1*). Consequently, the construction of carbon–nitrogen bonds is a central research area in synthetic organic chemistry. Alkenes are key precursors to nitrogen-containing compounds, owing to their abundance in petrochemical feedstocks and naturally occurring terpenes (*2*–*5*), as well as their ubiquity as synthetic intermediates. By leveraging the reactivity of the C(sp^2)–C(sp^2) π bond of alkenes, a plethora of synthetically useful reactions for the efficient introduction of nitrogen functional groups, including aziridination (*6*, *7*), hydroamination (*8*–*14*), or amino functionalization (*15*–*17*), have been developed. By contrast, approaches to C–N bond construction that proceed through complete cleavage of the strong C(sp^2)–C(sp^2) double bond remain rare, despite the broad potential of such approaches to unlock new synthetic strategies (Fig. 1A). The synthetic appeal of such cleavage reactions is further highlighted by the synthetic utility of ozonolysis, one of the most important methods to cleave C(sp^2)–C(sp^2) double bonds in both industrial and academic settings (Fig. 1B) (*18*, *19*). Recent advancements in this area and related oxidative cleavage reactions, e.g., using photoexcited nitroarenes as active oxidants (*20*) as well as oxidative dealkenylation processes enabled by intermediate ozonolides (*21*–*23*), have further advanced this field. Given the synthetic utility of these reactions and the synthetic relevance of nitrogen-containing compounds, the development of an alkene cleavage reaction directly leading to the formation of C–N bonds would likely become an invaluable tool for organic synthesis. However, the scarce previous reports of this reactivity are generally limited to the use of privileged alkenes, such as styrenes, leading to benzonitriles (*24*–*26*) and anilines (*27*, *28*), or conjugated dienes, leading to cinnamonitriles (*29*) that are all readily accessible by other methods, thereby limiting the overall synthetic utility of these methods. Very recently, Gandelman and co-workers reported an aza-variant of the ozonolysis reaction that proceeds through an analogous mechanism involving a [3+2]-cycloaddition between an in situ–generated nitrenium species (from oxidation of a diaryltriazene) and an alkene (*30*). Although elegant in its design, this methodology is still limited in alkene scope and accessible nitrogen substituents. The limitations of current methods for oxidative amination of alkenes through C–C cleavage thus call for the design of mechanistically distinct manifolds that allow for the direct formation of useful nitrogen-containing products, ideally under user-friendly reaction conditions.

A conceptually distinct strategy could involve the generation of an aziridine intermediate which, upon further oxidation, could undergo an electrocyclic rearrangement to generate an aza-allenium intermediate, leading to the insertion of a single nitrogen atom into a carbon–carbon double bond. Brown showed that aza-allenium osmium complexes can be accessed through nitrogen atom insertion from an osmium nitride complex into activated alkenes (*31*, *32*), whereas Levin extended this chemistry to indenes (*33*). By contrast, free aza-alleniums were synthesized and characterized by Würthwein (*34*). More relevant to our design are the reports from Gassman proposing free aza-alleniums as intermediates in the solvolysis of *N*–Cl aziridine species (*35*) (Fig. 1C) and in the anodic oxidative ring opening of *N*–H aziridines (*36*). Furthermore,

---

Laboratorium für Organische Chemie, ETH Zürich, Zürich, Switzerland
***Corresponding author. Email: bill.morandi@org.chem.ethz.ch**
†These authors contributed equally to this work.

Fig. 1. Context of this work. (**A**) Classical versus rare approaches to C–N bond construction using alkenes. (**B**) Ozonolysis of unactivated alkenes. (**C**) *N*-Chloro aziridines as precursors for transient aza-allenium salt generation (*35*). (**D**) Design of a nitrogen atom insertion into unactivated alkenes. (**E**) Development of an oxidative amination analogous to ozonolysis via transient aza-allenium formation.

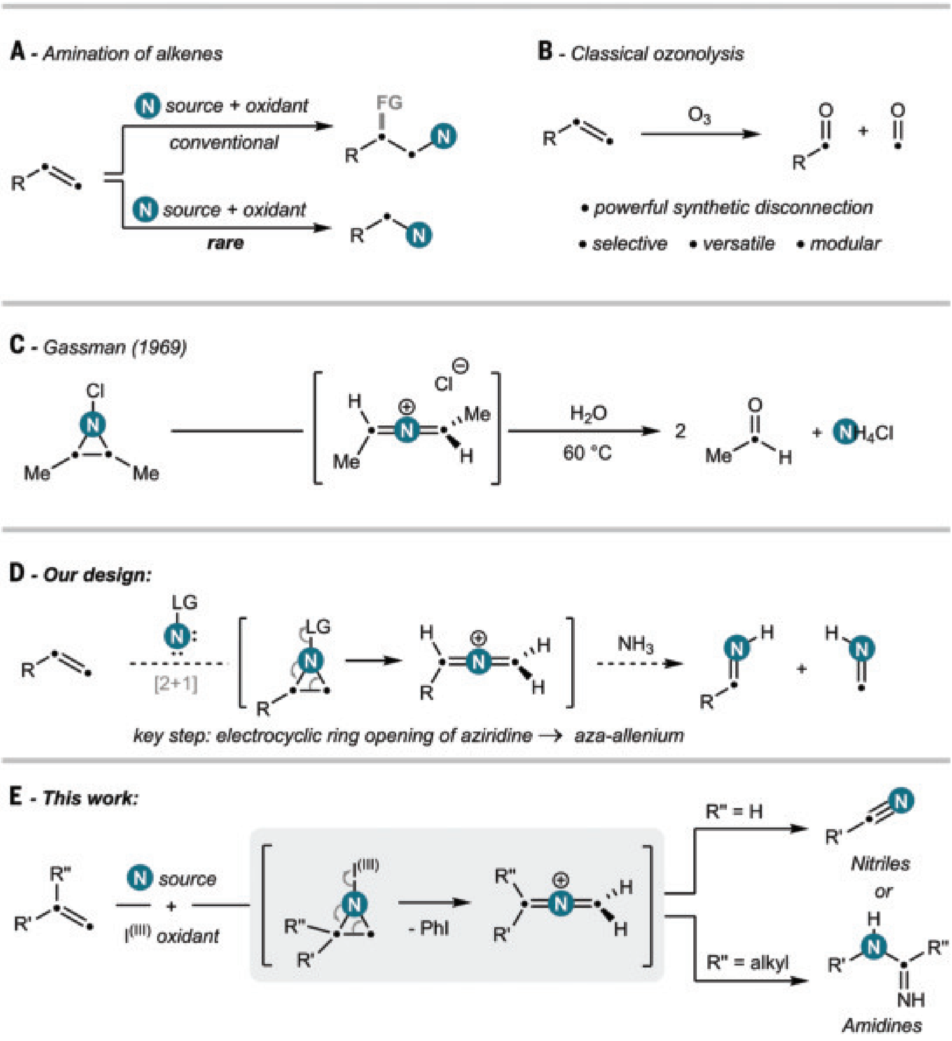

an analogous carbon insertion has been successfully developed by Suero and co-workers by leveraging a hypervalent iodine diazoacetate as a carbyne equivalent to trigger a cyclopropanation-electrocyclic opening sequence to access a wide range of insertion products (*37*). Inspired by these literature precedents, we envisaged that a strategy involving the in situ formation of a *N*–LG aziridine (LG, leaving group), followed by ring opening, would likely trigger the formation of a transient aza-allenium intermediate that could subsequently be intercepted by a suitable nucleophile, such as ammonia (Fig. 1D). Cleavage of the resulting hemi-aminal and further oxidation would then lead to the formation of nitriles, constituting overall a direct oxidative amination of alkenes. Such a transformation would be an important addition to the toolbox of organic chemists, enabling direct synthetic routes that previously relied on multistep protocols (*38*–*40*).

Here we report the successful development and application of this strategy. A wide range of terminal and internal alkenes, including cyclic substrates, formed the corresponding nitriles in high yields with excellent functional group compatibility. Additionally, we serendipitously discovered that 1,1-disubstituted alkenes undergo an additional aza-Beckmann rearrangement with exclusive regioselectivity and excellent stereoretention, resulting in a rare dealkenylative amination process delivering amidine products. Finally, preliminary chemical trapping experiments support the proposed mechanism and allowed us to access a diverse range of *N*-heterocycles.

Reaction development

At the outset of this project, we identified several key challenges associated with our reaction design: (i) low inherent reactivity of unactivated alkenes; (ii) premature quenching of the proposed aza-alleniums with the solvent; and (iii) challenge to orchestrate and control a complex multistep sequence. We focused our attention on the generation of synthetic equivalents to iodonitrene species, which have previously been proposed as intermediates in nitrogen insertion chemistry, using mixtures of ammonia and hypervalent iodine reagents (*41*–*46*). A benefit of this approach is that the ratio of ammonia to hypervalent iodine reagent can be varied, offering a handle to tune the rate of the different elementary steps of our proposed mechanism. However, a major challenge to overcome was the lack of reactivity of these reactants toward unactivated alkenes, as these were unreactive and even served as spectator functional groups in previous reports (*41*, *42*). Consistent with this hypothesis, a mixture of PIFA [bis-(trifluoroacetoxy)iodobenzene], a commercially available hypervalent iodine source, with ammonium carbamate, a surrogate

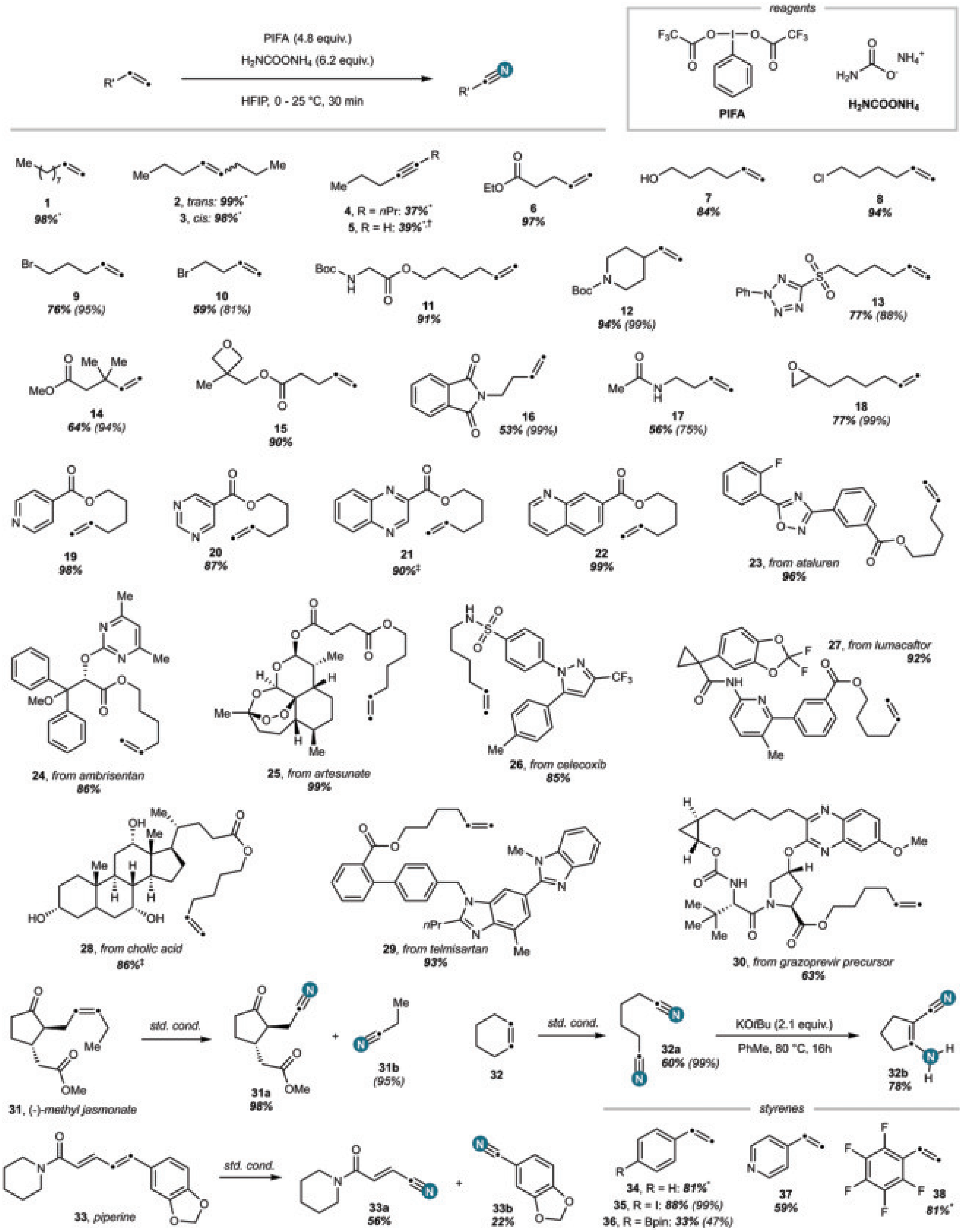

Fig. 2. Scope of the oxidative cleavage of linear alkenes. All reactions were performed without exclusion of air or moisture. The yields are given as isolated yields on 1.0-mmol scale (in parentheses: NMR yield on 0.1-mmol scale, using dibromomethane as internal standard). *GC (gas chromatography) yield (0.1-mmol scale; using *n*-dodecane as internal standard). †3.8 equiv. of PIFA and 5.2 equiv. of $H_2NCOONH_4$ were used. ‡Reaction was performed on 0.4-mmol (**21**) and 0.5-mmol scale (**28**), respectively. Terminal alkenes yield multiple C_1-containing by-products (see supplementary materials for details).

for ammonia, as the source of nitrogen, did not lead to any observable reaction with 1-decene as a model substrate in methanol. Inspired by a literature precedent, highlighting the increased reactivity of hypervalent iodine reagents in fluorinated and hydrogen bond–donating solvents (*47*), as well as the expected increased stability of aza-allenium (E = −3.7 on Mayr scale) (*48*) in poorly nucleophilic solvents, we next explored trifluoroethanol (TFE) and hexafluoroisopropanol (HFIP) (N_{TFE} = 1.1, N_{HFIP} = −1.9 on Mayr scale) (*49*). Gratifyingly, these solvents enabled the full conversion of the starting material to the expected nitrile product, alongside iodobenzene as the by-product from PIFA. With further optimization of the reaction conditions, we found that reducing the reaction time to 30 min alongside use of an excess of the hypervalent iodine oxidant and ammonium carbamate gave almost quantitative yield of the desired nonanitrile product (**1a**). Excess of both reagents is required, because the reaction involves multiple oxidation steps and ammonia, which likely forms by decarboxylation of ammonium carbamate in HFIP, acts as both the source of nitrogen and as a base (see tables S1 to S7 for detailed optimization). With these optimized reaction conditions in hand, we sought to explore the functional group compatibility of this transformation (see Fig. 2 for the scope of linear alkenes).

We found that symmetrical internal alkenes **2** and **3** quantitatively furnished two equivalents of the oxidative cleavage product, regardless of the stereochemistry of the alkene. When we subjected alkynes **4** and **5** to these reaction conditions, we also found the corresponding nitrile products, although in low yield and low conversion. This result is worth highlighting because the oxidative cleavage of alkynes to nitriles under metal-free conditions has thus far only been accomplished for activated, conjugated alkynes (*50*, *51*). Next, we investigated ester **6** and alcohol **7**, both of which cleanly afforded the nitrile product. Subsequently, we examined halogenated alkenes **8** to **10**, because for such substrates, cyanation using nucleophilic substitution strategies is more challenging. Under our conditions, they readily reacted to the corresponding nitriles. We found that unprotected amines are not tolerated under our conditions; however, Boc-protected amines **11** and **12** reacted smoothly. We also found that sufficiently electron-deficient heterocycles are compatible, as **13** gave the product in high yield. We were also pleased to see that substrate **14**, constituting a more sterically hindered alkene, reacted to the corresponding nitrile in high yield. Furthermore, substrates containing an oxetane ring (**15**), phthalimide (**16**), acetamide (**17**), and epoxide ring (**18**) all reacted smoothly. Next, we investigated whether our reaction was amenable to medicinally relevant molecules, including more complex substrates. Pyridine (**19**), pyrimidine (**20**), quinoxaline (**21**), and quinoline (**22**) containing alkenes all reacted smoothly, as did hexenyl esters derived from ataluren (**23**), ambrisentan (**24**), artesunate (**25**), celecoxib (**26**), lumacaftor (**27**), cholic acid (**28**), telmisartan (**29**), and a precursor of grazoprevir (**30**). Further, (-)-methyl jasmonate (**31**) reacted with full retention of stereochemistry to yield **31a** as a single diastereomer, as confirmed by two-dimensional (2D) nuclear magnetic resonance (NMR) analysis. Piperine (**33**), a naturally occurring conjugated diene, also reacted under our conditions to give both oxidative cleavage fragments in moderate yield, and with complete regioselectivity over the less electron-rich double bond. **33b** was notably isolated in lower isolated yield than **33a**, owing to its propensity for sublimation. Cyclohexene (**32**) yielded industrially relevant adiponitrile in quantitative yield. We further demonstrated a Thorpe-Ziegler reaction using stoichiometric amounts of KO^{t}Bu as a base, allowing for the aminative ring contraction of cyclohexene in two steps.

Finally, selected styrene derivatives, including styrene (**34**), 4-iodostyrene (**35**), 4-vinylpinacol boronic ester (**36**), 4-vinylpyridine (**37**), and a perfluorinated styrene derivative (**38**), were successfully transformed under the optimized reaction conditions.

Next, the reactivity of branched alkenes was investigated (see Fig. 3 for the scope of 1,1-disubstituted alkenes). When 2-methylundec-1-ene (**41**) was subjected to our reaction conditions, we observed complete conversion of the starting material to *N*-nonylacetimidamide in 88% NMR yield (0.10-mmol scale). No constitutional isomers were detected, indicating an exclusively regioselective C–N bond formation process. The direct conversion of branched alkenes to acetimidamides involves a net C(sp^3)–C(sp^2) σ bond activation and therefore constitutes a rare example of an aminodealkenylation reaction (*21*). When methylene cyclohexane (**39**) was subjected to our conditions, NMR analysis of a reaction aliquot revealed full conversion to the cyclic amidine species **39a**. Yet, after aqueous work-up and flash column chromatography, caprolactam was found as the only product in 98% isolated yield. We therefore hypothesize that the cyclic amidine is fully hydrolyzed in the work-up and during column chromatography (stationary phase: SiO$_2$) to the corresponding lactam. This finding represents an aza-analog to the classical Beckmann rearrangement (*52*), which is used on megaton scale annually by the chemical industry for the synthesis of caprolactam (*53*). We found that hydrolysis could be partially prevented by using different purification conditions (stationary phase: neutral Al$_2$O$_3$), yielding a mixture of cyclic amidine and lactam after purification. We were thus able to react methylene cyclopentane (**40**) in the same manner, yielding a mixture of 2-iminopiperidine and valerolactam in the process. Next, the reactivity of α-methylstyrene (**43**), a by-product of the cumene process and therefore a widely available and inexpensive feedstock chemical, was investigated under the reaction conditions. The use of TFE as the solvent was key to preventing undesired polymerization in this case, furnishing the desired *N*-phenylacetimidamide product in high yield. This is an interesting example of feedstock valorization, as the corresponding *N*-phenylamidine products are important heterocycle precursors for the synthesis of indoles, imidazoles, and pyrimidines (*54*).

We next subjected inexpensive naturally occurring terpenes to our reaction conditions. We were gratified to observe dealkenylative amidine formation for a range of branched alkene containing terpenes. The C(sp^3)–C(sp^2) σ bond activation operates with exclusive regioselectivity and with excellent stereoretention for all chiral substrates, as determined by a combination of x-ray diffraction and 1D or 2D NMR spectroscopy. Although Kwon's two-step aminodealkenylation reaction provides excellent yields across various substrates, it often leads to epimerization at the carbon center involved in C–N bond formation, particularly in monocyclic terpenoids (*21*). By contrast, our method consistently occurs with minimal or no detectable epimerization observed in all cases, indicating an efficient and stereoselective C–N bond formation process.

Examples include (+)-nootkatone (**44**), (+)-dihydrocarvone (**45**), and *cis*-(-)-limonene oxide (**46**), mirroring the functional group tolerance of the previous scope. (+)-Nootkatone is worth highlighting, because the formation of the corresponding amidine occurs with good selectivity over the more electron-deficient alkene. In addition, (+)-dihydrocarvone-derived amidine spontaneously cyclized to **45a**, and *cis*-(-)-limonene oxide–derived amidine was similarly found to undergo cyclization, but only at elevated temperatures. We then explored the reaction of silyl-protected (-)-isopulegol (**47**) and (-)-dihydrocarveol (**48**), both of which formed the corresponding amidines in excellent isolated yield. Subsequently, we demonstrated the utility of our methodology by exploring structurally complex betulin (**49**) and betulinic acid (**50**), both of which cleanly and exclusively reacted to the corresponding amidine products. Contrary to cyclic amidines, hydrolysis of the terpene-derived amidine products was never observed under work-up or column conditions. However, upon exposure to mild saponification conditions, we could develop chemodivergent protocols to access either acetamides or primary amines by controlled hydrolysis from the corresponding amidines. Our reaction conditions therefore enable the direct synthesis of unprotected amines and amides from naturally occurring terpenes in a mild two-step reaction with excellent stereoretention, offering a rapid entry into highly valuable aminated building blocks.

Mechanism and isotopic labeling applications

In Fig. 4, a preliminary mechanistic hypothesis for the reaction is presented. In accordance with previous literature (*41*–*46*), we propose the in situ formation of an electrophilic nitrogen species that engages in formal [2+1]-cycloaddition with the unactivated alkene **a**, furnishing activated aziridine species **b**. This species could then undergo a concerted electrocyclic ring opening and dissociation of iodobenzene, which was stoichiometrically observed in all crude reaction mixtures by ^{1}H NMR, forming aza-allenium salt **c** after the formal, direct insertion of a nitrogen atom into the C(sp^2)–C(sp^2) double bond of the

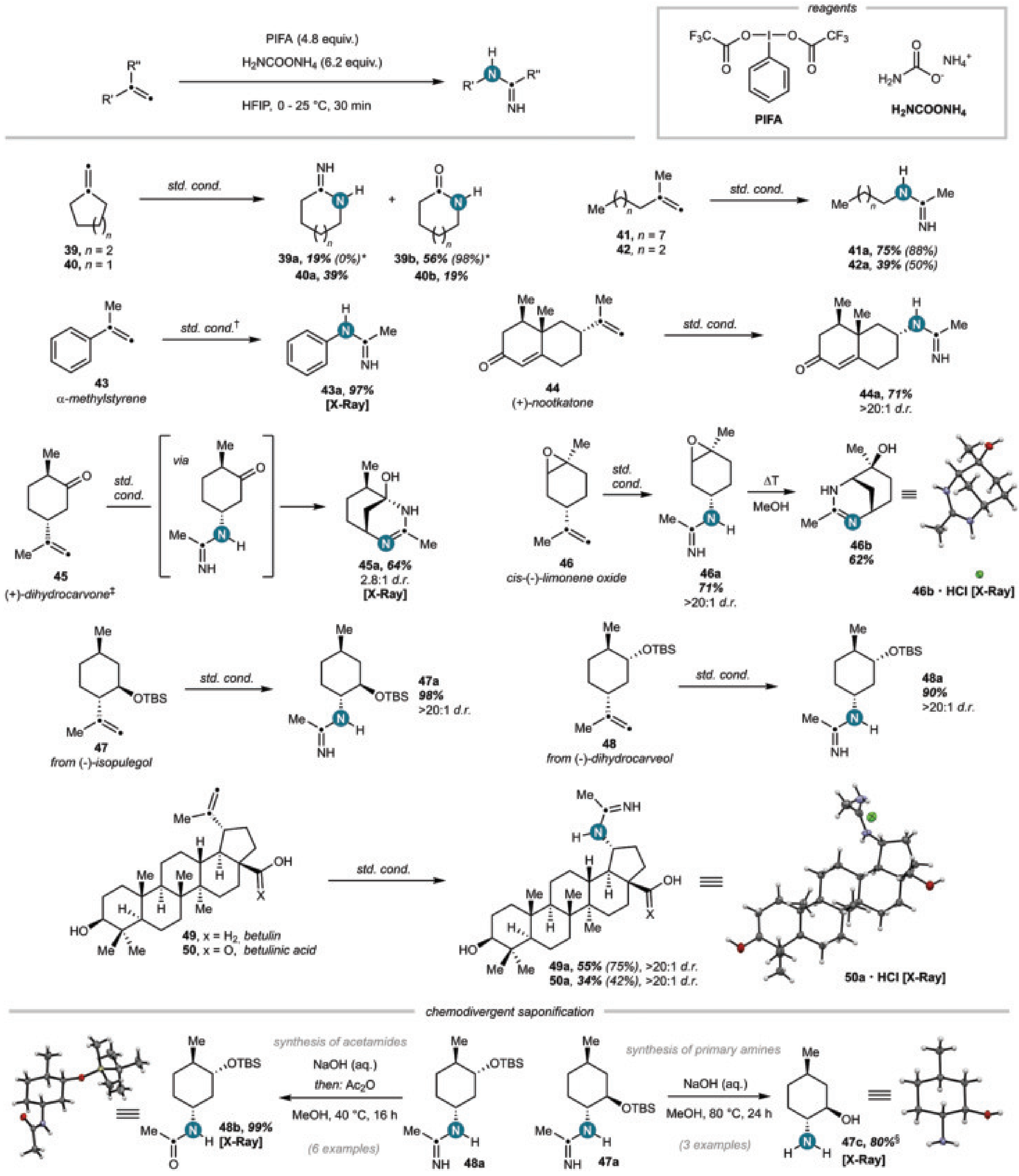

Fig. 3. Scope of the oxidative cleavage of branched alkenes. All reactions were performed without exclusion of air or moisture. The yields are given as isolated yields on 1.0-mmol scale (in brackets: NMR yield on 0.1-mmol scale, using dibromomethane as internal standard). *Isolated yield when SiO_2 instead of neutral Al_2O_3 was used for flash column purification. †TFE (0.1 M) was used instead of HFIP. ‡Commercial (+)-dihydrocarvone was used [mixture of 77% *n*-(+)-dihydrocarvone + 20% *iso*-(+)-dihydrocarvone]. §NMR yield on 0.1-mmol scale, using mesitylene as internal standard. Single-crystal x-ray structures are depicted with ellipsoids at 50% probability (**46b·HCl**, **47c**) and 30% probability (**48b**, **50a·HCl**), respectively. Terminal alkenes yield multiple C_1-containing by-products (see supplementary materials for details). dr, diastereomeric ratio; TBS, *tert*-butyldimethylsilyl.

starting material. The mass of intermediate **c** was detected via high-resolution mass spectrometry (see supplementary materials for details), supporting that this species could be an intermediate in the reaction. The intermediacy of aza-allenium was further supported by a trapping experiment using (-)-isopulegol (**51**) furnishing labile imine species **51a**, which we observed in the crude reaction mixture by NMR

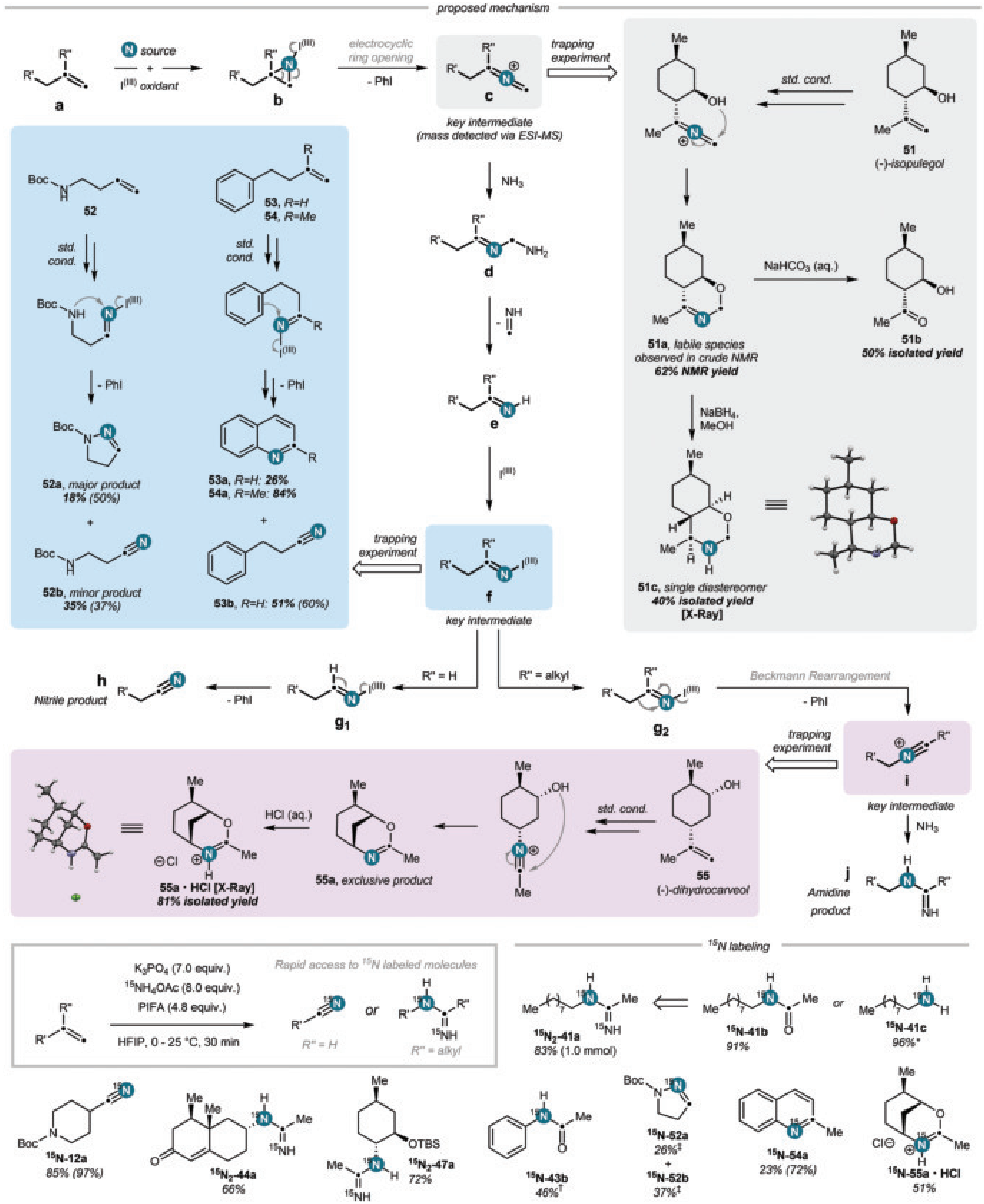

Fig. 4. Preliminary mechanistic proposal for the oxidative amination of unactivated alkenes and ^{15}N labeling studies. All reactions were performed without exclusion of air or moisture unless otherwise stated. The yields are given as isolated yields on 1.0-mmol scale (or 0.1 mmol for ^{15}N labeling; in parentheses: NMR yield on 0.1-mmol scale, using dibromomethane as internal standard). Single-crystal x-ray structures are depicted with ellipsoids at 50% probability. *NMR yield on 0.1-mmol scale, using mesitylene as internal standard. †TFE was used instead of HFIP; reacting α-methylstyrene under standard ^{15}N labeling conditions yields the corresponding amide exclusively. ‡The reaction was set up in a glovebox. ESI-MS, electrospray ionization mass spectrometry.

spectroscopy. This unstable species could successfully be hydrolyzed to **51b** or reduced to **51c** as a single diastereomer that was characterized by single-crystal x-ray diffraction.

Following the formation of aza-allenium salt **c**, aminolysis by ammonia generates hemiaminal **d**, which can form imine species **e** after proton transfer and extrusion of methanimine. Imine **e** is proposed to coordinate to another equivalent of I$^{(III)}$, which causes a stepwise oxidation event to the corresponding nitrile **h** in the case of an aldimine. The intermediacy of an *N*-electrophilic imine intermediate **f** was supported by isolating the corresponding dihydropyrazole (**52a**) as a major product from reacting *N*-Boc–protected aminobut-3-ene (**52**). When 4-phenylbutene (**53**) reacted under our conditions, we obtained nitrile product **53b** in 60% NMR yield, while also observing quinoline (**53a**) as the minor product in 26% isolated yield, formally following an intramolecular electrophilic aromatic substitution and oxidation sequence (*55*). When the α-methylated analog (**54**) reacted, we observed exclusive formation of 2-methylquinoline (**54a**) in high yield. These combined results indicate that *N*-electrophilic imine species are likely key intermediates in the reaction.

In the case of a ketimine, the oxidation event is proposed to occur via a Beckmann rearrangement to nitrilium cation **i**. The nitrilium ion is trapped by excess ammonia, thus furnishing an amidine **j**.

When we subjected (-)-dihydrocarveol (**55**) to our reaction, which contains a branched alkene group adjacent to a secondary alcohol, we observed full conversion to an imidate product (**55a**) following an intramolecular trapping event of the nitrilium cation after the Beckmann rearrangement. Protonation using dilute aqueous acid allowed us to crystallize and characterize the hydrochloride salt.

Overall, the Beckmann rearrangement occurs with excellent retention of stereochemical information and complete regioselectivity. In addition to their mechanistic value, the trapping experiments collectively demonstrate that our methodology can also be used for the direct synthesis of synthetically relevant *N*-heterocycles, such as 1,3-oxazinanes, *N*-substituted 4,5-dihydro-1*H*-pyrazoles, or quinolines.

Lastly, we found that ammonium carbamate can be replaced by a combination of ammonium acetate and potassium phosphate, which we could exploit to synthesize various ^{15}N analogs of nitriles (**^{15}N-12a**, **^{15}N-52b**), amidines (**$^{15}N_2$-41a**, **$^{15}N_2$-44a**, **$^{15}N_2$-47a**), and saponification products thereof (**^{15}N-41b**, **^{15}N-41c**). Likewise, we could access ^{15}N analogs of various trapping products (**^{15}N-52a, ^{15}N-54a, ^{15}N-55a·HCl**), highlighting that our methodology enables rapid ^{15}N incorporation as a unified approach to the synthesis of labeled organic molecules, including heterocycles that would be challenging to access otherwise.

In summary, we have developed an oxidative amination reaction, in which linear alkenes are cleaved to nitriles and branched alkenes are transformed into amidines. We posit a mechanism involving nitrogen atom insertion into the C(sp^2)–C(sp^2) bond of unactivated alkenes, taking advantage of transient aza-allenium intermediates in a synthetically useful application. The reaction setup is operationally simple, requiring no exclusion of air or moisture, and is compatible with many functionalities. In a broader context, this study demonstrates that nitrogen insertion into alkenes can enable the formation of aza-allenium species as reactive nitrogen-containing intermediates with broad synthetic utility and outstanding potential for downstream diversification, opening avenues for the discovery and preparation of important nitrogen-containing products.

REFERENCES AND NOTES

1. E. Vitaku, D. T. Smith, J. T. Njardarson, *J. Med. Chem.* **57**, 10257–10274 (2014).
2. B. Dauban, *Darses, A. Jarvis, Comprehensive Organic Synthesis*, P. Knochel, G. A. Molander, Eds. (Elsevier, ed. 2, 2014), chap. 7.19, pp. 538–604.
3. P. Ertl, T. Schuhmann, *J. Nat. Prod.* **82**, 1258–1263 (2019).
4. R. F. Lusi, M. A. Perea, R. Sarpong, *Acc. Chem. Res.* **55**, 746–758 (2022).
5. A. Corma, S. Iborra, A. Velty, *Chem. Rev.* **107**, 2411–2502 (2007).
6. J. L. Jat *et al*., *Science* **343**, 61–65 (2014).
7. Q.-Q. Cheng *et al*., *Nat. Catal.* **3**, 386–392 (2020).
8. M. Beller, J. Seayad, A. Tillack, H. Jiao, *Angew. Chem. Int. Ed.* **43**, 3368–3398 (2004).
9. Y. Miki, K. Hirano, T. Satoh, M. Miura, *Angew. Chem. Int. Ed.* **52**, 10830–10834 (2013).
10. S. Zhu, N. Niljianskul, S. L. Buchwald, *J. Am. Chem. Soc.* **135**, 15746–15749 (2013).
11. J. Gui *et al*., *Science* **348**, 886–891 (2015).
12. D. G. Kohler, S. N. Gockel, J. L. Kennemur, P. J. Waller, K. L. Hull, *Nat. Chem.* **10**, 333–340 (2018).
13. A. J. Musacchio *et al*., *Science* **355**, 727–730 (2017).
14. S. Ma, J. F. Hartwig, *Acc. Chem. Res.* **56**, 1565–1577 (2023).
15. Z. Wu, M. Hu, J. Li, W. Wu, H. Jiang, *Org. Biomol. Chem.* **19**, 3036–3054 (2021).
16. V. C. M. Gasser, S. Makai, B. Morandi, *Chem. Commun.* **58**, 9991–10003 (2022).
17. K. Hirano, M. Miura, *J. Am. Chem. Soc.* **144**, 648–661 (2022).
18. S. G. Van Ornum, R. M. Champeau, R. Pariza, *Chem. Rev.* **106**, 2990–3001 (2006).
19. T. J. Fisher, P. H. Dussault, *Tetrahedron* **73**, 4233–4258 (2017).
20. A. Ruffoni, C. Hampton, M. Simonetti, D. Leonori, *Nature* **610**, 81–86 (2022).
21. Z. He, J. A. Moreno, M. Swain, J. Wu, O. Kwon, *Science* **381**, 877–886 (2023).
22. B. W. Dehnert, J. H. Dworkin, O. Kwon, *Synthesis (Stuttg.)* **56**, 71–86 (2024).
23. A. J. Smaligo *et al*., *Science* **364**, 681–685 (2019).
24. W. Xue *et al*., *Angew. Chem. Int. Ed.* **62**, e202314364 (2023).
25. Q. Liu *et al*., *Tetrahedron Lett.* **57**, 2620–2623 (2016).
26. J.-H. Xu, Q. Jiang, C.-C. Guo, *J. Org. Chem.* **78**, 11881–11886 (2013).
27. T. Wang, N. Jiao, *Acc. Chem. Res.* **47**, 1137–1145 (2014).
28. J. Liu *et al*., *Research* **2020**, 7947029 (2020).
29. Y. Fu, Y. Leng, H. Bai, J. Xu, N. Chen, *Org. Chem. Front* (Advance Article, 2024), .
30. A. Koronatov *et al*., *Nat. Chem.* **17**, 101–110 (2025).
31. S. Brown, *J. Am. Chem. Soc.* **121**, 9752–9753 (1999).
32. A. G. Maestri, S. D. Taylor, S. M. Schuck, S. N. Brown, *Organometallics* **23**, 1932–1946 (2004).
33. P. Q. Kelly, A. S. Filatov, M. D. Levin, *Angew. Chem. Int. Ed.* **61**, e202213041 (2022).
34. E.-U. Würthwein, *Angew. Chem.* **93**, 110–111 (1981).
35. P. G. Gassman, D. K. Dygos, *J. Am. Chem. Soc.* **91**, 1543–1544 (1969).
36. P. G. Gassman, I. Nishiguchi, H. Yamamoto, *J. Am. Chem. Soc.* **97**, 1600–1602 (1975).
37. Z. Wang, L. Jiang, P. Sarró, M. G. Suero, *J. Am. Chem. Soc.* **141**, 15509–15514 (2019).
38. Y. Rew *et al*., *J. Med. Chem.* **55**, 4936–4954 (2012).
39. D. V. Tsyganov *et al*., *J. Nat. Prod.* **76**, 1485–1491 (2013).
40. J. Fiandor, S. Y. Tam, *Tetrahedron Lett.* **5**, 597–600 (1990).
41. J. C. Reisenbauer, O. Green, A. Franchino, P. Finkelstein, B. Morandi, *Science* **377**, 1104–1109 (2022).
42. C. Hui, L. Brieger, C. Strohmann, A. P. Antonchick, *J. Am. Chem. Soc.* **143**, 18864–18870 (2021).
43. R. Luisi, J. A. Bull, *Molecules* **28**, 1120 (2023).
44. T. Glachet *et al*., *J. Am. Chem. Soc.* **141**, 13689–13696 (2019).
45. A. Lin, A. Ghosh, S. Yellen, Z. T. Ball, L. Kürti, *J. Am. Chem. Soc.* **146**, 21129–21136 (2024).
46. B. B. Botlik *et al*., *Angew. Chem. Int. Ed.* **63**, e202408230 (2024).
47. I. Colomer, C. Batchelor-McAuley, B. Odell, T. J. Donohoe, R. G. Compton, *J. Am. Chem. Soc.* **138**, 8855–8861 (2016).
48. G. M. Böttger, R. Fröhlich, E.-U. Würthwein, *Eur. J. Org. Chem.* 2000, 1589–1593 (2000). 10.1002/(SICI)1099-0690(200004)2000:8<1589:AID-EJOC1589>3.0.CO;2-T
49. *Mayr's Database Of Reactivity Parameters*; https://www.cup.lmu.de/oc/mayr/reaktionsdatenbank/ [accessed 19 April 2024].
50. N. Okamoto, M. Ishikura, R. Yanada, *Org. Lett.* **15**, 2571–2573 (2013).
51. U. Dutta, D. W. Lupton, D. Maiti, *Org. Lett.* **18**, 860–863 (2016).
52. D. K. Verma, Y. Dewangan, C. Verma, *Handbook of Organic Name Reactions* (Elsevier, ed. 1, 2023), chap. 6.2.
53. J. Tinge *et al*., in *Ullmann's Encyclopedia of Industrial Chemistry* (Wiley, 2018), pp. 1–31.
54. X.-F. Wu, Ed., *Transition Metal-Catalyzed Heterocycle Synthesis Via C-H Activation* (Wiley, 2016).
55. M. Kitamura, M. Yoshida, T. Kikuchi, K. Narasaka, *Synthesis* **15**, 2415–2426 (2003).

ACKNOWLEDGMENTS

We thank J. Reisenbauer, A. Garrido-Castro, F. Ruepp, T. Jankins, and J. Bode for valuable discussions. We thank B. Kohli for synthesizing substrates **17**, **47**, **48**, and **54**. We thank the Molecular and Biomolecular Analysis Service (MoBiAS), the X-ray structure service (SMoCC), and the LOC NMR Service at ETH Zürich for technical assistance. We further thank the whole Morandi group for critical proofreading of the manuscript. **Funding:** This project was financially supported by ETH Zürich. A.-S.K.P. acknowledges a fellowship from the Fonds der Chemischen Industrie (FCI). B.B.B. acknowledges a fellowship from the Scholarship Fund of the Swiss Chemical Industry (SSCI). X-ray data were recorded on a rotating anode diffractometer cofunded by SNF (R'Equip Project no. 206021_213224). **Author contributions:** Y.B. conceived the project. Y.B., A.-S.K.P., N.N., B.B.B., and F.F. conducted the experimental work and analyzed the data. B.M. supervised the research. Y.B. and B.M. wrote the manuscript with input from all authors. **Competing interests:** The authors declare no competing interests. **Data and materials availability:** X-ray data for compounds (**43a · TFA, 45a, 46b · HCl, 50a · HCl, 47b, 47c, 48b, 51c, 55a · HCl**) are freely available at the Cambridge Crystallographic Data Centre under deposition CCDC 2355911-2355914, 2347635-2347637, and 2403649-2403650. All other data are in the supplementary materials. **License information:**

SUPPLEMENTARY MATERIALS

science.org/doi/10.1126/science.adq4980
Materials and Methods
Supplementary Text
Figs. S1 to S7
Tables S1 to S6
References (*56*–*91*)

Submitted 16 May 2024; resubmitted 19 November 2024
Accepted 29 January 2025
10.1126/science.adq4980

Myeloid MRD Panel

The ultra-sensitive detection of measurable residual disease (MRD) in acute myeloid leukaemia (AML) is a critical tool for advancing clinical research in AML. Next-generation sequencing (NGS)-based AML MRD is being more widely adopted in drug development and studies aiming to improve clinical management of AML. Clinical research studies into MRD continue to drive deeper understanding of AML remission and relapse, including evidence highlighting that MRD negativity is associated with a better 5-year survival rate compared to MRD positive defined samples.1 Being able to sensitively detect even a few residual leukemic cells provides a more comprehensive picture of the current AML status of a sample. Oxford Gene Technology's (OGT) new highly targeted SureSeq Myeloid MRD Panel enables the detection of 13 key AML MRD-associated biomarkers. Key targets include very large, ultra-low frequency FLT3-ITDs (even up to 300 bp) that are traditionally challenging to detect. This streamlined, guideline-driven panel content expands on OGT customer's MRD detection capabilities to deliver a better understanding of the current AML status, and ensures genomic insights are not missed. Customers can also effortlessly adapt NGS workflows to meet all their sensitivity, sample batching and sequencing requirements - by selecting from a range of pre-optimized workflows, users benefit from the unmatched flexibility of this new NGS MRD panel. OGT specializes in the development of superior hybrid capture technology that excels in the detection of complex structural variants and eliminates inaccurate calls caused by alternative PCR-based approaches. By employing OGT's unparalleled bait design process, informed by the team's unique expertise, the company has developed the SureSeq Myeloid MRD Panel to offer enhanced and reliable, superior detection. OGT partners with all customers to get them started with their MRD analysis without adding to their lab's bioinformatics burden and ensures their MRD workflows always operate seamlessly. The company's complimentary NGS analysis software, Interpret, is available on the cloud or as a local install and provides a powerful bioinformatic analysis pipeline. This is all aided by OGT's expert support team who are readily available to support customers in their workflow implementation and maintenance.

Oxford Gene Technology
For Info: +1 914 467 5285

3D multi-omics solutions

Enhanc3D Genomics, an innovator in 3D genomics technology, announced the launch of a suite of integrated multi-omics solutions to accelerate and improve the precision of drug discovery. Based on the company's proprietary 3D genomics platform, integrated with extensive multi-omics analysis, the new 3D multi-omic offerings provide partners with a powerful end-to-end solution to support and enhance decision-making through every stage of the drug discovery and development process. The multi-omic platform is based on patented Promoter Capture Hi-C technology, offering high-resolution, genome-wide regulatory maps of any cell type, sub-type, or state, by capturing interactions between promoters and regulatory regions. The platform is uniquely able to analyze these interactions across the entire genome within one assay. By integrating 3D genomic data and data from the 3D Multi-Omic Atlas – the Company's extensive repository of multi-omic data across human cell types – the new solutions provide deep, data-driven insights into disease mechanisms and therapeutic opportunities. The new suite of multi-omics solutions offers differentiated capabilities across the entire drug development pipeline to support partners through their drug discovery journey. GenLinkConnect helps to accelerate target identification and prioritization. GenLinkResponse is used for drug response analysis of cellular regulation. GenLinkProfile is used for cell-specific profiling of regulatory elements and disease mechanisms to accelerate drug development. The solutions are supported by advanced visualization and data management software, GenLinkHub, which is visualization software enabling users to pinpoint key genomic interactions and discover novel therapeutic targets. It transforms complex multi-omics data sets into intuitive 3D representations by layering them over high resolution 3D genome maps, for easier interpretation.

Enhanc3D Genomics
For Info: (0)1223 942 520
www.enhanc3dgenomics.com

Informatics platform

Sapio Lab Informatics Platform further optimizes productivity across lab workflows. These advancements streamline lab operations, enhance accuracy, and support the growing demands of scientific research. The Immunogenicity module automates workflows for streamlined validation and robust data analysis. It improves GMP workflows by integrated monitoring and testing capabilities which reduce system load and enhance precision. Enhanced chemistry representation, stereoisomer management with advanced relative stereochemistry support and refined substructure search capabilities. And the expanded molecular biology features, has new capabilities for batch cloning and sequence assembly, and the introduction of a protein sequencer viewer. The new Immunogenicity (IgX) module simplifies control mapping, supports multiple validation workflows, and automates data analysis within Sapio LIMS (Laboratory Information Management System) and ELN (Electronic Lab Notebook). By reducing manual effort and ensuring data integrity, these features enable researchers to handle complex immunogenicity workflows more effectively while maintaining accuracy and reliability. The latest updates to Sapio's GMP (Good Manufacturing Practice) module focus on refining monitoring and testing workflows, providing greater flexibility and precision. GMP workflows have been integrated into the Integrated Data View (IDV) outside the ELN, reducing system load and improving material and instrument tracking capabilities. Environmental monitoring routines have been enhanced to capture a broader range of data, including text, True/False metrics, and numeric values. These updates allow users to add notes and additional metadata to batch records in test configurations, receive samples, launch testing workflows, and process analytical data more efficiently, streamlining overall GMP processes. The chemistry module in Sapio LIMS and ELN now includes upgraded capabilities for managing and analyzing chemical data.

Sapio Sciences
For Info: +44 (0)7760 766 213
www.sapiosciences.com

Electronically submit your new product description or product literature information! Go to www.science.org/about/new-products-section for more information.


Career Trends
Career Trends
Career Trends
Career Trends
Career Trends
Career Trends
Work and Wellbeing
Science Careers

Advancing Towards
Artificial General Intelligence

BIGAI

About Us

Beijing Institute for General Artificial Intelligence (BIGAI) is a leading research institution advancing the frontiers of artificial general intelligence. Our mission is to develop intelligent systems with human-like cognitive abilities through fundamental scientific research and innovation.

Through strategic partnerships with Peking University, Tsinghua University, and other premier institutions, we co-supervise hundreds of PhD students annually, creating a vibrant research ecosystem that rivals leading international labs. Our extensive collaboration network provides overseas scientists with exceptional research support and the opportunity to mentor top talent in AGI development. This rich academic environment, combined with our focus on fundamental breakthroughs, creates an ideal setting for ambitious researchers looking to make significant impacts in the field.

What We Offer

- **Competitive salary**
- **Talent housing / Staff accommodation**
- **Medical insurance**
- **Children's education support**
- **Relaxed and free academic atmosphere**
- **Project research funding/grants**

We need you

BIGAI invites global talent to join us in various positions, including Researchers, Assistant Researchers, and Engineers. Through our partnership with Peking University, we also provide joint appointment opportunities. Our research and engineering directions cover all aspects of artificial intelligence, including:

- Computer Vision
- Natural Language Processing
- Computational Cognition and Commonsense Reasoning
- Machine Learning
- Intelligent Graphics and Interaction
- Embodied Intelligence and Robotics
- Multi-Agent Systems

eng.bigai.ai **hr@bigai.ai**

OPPORTUNITIES IN CHINA

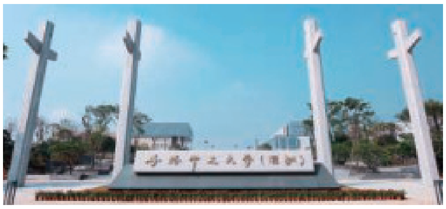

Faculty Positions (Tenured or Tenure-Track) in Artificial Intelligence-Professor/Associate Professor/Assistant Professor, School of Artificial Intelligence (SAI)

The Chinese University of Hong Kong, Shenzhen

香港中文大學（深圳）
The Chinese University of Hong Kong, Shenzhen

Newly established, The School of Artificial Intelligence (SAI) at The Chinese University of Hong Kong, Shenzhen (CUHK-Shenzhen) is pleased to invite applications for full-time faculty positions at all academic ranks with multiple positions. We seek outstanding individuals who are eager to contribute to the advancement of artificial intelligence research and education. Candidates will join a vibrant, interdisciplinary environment that values academic excellence, innovative research, and impactful teaching. We welcome candidates with expertise in, but not limited to, the following areas:

- **Natural Language Processing (NLP):** Large language models (LLMs), sentiment analysis, multilingual AI, and generative AI.
- **Machine Learning and AI Foundations:** Reinforcement learning, transfer learning, representation learning, trustworthy/explainable AI, and computational cognitive science.
- **Embodied AI:** Human-robot interaction, multi-modal perception, and AI for autonomous decision-making systems.
- **Large-scale AI and Distributed Machine Learning:** Scalable AI systems, distributed computing architectures, and multi-agent learning frameworks.
- **Robotics and Autonomous Systems:** Motion planning, intelligent navigation, embodied intelligence, robot design, nano-robots, swarm robotics, medical robotics, and AI for dynamic environments.
- **AI Ethics and Society:** Fairness, accountability, transparency, and the social implications of AI technologies.
- **Emerging AI Paradigms:** Neuro-symbolic AI, lifelong learning, quantum AI, and cognitive-inspired computing models.
- **AI and Applications:** AI for Science, AI for Business and Economics, AI for Medicine, AI for Society, etc.
- **Signal Processing:** AI-driven statistical signal processing, graph signal processing, and data-driven signal analysis for complex systems.
- **Mathematical Sciences:** Statistics, advanced computational mathematics, numerical optimization techniques, and mathematical foundations for AI and machine learning.

Qualified candidates have a doctoral degree in Computer Science, Electrical Engineering, Mathematical Science, and other related fields, complemented by postdoctoral training and relevant work experience in related research areas. Applicants for professorships at the rank of Professor or Associate Professor are expected to have an established research program with a funding history, independent research and teaching experiences, and an excellent publication record. We also welcome candidates with teaching experience in related fields for Lecturer and Senior Lecturer positions.

Interested candidates are invited to submit their cover letter, curriculum vitae, teaching statement, research statement (including future research plan) and 3 reference letters (should be sent directly from referrers) to the Search Committee at talent4sai@cuhk.edu.cn. Applications will be reviewed on a rolling basis until the positions at the respective ranks are filled.

WORKING LIFE

By **Eric Martiné**

Goodbye to a dream

When I checked myself out of a psychiatric hospital for the second time in 2 years, I finally realized something had to change. I'd been in denial for months, ignoring the mounting symptoms of depression as I pushed myself harder and harder in the lab. I had spent half my life working toward my dream of being a scientist. It had given me a sense of purpose. But now it dawned on me that, for the sake of my health, I was going to have to let that dream go.

"Ph.D. by the end of your 20s, betcha!" reads the inscription in the book my biology teacher gave me at my middle school graduation. She sparked my love of science, and her guidance and support gave me a sense of stability during a turbulent time. My parents had split up, and I found myself caring for my suicidal mother, who was struggling with depression and alcoholism. Instead of collapsing under the enormous weight, I found safety in science. "If I can explain the shaking world around me, I can deprive it of its gruesomeness," I thought.

As I took on the responsibility of running a household and looking after my mother, the scientist in me emerged, transforming me into a striving, straight A student within a year. I dreamt of doing a Ph.D. in biology, and with my new, confident self, I was heading straight toward this goal. Nothing could stop me.

> "I was alarmed ... as the seemingly solid foundation I'd built my life on rapidly eroded."

Nothing, that is, except for myself. Years later, I'd finally started my Ph.D. studies in biogeography when my past caught up with me. I'd just moved to a new city after a long relationship had shattered, and felt terribly lonely and utterly joyless. I couldn't concentrate, and even basic tasks like reading papers or writing code became increasingly difficult. I was alarmed but unable to act as the seemingly solid foundation I'd built my life on rapidly eroded.

When I finally reached out to a therapist, it was already too late. My mother used to talk of her depression "co-opting" her, describing herself as being completely at its mercy. I could never comprehend why she was so resigned to her misery—but now I saw that when depression rules your mind, you are not susceptible to reason. I became suicidal, and my therapist, alarmed, sent me to a psychiatric hospital.

My hospital stay was the first chance I'd had to talk about what I'd experienced as a child. In therapy, I came to understand how I'd turned to science to protect myself when I had to care for an unwell parent at such a young age. I'd continued to use science as an adult, I realized, as a way of trying to control the uncontrollable. I had detached myself not only from my negative feelings, but from almost all emotions, by viewing them "scientifically," as nothing more than chemical reactions of my brain to the environment. Realizing these strategies were dysfunctional helped me find better ways to cope with depression. After providing years of emotional support for my mother, I realized I needed to put my own health first.

A year later, I returned to my Ph.D. My professor was supportive, and gave me the chance to start over with a new project. I pushed harder than ever, trying to compensate for the time lost while I was hospitalized. I was desperate, thinking, "If I fail, everything I built my life on will be in vain." But I struggled to keep up, and my initial euphoria at being back at university faded rapidly. I drifted, once more, straight into crisis.

My second stay in the hospital finally cleared my mind. I'd become so obsessed with rationality that I had put my life at risk—twice. Admitting that I needed to leave science and focus on self-care and acceptance was frightening. At first, I felt more lost than ever before. But ultimately, failing in academia was the greatest relief I ever experienced. And now I have a new goal: I want to give back the precious care I was lucky to receive—by becoming a psychiatric nurse. ■

Eric Martiné is a former Ph.D. student at Philipps University of Marburg.

If you are having thoughts of suicide, call or text 988 in the United States or go to findahelpline.com for numbers in other countries.

ILLUSTRATION: ROBERT NEUBECKER

NOMIS & Science
YOUNG EXPLORER AWARD 2025

Research at the intersection of the social and life sciences

Unconventional. Interdisciplinary. Bold.

The NOMIS & *Science* Young Explorer Award recognizes and rewards early-career M.D., Ph.D., or M.D./Ph.D. scientists who perform research at the intersection of the social and life sciences. Essays written by these bold researchers on their recent work are judged for clarity, scientific quality, creativity, and demonstration of cross-disciplinary approaches to address fundamental questions.

A cash prize of up to USD 15,000 will be awarded to essay winners, and their engaging essays will be published in *Science*. Winners will also be invited to share their work and forward-looking perspective with leading scientists in their respective fields at an award ceremony.

Apply by May 15, 2025
at www.science.org/nomis

NOMIS
FOUNDATION
Creating the Spark

Science
AAAS